DISSERTATION / DOCTORAL THESIS

Titel der Dissertation /Title of the Doctoral Thesis

„Strongly interacting dark matter candidates and the search for dark radiation from dark matter decays“

verfasst von / submitted by

Marco Nikolic, BSc MSc

angestrebter akademischer Grad / in partial fulfilment of the requirements for the degree of

Doktor der Naturwissenschaften (Dr.rer.nat.)

Wien, 2023 / Vienna, 2023

Studienkennzahl lt. Studienblatt / degree programme code as it appears on the student record sheet:	UA 796 605 411
Dissertationsgebiet lt. Studienblatt / field of study as it appears on the student record sheet:	Physik
Betreut von / Supervisor:	Ass.-Prof. Mag. Dr. Josef Pradler

Abstract

In this PhD thesis, we study: 1) the viability of strongly interacting massive particles (SIMPs), including SIMP bound states and, 2) “dark radiation” originating from unstable dark matter in direct detection experiments and in PTOLEMY.

We consider SIMPs emerging from chiral symmetry breaking in dark $Sp(4)_c$ gauge theories, similar to pions in QCD. These particles become massive when the flavour symmetry is explicitly broken, e.g. in the presence of a mass term in the UV-complete Lagrangian. In order to understand the particle structure and breaking patterns of $Sp(4)_c$ theories, we provide an effective description of $Sp(4)_c$ theories, the mass spectrum of generated particles, their flavour multiplet structure and scattering channels for $N_f = 2$ fundamental dark fermions in presence of small mass splittings and a $U(1)'$ gauge coupling. We find 5 SIMPs, 10 vector mesons, 5 axial-vector mesons, and one iso-singlet in our theory. In addition, we study the potential formation of bound states comprised of two SIMPs and its effect on the freeze-out history in the early universe. In the first analysis, we show that the strength of the reaction $3\pi \to \pi X$ regulates the freeze out of free SIMPs π in the presence of bound states X.

Measurements of dark radiation being a decay product of dark matter, offer a new possibility to shed light on the particle nature of dark matter. For this purpose, we consider dark radiation in the form of Standard Model neutrinos and neutrinos that couple to baryon number, produced in two-body decays of a dark matter progenitor. We analyze the sensitivity - exclusion limits and discovery reach - in xenon-based dark matter direct detection experiments and in the proposed neutrino experiment PTOLEMY. From a Likelihood-analysis we find that direct detection experiments with an exposure less than 1 ton yr are not able to detect dark radiation in the form of Standard Model neutrinos from MeV-mass dark matter. However, experiments with futuristic exposure of 100 ton yr, like DARWIN, offer a possibility of detection. Baryonic neutrinos are in principle detectable in current generation experiments. On the other hand, PTOLEMY will be able to measure dark radiation originating from sub-eV dark matter decays with an exposure of 100 g yr in a mass range $(1, 1000)$ meV and a progenitor lifetime greater than the age of the universe.

Zusammenfassung

In dieser Doktorarbeit untersuchen wir: 1) die Theorie über stark wechselwirkende massive Teilchen (SIMPs), einschließlich gebundener Zustände aus SIMPs, und 2) „dunkle Strahlung", die von instabiler dunkler Materie stammt, in Direktdetektionsexperimenten und in PTOLEMY.

Wir betrachten stark wechselwirkende massive Teilchen (SIMPs), die aus der chiralen Symmetriebrechung in dunklen $Sp(4)_c$-Eichtheorien hervorgehen, ähnlich wie Pionen in der Quantenchromodynamik (QCD). Diese Teilchen werden massiv, wenn die Flavoursymmetrie explizit gebrochen wird, zum Beispiel in Gegenwart eines Massenterms im UV-Lagrangian. Um die Teilchenstruktur und die Symmetriebrechung der $Sp(4)_c$-Theorien zu verstehen, liefern wir eine effektive Beschreibung der $Sp(4)_c$-Theorien, das Massenspektrum der erzeugten Teilchen, ihre Flavourmultiplettstruktur und Streuung für $N_f = 2$ fundamentale dunkle Fermionen in Anwesenheit kleiner Massendifferenzen und einer $U(1)'$-Eichkopplung. In unserer Theorie finden wir 5 SIMPs, 10 Vektor-Mesonen, 5 Axialvektor-Mesonen und ein Iso-Singlet. Darüber hinaus untersuchen wir die mögliche Bildung von gebundenen Zuständen, die aus zwei SIMPs bestehen, und deren Auswirkungen auf den Verlauf des freeze-out im früheren Universum. In der ersten Analyse zeigen wir, dass die Reaktion $3\pi \to \pi X$ den freeze-out freier SIMPs π in Anwesenheit von gebundenen Zuständen X reguliert.

Messungen der dunklen Strahlung, die ein Zerfallsprodukt der dunklen Materie ist, bieten eine neue Möglichkeit, die Teilchennatur der dunklen Materie zu erforschen. Zu diesem Zweck betrachten wir dunkle Strahlung in Form von Neutrinos aus dem Standardmodell und Neutrinos, die an die Baryonenzahl koppeln. Diese Neutrinos können in Zweikörperzerfällen der dunklen Materie entstehen. Wir analysieren die Sensitivität - Ausschlussgrenzen und Entdeckungsbereiche - in Xenon-basierten Dunkle-Materie-Direktdetektionsexperimenten und im Neutrino-Experiment PTOLEMY. Aus einer Likelihood-Analyse ergibt sich, dass Experimente zum direkten Nachweis von dunkler Materie mit einer Exposition von weniger als 1 ton yr nicht in der Lage sind, dunkle Strahlung in Form von Standardmodell-Neutrinos aus dunkler Materie mit einer MeV-Masse nachzuweisen. Jedoch bieten Experimente mit einer futuristischen Exposition von 100 ton yr, wie DARWIN, eine Möglichkeit zur Entdeck-

ung. Baryonische Neutrinos sind prinzipiell in aktuellen Experimenten nachweisbar. Andererseits wird PTOLEMY mit einer Exposition von 100 g yr in der Lage sein, dunkle Strahlung aus Zerfällen von dunkler Materie mit einer Masse von sub-eV in einem Massenbereich von $(1, 1000)$ meV und einer Lebensdauer der dunklen Materie, die größer als das Alter des Universums ist, nachzuweisen.

Acknowledgements

I would like to express my sincere gratitude to all those who have contributed to the completion of this research and this thesis.

First of all, I would like to thank my supervisor Josef Pradler, who guided me and supported me during my PhD. His door was always open for me to ask questions. I would also like to express my gratitude to Massimiliano Procura at the University of Vienna for being my second supervisor in the first year of my PhD. His insightful discussions have greatly enriched my research experience, for which I am very grateful.

I would also like to thank my colleague and friend Xiaoyong Chu. His insightful discussions and shared enthusiasm for physics have not only enriched our collaborative projects but have also been a source of inspiration for my own research project. His friendship has made the challenges of scientific exploration more manageable and more fun. He was always there for me.

Furthermore, I would like to express my thanks to Suchita Kulkarni, Axel Maas, Seán Mee and Fabian Zierler for the collaboration and their support, without which this project would not have been possible.

Additionally, I would also like to express my sincere gratitude to my family and friends for their encouragement, support, patience and understanding. Your unwavering support means a lot to me.

Last but not least, I want to thank Lisa Foukal for supporting and motivating me during my Master and PhD. She is always by my side and encourages me not to give up. Her belief in my abilities has been a driving force.

Thank you all for your contributions, support, and encouragement.

Contents

Preface

This PhD thesis is split into two topics. It deals with the theory of strongly interacting massive particles (SIMPs) and dark radiation (DR) from unstable dark matter (DM) in direct detection experiments and the proposed neutrino experiment PTOLEMY.

The first topic is based on the following publication and work in progress:

- [1] S. Kulkarni, A. Maas, S. Mee, M. Nikolic, J. Pradler and F. Zierler, *Low-energy effective description of dark $Sp(4)$ theories*, SciPost Phys. 14 (2023) 044 [2202.05191].
- [2] X. Chu, M. Nikolic, J. Pradler, in preparation.

In the first project [1] the structure of SIMPs in $Sp(4)_c$ gauge theories is investigated. The general idea is based on the fact that SIMPs are Nambu-Goldstone bosons generated by chiral symmetry breaking. We construct the effective theory of SIMPs, taking into account non-degenerate masses and a $U(1)'$ coupling. In addition, we include spin-1 states, the pseudoscalar η' arising from an axial anomaly and study the multiplet structure, mass hierarchies and the validity of the theory with lattice simulations. The author of this thesis leads the work on sections $1, 2, 3, 5$ and appendices A, B, C in this paper.

In the second project [2], we investigate the possibility that SIMPs form bound states in the early universe. Such bound states may play a crucial role in the dark sector freeze-out, potentially changing the standard SIMP picture. It presents work in progress and a publication is in preparation.

The second topic about dark radiation is based on the two following publications:

- [3] M. Nikolic, S. Kulkarni and J. Pradler, *Sensitivity of direct detection experiments to neutrino dark radiation from dark matter decay and a modified neutrino-floor*, Eur. Phys. J. C 82 (2022) 650 [2008.13557].
- [4] K. Bondarenko, A. Boyarsky, M. Nikolic, J. Pradler and A. Sokolenko, *Probing sub-eV Dark Matter decays with PTOLEMY*, JCAP 03 (2021) 089 [2012.09704].

In these projects, we study the sensitivity to dark radiation in the form of Standard Model neutrinos (SM neutrinos) in xenon-based direct detection [3] experiments and PTOLEMY [4]. We employ likelihood statistics and perform hypothesis testing in order to discriminate between dark radiation signals and irreducible backgrounds. In addition, we establish conservative exclusion limits on dark radiation when neglecting any backgrounds. The project [3] builds in part on the author's master thesis [5], where we concluded, that xenon-based direct detection experiments are not capable of detecting dark radiation in the form of Standard Model neutrinos, assuming exposures less than 1 ton yr. In this thesis, we additionally study the sensitivity for futuristic exposures and various fractions of decaying dark matter. For this case, we switch from an unbinned to a binned Likelihood analysis in order to compute the sensitivity for large statistics. In addition, we introduce dark radiation in the form of baryonic neutrinos, that couple to baryons via a $U(1)$ gauge interaction. The author of this thesis focused on all sections in the project [3] and on the sections $3, 3.1, 3.2.1, 4$ and appendices A, B in the project [4].

The thesis is structured as follows: in Part I, we motivate the existence of dark matter, providing the theoretical background of standard cosmology, the thermal history of the universe, indirect evidence of dark matter in the universe and the methods to search for dark matter. In Part II the focus is on thermal relic dark matter candidates, in particular on SIMPs and their difference to weakly interacting massive particles (WIMPs) by deriving their relic abundance today. Then, the effective theory of SIMPs in $Sp(4)$ gauge theories and the corresponding project [1] are shown. At the end of this part, the implications of the existence of SIMP bound states are discussed. In Part III we provide theoretical concepts of dark radiation in the form of Standard Model and baryonic neutrinos followed by the publications [3, 4], discussing the sensitivity limits in direct detection experiments and PTOLEMY. Detailed calculations and additional work based on these publications are presented in the appendices to each Part. Finally, in Part IV we summarize all important results of all Parts and publications.

Part I

Introduction

CHAPTER 1

Standard cosmology and new physics beyond the Standard Model

In physics, our understanding of the universe today is well described by quantum field theory (QFT) on small scales and general relativity on large scales. Within the framework of QFT, the Standard Model (SM) provides a content of particles including their antipartners interacting through strong, weak, electromagnetic force and the Higgs boson, see Fig. 1.1. However, astrophysical observations, such as the cosmic microwave background (CMB) [6] or rotation curves of galaxies [7], point to the existence of a dark sector, making the particle content incomplete.

Whereas the Standard Model explains particles and their interaction on small scales, the standard cosmological model (ΛCDM) provides information about the evolution of the universe and its composition in the framework of general relativity. It is the simplest model, that explains the origin of the CMB, large-scale structure formation, and the expansion history of

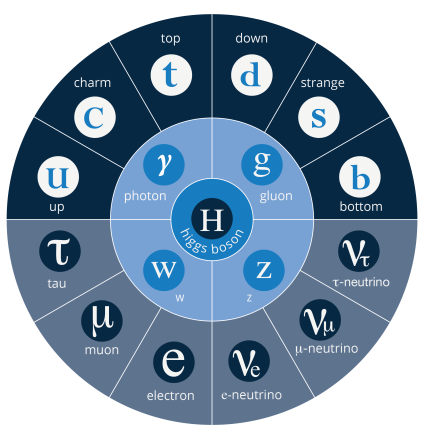

Figure 1.1: The Standard Model contains quarks, leptons, gauge bosons and the Higgs boson. The figure is taken from Ref. [8].

the universe. The energy content of the universe today is divided roughly into three parts: baryonic matter, cold collisionless dark matter and dark energy. The dark sector containing dark matter and dark energy, constitutes about 95% of the universe today, making it an important field of research.

Although, dark matter is an essential component to complete the picture of an expanding universe, its particle nature and the connection to the Standard Model sector is not fully understood. Today's observations indicate that dark matter should have three main properties: it should not interact with light, it should be stable and it should only interact through gravitation with ordinary matter. However, observations do not exclude models of dark matter with slight deviations from these properties, such as tiny electromagnetic charge, decaying dark matter or small couplings to Standard Model particles [9–11]. Allowing dark matter to couple to the Standard Model sector opens the door to phenomenology and experimental exploration.

A large community is working on models that predict dark matter candidates in a wide range of masses with different coupling strengths to the Standard Model [11]. These models are tested by experiments and astrophysical observations, like XENONnT [12], CRESST [13], LUX [14], Planck [6], just to name a few. The strategy of such experiments and observations is to reduce the parameter space of such models until dark matter is revealed. However, such experiments also face challenges, like irreducible backgrounds, making dark matter search more difficult. The most prominent model is the weakly interacting massive particle (WIMP), which couples to the Standard Model weakly and is especially searched in direct detection experiments (see review article [10] for more details).

In the following, we will motivate the existence of dark matter in the universe, explaining the standard cosmology model, the thermal history of the universe followed by indirect astrophysical observations of dark matter. At the end of the introductory part, we discuss the experimental methods used to search for dark matter.

1.1 The ΛCDM model

The standard cosmology or ΛCDM model describes the evolution of the universe and its energy composition on large scales in the framework of general relativity, assuming a homogeneous and isotropic universe. The equations of cosmology are known as the first and second Friedmann equation

$$\frac{\dot{a}(t)^2 + K}{a(t)^2} - \frac{\Lambda}{3} = \frac{8\pi G}{3}\rho(t), \tag{1.1.1}$$

$$\frac{\ddot{a}(t)}{a(t)} = -\frac{4\pi G}{3}\left[3p(t) + \rho(t)\right] + \frac{\Lambda}{3}, \tag{1.1.2}$$

where $a(t)$ is the scale of expansion, K is the spatial curvature and Λ is the cosmological constant. The cosmic scale factor $a(t) = \frac{1}{1+z}$ is related to the redshift z and is defined such that $a = 1$ at the present time. The full energy density of the universe is composed of a visible sector of all SM particles and a dark matter sector,

$$\rho = \rho_{\text{SM}} + \rho_{\text{DM}}, \tag{1.1.3}$$

where $\rho_{\text{SM}} = \rho_b + \rho_R$ splits again into baryonic matter and radiation, plus further smaller contributions. The pressure $p(t) = w\rho(t)$ is related to the energy density through the equation of state, defined by the dimensionless quantity w for radiation ($w = 1/3$), non-relativistic matter ($w = 0$) and dark energy ($w = -1$). The spatial curvature K characterizes three different geometries of the universe,

$$K = \begin{cases} -1 & \text{hyperpolic} \\ 0 & \text{flat (Euclidean)} \\ 1 & \text{closed} \end{cases} . \tag{1.1.4}$$

Whereas in a hyperbolic universe, expansion overcomes gravity attraction and the universe would expand forever, in a closed universe space-time will be contracted by gravity. Current data [6] show that the universe is nearly flat. The cosmological constant Λ was first introduced by Einstein in order to counterbalance gravity attraction and to obtain a static universe. However, it turned out that a static universe is unstable. Much later, the acceleration of the expansion was confirmed and $\Lambda = (4.24 \pm 0.11) \times 10^{-66}$ eV^2 is associated with dark energy and positive definite [6].

The time evolution of the energy density is given by the fluid equation

$$\dot{\rho} = -3H(\rho + p), \tag{1.1.5}$$

where $H(t) = \frac{\dot{a}(t)}{a(t)}$ is the Hubble parameter related to the expansion of the universe. The solution $\rho \sim a^{-3(1+w)}$ represents the evolution of the energy density of the individual components,

$$\rho \sim \begin{cases} a^{-4} & \text{radiation} \\ a^{-3} & \text{matter} \\ \text{const.} & \text{dark energy} \end{cases} . \tag{1.1.6}$$

In the following Sec. 1.2 we will see, that there will be epochs dominated by radiation, matter and dark energy density. This has an effect on the expansion history of the universe.

The first Friedmann equation can be expressed in terms of the Hubble parameter,

$$H^2 \simeq H_0^2 \left(\Omega_{R,0} a^{-4} + \Omega_{M,0} a^{-3} + \Omega_{\Lambda,0}\right), \tag{1.1.7}$$

where the density parameters $\Omega = \frac{\rho}{\rho_{\text{crit}}}$ at present time are measured by Planck [6],

$$\Omega_{M,0} \simeq 0.3111 \pm 0.0056, \qquad \Omega_{\Lambda,0} \simeq 0.6889 \pm 0.0056, \qquad \Omega_{R,0} \simeq 1 - \Omega_{M,0} - \Omega_{\Lambda,0}. \tag{1.1.8}$$

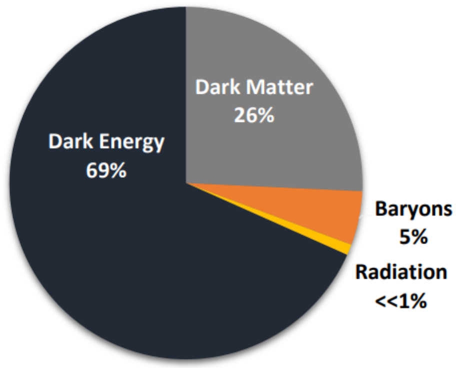

Figure 1.2: The universe's energy budget

Hence, the energy content of the universe is structured as follows. The universe consists mainly of 31% of matter and 69% of dark energy today. Matter splits again into 4.93(6)% of baryonic matter and 26.5(7)% of dark matter [15]. The rest is radiation, like photons and neutrinos, see Fig. 1.2. The Hubble parameter H_0 related to the cosmological expansion at present time was determined by observations referred to the CMB [6] in combination with baryon acoustic oscillations [16], gravitational lensing combined with time delay measurements (strong gravitational lensing) [17–20] and other local distance ladder measurements with Cepheid's and supernovae as standard candles [21–23], just to name a few. However, there is a tension [24] in the values of H_0 between early and late-time measurements. There is still a discussion about the origin of this tension, whether it is due to underestimated systematical errors or if it points to the existence of new physics beyond the ΛCDM model.

In the following chapter we will give an overview of the thermal history of the universe and the time when dark matter decouples from the visible sector of all SM particles.

1.2 The thermal history of the universe

The thermal history of the universe is explained by the "Hot Big Bang model" today [25, 26]. The universe was hot, dense and dominated by radiation. As the universe expanded[1], its temperature decreased and underwent many transitions, like electroweak and QCD phase transition. In the following sections, we will only provide an overview of the most important

[1]In the ΛCDM model the universe is 13.8 billion years old. Moreover, the universe may have experienced an initial short period of accelerated expansion known as cosmic inflation, which could also provide a solution to the flatness and horizon problem [27]. The flatness problem is a fine-tuning problem, where initial values, e.g. the Hubble parameter has to be fine-tuned in order to obtain a flat universe today. The horizon problem describes the fact, that causally disconnected events cannot share temperature, whereas CMB data shows a homogeneous observable universe close to thermal equilibrium. At the end of inflation during reheating Standard Model particles as well as dark matter particles would be produced [28].

eras after the QCD transition, when quarks and gluons were bound into hadrons due to the strong force and the electroweak force was broken into electromagnetism and the short-ranged nuclear weak force.

Event	z	T
Neutrino decoupling	10^9	1 MeV
e^-e^+ annihilation	10^9	500 keV
Big bang nucleosynthesis	10^8	100 keV
Radiation-matter equality	3387	0.8 eV
Recombination	1290	0.3 eV
Photon decoupling	1120	0.26 eV
Dark ages	$1200-30$	$300-7$ meV
Reionization	$20-6$	3 meV
matter-dark energy equality	0.4	0.33 meV
present universe	0	0.23 meV

Table 1.1: The thermal history of the universe. Here, T is the photon temperature and z is the redshift. Table taken from Refs. [25, 29].

1.2.1 An expanding universe and equilibrium physics

The expansion of the universe is an adiabatic process [25, 29] since the fluid equation (1.1.6) can be identified with the first law of thermodynamics $dU + pdV = TdS = 0$ with internal energy $U = \rho V$ and $V \sim a^3$. In this case, the entropy $S \simeq sa^3 \simeq$ const. is conserved, where $s = \frac{S}{V} = \frac{\rho+p}{T}$ is the entropy density. Cosmological observations, e.g. the cosmic microwave background and the abundance of light elements produced during Big Bang nucleosynthesis indicate, that particle species were in thermal equilibrium in the early universe. Each particle decouples from the thermal bath, when its interaction rate, which keeps it in the thermal equilibrium, reaches the Hubble parameter and subsequently drops below it,

$$\begin{array}{c|c} \text{thermal equilibrium} & \text{decoupling} \\ \Gamma_{\text{int}} \gg H & \Gamma_{\text{int}} \simeq H. \end{array}$$

There are two main reasons for decoupling. First, the temperature drops and interaction may be kinematically suppressed. Second, the expansion of the universe leads to a larger mean free path, making it more difficult for particles to meet. The dynamics of particles in thermal equilibrium is described by the phase space distribution $f(E,T) = \frac{1}{e^{(E-\mu)/T} \pm 1}$ with a chemical potential μ and $+1\,(-1)$ for fermions (bosons). Then, the following quantities can be defined,

$$n(T) = g \int \frac{d^3p}{(2\pi)^3} f(E,T), \quad \rho(T) = g \int \frac{d^3p}{(2\pi)^3} E f(E,T), \tag{1.2.1}$$

where n is the number density, ρ is the energy density and g are degrees of freedom. For relativistic and non-relativistic particles, we listed n and ρ in Tab. 1.2. For relativistic particles, we used $T \gg \mu$ [30]. The total entropy density is then given by the sum over relativistic fermions and bosons and yields $s = \frac{2\pi^2}{45} g_{\star s}(T) T^3$, where $g_{\star s}$ are relativistic degrees of freedom associated with the entropy density,

$$g_{\star s}(T) = \sum_{i=\text{ bosons}} g_i \left(\frac{T_i}{T}\right)^3 + \frac{7}{8} \sum_{i=\text{ fermions}} g_i \left(\frac{T_i}{T}\right)^3 . \tag{1.2.2}$$

	relativistic		non-relativistic
	boson	fermion	
$f(E,T)$	$\frac{1}{e^{(E-\mu)/T}-1}$	$\frac{1}{e^{(E-\mu)/T}+1}$	$e^{-(E-\mu)/T}$
$n(T)$	$g\frac{\zeta(3)}{\pi^2}T^3$	$\frac{3g}{4}\frac{\zeta(3)}{\pi^2}T^3$	$g\left(\frac{mT}{2\pi}\right)^{3/2} e^{-(m-\mu)/T}$
$\rho(T)$	$g\frac{\pi^2}{30}T^4$	$\frac{7g}{8}\frac{\pi^2}{30}T^4$	mn

Table 1.2: Distribution function, number density and the mass density defined for relativistic and non-relativistic particles. We used $T \gg \mu$ for relativistic particles.

1.2.2 Radiation dominated universe

Neutrino decoupling and cosmic neutrino background - The relevant interaction that keeps neutrinos in thermal equilibrium is [15, 25, 26, 29–33],

$$e^- + e^+ \rightleftharpoons \nu + \bar{\nu}. \tag{1.2.3}$$

The decoupling temperature of neutrinos is estimated in the following way: on dimensional grounds the thermally averaged cross section for $T \ll m_W$ is given by

$$\langle \sigma v \rangle \simeq G_F^2 T^2, \tag{1.2.4}$$

where $G_F \simeq 1.67 \times 10^{-5}$ GeV^{-2} is the Fermi constant and $m_W \simeq 80$ GeV is the mass of the W-boson [15]. Neutrinos decouple, when the interaction rate $\Gamma_\nu = n_\nu \langle \sigma v \rangle \simeq G_F^2 T^5$ reaches the value of the Hubble parameter,

$$\Gamma_\nu \simeq H \quad \Leftrightarrow \quad \frac{\Gamma_\nu}{H} \simeq G_F^2 M_{\text{Pl}} T^3 \simeq \left(\frac{T}{\text{MeV}}\right)^3 \simeq 1, \tag{1.2.5}$$

where $H \simeq \sqrt{g_\star} \frac{T^2}{M_{\text{Pl}}}$ is the Hubble parameter for a radiation-dominated universe, $n_\nu \sim T^3$ is the number density of neutrinos and $M_{\text{Pl}} \simeq 1.22 \times 10^{19}$ GeV is the Planck mass. Hence, neutrinos decouple around $T \simeq$ MeV. The relativistic degrees of freedom associated with the energy density $\rho = \frac{\pi^2}{30} g_\star T^4$ are given by

$$g_\star(T) = \sum_{i=\text{ bosons}} g_i \left(\frac{T_i}{T}\right)^4 + \frac{7}{8} \sum_{i=\text{ fermions}} g_i \left(\frac{T_i}{T}\right)^4 . \tag{1.2.6}$$

In this case, $g_\star = 2 + \frac{7}{8} \times 4 + \frac{7}{8} \times 6 = 10.75$, since photons, electrons, positrons, neutrinos and antineutrinos are relativistic at $T \simeq$ MeV. These neutrinos are known as the cosmic neutrino background (CνB) and have a small relic abundance today.

e^- e^+ **annihilation -** Shortly after neutrinos decouple, the temperature drops below the electron mass, $T \lesssim m_e$, leading to electron-positron annihilation to photons

$$e^- + e^+ \to \gamma + \gamma. \tag{1.2.7}$$

The other direction is kinematically suppressed since photons do not have sufficient energy to create two electrons. This process implies heating of the photon bath, but not of the decoupled neutrinos [15, 25, 26, 29–33]. The photon temperature no longer falls with $1/a$. Electron-positron annihilation is stopped by the matter–antimatter asymmetry and electrons stay in kinetic equilibrium with photons by Thomson scattering $e^- + \gamma \rightleftharpoons e^- + \gamma$. The decoupling of photons happens later and will be discussed in Sec. 1.2.4. Since neutrinos decoupled[2], the relativistic degrees of freedom associated with the entropy density[3] in the thermal equilibrium changed from

$$g_{\star s} = 2 + \frac{7}{8} \times 4 = \frac{11}{2}, \quad T > m_e \tag{1.2.8}$$

to

$$g_{\star s} = 2, \quad T \lesssim m_e. \tag{1.2.9}$$

Since entropy is conserved, $sa^3 \simeq$ const., before and after e^-e^+- annihilation and $T_\nu \propto 1/a$, we have

$$(sa^3)_{\text{before}} \simeq (sa^3)_{\text{after}} \quad \Leftrightarrow \quad \frac{g_{\star s}(T > m_e)(aT_\nu)^3}{g_{\star s}(T \lesssim m_e)(aT_\gamma)^3} \simeq \frac{11}{4}\left(\frac{T_\nu}{T_\gamma}\right)^3, \tag{1.2.10}$$

where the entropy density $s = \frac{2\pi^2}{45} g_{\star s}(T) T^3$ and $\left(g_{\star s}(aT_\gamma)^3\right)_{\text{before}} \simeq \left(g_{\star s}(aT_\nu)^3\right)$. Then, the neutrino temperature yields

$$T_\nu \simeq \left(\frac{4}{11}\right)^{1/3} T_\gamma. \tag{1.2.11}$$

The CνB today has a temperature lower than the CMB [15, 30],

$$T_{\nu,0} \simeq \left(\frac{4}{11}\right)^{1/3} T_0 \simeq 1.93 \text{ K} \simeq 1.66 \times 10^{-4} \text{ eV}. \tag{1.2.12}$$

Since $|\Delta m^2_{\text{sol}}| \simeq 10^{-4}$ eV^2, $|\Delta m^2_{\text{atm}}| \simeq 10^{-3}$ eV^2 [15], the CνB contains at least two non-relativistic neutrinos today. The lightest neutrino can still be relativistic. The CνB is not

[2] Here, we assume instantaneous decoupling. In reality, neutrinos do not decouple instantaneously, but have an effect on e^-e^+ annihilation, so that $N_{\text{eff}} \neq 3$, where N_{eff} describes any contribution to the radiation density, excluding photons.

[3] Photons, electrons, positrons, neutrinos and antineutrinos are relativistic at temperatures $T > m_e$ ($g_\gamma = 2, g_{e^-} = g_{e^+} = 2$). When the temperature falls to $T \lesssim m_e$ electrons and positrons become non-relativistic.

detectable yet, since the neutrino energies are too low. In Part III and the publication [4], we discuss a proposed experiment, that might be able to detect CνB and additionally, can provide accurate measurements of neutrino masses.

Big Bang nucleosynthesis - In this era light elements up to lithium are created [25, 33, 34]. All other elements are either produced by fusion processes in stars or during supernovae. Neutrons and protons are in thermal equilibrium through the weak interactions

$$\nu_e + n \rightleftharpoons p + e^- \tag{1.2.13}$$
$$e^+ + n \rightleftharpoons p + \bar{\nu}_e \tag{1.2.14}$$
$$n \rightleftharpoons p + e^- + \bar{\nu}_e. \tag{1.2.15}$$

Since the chemical potentials of electrons and neutrinos are small, $\mu_p \simeq \mu_n$ from chemical equilibrium. Then, the ratio between neutrons and protons freezes out with

$$\frac{n_n}{n_p} \simeq \left(\frac{m_n}{m_p}\right)^{\frac{3}{2}} e^{-\frac{m_n - m_p}{T}} \simeq \frac{1}{6}, \tag{1.2.16}$$

where the mass difference is $m_n - m_p \simeq 1.29$ MeV [15]. For $T \gg$ MeV the ratio is close to one and the number of neutrons and protons are equal. The interesting part happens, when the temperature drops below 1 MeV. Then, the number of neutrons falls drastically and the number of protons is six times higher. In Refs. [30, 33] it was shown that the proton-to-neutron ratio will freeze out at $T \simeq 0.8$ MeV. The neutron decay is slow, but reduces the proton-to-neutron ratio in the next $t \simeq 3$ min further until neutrons are bound into helium around $T \sim 0.1$ MeV,

$$\frac{n_n}{n_p} e^{-t/\tau_n} \simeq \frac{1}{7}, \tag{1.2.17}$$

where $\tau_n \simeq 15$ min is the lifetime of free neutrons. The production of light elements happens by the reactions

$$p + n \rightleftharpoons d + \gamma, \tag{1.2.18}$$
$$d + d \rightleftharpoons n + {}^3He, \tag{1.2.19}$$
$$d + d \rightleftharpoons p + T \tag{1.2.20}$$
$${}^3He + d \rightleftharpoons p + {}^4He. \tag{1.2.21}$$

and many other reactions.[4] For deuterium production $p + n \rightleftharpoons d + \gamma$, one can calculate the equilibrium ratio (Saha equation)

$$\frac{n_d}{n_p n_n} = \frac{3}{4}\left(\frac{2\pi}{T}\frac{m_d}{m_p m_n}\right)^{3/2} e^{E_d/T}, \tag{1.2.22}$$

[4]For instance, tritium T is unstable and will decay.

where the binding energy of deuterium is $E_d = m_n + m_p - m_d \simeq 2.2$ MeV. Next, we assume $n_p \simeq n_b \sim \eta n_\gamma \sim \eta \frac{2\zeta(3)}{\pi^2} T^3$ and

$$\frac{n_d}{n_p} \simeq \eta \left(\frac{T}{m_n}\right)^{3/2} e^{E_d/T}, \tag{1.2.23}$$

where the baryon-to-photon ratio is $\eta = \frac{n_b}{n_\gamma} \simeq 6 \times 10^{-10}$ [15]. The deuterium abundance at $T \simeq 1$ MeV is negligible small, $n_d/n_p \simeq 10^{-13}$. For $T \lesssim 0.065$ MeV deuterium becomes relevant. The deuterium production is delayed due to the photodissociation from photons at the end of the high-energy tail of their spectrum $E_\gamma > E_d$ [15].

Helium is produced, once deuterium is formed. Most of the remaining neutrons end up in helium ^4He, hence the helium-to-proton mass fraction is given by

$$\frac{m_{He}}{m_H + m_{He}} = \frac{4n_{He}}{n_H + 4n_{He}} = \frac{2n_n}{n_n + n_p} = \frac{1}{4}, \tag{1.2.24}$$

where we used $n_n \simeq \frac{1}{7} n_p$ and that all neutrons end up in helium, $n_{He} = \frac{1}{2} n_n$. The number density of hydrogen is given by protons, not in helium, $n_H = n_p - n_n$. This corresponds to an abundance ratio $^4He/H = 1/12$, since the helium is four times larger than hydrogen. Lithium is formed by reactions with helium and leads to smaller abundance [34]. However, there is a discrepancy between the primordial lithium abundance predicted by standard Big Bang nucleosynthesis + CMB and observations of metal-poor stars. This is known as the *primordial lithium problem* [15, 35] and possibly points to new physics.

1.2.3 Radiation-matter equality

The radiation-matter equality is reached when the radiation and matter densities become equal, $\rho_R(T_{\text{eq}}) = \rho_M(T_{\text{eq}})$. As discussed in Sec. 1.1 the radiation and matter densities scale with a^{-4} and a^{-3}, respectively. Since we know how the densities evolve in time, the redshift at radiation-matter equality [6, 29, 30] is given by

$$z_{\text{eq}} = \frac{\rho_{M,0}}{\rho_{R,0}} - 1 \simeq 3387 \pm 21, \tag{1.2.25}$$

where $\rho_{M,0}, \rho_{R,0}$ are matter and radiation densities at present time. This corresponds to a temperature $T_{\text{eq}} \simeq 0.8$ eV. As the temperature decreases, matter will dominate over radiation density. At this point, the universe changes its expansion behaviour from $a(t) \sim t^{1/2}$ (radiation-dominated) to $a(t) \sim t^{2/3}$ (matter-dominated) [30]. Consequently, the Hubble parameter evolves from $H = \frac{1}{2t}$ to $H = \frac{2}{3t}$. As the radiation density decreases, so does the radiation pressure, which acts as a counterpart to gravity and is responsible for keeping the baryonic matter from collapsing and forming structures. As we will discuss in the next section, when photons and baryonic matter decouple, matter could form massive and denser regions. Since dark matter is not affected by photons and radiation pressure, gravitational attraction allowed dark matter to collapse earlier and to build up high density regions. The baryonic matter would then be accumulated in these dark matter clusters by gravitational attraction after photon decoupling [30].

1.2.4 Matter dominated universe

Recombination and photon decoupling - The recombination epoch happened around $T \lesssim 0.26$ eV [25, 26, 29–31]. Before this era, matter and radiation were coupled tightly through Thomson scattering $e^- + \gamma \rightleftharpoons e^- + \gamma$ and the universe was not transparent. Since the universe expanded, the temperature decreased continuously and the energy of protons and electrons was sufficiently low to form electrically neutral hydrogen through $p + e^- \rightleftharpoons H + \gamma$ (recombination). Consequently, the number of free electrons and protons reduces drastically and Thomson scattering becomes insufficient to maintain kinetic equilibrium between matter and radiation. Thus, matter and radiation decouple from each other. At this point, the mean free path of photons exceeds the Hubble radius $l_H = H^{-1}$ and photons were able to propagate freely. The universe became transparent. These photons are the cosmic microwave background (CMB) and have a temperature $T_0 \simeq 2.7$ K today [6].

The time of recombination can be derived as follows [25, 26, 30–33]. Denote n_H, n_p, n_e as the number densities of hydrogen, free protons and free electrons. For simplicity, assume all protons and electrons form hydrogen and no other elements. Since hydrogen, protons and electrons are non-relativistic, the number density is defined as in Tab. 1.2, where the degrees of freedom are $g_H = 2g_p = 2g_e = 4$ and μ_i is the chemical potential. Since the universe is electrically neutral, $n_e = n_p$. In addition, the recombination reaction $p + e^- \rightleftharpoons H + \gamma$ maintain chemical equilibrium and the chemical potentials are $\mu_H = \mu_p + \mu_e$ ($\mu_\gamma = 0$). Then, we can write,

$$\frac{n_H}{n_p n_e} \simeq \frac{g_H}{g_p g_e} \left(\frac{m_e T}{2\pi}\right)^{-3/2} e^{E_B/T}, \tag{1.2.26}$$

where $E_B = m_p + m_e - m_H = 13.6$ eV is the binding energy of hydrogen in the ground state. Here, we approximated the hydrogen mass as $m_H \simeq m_p$ outside the exponential function. Define $X_e = \frac{n_e}{n_b}$ as the fraction of ionization, then we can express Eq. (1.2.26) as

$$\frac{1 - X_e}{X_e^2} = \frac{n_H n_b}{n_p n_e} \simeq \frac{4\sqrt{2}\xi(3)}{\sqrt{\pi}}\eta \left(\frac{T}{m_e}\right)^{3/2} e^{E_B/T}, \tag{1.2.27}$$

where $n_b = n_H + n_p \simeq \eta\frac{2\xi(3)}{\pi^2}T^3$ is the baryon number density and $\eta = \frac{n_b}{n_\gamma} \simeq 6\times10^{-10} \ll 1$ [15] is the baryon to photon ratio after e^+e^- annihilation. This equation is called the *Saha equation*[5] and describes the ionization in thermal equilibrium. For $T \gg E_B$, the RHS $\ll 1$ and hence, all protons and electrons were free, $X_e \sim 1$. Assume the recombination ends, when 90% of electrons and protons formed hydrogen, $X_e = 0.1$, then, the recombination temperature is obtained by solving the Saha equation,

$$T_{\rm rec}^{3/2} e^{E_B/T_{\rm rec}} = \frac{\sqrt{\pi}}{4\sqrt{2}\xi(3)} \frac{m_e^{3/2}}{\eta} \left(\frac{1 - X_e}{X_e^2}\right) \quad \Rightarrow \quad T_{\rm rec} \simeq 0.3 \text{ eV}. \tag{1.2.28}$$

[5] According to [30] the time of recombination was derived through the Boltzmann equation $\dot{n}_e + 3Hn_e = -\langle\sigma v\rangle_{\rm rec}(n_e^2 - (n_e^{\rm eq})^2)$ with the thermally averaged recombination cross section $\langle\sigma v\rangle_{\rm rec} = \frac{4\pi^2\alpha}{m_e^2}\frac{E_B}{\sqrt{3m_eT}}$ for hydrogen in ground state.

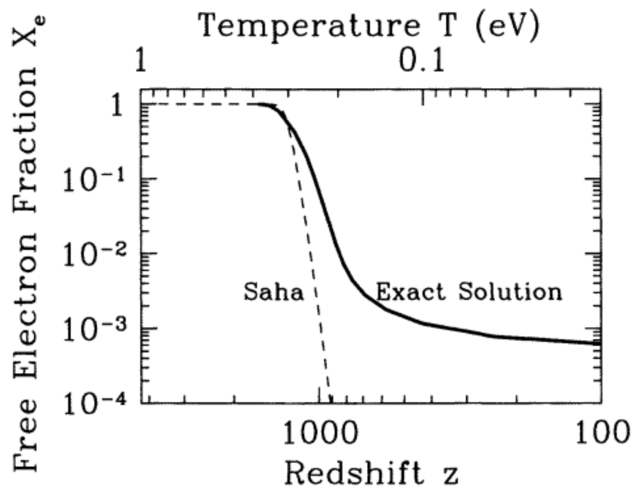

Figure 1.3: The difference between the Saha equation and the 2-level process by Peebles [31]. Ground state recombination has a small effect. Hydrogen can only be formed by capturing electrons in higher orbitals. Then, the excited states decay to the ground state.

This corresponds to a redshift factor $z_{\rm rec} \simeq 1290$. The Saha equation is a good approximation for the evolution of free electrons, but is only valid as long as the chemical equilibrium is maintained by the recombination reaction $p + e^- \rightleftharpoons H + \gamma$. However, as n_p, n_e, X_e falls toward the end of recombination, the reaction $p + e^- \rightleftharpoons H + \gamma$ is no longer able to maintain equilibrium[6], since it is less probable to find a partner to recombine. In addition, the ionization of hydrogen prevents the formation of hydrogen in the ground state. The only way to form hydrogen are excited states ($2s$, $2p$), that decay to the ground state. An accurate evolution of the fractional ionization X_e is obtained by the 2-level recombination process by Peebles, for more details see [31, 36]. The difference between the Saha equation and the derivation by Peebles is shown in Fig. 1.3.

Photons decouple from the thermal equilibrium, when $\Gamma_\gamma = n_e \sigma_T \simeq H$, where $\sigma_T = \frac{8\pi\alpha^2}{3m_e^2} \simeq 6.65 \times 10^{-25}$ cm^2 [15] is the Thomson cross section and α is the fine structure constant. Then, we can estimate the temperature, when photons are decoupled,

$$\Gamma_\gamma(T_{\rm dec}) \simeq H(T_{\rm dec}) \quad \Leftrightarrow \quad T_{\rm dec} X_e(T_{\rm dec})^{2/3} \simeq \left(\frac{\pi^2}{2\zeta(3)\eta} \frac{H_0 \sqrt{\Omega_{M,0}}}{\sigma_T} \right)^{2/3} \frac{1}{T_0}, \tag{1.2.29}$$

where $H(T) = H_0 \sqrt{\Omega_{M,0}} \left(\frac{T}{T_0} \right)^{3/2}$ in a matter-dominated universe, $n_e = X_e n_b$ and $X_e \approx 0.007$. The decoupling temperature is then given by $T_{\rm dec} \simeq 0.26$ eV. This corresponds to a redshift factor $z_{\rm dec} \simeq 1130$. We see that photons decouple at the end of the recombination epoch, when the universe is neutral.

[6]The chemical equilibrium is maintained as long as $\Gamma_{p+e^- \rightleftharpoons H+\gamma} > H$.

Dark ages and Reionization - After recombination the universe is filled with CMB photons decoupled from matter. The photons are in the visible range, but become infrared due to the redshift. There are no stars yet, but matter collapses by gravitational force. As the universe expands, the temperature drops continuously and the first stars begin to form around $z \sim 30$ [37]. The period between the last scattering of CMB photons and the formation of the first stars is known as the *dark ages* [38]. Towards the end of the dark ages, the *reionization epoch* starts. The universe is filled (up to small abundances of light elements, like helium and lithium) with hydrogen gas. The appearance of stars during the dark ages ionizes the hydrogen gas surrounding them. During this time, the first galaxies are formed. As the number of stars and galaxies increases, the intergalactic medium becomes more ionized, leading to the ionization of the whole universe today. One powerful probe of reionization despite CMB and Lyα[7] is the spin-flip or hyperfine line of neutral hydrogen [39, 40]. Photons can be absorbed by hydrogen in the ground state or be emitted with a wavelength of 21 cm. The EDGES collaboration [41] reported events of a 21 cm absorption line but is in contradiction with the SARAS3 radio telescope [42], that measured radio signals from hydrogen in the early universe.

1.2.5 Dark-energy dominated universe

Present universe - After 13.8 Gyr [6] the universe reached its present state. All stars, planets and galaxies were formed and the black body spectrum of the CMB photons cooled down to a temperature of 2.7 K. The matter-dark energy equality happened around $T \simeq 0.33$ meV ($t \simeq 9$ Gyr) [29]. Since then, the universe has been dark energy-dominated and has been expanding at an accelerated pace with $a(t) \propto \exp(H_0 t)$.

1.2.6 Dark matter freeze-out scenario

In the early stages of the universe, dark matter may well have been in thermal equilibrium with the Standard Model sector. Here, we concentrate on thermal relic dark matter[8]. The dominant interaction, that keeps dark matter in equilibrium, depends on the dark matter model [43, 44]. At some point in time, the interaction becomes slow and dark matter decouples from the rest of the particles. After decoupling the energy content of dark matter is only altered by the expansion of the universe and no longer by interactions with the Standard Model sector. This moment of decoupling is known as the freeze-out and happens before radiation-matter equality. The freeze-out temperature $T_F = \frac{m_{\mathrm{DM}}}{x_F}$ can be estimated by the dimensionless quantity $x_F \simeq 20$ appearing in the Boltzmann equation. In Part II the focus will be on thermal dark matter candidates and their freeze-out scenario.

[7]The Lyman α line corresponds to photons that are emitted when an excited hydrogen state $H(2p)$ decays to the ground state.

[8]There exist also other dark matter candidates with different production mechanisms, e.g. FIMPs, axions or primordial black holes.

1.3 Evidence for dark matter

The existence of dark matter is supported by many observations, indicating dark matter to be electrically neutral, long-lived and gravitationally interacting. As we already mentioned in Sec. 1.1 the introduction of the dark sector is essential to complete the picture of an expanding universe. There exist many indirect astrophysical observations and unsolved problems pointing to the existence of dark matter. In this chapter, we show some examples.

1.3.1 Dark matter observations

Coma cluster - In 1933 Fritz Zwicky [45] noticed an inconsistency in the total mass of the Coma cluster. He estimated the total mass of the Coma cluster by counting the individual galaxies and compared it with the mass obtained from the virial theorem

$$M = \frac{3R}{G}\langle v_{\parallel}^2 \rangle, \tag{1.3.1}$$

where $\langle v_{\parallel}^2 \rangle$ is the velocity dispersion parallel to the line of sight. The velocity $v_{\parallel}$ is found via Doppler shift. Since the estimated mass was smaller than the virial mass, he concluded, that the amount of invisible matter in the cluster is ~ 100 times larger than the total mass of visible matter. This was the first indication of the presence of dark matter in galaxy clusters.

Rotation curves of galaxies - Later, in 1969, Vera Rubin [7] discovered a discrepancy in velocity curves in spiral galaxies from observations and expectation, see Fig.1.4. From Newtonian mechanics stars at a distance r from the center of the galaxy with circular velocity $v(r)$ follow the equations

$$v(r) = \sqrt{\frac{GM(r)}{r}}, \qquad M(r) = 4\pi \int_0^r dr' r'^2 \rho(r'), \tag{1.3.2}$$

where $M(r)$ is the total mass within a radius r and $\rho(r)$ is the mass density. Since the population of stars decreases in the outer regions of the galaxy, the interior mass becomes constant and the velocity curves drop, $v(r) \sim \frac{1}{\sqrt{r}}$. Instead, velocity curves become constant, indicating that at large distances the total Mass $M(r)$ increases with r. Consequently, additional mass is required to be consistent with Newton's law and dark matter was indirectly observed.

Anisotropies of the cosmic microwave background - As already discussed in Sec. 1.2 CMB photons have their origin at the end of the recombination era. Anisotropies in the CMB black body spectrum are caused by density inhomogeneities at recombination and when CMB passes through the entire universe [15, 47, 48]. For instance, due to gravitational fluctuations photons from high density regions are redshifted, since they have to climb out of gravitational wells. These anisotropies are strongly related to the density parameters Ω of baryons, dark matter and dark energy today, being the cornerstone of the ΛCDM model.

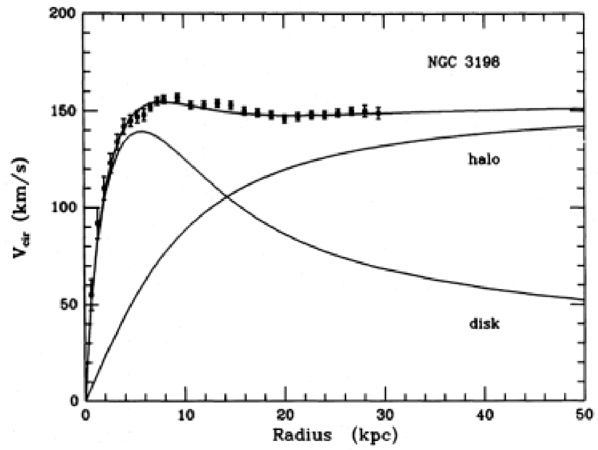

Figure 1.4: Circular velocity curves of the galaxy NGC 3198 at redshift 0.002 [46]. The visible matter of the disk galaxy is not enough to explain the observed rotation curves.

Bullet cluster - The *Bullet cluster* shows two colliding galaxy clusters at a redshift $z = 0.296$, see Fig. 1.5, providing compelling evidence for the existence of dark matter [49]. The figure illustrates how hot gas mostly made of baryonic matter (red) moves differently than dark matter (blue) in collisions. When the baryonic gas collides, it interacts and is slowed down by drag force. Whereas baryonic matter interacts with itself, dark matter remains unaffected. In other words, this showcase indicates that dark matter does not strongly interact with baryonic matter and with itself (except gravitational).

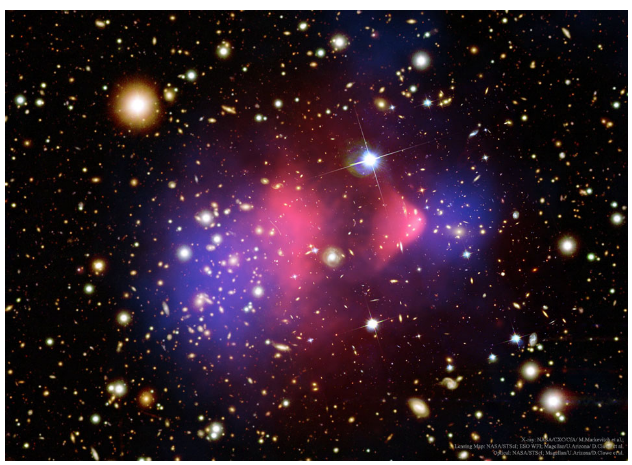

Figure 1.5: The Bullet cluster consists of two colliding galaxy clusters containing baryonic matter (red) and dark matter (blue). The collision moment shows that baryonic matter interacts with itself, but dark matter is unaffected. The hot gas was detected by X-rays and dark matter by gravitational lensing. The figure is taken from Ref. [50].

1.3.2 Simulations vs. observations

Cosmological simulations within the ΛCDM paradigm, i.e. assuming cold, collisionless dark matter, match observations on large scales. However, simulations are not always consistent with observations on small scales. In the following, we show three known problems on small scales, where simulations disagree with observations.

Missing satellite puzzle - The *missing satellite* puzzle [51–55] describes a discrepancy between the number of satellite galaxies in cosmological simulations and the observations of rotational curves of dwarf galaxies, orbiting the Milky way. One possible explanation for this problem may be, that dwarf galaxies were not able to collect sufficient amount of baryonic matter and gas to form stars. Hence, these galaxies are ultra-faint making them difficult to detect. Other solutions may be, that dwarf galaxies merged with the host galaxy during formation, photoionization may prevent the formation of stars, supernovae may eject baryonic gas from the galaxy, or stars of the dwarf galaxy were stripped away by tidal forces leaving ultra-faint diffuse small galaxies consisting of dark matter. Around 10 ultra-faint dwarf galaxies with 99.9% of dark matter were observed [56]. Including these feedback mechanisms in the simulations, the discrepancy reduces.

The too big to fail problem - The *too big to fail* problem [55, 57] is closely related to the missing satellite puzzle. In addition to the missing satellite problem, ΛCDM simulations predict also more massive satellites than observed. Whereas the missing satellite problem can be solved by ultra-faint satellites, these satellite galaxies are so massive that visible matter must have formed and we would be able to detect them. In other words, such galaxies are *too big to fail* to host stars.

Cusp vs. core problem - Whereas N-body simulations predict cuspy dark matter profiles in the inner region of galaxies, observations indicate galaxies with a central core [58]. This is known as the *core cusp problem.* Navarro, Frenk and White [59] identified a spherical symmetric density profile via N-body simulations,

$$\rho(r)_{\mathrm{NFW}} = \frac{\rho_0}{\frac{r}{r_s}\left(1+\frac{r}{r_s}\right)^2}, \tag{1.3.3}$$

where r_s, ρ_s are the scaling radius and density. For small radii, the NFW density profile shows cuspy behaviour in the dark matter distribution, $\rho \sim 1/r$. At large distances the profile scales with $1/r^2$, leading to constant velocity rotations curves, as expected. Core profiles, however, have a constant mass density towards the center of the galaxy.

Diversity problem - The *diversity problem* in dwarf galaxies [55, 60] is related to the core vs. cusp problem. Rotational curves are a powerful tool to identify the density profile of baryonic and dark matter. Observing the maximum rotational velocity or the total mass, the shape of the dark matter density profile should be fully understood. Haloes with similar mass should have similar density profiles. However, a diversity in rotational curves in the innermost regions of dwarf galaxies is observed. This effect may partly be explained by outflows or inflows of baryonic matter, which redistribute dark matter and increase or decrease the density around the center [55]. Another solution may be self-interacting dark matter (SIDM) [61], which is a model beyond the ΛCDM model.

1.4 Self-interacting dark matter

In the last section, four problems were mentioned, where simulations based on the ΛCDM model do not agree with observations on small scales. One possible solution to these problems could be self-interacting dark matter, which was first proposed by Spergel & Steinhardt as a solution to the core vs. cusp and missing satellite problem [62]. The introduction of self-interacting dark matter can alter the density profile around the center. This effect can turn a cuspy profile into a core. In addition, self-interacting dark matter can also solve the "too big to fail" problem, since it leads to smaller circular velocities in the inner region of galaxies [63, 64].
The local collision rate [55] in a halo is given by

$$R_{\rm scat} = \frac{\sigma v_{\rm rel} \rho_{\rm DM}}{m_{\rm DM}} \simeq 0.1{\rm Gyr}^{-1} \times \left(\frac{\rho_{\rm DM}}{0.1{\rm M}_\odot/{\rm pc}^3}\right)\left(\frac{v_{\rm rel}}{50\ {\rm km/s}}\right)\left(\frac{\sigma/m_{\rm DM}}{1\ {\rm cm}^2/{\rm g}}\right), \tag{1.4.1}$$

where $\rho_{\rm DM}$ is the dark matter density, $m_{\rm DM}$ is the dark matter mass, σ is the self-interacting cross section and $v_{\rm rel}$ is the relative velocity. A typical dwarf sized galaxy has a central density $\rho_{\rm DM} \sim 0.1{\rm M}_\odot/{\rm pc}^3$ and $v_{\rm rel} \simeq 50$ km/s. In this case, $\sigma/m_{\rm DM} \sim 1$ cm^2/g is required in order to have an effect on the halo density. This corresponds approximately to one scattering per 10 Gyr. On the one hand, at dwarf scales with $v_{\rm rel} \simeq 50$ km/s a large self-interacting cross section is necessary, $\sigma/m_{\rm DM} \sim 0.5 - 5$ cm^2/g, to solve small scale anomalies [55, 61], while being consistent on larger scales. On the other hand, at cluster scales with $v_{\rm rel} \simeq 1000$ km/s the observation of the Bullet cluster provides an upper bound $\sigma/m_{\rm DM} \lesssim 1$ cm^2/g [65], leading to weaker self-scatterings. Some clusters prefer self-interacting dark matter models with $\sigma/m_{\rm DM} \sim 0.1$ cm^2/g [66]. In this case, a constant cross section is ruled out. In general, self-interacting cross sections are velocity-dependent, as many particle models predict.

1.5 The search of dark matter

Last but not least, we discuss how dark matter can be searched in experiments in general [10, 55, 67, 68]. Current experiments assume that dark matter couples to Standard Model particles via an additional interaction apart from gravitational attraction. If dark matter interacted with the Standard Model in the early universe, then it must also do so today, even when the probability of interaction is generally small. In Fig. 1.6 a schematic view of possible dark

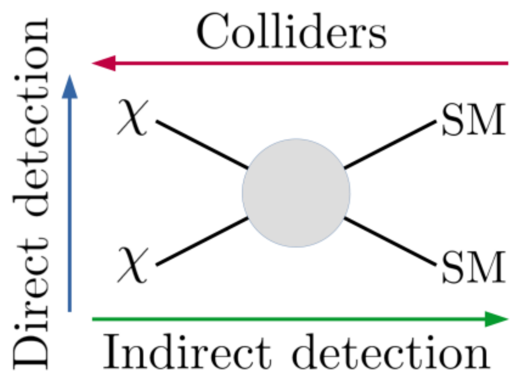

Figure 1.6: Experimental methods to search for dark matter. Figure taken from Ref. [67].

matter searches is shown. The interaction with the Standard Model is mainly divided into three categories:

- **Indirect detection** DM DM $\to$ SM SM and DM $\to$ SM SM:
  Indirect detection experiments focus on detecting annihilation products and decay products of dark matter, like gamma rays, neutrinos or charged leptons. Whereas photons and neutrinos are mostly unaffected during propagation, charged leptons, on the other hand, feel magnetic fields and interact with the interstellar medium based on the Standard Model annihilations. Constraints on the annihilation cross section and the lifetime of dark matter are provided by measuring cosmic ray events, e.g. in AMS-02 [69] and PAMELA [70]. The telescopes MAGIC [71], VERITAS [72] and H.E.S.S [73] are a system of imaging atmospheric Cherenkov telescopes at Earth, measuring cosmic gamma rays in a GeV$-$TeV energy range. Other gamma-ray detectors are Fermi-LAT [74], HAWC [75] and a new generation of ground-based gamma-ray telescopes Cherenkov Telescope Array (CTA) [76]. For example, constraints from neutrino detection are provided by ANTARES [77], IceCube [78] and SuperKamiokande [79].

- **Direct detection** DM SM $\to$ DM SM:
  Direct detection experiments search for nuclear or electron recoils of dark matter in our galaxy. As heavy dark matter (GeV$-$TeV) can generate sufficiently large recoil energies, sub-GeV dark matter is searched by absorption or scattering off electrons. Additionally, nuclear recoils can be detected in combination with electron scatterings, like Bremsstrahlung and Migdal effect [80–84] in order to enhance the sensitivity to sub-GeV dark matter. Direct detection experiments try to detect recoil energies in order to determine the coupling and cross section of dark matter to matter and the dark matter mass [67, 68]. Current experimental constraints are provided by XENON1T [12], CRESST [13], LUX [14], SENSEI [85] and PANDAX-II [86], just to name a few. However, such experiments are also challenged with irreducible backgrounds, reducing the

sensitivity to dark matter. Irreducible backgrounds in xenon-based direct detection experiments will be discussed in Part III in more detail.

- **Collider searches** SM SM $\rightarrow$ DM DM: Colliders can probe new physics by detecting new particles or missing energy. Since dark matter interacts feebly with ordinary matter, it would escape the detector and would induce events of missing transverse energy. In addition, one can also constrain the coupling and mass of mediators between the Standard Model and dark matter particles. Current collider experiments are ATLAS [87], CMS [88], LHCb [89], BaBar [90] and Belle II [91], just to name a few.

Major efforts are being made to explore the nature of dark matter, but no dark matter signal has yet been found. In the end, we discuss possible excesses, that can be interpreted as dark matter. There is a controversial dark matter claim made by the experiment DAMA/LIBRA [92], that measured the annual modulation of their event rate as is also predicted by dark matter of a time-dependent rate due to the movement of the Earth around the Sun. However, this result is in contradiction with constraints from direct detection experiments. Therefore, experiments, like COSINE-100 and ANAIS-112 are built to verify the results by DAMA/LIBRA[9]. A few years ago, XENON1T observed low-energy electron recoils [96], that could be interpreted as solar axions or bosonic dark matter. There was also a discussion about whether this signal has its origin in additional backgrounds, e.g. β-decays of tritium. However, the upgraded experiment XENONnT reported no excess above background in the low energy region [97]. The AMS-02 detector on the International Space Station (ISS) detected an excess of high energy positrons from cosmic rays [98], that could be sourced by dark matter annihilations.

[9] The COSINE-100 experiment found an annual modulation with almost opposite phase to DAMA/LIBRA [93]. On the other hand, ANAIS-112 collaboration sees no modulation [94, 95]. More data needs to be taken to confirm or refute the DAMA/LIBRA experiment.

Part II

Strongly interacting massive dark matter candidates

CHAPTER 2

Thermal relic dark matter

After summarizing important facts about the universe and dark matter in general, we discuss possible descriptions of dark matter candidates. There exist many models about dark matter [11] with different mass ranges, different production processes and different coupling strengths to Standard Model particles, e.g. axions, WIMPs, FIMPs, primordial black holes, just to name a few. All these models are continuously tested by experiments and astrophysical observations in order to reduce their parameter space in the region of interest. In this part, we mainly focus on the specific thermal relic dark matter candidate SIMP (strongly interacting massive particle), that was thermally created in the early universe. As a reminder, we first discuss the freeze-out mechanism of weakly interacting massive particles (WIMPs). The SIMP mechanism works in a similar way, but differs in dark matter mass and interactions with the Standard Model sector.

2.1 WIMP mechanism

The most prominent dark matter candidates are weakly interacting massive particles (WIMPs), that are thermally produced in the early stages of the universe [30, 43, 44, 99–102]. In the beginning the dark matter sector and the SM sector are in thermal equilibrium[1] via annihilation channels $2\mathrm{DM} \rightleftharpoons 2\mathrm{SM}$, where two dark matter states annihilate to create SM particles (and vice versa), see Fig. 2.1. Both sectors share a single temperature as long as the thermal equilibrium is sustained. During the expansion of the universe, the temperature drops continuously. Consequently, the $2\mathrm{DM} \to 2\mathrm{SM}$ annihilation rate starts to decrease, since it is less likely to find a partner to annihilate. In parallel, the continuous decrease of temperature leads to suppression of the annihilation direction $2\mathrm{DM} \leftarrow 2\mathrm{SM}$. The reason is, that the SM sector has less energy available to produce dark matter states. At some point in time, dark matter is no longer in thermal equilibrium and decoupled from the SM sector, when the annihilation reaction almost stops. This is known as the freeze-out. The freeze-out moment happens when

[1]Full thermal equilibrium requires kinetic and chemical equilibrium.

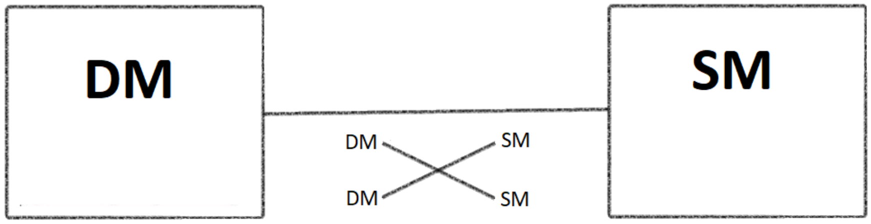

Figure 2.1: The WIMP paradigm. Dark matter is in thermal equilibrium with the SM via the annihilation process DM DM $\to$ SM SM.

the annihilation rate decreases and reaches the value of the Hubble parameter,

$$\Gamma_{2\to 2}\Big|_{T=T_F} \simeq H\Big|_{T=T_F}. \tag{2.1.1}$$

Here, T_F denotes the temperature at the freeze-out. The time evolution of the number density of dark matter is derived by the Boltzmann equation [43],

$$\frac{dn_{\rm DM}}{dt} + 3Hn_{\rm DM} = -\langle\sigma v\rangle_{2\to 2}\left[n_{\rm DM}^2 - \left(n_{\rm DM}^{\rm eq}\right)^2\right], \tag{2.1.2}$$

where $n_{\rm DM}^{\rm eq}$ is the number density of dark matter in thermal equilibrium and $\langle\sigma v\rangle_{2\to 2}$ is the thermally averaged cross section for the annihilation process 2DM $\to$ 2SM[2]. The second term on the left-hand side represents the reduction of the number density due to the expansion of the universe. The first and second terms on the right-hand side represent the annihilation and creation of dark matter. For simplicity, assume the chemical potential of dark matter is negligible small [30] and one particle species with mass $m_{\rm DM}$. The mass of WIMPs can be estimated by the freeze-out condition (2.1.1). For convenience, we define the number density as follows [30, 44]

$$n_{\rm DM} = \frac{\rho_{\rm DM}}{m_{\rm DM}} = \frac{\xi m_p \eta s}{m_{\rm DM}} = \frac{cT_{\rm eq}s}{m_{\rm DM}}, \tag{2.1.3}$$

where $\rho_{\rm DM}$ is the mass density of dark matter, $m_{\rm DM}$ is the mass of dark matter, $\xi = \rho_{\rm DM}/\rho_b$ is the ratio between the number densities of dark matter and baryons, m_p is the proton mass, $\eta = n_b/s$ is the ratio between the number density of baryons and the entropy density, s is the entropy density and $T_{\rm eq} \sim 0.8$ eV is the temperature at matter-radiation equality. The matter-radiation equality is determined, when $\rho_M^{eq} \sim \rho_R^{eq}$. Then, some of these quantities can be estimated as[3]

$$s = \frac{\kappa}{c}T^3 = \frac{2\pi^2}{45}g_{\star s}(T)T^3, \quad T_{eq} = \frac{\xi m_p \eta}{c}, \quad c = \frac{3}{4}\frac{\xi}{\xi+1}\frac{g_\star(T_{\rm eq})}{g_{\star s}(T_{\rm eq})}, \tag{2.1.4}$$

[2]Dark matter can annihilate to any number of final states. These annihilation channels will be summed up in the cross section [43].

[3]The entropy density is estimated for a radiation-dominated universe since the freeze-out moment happens later. It can be calculated by $s = \frac{p+\rho}{T}$, where p is the pressure [30]. The temperature at matter-radiation equality $T_{\rm eq}$ can be obtained from the radiation density $\rho_R = \frac{\pi^2}{30}g_\star(T)T^4$ at $T = T_{\rm eq}$.

where $g_\star(T), g_{\star s}(T)$ are relativistic degrees of freedom associated with energy (1.2.6) and entropy density (1.2.2). In addition, the Hubble parameter is given by [30]

$$H \simeq \sqrt{\frac{8\pi\rho_R}{3M_{\rm Pl}^2}} \simeq 1.67\sqrt{g_\star(T)}\frac{T^2}{M_{\rm Pl}}. \tag{2.1.5}$$

Now, we can estimate the mass of WIMPs by the freeze-out condition,

$$\Gamma_{2\to2}\Big|_{T=T_F} \simeq H\Big|_{T=T_F} \Leftrightarrow n_{\rm DM}\langle\sigma v\rangle_{2\to2}\Big|_{T=T_F} \simeq 1.67\sqrt{g_\star(T_F)}\frac{T_F^2}{M_{\rm Pl}}. \tag{2.1.6}$$

The mass of dark matter particles is obtained by solving the above equation,

$$m_{\rm DM} \simeq 0.77\alpha_{\rm eff}\left(\frac{\kappa T_{\rm eq}\,M_{\rm Pl}}{x_F\sqrt{g_\star(T_F)}}\right)^{\frac{1}{2}}, \tag{2.1.7}$$

where we parameterized the thermally averaged cross section with an effective coupling $\alpha_{\rm eff}$,

$$\langle\sigma v\rangle_{2\to2} = \frac{\alpha_{\rm eff}^2}{m_{\rm DM}^2}. \tag{2.1.8}$$

Since we consider dark matter in a TeV range, the temperature scale[4] allows us to set $g_{\star,s}(T_F) \sim g_\star(T_F) \simeq 106.75$ [26]. For a standard freeze out moment $x_F \simeq 20$ the mass of WIMPs reads

$$m_{\rm DM} \simeq \alpha_{\rm eff} \times (10\ \text{TeV}). \tag{2.1.9}$$

The WIMP may be heavier than all known particles in the Standard Model, but on the electroweak scale if $\alpha_{\rm eff} \sim 10^{-2}$ is of the order of the electroweak coupling [99]. Next, we derive an analytical expression of the dark matter relic abundance and show, that $\langle\sigma v\rangle_{2\to2}$ requires to be close to the weak scale in order to obtain the correct relic abundance for a GeV-TeV dark matter particle. We mainly follow the Refs. [30, 43, 100, 102]. The Boltzmann equation can be expressed in terms of the comoving number density (yield) $Y = \frac{n_{\rm DM}}{s}$,

$$\frac{dY}{dt} = -s\,\langle\sigma v\rangle_{2\to2}\left(Y^2 - Y_{eq}^2\right), \tag{2.1.10}$$

where the yield for non-relativistic particles in equilibrium is given by $Y_{\rm eq} = \frac{n_{\rm DM}^{\rm eq}}{s}$. The yield of dark matter before the freeze-out falls exponentially as the temperature of the universe continues to decrease and the annihilation of SM particles into dark matter states slows down. For convenience, we work with the dimensionless quantity $x = \frac{m_{\rm DM}}{T}$ and rewrite the Boltzmann equation as

$$\frac{dY}{dx} = -\frac{s}{Hx}\langle\sigma v\rangle_{2\to2}\left(Y^2 - Y_{eq}^2\right) \simeq -0.26\frac{g_{\star,s}(T)}{\sqrt{g_\star(T)}}\frac{m_{\rm DM}M_{\rm Pl}}{x^2}\langle\sigma v\rangle_{2\to2}\left(Y^2 - Y_{eq}^2\right). \tag{2.1.11}$$

[4]At temperatures $T \simeq 200$ GeV, all SM particles are relativistic in the thermal. Then, the effective degrees of freedom are $g_\star = 28 + \frac{7}{8}\times 90 = 106.75$, 28 degrees of freedom from bosons and 90 from fermions [26].

The dark matter relic abundance is expressed in terms of the yield after the freeze-out ($x \to \infty$),

$$\Omega_{\rm DM} h^2 = \frac{\rho_{\rm DM}}{\rho_{\rm crit}} h^2 \bigg|_{x\to\infty} = \frac{n_{\rm DM} m_{\rm DM}}{\rho_{\rm crit}} h^2 \bigg|_{x\to\infty} \simeq 2.8\times 10^8 \left(\frac{m_{\rm DM}}{\rm GeV}\right) Y(x\to\infty), \tag{2.1.12}$$

where $\rho_{\rm crit} = \frac{3H^2}{8\pi G} \sim 1.054\times 10^{-5}\ h^2$ GeV cm^{-3} is the critical energy density, $n_{\rm DM}(x\to\infty) = s_\infty Y(x\to\infty)$, $s_\infty = 2970$ cm^{-3} is the entropy density at present time and $h \sim 0.67$ [6] is related to the Hubble parameter $H = h \times 100$ km s^{-1} Mpc^{-1}. For convenience, we define the difference $\Delta(x) = Y(x) - Y_{\rm eq}(x)$. Then, the Boltzmann equation after the freeze-out ($x \gg x_F$, $Y_{\rm eq} \overset{x\to\infty}{\to} 0$) reduces to

$$\frac{d\Delta(x)}{dx} \simeq -0.26 \frac{g_{\star,s}(T_F)}{\sqrt{g_\star(T_F)}} \frac{m_{\rm DM} M_{\rm Pl}}{x^2} \langle\sigma v\rangle_{2\to 2} \Delta^2(x). \tag{2.1.13}$$

We can solve this equation by the method "separation of variables",

$$\int_{\Delta(x_F)}^{\Delta(\infty)} \frac{d\Delta}{\Delta^2} \simeq -0.26 \frac{g_{\star,s}(T_F)}{\sqrt{g_\star(T_F)}} m_{\rm DM} M_{\rm Pl} \langle\sigma v\rangle_{2\to 2} \int_{x_F}^{\infty} \frac{dx}{x^2}. \tag{2.1.14}$$

Then, we can express the yield after freeze out as

$$\Delta(x\to\infty) \simeq Y(x\to\infty) \simeq \frac{x_F \Delta(x_F)}{0.26 \frac{g_{\star,s}(T_F)}{\sqrt{g_\star(T_F)}} m_{\rm DM} M_{\rm Pl} \langle\sigma v\rangle_{2\to 2} \Delta(x_F) + x_F}. \tag{2.1.15}$$

The only remaining quantity to determine is the difference $\Delta(x_F)$. This is achieved by taking the Boltzmann equation at the freeze-out ($x \simeq x_F, \Delta(x) \ll Y_{\rm eq}(x)$),

$$\frac{dY_{\rm eq}(x)}{dx} \simeq -0.26 \frac{g_{\star,s}(T_F)}{\sqrt{g_\star(T_F)}} \frac{m_{\rm DM} M_{\rm Pl}}{x^2} \langle\sigma v\rangle_{2\to 2} \Delta(x) \underbrace{(\Delta(x) + 2Y_{\rm eq}(x))}_{\simeq 2Y_{\rm eq}(x)}. \tag{2.1.16}$$

Since $\frac{dY_{\rm eq}}{dx} \sim -Y_{\rm eq}$ for large enough x, we can express Δ at $x \simeq x_F$ as

$$\Delta(x_F) \simeq \frac{x_F^2}{0.52 \frac{g_{\star,s}(T_F)}{\sqrt{g_\star(T_F)}} m_{\rm DM} M_{\rm Pl} \langle\sigma v\rangle_{2\to 2}}. \tag{2.1.17}$$

Then, inserting in Eq. (2.1.14) yields,

$$Y(x\to\infty) \simeq \frac{x_F}{0.26 \frac{g_{\star,s}(T_F)}{\sqrt{g_\star(T_F)}} m_{\rm DM} M_{\rm Pl} \langle\sigma v\rangle_{2\to 2}}. \tag{2.1.18}$$

Now, we have all the ingredients to express the relic abundance of WIMPs,

$$\Omega_{\rm DM} h^2 \simeq\sim 2.8\times 10^8 \left(\frac{m_{\rm DM}}{\rm GeV}\right) Y(x\to\infty) \simeq 8.8\times 10^{-11} \frac{\sqrt{g_\star(T_F)} x_F}{g_{\star,s}(T_F)} \left(\frac{\rm GeV^{-2}}{\langle\sigma v\rangle_{2\to 2}}\right). \tag{2.1.19}$$

In order to obtain the correct relic abundance for dark matter, the thermally averaged cross section requires to be close to the weak scale,

$$\Omega_{\rm DM} h^2 \simeq 0.12 \ \Rightarrow\ \langle\sigma v\rangle_{2\to 2} \simeq 1.4\times 10^{-9} {\rm GeV}^{-2}. \tag{2.1.20}$$

Exemplary, we show the relic abundance for a WIMP mass $m_{\rm DM} = 100$ GeV in Fig. 2.2.

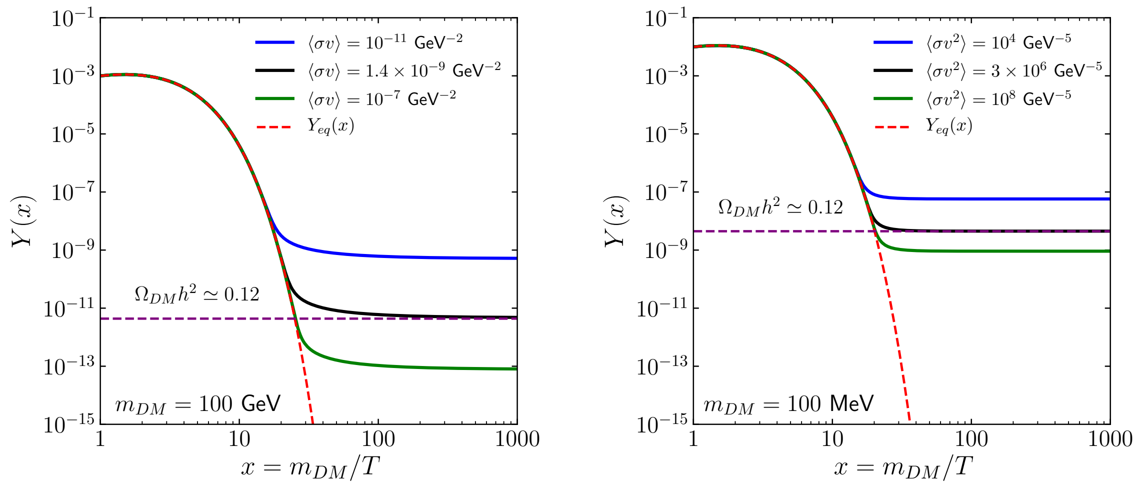

Figure 2.2: The relic abundance for WIMPs (left) and SIMPs (right).

2.2 SIMP mechanism

Since WIMPs have not been observed in different experiments and astrophysical observations, we have to ask, whether the theory of thermal WIMPs really describes the nature of dark matter. What if dark matter is not a WIMP? What if dark matter is secluded from the Standard Model in the thermal bath from the beginning? What if, dark matter has only self-interactions? A large community is working on these questions in order to find the particle nature of dark matter. Here, we present one theory by Hochberg et al. [44, 103], that could answer these questions. They constructed the theory of strongly self-interacting dark matter candidates, called strongly interacting massive particles (SIMPs). In the following, we explain the SIMP mechanism.

Assume the dark sector is isolated from the Standard Model bath. A $2 \to 2$ process would not deplete the number density of dark matter in an isolated system, but keeps the dark matter particles at one single temperature. The first number changing process would be $3 \to 2$, where three dark matter particles annihilate to create two dark matter states[5], see Fig. 2.3. The reverse direction $2 \to 3$ is energetically suppressed around freeze-out since dark matter is non-relativistic and the energy is not sufficient to produce three particles out of two dark matter states. The number changing process $3 \to 2$ implies heating in the isolated dark matter sector [104], see Fig. 2.4. The consequence would be relativistic dark matter states (see Fig. 2.5), which are excluded by galaxy structure formation [105]. However, there is a solution to this problem. Allowing dark matter to couple to the Standard Model, energy can be exchanged with the SM sector and the dark matter sector can be cooled.

[5]Since the $3 \to 2$ process is the dominant channel at the freeze out, the chemical potential of dark matter is zero [103].

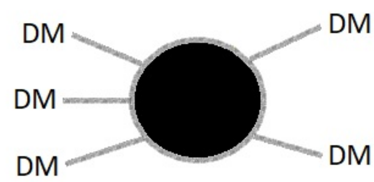

Figure 2.3: The $3 \to 2$ self interaction. This process implies heating in the dark matter sector and is responsible for the freeze out of SIMPs.

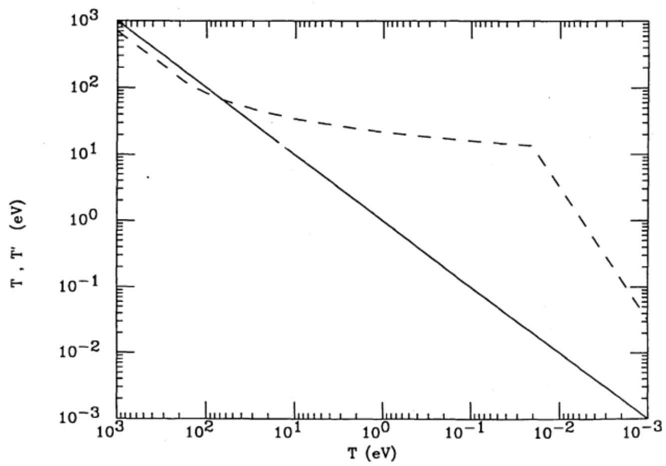

Figure 2.4: Temperature evolution of self-interacting dark matter (dotted line) without communication with the SM sector (solid line). The rapid fall of the temperature indicates the freeze out of number changing processes [104].

The time evolution of the number density of dark matter is given by the Boltzmann equation[6],

$$\frac{dn_{\rm DM}}{dt} + 3Hn_{\rm DM} = -\langle\sigma v^2\rangle_{3\to2}(n_{\rm DM}^3 + n_{\rm DM}^2 n_{\rm DM}^{\rm eq}), \tag{2.2.1}$$

where $n_{\rm DM}^{\rm eq}$ is the number density of dark matter particles in thermal equilibrium and $\langle\sigma v^2\rangle_{3\to2}$ is the thermal averaged cross section of the $3 \to 2$ process. For simplicity, we assume, there is only one particle species with mass $m_{\rm DM}$. In Chapter 3 we will also discuss the case, where particles with different masses appear. The dark matter sector decouples from the Standard Model bath (freeze-out) when the interaction rate decreases and reaches the value of the Hubble parameter,

$$\Gamma_{3\to2}\Big|_{T=T_F} \simeq H\Big|_{T=T_F}. \tag{2.2.2}$$

[6]We neglect here the annihilation channel, where dark matter annihilates to Standard Model particles. This process is sub-dominant, otherwise, dark matter is again driven by the WIMP mechanism.

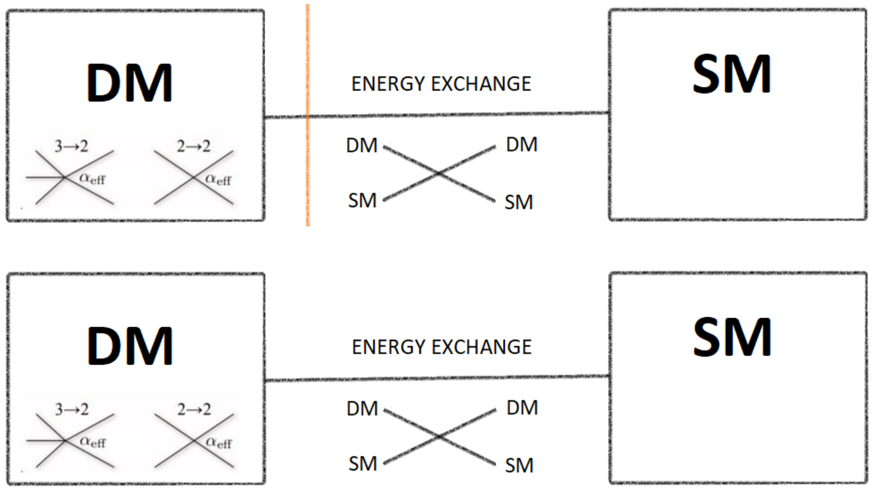

Figure 2.5: The SIMP paradigm isolated (top) and coupled to the Standard Model (bottom). The dark sector cannot be completely secluded from the Standard Model sector since the number changing process $3 \to 2$ heats up the dark sector only, creating relativistic dark matter states, which are excluded by galaxy structure formation [105].

Here, T_F denotes the temperature at the freeze-out. The interaction rate decreases for two reasons. First, the universe expands and it is less likely to find a partner to interact with. Second, the universe cools down and particles have less energy. We can again estimate the mass of SIMPs by the freeze-out condition,

$$\Gamma_{3\to 2}\Big|_{T=T_F} \simeq H\Big|_{T=T_F} \Leftrightarrow n_{\text{DM}}^2 \langle \sigma v^2 \rangle_{3\to 2}\Big|_{T=T_F} \simeq 1.67\sqrt{g_\star(T_F)}\,\frac{T_F^2}{M_{\text{Pl}}}. \tag{2.2.3}$$

Then, the mass[7] of SIMPs is given by,

$$m_{\text{DM}} \simeq 0.84\alpha_{\text{eff}} \left(\frac{(\kappa T_{\text{eq}})^2 M_{\text{Pl}}}{x_F^4 \sqrt{g_\star(T_F)}} \right)^{\frac{1}{3}}, \tag{2.2.4}$$

where we parameterized the thermally averaged “cross section” as follows

$$\langle \sigma v^2 \rangle_{3\to 2} = \frac{\alpha_{\text{eff}}^3}{m_{\text{DM}}^5}. \tag{2.2.5}$$

Here, α_{eff} is the effective coupling of the $3 \to 2$ process and can be larger than 1. On dimensional grounds $\sigma_{3\to 2}$ is not a cross section since it has units $1/E^5$. Since we consider dark matter masses of order MeV, the temperature scale allows us to set $g_{\star,s}(T_F) \sim g_\star(T_F) \simeq 10.75$. For $x_F \simeq 20$ the mass of SIMPs is several tens of MeV,

$$m_{\text{DM}} \simeq \alpha_{\text{eff}} \times (40 \text{ MeV}). \tag{2.2.6}$$

[7] In the SIMP Miracle paper [44] the pre-factor is different since the Hubble parameter is approximated as $H \simeq \sqrt{\frac{\rho_R}{3\overline{M}_{\text{Pl}}^2}} \sim 0.33\sqrt{g_\star(T)}\frac{T^2}{\overline{M}_{\text{Pl}}}$, where $\overline{M}_{\text{Pl}} = \frac{M_{\text{Pl}}}{\sqrt{8\pi}}$ is the reduced Planck mass.

Whereas WIMPs have a mass in the GeV−TeV range, SIMPs are comparably lighter. In addition, the freeze-out mechanism and the relic abundance are controlled by the strength of the $3 \to 2$ process. This is only possible, however, if the $3 \to 2$ process is dominant and 2DM → 2SM annihilations are suppressed,

$$\left.\frac{\Gamma_{\rm ann}}{\Gamma_{3\to 2}}\right|_{T=T_F} \lesssim 1, \tag{2.2.7}$$

where $\Gamma_{\rm ann}$ is the interaction rate of 2DM → 2SM channels. Otherwise, the freeze-out moment is driven by the WIMP mechanism. Since the cooling of the dark matter sector is essential, we require the ratio of the interaction rates between the cooling process $\Gamma_{\rm cool}$ and the annihilation $\Gamma_{\rm ann}$ to be small [44],

$$\frac{\Gamma_{\rm ann}}{\Gamma_{\rm cool}} = \frac{n_{\rm DM}\langle\sigma v\rangle_{\rm ann}}{n_{\rm SM}\langle\sigma v\rangle_{\rm cool}} \simeq \frac{n_{\rm DM}}{n_{\rm SM}} \lesssim 1, \tag{2.2.8}$$

where $n_{\rm SM}$ is the relativistic number density[8] given in Tab. 1.2 and $\langle\sigma v\rangle_{\rm ann} \sim \langle\sigma v\rangle_{\rm cool}$. For the last equality, we take a DM particle with 50 MeV mass. From the above conditions it follows,

$$\Gamma_{\rm ann}\Big|_{T=T_F} \lesssim \Gamma_{3\to 2}\Big|_{T=T_F} \lesssim \Gamma_{\rm kin}\Big|_{T=T_F}. \tag{2.2.9}$$

In summary, dark matter maintains thermal equilibrium via DM SM → DM SM, while annihilations to SM are suppressed. The Boltzmann equation can be expressed in terms of the comoving number density (yield) $Y = \frac{n_{\rm DM}}{s}$,

$$\frac{dY}{dt} = -s^2\langle\sigma v^2\rangle_{3\to 2}\left(Y^3 - Y^2 Y_{eq}\right) \tag{2.2.10}$$

In terms of the dimensionless quantity $x = \frac{m_{\rm DM}}{T}$, the Boltzmann equation reads [100],

$$\frac{dY}{dx} \simeq -0.115\frac{g_{\star,s}^2(T)}{\sqrt{g_\star(T)}}\frac{M_{\rm Pl}m_{\rm DM}^4}{x^5}\langle\sigma v^2\rangle_{3\to 2}\left(Y^3 - Y^2 Y_{eq}\right), \tag{2.2.11}$$

where the yield in equilibrium for non-relativistic particles is given by

$$Y_{\rm eq} = \frac{n_{\rm DM}^{\rm eq}}{s} \simeq 0.145\frac{g_{\rm DM}}{g_{\star,s}(T)}x^{3/2}e^{-x}. \tag{2.2.12}$$

An approximated analytical solution for the relic abundance was also found in Ref. [100]. We focus only on the time after the freeze-out ($x \to \infty$), where the relic abundance for a MeV dark matter is again given by Eq. (2.1.12),

$$\Omega_{\rm DM}h^2 = \left.\frac{\rho_{\rm DM}}{\rho_{\rm crit}}h^2\right|_{x\to\infty} = \left.\frac{n_{\rm DM}m_{\rm DM}}{\rho_{\rm crit}}h^2\right|_{x\to\infty} \sim 2.8\times 10^5\left(\frac{m_{\rm DM}}{\rm MeV}\right)Y(x\to\infty). \tag{2.2.13}$$

[8]When T drops below 100 MeV, the only relativistic particles in the thermal bath are electrons, positrons, photons, neutrinos and anti-neutrinos.

In terms of the difference $\Delta(x) = Y(x) - Y_{\rm eq}(x)$ the Boltzmann equation after the freeze-out ($x \gg x_F$, $Y_{\rm eq} \overset{x\to\infty}{\to} 0$) is written as

$$\frac{d\Delta(x)}{dx} \simeq -0.115\frac{g_{\star,s}^2(T_F)}{\sqrt{g_\star(T_F)}}\frac{M_{\rm Pl}m_{\rm DM}^4}{x^5}\langle\sigma v^2\rangle_{3\to2}\Delta^3(x). \tag{2.2.14}$$

In order to solve the differential equation, we integrate over x and Δ separately,

$$\int_{\Delta(x_F)}^{\Delta(\infty)}\frac{d\Delta}{\Delta^3} \simeq -0.115\frac{g_{\star,s}^2(T_F)}{\sqrt{g_\star(T_F)}}M_{\rm Pl}m_{\rm DM}^4\langle\sigma v^2\rangle_{3\to2}\int_{x_F}^{\infty}\frac{dx}{x^5} \tag{2.2.15}$$

Thus, we can express the yield after freeze-out as

$$\Delta(x\to\infty) \simeq Y(x\to\infty) \simeq \frac{\sqrt{2}x_F^2\Delta(x_F)}{\sqrt{0.115\frac{g_{\star,s}^2(T_F)}{\sqrt{g_\star(T_F)}}M_{\rm Pl}m_{\rm DM}^4\langle\sigma v^2\rangle_{3\to2}\Delta(x_F)^2 + 2x_F^4}}. \tag{2.2.16}$$

The yield difference $\Delta(x_F)$ at freeze out ($x \sim x_F, \Delta(x) \ll Y_{\rm eq}(x)$) is obtained by considering the Boltzmann equation around the freeze out,

$$\frac{dY_{\rm eq}}{dx} \simeq -0.115\frac{g_{\star,s}^2(T_F)}{\sqrt{g_\star(T_F)}}M_{\rm Pl}m_{\rm DM}^4\langle\sigma v^2\rangle_{3\to2}\frac{\Delta(x)}{x^5}\underbrace{(Y_{\rm eq}(x)+\Delta(x))^2}_{\sim Y_{\rm eq}(x)^2}. \tag{2.2.17}$$

Due to the fact that $\frac{dY_{\rm eq}}{dx} \sim -Y_{\rm eq}$ for large enough x, we can solve the Boltzmann equation for Δ,

$$\Delta(x_F) \simeq \frac{x_F^5}{0.115\frac{g_{\star,s}^2(T_F)}{\sqrt{g_\star(T_F)}}M_{\rm Pl}m_{\rm DM}^4\langle\sigma v^2\rangle_{3\to2}Y_{\rm eq}(x_F)}. \tag{2.2.18}$$

Then, Eq. (2.2.16) is given by

$$Y(x\to\infty) \simeq \frac{4g_\star^{1/4}(T_F)}{g_{\star,s}(T_F)m_{\rm DM}^2\sqrt{M_{\rm Pl}\langle\sigma v^2\rangle_{3\to2}}} \tag{2.2.19}$$

$$\times\frac{x_F^5}{\sqrt{x_F^6 + 0.23\frac{g_{\star,s}^2(T_F)}{\sqrt{g_\star(T_F)}}M_{\rm Pl}m_{\rm DM}^4\langle\sigma v^2\rangle_{3\to2}Y_{\rm eq}^2(x_F)}} \tag{2.2.20}$$

$$\simeq \frac{4g_\star^{1/4}(T_F)x_F^2}{g_{\star,s}(T_F)m_{\rm DM}^2\sqrt{M_{\rm Pl}\langle\sigma v^2\rangle_{3\to2}}} \tag{2.2.21}$$

where $0.23\frac{g_{\star,s}^2(T)}{\sqrt{g_\star(T)}}M_{\rm Pl}m_{\rm DM}^4\langle\sigma v^2\rangle_{3\to2}Y_{\rm eq}^2 \ll x_F^6$ for $m_{\rm DM} \sim O(100\text{ MeV})$. In the end, the dark matter relic abundance is approximated as

$$\Omega_{\rm DM}h^2 \simeq 2.8\times10^5\left(\frac{m_{\rm DM}}{\rm MeV}\right)Y(x\to\infty) \simeq 320\frac{g_\star^{1/4}(T_F)x_F^2}{g_{\star,s}(T_F)}\left(\frac{\rm MeV}{m_{\rm DM}}\right)\sqrt{\frac{\rm GeV^{-5}}{\langle\sigma v^2\rangle_{3\to2}}}. \tag{2.2.22}$$

For a standard freeze out moment $x_F \simeq 20$ and a dark matter relic abundance $\Omega_{\rm DM} h^2 \simeq 0.12$ [6], the thermally averaged cross section $\langle \sigma v^2 \rangle_{3\to 2} \simeq 3 \times 10^6$ GeV^{-5} for a dark matter mass $m_{\rm DM} = 100$ MeV, indicating a strong scale. In Fig. 2.2 we illustrate the dark matter yield for a dark matter mass 100 MeV and different values of averaged cross sections. Whereas the relic abundance of WIMPs is mass independent, the relic abundance of SIMPs scales with $1/m_{\rm DM}$. In the next chapter, one specific SIMP model is described.

CHAPTER 3

Publication about SIMPs

In the following publication [1] we investigate one specific model of SIMPs, where SIMPs are Nambu-Goldstone bosons generated by chiral symmetry breaking in $Sp(4)_c$ gauge theories[1]. This project is based on the first papers by Hochberg et al. [44, 103, 106]. For simplicity, we consider $N_f = 2$ dark fermions in the fundamental representation of $Sp(4)_c$[2]. The fundamental representation of symplectic groups is always pseudo-real, see App. A.1 for more details. In the absence of a mass term and a mediator between the Standard Model and the dark sector, the UV-complete Lagrangian of dark fermions has a global flavour symmetry $SU(4)$, which breaks spontaneously to $Sp(4)$ via a fermion vacuum condensate (see Sec. 3 for more details). Whenever a continuous symmetry is broken, massless Nambu-Goldstone bosons are produced. These Goldstone bosons or SIMPs are composite states made of dark fermions and live in the coset space $SU(4)/Sp(4)$, see table in Sec. 3. Whereas at high energies strong interactions are weak and both dark fermions and dark gluons are "asymptotic free", at low energies confinement leads to colourless bound states [107], where the coupling is strong[3]. In the presence of a mass term or a coupling to the Standard Model, the global flavour symmetry is explicitly broken. Consequently, Nambu-Goldstone bosons become massive. We investigate various breaking patterns, where either SIMPs carry non-degenerate masses or are coupled to a $U(1)'$ mediator. The former requires small mass splitting in the dark fermion sector. The latter depends on the charge assignment of the fermions. Moreover, there are no baryons in this theory due to the pseudo-reality. Glueballs are too heavy and are integrated out.

The dynamics of low-energetic SIMPs is captured in the effective Lagrangian. It contains kinetic, mass and interaction terms. The $3 \to 2$ interaction is absent in the chiral Lagrangian, but can be included by the Wess-Zumino-Witten interaction [108–111]. In addition, the $Sp(4)_c$ gauge theory contains an iso-singlet η' due to axial anomaly at the quantum level.

[1] A $Sp(4)_c$ theory has four colour degrees of freedom.

[2] We refer to dark fermions in this theory in order to distinguish from quarks in the Standard Model.

[3] This theory has many parallels to two flavour QCD. Pions in QCD are generated in a similar way, but fermions transform under the complex representation of the gauge group $SU(3)_c$. In this case, the global flavour symmetry $SU(N_f)_L \times SU(N_f)_R$ breaks spontaneously to $SU(N_f)_V$, where N_f is the number of light quarks involved.

Moreover, the 10 vector and 5 axial-vector mesons were introduced as gauge fields of a $SU(4)$ symmetry, as described in Sec. 3. We derived the gauged Wess-Zumino-Witten interaction with spin-1 states and an extra $U(1)'$ gauge group. In the end, we analyze the multiplet structure under $U(1)'$ and when SIMPs carry non-degenerate masses. In parallel, the theory is linked to lattice simulations, providing decay constants, mass hierarchies and testing the validity of the theory.

Low-energy effective description of dark $Sp(4)$ theories

Suchita Kulkarni, Axel Maas, Seán Mee, Marco Nikolic,
Josef Pradler & Fabian Zierler

Published in: SciPost Foundation
DOI: 10.21468/SciPostPhys.14.3.044
Preprint version in arXiv: arXiv:2202.05191 [hep-ph]
Main contributions: sections $2, 3.1, 3.2, 5$ and appendices A, B, C

SciPost | SciPost Phys. 14, 044 (2023)

Low-energy effective description of dark $Sp(4)$ theories

Suchita Kulkarni[1⋆], Axel Maas[1†], Seán Mee[1‡], Marco Nikolic[2∘], Josef Pradler[2§] and Fabian Zierler[1△]

1 Institute of Physics, NAWI Graz, University of Graz, Universitätsplatz 5, A-8010 Graz, Austria
2 Institute of High Energy Physics, Austrian Academy of Sciences, Nikolsdorfergasse 18, 1050 Vienna, Austria

⋆ suchita.kulkarni@uni-graz.at , † axel.maas@uni-graz.at , ‡ sean.mee@uni-graz.at , ∘ marco.nikolic@oeaw.ac.at , § josef.pradler@oeaw.ac.at , △ fabian.zierler@uni-graz.at

Abstract

Strongly interacting massive particles are viable dark matter candidates. We consider a dark $Sp(4)$ gauge theory with $N_f = 2$ fermions in the pseudo-real fundamental representation and construct the chiral low-energy effective theory. We determine the flavour multiplet structure and the chiral Lagrangian, including the Wess-Zumino-Witten term for mass-degenerate and non-degenerate flavours. We then study the possible charge assignments under a $U(1)'$ gauge symmetry, emphasizing on dark state stability, and provide the full Lagrangian description for Goldstone bosons and vector resonances, including the Wess-Zumino-Witten term. Finally, we use dedicated lattice simulations to determine the chiral low-energy effective theory's validity and low-energy constants. This work represents a self-consistent study of this non-Abelian theory. It thereby provides a framework for future phenomenological exploration in connection to the dark matter problem.

Received 11-03-2022
Accepted 01-12-2022
Published 22-03-2023
doi:10.21468/SciPostPhys.14.3.044

Check for updates

Contents

SciPost SciPost Phys. 14, 044 (2023)

1 Introduction

The absence of concrete, non-gravitational experimental signals for dark matter (DM) necessitates the unbroken exploration of a wide variety of scenarios. Among these are extensions of the Standard Model (SM) featuring a dark non-Abelian sector in the ultra-violet (UV) regime with confinement below some scale Λ in the infra-red (IR) regime. Within these scenarios, confinement leads to bound states, containing potentially stable particles and opens up a new class of DM candidates. The stability of bound states in such theories is either ensured by means of introducing additional symmetries or, more naturally, the result of accidental global symmetries of the theory. The composite states can then be considered DM candidates and the viability of the theory can be explored further; for an overview on composite dynamics see [1] and references therein.

The construction and exploration of associated phenomenology of such theories is however far from obvious. While the UV Lagrangian is governed by a microscopic theory, the resulting low-energy Lagrangian in the IR is an effective theory. As such, it has a limited range of validity, and is parameterized by a number of low-energy constants (LECs) [2,3]. The range of validity and the LECs are determined by the underlying theory, and can, e.g., be obtained from lattice simulations [4,5]. In general, the formulation in the IR depends on the UV details such as the gauge group, the particle content and the representations of participating fields. For example, the chiral effective theory in isolation for the mass-degenerate $Sp(4)$ theory, including a determination of its range of validity and LECs, has been analysed on the lattice in [6–8].

It is certainly possible that such theories live in isolation from the SM. Indeed, DM can adjust its abundance in the early Universe free from SM interactions, e.g., by "cannibalizing" through number-changing 3-to-2 or 4-to-2 processes in the dark sector [9–18]. However, couplings to the SM additionally allow to regulate the dark sector temperature in relation to the SM one, and, of course, open the door to experimental exploration. In either case, strongly interacting dark sectors, see, *e.g.* [11, 12, 19–47] among many other works, are of high interest in such scenarios as their low energy states are often endowed with sizeable interactions. Particular interest have received strongly-interacting massive particles (SIMPs) that are the Goldstone bosons of a dark confining gauge group and where 3-to-2 interactions are enabled by the Wess-Zumino-Witten(WZW) term [11, 12, 29]. The presence of these $3 \to 2$ interactions in association with $2 \to 2$ self-interactions has generated sizeable further activity. For example, [32] explores Abelian gauged SIMPs within $SU(N)$ theories, [48] demonstrates the importance of higher order corrections to the chiral Lagrangian for self-scattering in $Sp(2N)$ theories, [33, 35] include dark vector resonances into the SIMP paradigm, while [36, 37] have analysed effects of isospin symmetry breaking (dark quark mass non-degeneracy) for dark matter phenomenology. In most of these works, however, either a specific subset of the low-energy effective theory was studied or a SM-like, i. e. $SU(N)$ gauge group and fundamental fermions, dark sector was considered. In addition, the masses and other parameters of the theory were varied independently, instead of deriving them from the underlying UV-complete theory. Only in a few cases contact to the UV theory was made by means of lattice simulations, see [22, 30, 31, 34, 49, 50].

It is the purpose of this paper to study one particular example of a confining gauge group self-consistently, from the UV-complete Lagrangian to the low-energy description in terms of the chiral Lagrangian. Concretely, we consider a $Sp(2N)$ gauge theory with $N_f = 2$ fermions in the pseudo-real fundamental representation. We allow for mass non-degeneracy of the two flavours, study possible gauge assignments under a new dark $U(1)$ symmetry and obtain the multiplet structure of resulting low energy spectrum of mesons and vector resonances. Importantly, our findings are supported and complemented by lattice simulations. Such unifying effort is a first of its kind in the study of a non-Abelian dark sector. It provides the grounds for a comprehensive and systematically controlled and extensible framework for future phenomenological studies of this theory. $Sp(2N)$ theories as we consider in this work have also been a longstanding topic of interest in the composite Higgs community [1, 51–58]. While in isolation these theories are identical to our case, the main difference is the portal phenomenology to the Standard Model. While in the case of composite Higgs theories, some of the $Sp(2N)$ quarks transform under the Standard Model gauge group, in our theory, the $Sp(4)$ quarks are singlets under the Standard Model. This leads to different decay patterns and requirements on the theory construction compared to those considered in composite Higgs literature. We also note that in our theory, there is no tree level mixing between $Sp(4)$ spectrum particles and the SM e.g. composite sigma – SM Higgs mixing.

The paper is organized as follows: in Sec. 2 we introduce the global flavour symmetries and clarify the quantum numbers and multiplet structure of states in the low-energy description. In Sec. 3 we systematically develop the chiral Lagrangian and WZW term for the Goldstone bosons, the pseudoscalar singlet and vector resonances for mass-degenerate quarks. In Sec. 4 we couple this theory to an Abelian gauge field, discuss possible charge assignments, study the stability of states against decay into gauge bosons, provide the gauged WZW term and comment on the radiatively induced mass splitting from such interactions. In Sec. 5 we allow for mass non-degeneracy, and determine how the spectrum and interactions change. In Sec. 6 we extend previous lattice simulations to cover the mass non-degenerate case, providing concrete results for bound state mass spectra and decay constants; preliminary results on this effort have been reported in [59]. We infer the range of validity of the chiral effective theory as a function of the mass splitting, delineating where the theory changes its character to a hierarchical "heavy-light" system. In addition, we determine the relevant LEC for the coupling to the $U(1)'$ gauge boson from lattice results as a function of the mediator sector. We conclude in Sec. 7 and compile in four appendices a host of technical details, including pertinent Feynman rules, useful expressions for operators and generators and states, and details of the lattice simulations including studies of the systematics.

2 Symmetry breaking patterns

2.1 Lagrangian and global symmetries

The construction of the low energy effective theory starts by recognizing the symmetries of the underlying microscopic theory in the ultraviolet (UV). In this chapter we first discuss the symmetries of the UV Lagrangian for massless fermions. We then consider spontaneous chiral symmetry breaking by the fermion condensate and show that this results in the same global symmetry as an explicit breaking induced by *degenerate* fermion masses. Finally, we show the resulting breaking patterns that correspond to *non-degenerate* fermion masses in the UV Lagrangian or fermions under different charge assignments when coupled to a $U(1)$ gauge group.

The UV Lagrangian of a $Sp(4)_c$ gauge theory — where the subscript c for "colour" on the group is used to highlight its gauge nature — with $N_f = 2$ fundamental Dirac fermions u and d is given by,

$$\mathcal{L}^{\mathrm{UV}} = -\frac{1}{2}\mathrm{Tr}\left[G_{\mu\nu}G^{\mu\nu}\right] + \bar{u}\left(\gamma_\mu D_\mu + m_u\right)u + \bar{d}\left(\gamma_\mu D_\mu + m_d\right)d\,, \tag{1}$$

where spinor, and colour indices are suppressed. We will call u and d (dark) "quarks" in analogy to QCD, even if they are singlets under the SM gauge group; $D_\mu = \partial_\mu + igA_\mu$ is the non-Abelian covariant derivative with gauge coupling g and associated (dark) "gluon" fields $A_\mu = A^a_\mu \tau^a$. We denote the generators of $Sp(4)_c$ by τ^a and the generators of a global $Sp(4)$ group by T^a. The generators of $Sp(4)$ are explicitly given in App. A. The Yang-Mills field strength tensor is given by $G_{\mu\nu} = \partial_\mu A_\nu - \partial_\nu A_\mu + ig\left[A_\mu, A_\nu\right]$ as usual.

The fermions in (1) are in a pseudo-real representation. Compared to a theory where fermions are in the complex representation such as in QCD, the global symmetry of the Lagrangian (1) is enlarged to a so-called Pauli-Gürsey symmetry [60, 61]. Following [60], this can be made explicit, by first introducing the left-handed (L) and right-handed (R) chiral Weyl components of the Dirac spinors u and d,

$$u = \begin{pmatrix} u_L \\ u_R \end{pmatrix}, \qquad d = \begin{pmatrix} d_L \\ d_R \end{pmatrix}. \tag{2}$$

One may subsequently group the left- and right-handed components,

$$\psi_L = \begin{pmatrix} u_L \\ d_L \end{pmatrix}, \qquad \psi_R = \begin{pmatrix} u_R \\ d_R \end{pmatrix}. \tag{3}$$

Using the chiral representation of the Dirac gamma matrices, we may now rewrite the fermionic kinetic term of the Lagrangian as

$$\mathcal{L}_{\text{fermionic}} = i \begin{pmatrix} \psi_L^* \\ \psi_R^* \end{pmatrix}^T \begin{pmatrix} \bar{\sigma}_\mu D^\mu & 0 \\ 0 & \sigma_\mu D^\mu \end{pmatrix} \begin{pmatrix} \psi_L \\ \psi_R \end{pmatrix}. \tag{4}$$

For this we have introduced the four-component notation $\sigma_\mu = (1, \vec{\sigma})$ and $\bar{\sigma} = (1, -\vec{\sigma})$ where σ_j are the usual Pauli matrices. We may now use the pseudo-reality condition of the colour group, i.e., the existence of a colour matrix S for which the relation $(\tau^a)^T = S\tau^a S$ holds for all generators τ^a, as well as the relation $\sigma_2 \sigma_\mu \sigma_2 = \bar{\sigma}_\mu^T$ and rewrite the fermionic kinetic term as

$$\mathcal{L}_{\text{kin}}^{\text{UV,f}} = i \begin{pmatrix} \psi_L^* \\ \sigma_2 S \psi_R \end{pmatrix}^T \begin{pmatrix} \bar{\sigma}_\mu D^\mu & 0 \\ 0 & \bar{\sigma}_\mu D^\mu \end{pmatrix} \begin{pmatrix} \psi_L \\ \sigma_2 S \psi_R^* \end{pmatrix} = i \Psi^\dagger \bar{\sigma}_\mu D^\mu \Psi \,. \tag{5}$$

In the last equality we introduced the notation where Ψ is a vector consisting of the four Weyl fermions in this theory, which is known as the Nambu-Gorkov formalism,

$$\Psi \equiv \begin{pmatrix} \psi_L \\ \tilde{\psi}_R \end{pmatrix} = \begin{pmatrix} u_L \\ d_L \\ \sigma_2 S u_R^* \\ \sigma_2 S d_R^* \end{pmatrix}, \tag{6}$$

from where one may appreciate a global $U(4)$ symmetry of the kinetic term. We observe that $\tilde{\psi}_R \equiv \sigma_2 S \psi_R^*$ transforms under the same representation of this global symmetry as ψ_L. In case of massless fermions this is the symmetry of the entire fermionic Lagrangian. The $U(4)$ symmetry is then broken to $SU(4)$ by the axial anomaly analogously as to in QCD. For a theory with N_f fermions the global flavour symmetry becomes $SU(2N_f)$.

In the massless fermion limit the remaining $SU(4)$ symmetry is subsequently broken spontaneously by the chiral condensate $\langle \bar{u}u + \bar{d}d \rangle \neq 0$. This can be seen by rewriting the chiral condensate in terms of the generalized vector of spinors Ψ as we did for the kinetic term of the Lagrangian [60],

$$\bar{u}u + \bar{d}d = -\frac{1}{2} \Psi^T \sigma_2 S E \Psi + \text{h.c.}\,, \tag{7}$$

$$E = \begin{pmatrix} 0 & \mathbb{1}_{N_f} \\ -\mathbb{1}_{N_f} & 0 \end{pmatrix}. \tag{8}$$

Here, E is a matrix in flavour space. Under a global $SU(4)$ transformation $\Psi \to U\Psi$ this expression transforms as

$$-\frac{1}{2} \Psi^T \sigma_2 S E \Psi \to -\frac{1}{2} \Psi^T U^T \sigma_2 S E U \Psi \,, \tag{9}$$

SciPost SciPost Phys. 14, 044 (2023)

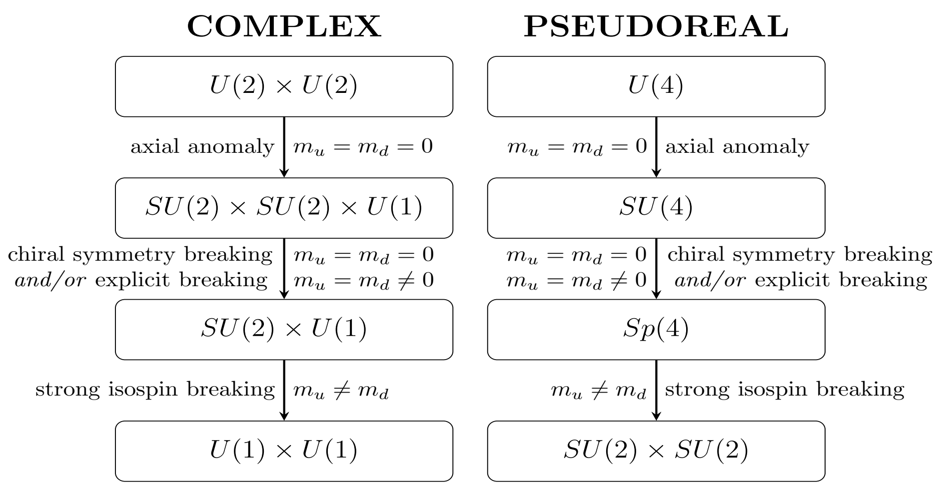

Figure 1: Comparison of breaking patterns in a theory with $N_f = 2$ fermions in pseudo-real (right) and complex (left) representation. In any step, the symmetry for pseudo-real representations is larger than for complex ones.

The condensate is thus invariant under all $SU(4)$ transformations U which fulfil $U^T E U = E$. This is exactly the $Sp(4)$ subgroup of the global $SU(4)$. The matrix E is an invariant tensor of $Sp(4)$ and the flavour space-equivalent of the colour matrix S. By counting the generators of $SU(4)$ and $Sp(4)$ we thereby obtain $15 - 10 = 5$ Goldstone bosons in this theory. In turn, for general N_f, the remaining symmetry group after chiral symmetry breaking is $Sp(2N_f)$.

Degenerate UV masses can be introduced by the term $m(\bar{u}u + \bar{d}d)$. They yield an additional, explicit breaking of the flavour symmetry from $SU(4)$ to $Sp(4)$. For a general *non-degenerate* mass term we may write

$$m_u \bar{u}u + m_d \bar{d}d = -\frac{1}{2}\Psi^T \sigma_2 M E \Psi + \text{h.c.} = -\frac{1}{2}\Psi^T \sigma_2 \begin{pmatrix} 0 & 0 & m_u & 0 \\ 0 & 0 & 0 & m_d \\ -m_u & 0 & 0 & 0 \\ 0 & -m_d & 0 & 0 \end{pmatrix} \Psi + \text{h.c.}\,. \tag{10}$$

This leaves only the $N_f = 1$, $Sp(2) = SU(2)$ symmetry for each flavour separately,[1] and thus a global $Sp(2) \times Sp(2)$ flavour symmetry. The breaking patterns are summarized in Fig. 1. The mass matrix $M = \text{diag}(m_u, m_d, m_u, m_d)$ containing the non-degenerate dark quark masses can then be read from (10),

$$ME = \begin{pmatrix} 0 & 0 & m_u & 0 \\ 0 & 0 & 0 & m_d \\ -m_u & 0 & 0 & 0 \\ 0 & -m_d & 0 & 0 \end{pmatrix},$$

where E is given in Eq. (8).

Another source of explicit symmetry breaking are gauge couplings to an external $U(1)$ vector field V^μ. Depending on the charge assignments of the fermions, this yields distinct

[1] The actual group is $U(2) \times U(2)$, but one $U(1)$ is broken by the axial anomaly, and the other $U(1)$ is just fermion number conservation. The global symmetry of a theory of N_1 fermions of mass m_{N_1} and N_2 fermions of mass m_{N_2} is $Sp(2N_1) \times Sp(2N_2)$. See e.g. [62] for a dark matter model with a $Sp(4) \times Sp(2)$ symmetry of the fermionic mass terms.

explicit symmetry breaking patterns parameterized by a matrix $\mathcal{Q}$ in the Weyl flavour space,

$$\mathcal{L}_{\text{break}} \sim V^{\mu}\Psi^{\dagger}\mathcal{Q}\partial_{\mu}\Psi\,. \tag{11}$$

For example, a breaking pattern $Sp(4) \to SU(2) \times U(1)$ can be realized, assuming that $\mathcal{Q}$ is diagonal. The choices of $\mathcal{Q}$ which preserve this nontrivial flavour subgroup are those for which $\mathcal{Q}^2 \propto \mathbb{1}$. This is incidentally the same condition usually proposed for anomaly cancellation [35]. We show in what follows that this is no accident, and that the nontrivial remaining flavour group ensures the anomalous vertex responsible for pion decay to vanish to all orders (in contrast to SM QCD.) We can also realize a further breakdown to a $Sp(4) \to U(1) \times U(1)$, which has some significant implications for the stability of composite states of the theory, allowing some of them to decay. An in-depth discussion of this is deferred to Sec. 4.

2.2 Symmetries of the low energy mesonic spectrum

We now turn to the symmetries of the low energy mesonic spectrum for *degenerate* and *non-degenerate* dark quarks. As can be seen in Fig. 1 the flavour symmetry of the $Sp(4)_c$ gauge theory is enlarged compared to a theory with a complex fermion representation such as QCD due to the pseudo-reality of the fundamental representation of $Sp(4)$. This entails that also the meson multiplets are enlarged in both the *degenerate* and *non-degenerate* case. There are now five instead of three Goldstone bosons of two flavour QCD. We denote the Goldstone bosons in this theory by $\pi^{A,\ldots,E}$.

The extra states are quark-quark and antiquark-antiquark states. The extra operators corresponding to the Goldstone bosons are given by [20, 22]

$$\pi^D = \bar{d}\gamma_5 SC\bar{u}^T\,, \tag{12}$$
$$\pi^E = d^T SC\gamma_5 u\,. \tag{13}$$

For convenience, we will call these states "diquark" states. In this case, only diquarks of differing flavour are possible; other operators of this form vanish identically for spin-0 composite states. They can occur, however, for other spin states such as $J = 1$ [8].

The multiplet structure of mesons for *mass-degenerate* fermions without coupling to any other symmetry is discussed in [6–8] as well as in studies of $SU(2)_c$, which has the same flavour symmetry as $Sp(4)_c$, with two fundamental fermions [63]. Besides the 5 Goldstone bosons there is another pseudoscalar singlet under $Sp(4)$ which is the analogue of the η' meson of QCD. In turn, the multiplet of the vector mesons is enlarged to a 10-plet (whose states we call $\rho^{F,\ldots,O}$) which includes the state that sources the analogue of the ω meson of QCD [8]. Due to the structure of $Sp(4)$, mesons are either in a 10-plet, 5-plet or a singlet representation of the global $Sp(4)$ flavour symmetry [63]. In appendix B.1 we give explicitly the operators that source the π and ρ mesons.

In case of *non-degenerate fermions*, the $Sp(4)$ flavour symmetry is broken to $SU(2)_u \times SU(2)_d$. It can be shown that the 5-plet splits into a degenerate 4-plet[2] and a singlet under $SU(2)_u \times SU(2)_d$. The 10-plet containing the ρ-mesons decomposes into a 4-plet of similar structure as the 4-plet of Goldstones and two degenerate triplets under each of the $SU(2)_{u/d}$ groups, *i.e.*, the remaining 6 states will have identical properties. The 4-plets contain in both cases the "open-flavour" mesons, *i.e.*, two meson operators of the form $\bar{u}\Gamma d$ – where Γ is either γ_5 for the Goldstones or γ_μ for the ρ-mesons – and two corresponding diquark states. In appendix B.2 we state the explicit transformations of the operators under $SU(2)_u \times SU(2)_d$.

[2]Note that $SU(2)_u \times SU(2)_d \sim O(4)$, and thus the 4-plet can be considered to be in the 4-dimensional fundamental vector representation of $O(4)$. This 4-plet can be decomposed into its two $SU(2)$ representations explicitly in a suitable two-dimensional tensor representation [64].

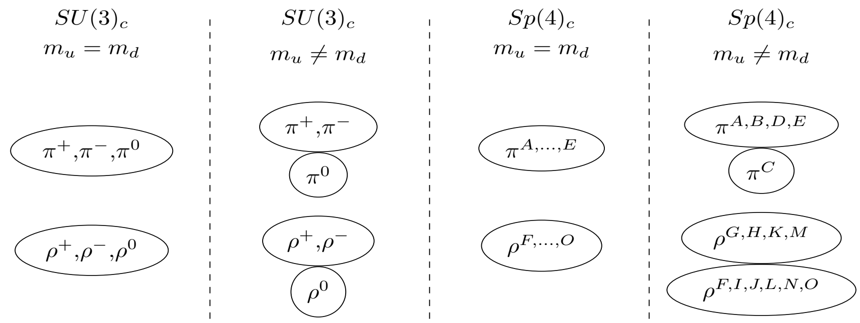

Figure 2: The flavour structure of the meson multiplets for an $Sp(4)_c$ gauge theory with $N_f = 2$, compared to QCD with the same number of quarks. The multiplets of $Sp(4)_c$ are enlarged due to additional diquark states. When the flavour symmetry is explicitly broken by non-degenerate fermion masses, $m_u \neq m_d$, the pseudoscalar and vector multiplets split further into smaller flavour-multiplets under the flavour group. The unflavoured π^C becomes a singlet.

The six other spin-1 states are given by linear combinations of $\bar{u}\Gamma u$, $\bar{d}\Gamma d$ and corresponding diquark operators. They can be written in the eigenbases of the two $SU(2)_{u/d}$.

Figure 2 groups mesons into degenerate and non-degenerate sets and compares them to QCD with two degenerate fundamental fermions. In the case of different UV fermion masses $m_u \neq m_d$, π^C becomes a singlet under the global flavour symmetry, whereas before it was part of a multiplet. This has consequences for its viability as a dark matter candidate: it is no longer protected by a flavour symmetry and, equipped with further interactions, may in principle decay. Finally, as already alluded to above, coupling the strongly interacting dark sector to a $U(1)$ gauge symmetry can further break the remaining flavour symmetry and affect the multiplet structure of the mesons. This will be addressed in Sec. 4.

2.3 Parity and diquarks

Conventionally, the transformation of a Dirac fermion under parity is defined as [65]

$$P : \psi(\mathbf{x}, t) \to \gamma_0 \psi(-\mathbf{x}, t)\,. \tag{14}$$

This implies that parity mixes left-handed and right-handed components. This can be made explicit by going to the chiral representation of the γ-matrices,

$$P : \quad \begin{array}{l} \psi_L(\mathbf{x}, t) \to \psi_R(-\mathbf{x}, t)\,, \\ \psi_R(\mathbf{x}, t) \to \psi_L(-\mathbf{x}, t)\,. \end{array} \tag{15}$$

This discrete transformation, which we shall refer to as "ordinary parity" leaves the Lagrangian invariant and is thus a symmetry. However, it is important to note that the global flavour symmetry mixes left-handed and right-handed components, and such transformation does not in general commute with the parity transformation law given above. In other words, the flavour eigenstates are not eigenstates of P. This has the consequence that a diquark Goldstone state is rather a scalar than a pseudoscalar under P:

$$\begin{aligned} \pi^E(\mathbf{x}, t) = d^T(\mathbf{x}, t) S C \gamma_5 u(\mathbf{x}, t) &\xrightarrow{P} d^T(-\mathbf{x}, t) \gamma_0^T S C \gamma_5 \gamma^0 u(-\mathbf{x}, t) \\ &= d^T(-\mathbf{x}, t) S C \gamma_5 u(-\mathbf{x}, t) = +\pi^E(-\mathbf{x}, t)\,. \end{aligned} \tag{16}$$

SciPost Phys. 14, 044 (2023)

Table 1: Parity assignments of the quark-antiquark bound-states and the additional diquark states. Under ordinary P-parity different parity-eigenstates occur in the same meson multiplet. Only under D-parity all Goldstones can be classified as pseudoscalars and all particles in the ρ-multiplets as vectors. An extension of this table is given in App. B.1.

	J^P	J^D
π^A, π^B, π^C	0^-	0^-
π^D, π^E	0^+	0^-
$\rho^H, \rho^M, \rho^N, \rho^O$	1^-	1^-
$\rho^F, \rho^G, \rho^I, \ldots, \rho^L$	1^+	1^-

The reason for it is the occurrence of the charge conjugation matrix C in the diquark states for which $\gamma_0^T C \gamma_0 = -C$ holds. Concretely, we find that the multiplet of the Goldstones bosons consists of 3 pseudoscalar mesons and 2 scalar diquarks and the multiplet containing the ρ is made up of 4 vectors and 6 axialvectors under P; these states may then change their ordinary parity under flavour transformations.

We are, however, free to obtain a better definition of parity by combining it with any other internal symmetry present in our Lagrangian, see e.g. [66]. Introducing an additional phase in the transformation properties of the spinors (14), we may choose a new parity D that now commutes with all flavour transformations [63]. It is given by

$$D : \psi(\mathbf{x}, t) \to \pm i P \psi(\mathbf{x}, t) P^{-1} = \pm i \gamma_0 \psi(-x, t)\,. \tag{17}$$

The extra phase cancels in all operators of the form $\bar{u}\Gamma d$ but produces an extra minus sign in the diquark operators. The new parity D is again a symmetry of the Lagrangian introduced below and all members of a meson multiplet share the same parity assignment under D. In this way, all Goldstones become pseudoscalars and all members of the ρ-multiplet become vectors under D; see Tab. 1 for an overview of P- and D-parity of the mesons considered in this work. For instance, the diquark π^E transforms under the parity assignment D as follows,

$$\begin{aligned} \pi^E(\mathbf{x}, t) = d^T(\mathbf{x}, t) S C \gamma_5 u(\mathbf{x}, t) &\xrightarrow{D} i^2 d^T(-\mathbf{x}, t) \gamma_0^T S C \gamma_5 \gamma^0 u(-\mathbf{x}, t) \\ &= -d^T(-\mathbf{x}, t) S C \gamma_5 u(-\mathbf{x}, t) = -\pi^E(-\mathbf{x}, t)\,. \end{aligned} \tag{18}$$

3 Chiral Lagrangian for degenerate fermion masses

In this section, we assume that the two fermion states u, d carry degenerate masses $m_u = m_d = m$ in the UV. First, we analyse the mass spectrum of Goldstone bosons in isolation from additional, external interactions. Second, we construct the chiral Lagrangian for vector and axial-vector excitations of the theory.

3.1 Low energy effective theory for the Goldstone bosons

In this section, we recap the construction of the chiral Lagrangian for the (pseudo-Nambu-) Goldstone bosons (PNGB), the "pions" of the theory. The final results agree with the literature [11]. Following [60], the effective theory of Goldstone fields can be written as fluctuations of the orientation of the chiral condensate Σ,

$$\Sigma = e^{i\pi/f_\pi} \Sigma_0 e^{i\pi^T/f_\pi}\,, \tag{19}$$

which, under the action of $U \in \mathrm{SU}(4)$, transforms as

$$\Sigma \to U\Sigma U^T\,. \tag{20}$$

Here, f_π is the Goldstone decay constant and Σ_0 is the orientation of the chiral condensate. The latter depends on the remaining symmetry group after spontaneous or explicit symmetry breaking. The Goldstone bosons are determined by the broken generators of the coset space $SU(2N_f)/Sp(2N_f)$. For our case of interest, with $N_f = 2$ flavours in the pseudo-real representation of the gauge group $Sp(4)_c$, there are five Goldstone bosons $\pi^{1,\dots,5}$ corresponding to the broken generators T^n $(n = 1,\dots,5)$ of the coset space $SU(4)/Sp(4)$ given by (A.6); the change of basis to $\pi^{A,\dots,E}$ used above is given towards the end of this subsection.

The Goldstone boson matrix takes the form,

$$\pi \equiv \sum_{n=1}^{5}\pi_n T^n = \frac{1}{2\sqrt{2}}\begin{pmatrix} \pi_3 & \pi_1 - i\pi_2 & 0 & \pi_5 - i\pi_4 \\ \pi_1 + i\pi_2 & -\pi_3 & -\pi_5 + i\pi_4 & 0 \\ 0 & -\pi_5 - i\pi_4 & \pi_3 & \pi_1 + i\pi_2 \\ \pi_5 + i\pi_4 & 0 & \pi_1 - i\pi_2 & -\pi_3 \end{pmatrix}. \tag{21}$$

The effective Lagrangian needs to preserve the reality condition, Lorentz invariance, chiral symmetry invariance (with vanishing UV masses), as well as parity and charge conjugation symmetry. This yields[3]

$$\mathcal{L} = \frac{f_\pi^2}{4}\mathrm{Tr}\left[\partial_\mu\Sigma\partial^\mu\Sigma^\dagger\right] - \frac{\mu^3}{2}\left(\mathrm{Tr}\left[M\Sigma\right] + \mathrm{Tr}\left[\Sigma^\dagger M^\dagger\right]\right) + \dots\,. \tag{22}$$

Here, μ has mass dimension one and is related to the chiral condensate as $\langle \bar{u}u + \bar{d}d\rangle = \mu^3\Sigma_0$; the prefactor $f_\pi^2/4$ in front of the first term ensures a canonically normalized kinetic term.[4] The ellipses stand for contributions, such as, e.g., $\mathrm{Tr}\left[\partial_\mu\Sigma\partial^\mu\Sigma^\dagger\right]^2$ with prefactors of accordingly higher mass-dimension.

In order to find the vacuum alignment Σ_0, we have to minimize the potential of the chiral Lagrangian, which in our case amounts to $\min_{\pi=0}\left(\mathrm{Tr}\left[M\Sigma + \Sigma^\dagger M^\dagger\right]\right)$. The minimum is then given by $\Sigma_0 = E \in Sp(4)$. Expanding the chiral field (19) in the "kinetic" and "mass" terms of the chiral Lagrangian in terms of Goldstone fields π yields the ordinary kinetic, mass, and interaction terms of even numbers of the Goldstone bosons,

$$\begin{aligned}\mathcal{L}_{\text{kin}} &= \mathrm{Tr}\left[\partial_\mu\pi\partial^\mu\pi\right] - \frac{2}{3f_\pi^2}\mathrm{Tr}\left[\pi^2\partial^\mu\pi\partial_\mu\pi - \pi\partial^\mu\pi\pi\partial_\mu\pi\right] + \mathcal{O}\left(\frac{\pi^6}{f_\pi^4}\right)\\ &= \frac{1}{2}\sum_{n=1}^{5}\partial_\mu\pi_n\partial^\mu\pi_n - \frac{1}{12f_\pi^2}\sum_{k,n=1}^{5}\left(\pi_k\pi_k\partial_\mu\pi_n\partial^\mu\pi_n - \pi_k\partial_\mu\pi_k\pi_n\partial^\mu\pi_n\right) + \mathcal{O}\left(\frac{\pi^6}{f_\pi^4}\right),\end{aligned} \tag{23}$$

$$\mathcal{L}_{\text{mass}} = -m_\pi^2\,\mathrm{Tr}\left[\pi^2\right] + \frac{m_\pi^2}{3f_\pi^2}\mathrm{Tr}\left[\pi^4\right] + \mathcal{O}\left(\frac{\pi^6}{f_\pi^6}\right) = -\frac{m_\pi^2}{2}\sum_{k=1}^{5}\pi_k^2 + \frac{m_\pi^2}{48f_\pi^2}\left(\sum_{k=1}^{5}\pi_k^2\right)^2 + \mathcal{O}\left(\frac{\pi^6}{f_\pi^6}\right). \tag{24}$$

The universal Goldstone mass is given by $m_\pi^2 = 2\mu^3 m/f_\pi^2$. By construction, only interactions of an even number of Goldstone bosons are present; $\mathrm{Tr}\left[\pi^n\right] = 0$ for n odd. We note in passing

[3]The mass term may be derived by treating M as a spurion field, as the global flavour symmetry should also be manifest in the effective theory. M has to transform as $M \to U^\star M U^\dagger$ with $U \in SU(4)$ and $\Psi \to U\Psi$ in order to ensure full chiral/flavour symmetry in (10), see [60] for more details. This leads to the chiral-invariant mass term at lowest order in M in (22) respecting the transformation of Σ in (20).

[4]The prefactor depends on the normalization of the generators as they enter exponential of (19). For instance, $f_\pi^{\text{Ref. [11]}} = 2f_\pi$ where $f_\pi^{\text{Ref. [11]}}$ is the decay constant used in [11] and differs from ours by a factor 2.

that the four-point interactions of same-flavour Goldstone bosons only emerge from the "mass term" (24).

A five-point interaction is induced by the Wess-Zumino-Witten (WZW) action [67–69]. The latter is written as an integral over the five-dimensional disc Q_5,

$$\begin{aligned}\mathcal{S}_{\text{WZW}} &= \frac{-iN_c}{240\pi^2}\int_{Q_5} \text{Tr}\left[(\Sigma^\dagger d\Sigma)^5\right] = \frac{-iN_c}{240\pi^2}\int_{Q_5} \text{Tr}\left[\left(\Sigma^\dagger \frac{\partial \Sigma}{\partial x} dx\right)^5\right] \\ &= \frac{-iN_c}{240\pi^2}\int_{Q_5} dx^\mu dx^\nu dx^\rho dx^\sigma dx^\lambda \text{Tr}\left[\Sigma^\dagger\partial_\mu\Sigma\Sigma^\dagger\partial_\nu\Sigma\Sigma^\dagger\partial_\rho\Sigma\Sigma^\dagger\partial_\sigma\Sigma\Sigma^\dagger\partial_\lambda\Sigma\right],\end{aligned} \tag{25}$$

where N_c is the number of colours. Expanding in terms of Goldstone fields and using Stokes' theorem as well as $dx^\mu dx^\nu dx^\rho dx^\sigma = dx^4\epsilon^{\mu\nu\rho\sigma}$ makes the five-point interaction evident in the Lagrangian density,

$$\mathcal{L}_{\text{WZW}} = \frac{2N_c}{15\pi^2 f_\pi^5}\epsilon^{\mu\nu\rho\sigma}\,\text{Tr}\left[\pi\partial_\mu\pi\partial_\nu\pi\partial_\rho\pi\partial_\sigma\pi\right] + \mathcal{O}\left(\pi^6/f_\pi^6\right) \tag{26}$$

$$\begin{aligned}&= \frac{2N_c}{15\pi^2 f_\pi^5}\epsilon^{\mu\nu\rho\sigma}\pi_i\partial_\mu\pi_j\partial_\nu\pi_k\partial_\rho\pi_l\partial_\sigma\pi_n\,\text{Tr}\left[T^iT^jT^kT^lT^n\right] + \mathcal{O}\left(\pi^6/f_\pi^6\right) \\ &= \frac{N_c}{10\sqrt{2}\pi^2 f_\pi^5}\epsilon^{\mu\nu\rho\sigma}\left(\pi_1\partial_\mu\pi_2\partial_\nu\pi_3\partial_\rho\pi_4\partial_\sigma\pi_5 - \pi_2\partial_\mu\pi_1\partial_\nu\pi_3\partial_\rho\pi_4\partial_\sigma\pi_5\pi_3\partial_\mu\pi_1\partial_\nu\pi_2\partial_\rho\pi_4\partial_\sigma\pi_5\right. \\ &\qquad \left. + \pi_4\partial_\mu\pi_1\partial_\nu\pi_2\partial_\rho\pi_5\partial_\sigma\pi_3 + \pi_5\partial_\mu\pi_1\partial_\nu\pi_2\partial_\rho\pi_3\partial_\sigma\pi_4\right) + \mathcal{O}\left(\pi^6/f_\pi^6\right).\end{aligned} \tag{27}$$

As can be seen in the final form, the WZW term yields purely flavour off-diagonal interactions. Moreover, the WZW conserves both P-parity and D-parity, since spatial derivatives change sign under these parity transformations.

The full chiral Lagrangian is then given by the sum of kinetic, mass, and WZW terms,

$$\mathcal{L} = \mathcal{L}_{\text{kin}} + \mathcal{L}_{\text{mass}} + \mathcal{L}_{\text{WZW}}. \tag{28}$$

We point out that four-point and five-point interactions between Goldstone bosons remain present in the massless limit $M \to 0$. The Feynman rules are given in the Appendix C. We note that the expressions here are connected to the basis in section 2 labelled by capital Latin letters $A, B, \ldots$, as

$$\begin{pmatrix}\pi^A\\ \pi^B\\ \pi^C\\ \pi^D\\ \pi^E\end{pmatrix} = \frac{1}{\sqrt{2}}\begin{pmatrix}1 & i & 0 & 0 & 0\\ 1 & -i & 0 & 0 & 0\\ 0 & 0 & \sqrt{2} & 0 & 0\\ 0 & 0 & 0 & i & 1\\ 0 & 0 & 0 & -i & 1\end{pmatrix}\cdot\begin{pmatrix}\pi_1\\ \pi_2\\ \pi_3\\ \pi_4\\ \pi_5\end{pmatrix}. \tag{29}$$

This defines $\pi^A = \pi^{B\dagger}$ and $\pi^D = \pi^{E\dagger}$, and is useful once U(1) charges are assigned in section 4. The generators of the new basis are given in (A.18).[5] Also, in Sec. 5 we describe the consequences of introducing a mass splitting between the fermions in the UV. It leads to different couplings among the Goldstone bosons and to a splitting of the low-energy mass spectrum.

[5] A similar relation is used in QCD with two flavours u, d where it relates the Goldstone bosons defined through the Pauli matrices of the flavour symmetry σ_i by $\pi_i = \bar{\Psi}\gamma_5\sigma_i\Psi$ ($i = 1, 2, 3$) with $\Psi = (u, d)^T$ to the commonly used pions $\pi^\pm = \bar{\Psi}\gamma_5\sigma^\pm\Psi$ and $\pi^0 = \bar{\Psi}\gamma_5\sigma^0\Psi$ as

$$\begin{pmatrix}\pi^+\\ \pi^-\\ \pi^0\end{pmatrix} = \frac{1}{\sqrt{2}}\begin{pmatrix}1 & i & 0\\ 1 & -i & 0\\ 0 & 0 & \sqrt{2}\end{pmatrix}\cdot\begin{pmatrix}\pi_1\\ \pi_2\\ \pi_3\end{pmatrix} \quad \text{(QCD)}. \tag{30}$$

There, we shall see that one Goldstone occupies the lightest mass state, which can be identified with the state $\pi_3 = \pi^C$, making its special role evident. Explicitly, the expanded chiral Lagrangian in the new basis reads

$$\begin{aligned}
\mathcal{L} =& \partial_\mu \pi^A \partial^\mu \pi^B + \frac{1}{2}\partial_\mu \pi^C \partial^\mu \pi^C + \partial_\mu \pi^D \partial^\mu \pi^E - m_\pi^2 \left(\pi^A \pi^B + \frac{1}{2}\pi^C \pi^C + \pi^D \pi^E \right) \\
&+ \frac{m_\pi^2}{12 f_\pi^2} \left(\pi^A \pi^B + \frac{1}{2}\pi^C \pi^C + \pi^D \pi^E \right)^2 \\
&- \frac{1}{12 f_\pi^2} \Bigg[4 \left(\pi^A \pi^B + \frac{1}{2}\pi_C^2 + \pi^D \pi^E \right) \left(\partial_\mu \pi^A \partial^\mu \pi^B + \frac{1}{2}\partial_\mu \pi^C \partial^\mu \pi^C + \partial_\mu \pi^D \partial^\mu \pi^E \right) \\
&- \left(\pi^A \partial^\mu \pi^B + \pi^B \partial^\mu \pi^A + \pi^C \partial^\mu \pi^C + \pi^D \partial^\mu \pi^E + \pi^E \partial^\mu \pi^D \right)^2 \Bigg]. \\
&+ \frac{16 N_c}{5\sqrt{2}\pi^2 f_\pi^5} \epsilon^{\mu\nu\rho\sigma} \Big[2 \left(\pi^A \partial_\mu \pi^B - \pi^B \partial_\mu \pi^A \right) \partial_\nu \pi^C \partial_\rho \pi^D \partial_\sigma \pi^E \\
&+ 2 \left(\pi^D \partial_\mu \pi^E - \pi^E \partial_\mu \pi^D \right) \partial_\nu \pi^C \partial_\rho \pi^A \partial_\sigma \pi^B + \pi^C \partial_\mu \pi^A \partial_\nu \pi^B \partial_\rho \pi^D \partial_\sigma \pi^E \Big] + \mathcal{O}\left(\pi^6\right),
\end{aligned} \tag{31}$$

where we used the relations

$$\begin{aligned}
\frac{1}{2}\sum_{n=1}^{5} \pi_n^2 =& \pi^A \pi^B + \frac{1}{2}\pi_C^2 + \pi^D \pi^E, \\
\frac{1}{2}\sum_{n=1}^{5} \partial_\mu \pi_n \partial^\mu \pi_n =& \partial_\mu \pi^A \partial^\mu \pi^B + \frac{1}{2}\partial_\mu \pi^C \partial^\mu \pi^C + \partial_\mu \pi^D \partial^\mu \pi^E, \\
\sum_{n=1}^{5} \pi_n \partial_\mu \pi_n =& \pi^A \partial^\mu \pi^B + \pi^B \partial^\mu \pi^A + \pi^C \partial^\mu \pi^C + \pi^D \partial^\mu \pi^E + \pi^E \partial^\mu \pi^D, \\
\frac{4\sqrt{2}}{3} \operatorname{Tr}\left[\pi \partial_\mu \pi \partial_\nu \pi \partial_\rho \pi \partial_\sigma \pi \right] =& 2 \left(\pi^A \partial_\mu \pi^B - \pi^B \partial_\mu \pi^A \right) \partial_\nu \pi^C \partial_\rho \pi^D \partial_\sigma \pi^E \\
&+ 2 \left(\pi^D \partial_\mu \pi^E - \pi^E \partial_\mu \pi^D \right) \partial_\nu \pi^C \partial_\rho \pi^A \partial_\sigma \pi^B \\
&+ \pi^C \partial_\mu \pi^A \partial_\nu \pi^B \partial_\rho \pi^D \partial_\sigma \pi^E .
\end{aligned} \tag{32}$$

3.2 The Pseudoscalar Singlet

Our theory, like in QCD, contains an iso-singlet state η'. The state is associated with the $U(1)_A$ subgroup of an extended flavour symmetry $U(4) = SU(4) \times U(1)_A$. This symmetry is broken anomalously at the quantum level, just as in the SM. However, unlike for the SM η', by construction this state receives no contribution from a heavier flavour like the strange quark, and so it can be close in mass to the Goldstone bosons outside the chiral limit. We can compare this state to the η' of QCD, with the distinction that there is just one η state in this theory, rather than a doublet which mixes and yields the η and η'. This meson is especially interesting as it can mix with the remaining singlet Goldstone boson π_3 once the flavour symmetry is broken down to $SU(2)_u \times SU(2)_d$. Also, depending on the mass hierarchy of the theory, it can be unstable, but potentially long-lived, which would have interesting implications for phenomenology.

We account for η' in the chiral Lagrangian by including the generator $T^0 = \frac{1}{2\sqrt{2}}\mathbb{1}_{4\times 4}$. We remark that while this state may be close in mass to the Goldstones, it is not identifiable as a Goldstone and thus can differ in mass from the Goldstones even for degenerate quark masses. We encode this into our low-energy theory by assigning η' a different decay constant from that

SciPost SciPost Phys. 14, 044 (2023)

of the Goldstones and by explicitly breaking the $U(1)_A$ symmetry through an additional mass term $\frac{\Delta m^2_{\eta'}}{2N_c}\left[\frac{f_\pi}{4}\ln\left(\frac{\det\Sigma}{\det\Sigma^\dagger}\right)\right]^2 = -\frac{\Delta m^2_{\eta'}}{2}\eta'^2$. The η' is then included in our chiral Lagrangian by performing an extra rotation on the vacuum[6]

$$\Sigma = \exp\left(\frac{2i\eta' T^0}{f_{\eta'}}\right)\exp\left(\frac{2i\pi}{f_\pi}\right)E\,. \tag{33}$$

The various interactions involving the η' can then be calculated from the relevant terms in the chiral Lagrangian. We find,

$$\mathcal{L} = \mathcal{L}^\pi_{\text{kin}} + \mathcal{L}^\pi_{\text{mass}} + \mathcal{L}^\pi_{\text{WZW}} + \frac{1}{2}\partial_\mu\eta'\partial^\mu\eta' - \frac{m_\pi^2 + \Delta m^2_{\eta'}}{2}\eta'^2 + \frac{m_\pi^2}{48 f_\pi^2}\eta'^4 + \frac{m_\pi^2}{8 f_\pi^2}\eta'^2\sum_{k=1}^{5}\pi_k^2 + \mathcal{O}\left(\pi^6\right), \tag{34}$$

where $\mathcal{L}^\pi_{\text{kin}}+\mathcal{L}^\pi_{\text{mass}}+\mathcal{L}^\pi_{\text{WZW}}$ is the Lagrangian for the Goldstone bosons π given in Eqs. (23), (24) and (26). Here, we used the redefinition $\eta' \to \frac{f_{\eta'}}{f_\pi}\eta'$ in order to ensure that the kinetic term for η' is canonically normalized. We hence find, that the decay constants of η' and the Goldstone fields are equal in the leading order of the chiral Lagrangian.[7] In the limit $\Delta m_{\eta'} \to 0$, the pseudoscalar singlet η' and the Goldstones π_n have the same mass $m_\pi = 2\mu^3 m/f_\pi^2$ at the lowest order in the chiral Lagrangian, since $\mathrm{Tr}[\pi^n] = \mathrm{Tr}[\eta'\pi^n] = \mathrm{Tr}[\eta'^2\pi^n] = \mathrm{Tr}[\eta'^3\pi^n] = 0$ for n odd and $n \leq 3$. For $\Delta m_{\eta'} \neq 0$, η' remains massive even in the chiral limit. Interactions with $\partial_\mu\eta'$ are absent and four-point interactions with η' are only generated by the mass term of the chiral Lagrangian.

In the mass degenerate case, the WZW term involving only pions and η' vanishes due to anti-symmetry of epsilon tensor and flavour structure of the coset space where the pions live. The phenomenology of such η' has been explored in the context of $Sp(4)$ composite Higgs theories [53, 57]. We once again stress that the phenomenology in our case will be different, for example the η' in our theory can not decay to SM particles at tree level. Any decay to SM final state will be mediated by the portal between SM and $Sp(4)$ gauge group.

3.3 Chiral Lagrangian including spin-1 states

In order to include the lightest vector and axial-vector states of the theory, we can use the concept of hidden local symmetry from QCD [71], as has already been done in [7]. Here, the spin-1 mesons are introduced as dynamical objects by describing them as the gauge bosons of a spontaneously broken local symmetry. We stress that this is an effective treatment and that the spin-1 states are not fundamental gauge fields and that the local symmetry is purely auxiliary.

To this end, we take a second copy of the $SU(4)$ flavour symmetry and “gauge it.” This introduces 15 vector bosons, corresponding to the gauged $SU(4)$. The symmetry is broken in the low-energy regime, and in addition to the five PNGBs $\pi^a T^a$, we have fifteen (exact) PNGB $\sigma^b T^b$. The latter are “eaten” by the vector bosons, providing them with the longitudinal degrees of freedom required for the massive vector fields,

$$\rho_\mu = \sum_{a=1}^{15}\rho^a_\mu T^a\,. \tag{35}$$

[6] Under the axial group $U(1)_A$ we have $\psi_{R/L} \to e^{\pm i\alpha}\psi_{R/L}$ and the chiral field transforms as $\Sigma \to e^{-2i\alpha}\Sigma$. Upon confinement, the flavour symmetry $U(4)$ breaks spontaneously to $Sp(4)\times U(1)_A$. The Goldstone bosons including the η' live in the coset space $U(4)/(Sp(4)\times U(1)_A)$. The determinant of the chiral field is then $\det\Sigma = \exp\left(\frac{2\sqrt{2}i\eta'}{f_{\eta'}}\right) \neq 1$.

[7] This is not overly surprising, as in the large N_c-limit the $U(1)_A$ anomaly vanishes, $f_{\eta'} = f_\pi(1 + O(1/N_c))$ [70], and η' can be considered as an additional Goldstone boson in line with the construction of the chiral field in Eq. (33).

The ρ^a_μ decompose into a lighter ten-plet and a heavier quintuplet, corresponding to the unbroken/broken generators of $SU(4)$, respectively. These can be identified with the ordinary vector and axial-vector multiplets in QCD, see Fig. 2. Explicitly ρ_μ is given by

$$\rho_\mu = \frac{1}{2\sqrt{2}} \begin{pmatrix} \rho^3 & \rho^1 - i\rho^2 & 0 & \rho^5 - i\rho^4 \\ \rho^1 + i\rho^2 & -\rho^3 & -\rho^5 + i\rho^4 & 0 \\ 0 & -\rho^5 - i\rho^4 & \rho^3 & \rho^1 + i\rho^2 \\ \rho^5 + i\rho^4 & 0 & \rho^1 - i\rho^2 & -\rho^3 \end{pmatrix}_\mu + \frac{1}{2\sqrt{2}} \begin{pmatrix} \rho^{14} + \rho^{15} & \rho^{13} - i\rho^8 & \sqrt{2}\rho^{10} - i(\rho^6 + \rho^9) & \rho^{11} - i\rho^7 \\ \rho^{13} + i\rho^8 & \rho^{15} - \rho^{14} & \rho^{11} - i\rho^7 & \sqrt{2}\rho^{12} - i(\rho^6 - \rho^9) \\ \sqrt{2}\rho^{10} + i(\rho^6 + \rho^9) & \rho^{11} + i\rho^7 & -(\rho^{14} + \rho^{15}) & -(\rho^{13} + i\rho^8) \\ \rho^{11} + i\rho^7 & \sqrt{2}\rho^{12} + i(\rho^6 - \rho^9) & -(\rho^{13} - i\rho^8) & -(\rho^{15} - \rho^{14}) \end{pmatrix}_\mu , \tag{36}$$

with the first line defining the matrix describing the lightest axial-vector states under D-parity, and the second line being the vector states under D. We may then complement our chiral Lagrangian by adding the kinetic and mass terms for the spin-1 states,

$$\mathcal{L}_\rho = -\frac{1}{2}\,\mathrm{Tr}\left(\rho_{\mu\nu}\rho^{\mu\nu}\right) + \frac{1}{2}m_\rho^2\,\mathrm{Tr}\left(\rho_\mu\rho^\mu\right), \tag{37}$$

with $\rho_{\mu\nu} = \partial_\mu\rho_\nu - \partial_\nu\rho_\mu - ig_\rho\left[\rho_\mu, \rho_\nu\right]$ being the non-Abelian field strength tensor. The ρ mass can be expressed in terms of low-energy constants (LECs) of the full $SU(4)\times SU(4)$ theory [8]. We retain here m_ρ as a free parameter, but it will be ultimately fixed by the ultraviolet theory, see section 6. By inspection of the ρ matrix in the generator basis (36), we can identify the QCD-like spin-1 states. Transformations between these two bases are given in Appendix A, see in particular equation (A.17)

The interactions between the Goldstone bosons and spin-1 states may be obtained by introduction of a "covariant derivative",

$$D_\mu\Sigma = \partial_\mu\Sigma + ig_\rho\left(\rho_\mu\Sigma + \Sigma\rho_\mu^T\right), \tag{38}$$

where g_ρ is the phenomenological coupling between spin-1 meson states and the Goldstones. In practice, coupling the axial-vectors in this way results in non-diagonal kinetic terms when we promote our derivatives to covariant ones in the leading order chiral Lagrangian. Coupling both vectors and axial-vectors in this way ensures that axial vector states are always higher in mass than the vector states. To make this explicit, we follow [72] and expand our kinetic term to quadratic order in the fields. The kinetic terms for Goldstone and axial-vector fields are non-diagonal:

$$\mathcal{L}_{\mathrm{kin}} = \frac{1}{2}\,\mathrm{Tr}\left(\partial_\mu\pi - \frac{1}{\sqrt{2}}f_\pi g_\rho a_\mu\right)^2, \tag{39}$$

where $a_\mu = \sum_{k=1}^5 \rho_\mu^k T^k$ is the matrix describing the five axial-vector states, defined in (36). The action is diagonalized by the field re-definitions

$$\begin{aligned} &a_\mu \to \tilde{a}_\mu + \frac{g_\rho}{\sqrt{2}m_\rho^2}\tilde{f}_\pi\partial_\mu\tilde{\pi}, \qquad \pi \to Z^{-1}\tilde{\pi}, \qquad f_\pi \to Z^{-1}\tilde{f}_\pi, \\ &Z^2 = \left(1 - g_\rho^2\tilde{f}_\pi^2/2m_\rho^2\right) \approx \left(1 + g_\rho^2\tilde{f}_\pi^2/2m_\rho^2\right)^{-1}, \end{aligned} \tag{40}$$

where the tilde superscript is reserved for the physical basis, and can be dropped once the action contains only physical states. This splits the vector and axial-vector states in terms of their masses, with the axial-vector mass now related by

$$m_a^2 = m_\rho^2/Z^2. \tag{41}$$

SciPost SciPost Phys. 14, 044 (2023)

The exact value of Z, and therefore the relative mass of the axial-vectors, now depends on the low-energy constants g_ρ, f_π and m_ρ. The value of g_ρ is often estimated by the Kawarabayashi-Suzuki-Riazuddin-Fayyazuddin (KSRF) relation [73, 74] $2g^2_{\rho\pi\pi} \approx \frac{m_\rho^2}{f_\pi^2}$, which implies that $Z^2 \approx \frac{1}{2}$. This value of Z ensures that axial-vector states are heavier than vector states by a factor of $\sim \sqrt{2}$. The KSRF relation has been tested on the lattice for $Sp(4)_c$ gauge theory with quenched fundamental fermions, with the discrepancy between lattice and theoretical values being $\sim 10\%$ [8]. We can conclude that the axial-vector states should always be significantly heavier than the vectors. In what follows, we will usually neglect these states, assuming them to be decoupled.

We stress, however, that the applicability of KSRF in symplectic theories is not yet a settled issue. Studies on $SU(2)$ gauge theories have found that the relation overestimates the value of the $\rho\pi\pi$ coupling by $> 20\%$ [75]. We reference it here only to provide a rough estimate on mass splitting between vector and axial-vector states.

3.4 The WZW action including spin-1 states

In this section we show how to include the spin-1 composite states in the "anomalous" dark sector interactions induced by the WZW action. In the spirit of the construction above, it is clear that the action (25) alone is not "gauge-invariant" and additional terms must be added to restore invariance; they may be obtained iteratively by the Noether method.

To proceed, we use the Hidden Local Symmetry framework, and following [72, 76], we first define the fields[8]

$$L \equiv d\Sigma\Sigma^\dagger,\ R \equiv \Sigma^\dagger d\Sigma, \tag{42}$$

with $d\Sigma = dx^\mu \partial_\mu \Sigma$, in terms of which the WZW action may be rewritten in the compact form,

$$\Gamma_{\rm WZW} = C\int_{Q_5} \mathrm{Tr}\,(L)^5 = C\int_{Q_5} \mathrm{Tr}\,(R)^5\,, \tag{43}$$

with C the prefactor of the integral in (25). We recall that the chiral field transforms as $\Sigma \to U\Sigma U^T$ with $U \in Sp(4)$. Restricting our focus to the lighter spin-1 ten-plet, infinitesimally, U is given by $\mathbb{1} + iG + \dots$ with $G = G^a T^a$, $a = 6, \dots, 15$ an element of the Lie algebra; the generators are given in App. A. The infinitesimal transformation is then

$$\Sigma \to \Sigma + i\left(G\Sigma + \Sigma G^T\right) + \dots\,, \tag{44}$$

i.e., the infinitesimal variation in Σ under $Sp(4)$ is given by $\delta\Sigma = i\left(G\Sigma + \Sigma G^T\right)$. The ensuing variation of WZW action is then given by

$$\delta\Gamma_{\rm WZW} = 5Ci\int_{Q_5} \mathrm{Tr}\left(dGL^4 + dG^TR^4\right) = -5Ci\int_{M^4} \mathrm{Tr}\left(dGL^3 - dG^TR^3\right). \tag{45}$$

In the second equality we have used the property of the exact forms $dL - L^2 = dL^3 - L^4 = 0$, $dR + R^2 = dR^3 + R^4 = 0$, and applied Stokes' theorem. Now we introduce the 1-form $\rho = \rho_\mu dx^\mu$, and use the leading order expression for the variation in ρ, $\delta\rho \approx dG$, to find the first correction the WZW action,

$$\Gamma^{(1)}_{\rm WZW} = \Gamma_{\rm WZW} + 5Cig_\rho\int_{M^4} \mathrm{Tr}\left(\rho L^3 - \rho^T R^3\right). \tag{46}$$

[8]Unlike in QCD [72] field $L(R)$ does not transform as a nonet under the left(right)-handed part of the chiral symmetry. Our considered theory possesses an enlarged flavour symmetry, and we consider only the two-flavour case. We use this notation only to save space, and for some consistency with the literature.

SciPost SciPost Phys. 14, 044 (2023)

This process can be repeated to iteratively build the full expression for the gauged WZW action. We simply find the variation in this first correction under local $Sp(4)$ and determine the appropriate counterterm whose variation in ρ will cancel it. We now present the particular form of the gauged action for $Sp(4)_c$ gauge theory:

$$\begin{aligned}\Gamma_{\rm WZW}(\Sigma,\rho) = \Gamma^{(0)}_{\rm WZW} &+ 5Cig_\rho \int_{M^4} \mathrm{Tr}\left(\rho L^3 - \rho^T R^3\right) \\ &+ \frac{5}{2}Cg_\rho^2 \int_{M^4} \mathrm{Tr}\left(\rho L \rho L - \rho^T R \rho^T R\right) \\ &+ 5Cg_\rho^2 \int_{M^4} \mathrm{Tr}\left(d\rho\, d\Sigma \rho^T \Sigma^\dagger - d\rho^T d\Sigma^\dagger \rho \Sigma\right) \\ &- 5Cig_\rho^3 \int_{M^4} \mathrm{Tr}\left(\rho^3 L - \left(\rho^T\right)^3 R + \rho\Sigma\rho^T\Sigma^\dagger \rho L - \rho^T \Sigma^\dagger \rho \Sigma \rho^T R\right) \\ &- 5Cg_\rho^4 \int_{M^4} \mathrm{Tr}\left(\rho^3 \Sigma \rho^T \Sigma^\dagger - \left(\rho^T\right)^3 \Sigma^\dagger \rho \Sigma\right),\end{aligned} \tag{47}$$

with L and R given by (42). It should be noted that the previous expression is not just valid for working out interactions involving composite vector states. It is valid for any symmetry with the transformation law (44). This means that gauging the full $SU(4)$ flavour symmetry, rather that just the $Sp(4)$ subgroup, allows us to characterize the interactions involving also the axial-vector quintuplet. We stress that the gauged expression for the WZW action allows studying number changing interactions that include vector states. If the kinematic conditions are favourable, i.e., if vectors and scalars are close in mass, this will affect the SIMP mechanism for DM freeze-out [33]. We also note that the explicit construction of WZW including the rho mesons has allowed us to realize that two of the remaining ρ mesons are unstable due to the AVV anomaly. Thus, not all (off-diagonal) ρ mesons of the theory are stable as claimed in [29]. The generic expressions for the WZW term for $SU(2N_f)/Sp(2N_f)$ breaking have been previously presented in [77] and for general coset space they are presented in [78]. It should be noted that the use of Hidden Local Symmetry (HLS) has allowed us to use gauge invariance, thus fixing all free parameters of the Lagrangian shown in Eq. 47. The HLS formalism in general holds for a complex representation of $SU(N)$ gauge group. We expect it to be valid also in our theory, however no explicit lattice tests exist.

4 SIMPs under Abelian gauge symmetries

Eventually, we want to couple the non-Abelian dark sector to the SM. A simple, but by no means the only option is to gauge (part of) the theory under a new Abelian dark gauge group $U(1)'$.[9] The new (massive) vector V^μ may then kinetically mix with SM hypercharge. Denoting the respective field strengths by $V_{\mu\nu}$ and $B_{\mu\nu}$, the interaction is given by,

$$\mathcal{L}_{\rm int} = \frac{\varepsilon}{2\cos\theta_W} B_{\mu\nu} V^{\mu\nu}, \tag{48}$$

where θ_W is the SM weak angle. The consequences and phenomenology of this "vector portal" have been studied in great detail; see [80–82] and references therein. For example, after electroweak symmetry breaking and when the V^μ-mass is well below the electroweak scale, (48)

[9] See e.g. [79], where a $Sp(2N)$ gauge theory with $2N_f$ Weyl fermions is coupled to the SM through an axion-like mediator. We also note in passing that the vector portal induces at loop-level also a Higgs-portal coupling. Since we only consider leading-order effects, this loop-suppressed contribution is left for future work. Note that any explicit Higgs portal coupling will be at least a dimension-five operator, due to the fermionic nature of our dark quarks, and thus will be suppressed as well, and is hence likewise postponed.

Table 2: Possible charge assignments, their associated symmetry breaking patterns, and ensuing multiplet structure. When π^C is a singlet, it is not protected by the flavour symmetry and can in principle decay.

Charge Assignment $\mathcal{Q}$	Breaking Pattern	Multiplet Structure
$\mathrm{diag}(+a,-a,-a,+a)$	$Sp(4) \to SU(2) \times U(1)$	$\begin{pmatrix} \pi^C \\ \pi^D \\ \pi^E \end{pmatrix}, \begin{pmatrix} \pi^A \\ \pi^B \end{pmatrix}$
$\mathrm{diag}(+a,+a,-a,-a)$	$Sp(4) \to SU(2) \times U(1)$	$\begin{pmatrix} \pi^C \\ \pi^A \\ \pi^B \end{pmatrix}, \begin{pmatrix} \pi^D \\ \pi^E \end{pmatrix}$
$\mathrm{diag}(+a,+b,-a,-b)$, $a \neq b$	$Sp(4) \to U(1) \times U(1)$	$(\pi^C), \begin{pmatrix} \pi^A \\ \pi^B \end{pmatrix}, \begin{pmatrix} \pi^D \\ \pi^E \end{pmatrix}$
$\begin{pmatrix} 0 & 0 & a & 0 \\ 0 & 0 & 0 & \pm a \\ a & 0 & 0 & 0 \\ 0 & \pm a & 0 & 0 \end{pmatrix}$	$Sp(4) \to SU(2) \times U(1)$	$\begin{pmatrix} \pi^C \\ \pi^{A,B} \\ \pi^{E,D} \end{pmatrix}, \begin{pmatrix} \pi^{D,E} \\ \pi^{B,A} \end{pmatrix}$
other off-diagonal assignments	$Sp(4) \to U(1) \times U(1)$	$(\pi^C), \begin{pmatrix} \pi^A \\ \pi^E \end{pmatrix}, \begin{pmatrix} \pi^B \\ \pi^D \end{pmatrix}$ or similar

induces "photon-like" interactions with SM fermions f, $\epsilon q_f \bar{f} \gamma_\mu f V^\mu$ where q_f is the electric charge of f. The new vector is then commonly referred to as "dark photon." For the purpose of this work, our principal interest lies in exploring the various options of coupling V^μ to the non-Abelian dark sector. The study of its phenomenological consequences is left for future work.

4.1 Charge assignment in the UV

In what follows, we explore the possible charge assignments of the Dirac flavours under $U(1)'$. We summarize the findings in Tab. 2. Since the Weyl basis is used to make the global symmetries of the theory manifest, we may also look at the transformation properties of the Weyl spinors under $U(1)'$. The "vector" Ψ which collects the Weyl spinors of our theory is related to the Dirac fields through (6). Fixing the charges of our Dirac fields is therefore sufficient in fixing the charge assignment in the basis of Weyl spinors.

Under a local $U(1)'$ transformation with gauge parameter $\alpha(x)$, the components of Ψ transform as

$$\Psi^{ia} \to \exp\left[i\alpha(x)\mathcal{Q}_{ij}\right]\Psi^{ja} \simeq \Psi^{ia} + i\alpha(x)\mathcal{Q}_{ij}\Psi^{ja}\,, \tag{49}$$

with i, j flavour indices and a denoting the colour index of each component of Ψ. The introduction of the covariant derivative then renders the theory invariant under $U(1)'$ gauge transformations,

$$\partial_\mu \Psi^{ia} \to D_\mu \Psi^{ia} = \partial_\mu \Psi^{ia} + ie_D V_\mu \mathcal{Q}_{ij} \Psi^{ja}\,. \tag{50}$$

$\mathcal{Q}_{ij}$ is a symmetric matrix in flavour space containing the $U(1)'$ charges of our Weyl flavours; e_D is the $U(1)'$ gauge coupling and the gauge field transforms as $V^\mu \to V^\mu + \frac{1}{e_D}\alpha(x)V^\mu$.

To begin with, let us restrict ourselves to the particular case of diagonal charge prescriptions. To obtain vector-like couplings, the definition of Ψ in (6) implies that the first (second) and third (fourth) components must have opposite charge. Now for any vector-like charge assignment in Dirac flavour space (a, b), the charge matrix for the Weyl spinors is then given by

$$\mathcal{Q} = \text{diag}(+a, +b, -a, -b) \quad \text{(vector-like assignment)}. \tag{51}$$

Gauging the theory under $U(1)'$ may provide a source of explicit global symmetry breaking. To understand this, we study how the gauge interaction term in the Lagrangian,

$$\mathcal{L} \supset -e_D V_\mu \left(\left(\Psi^i\right)^\dagger_a \overline{\sigma}^\mu \mathcal{Q}_{ij} \Psi^{ja} \right), \tag{52}$$

transforms under the *remaining* flavour symmetry $Sp(4)$ as

$$\Psi^{ia} \to V_{ij}\Psi^{ja} = \left(1 + i\theta^N T^N_{ij} + \dots\right)\Psi^{ja}, \tag{53}$$

with i, j flavour indices. Here, $N = F, \dots, O$, correspond to the $Sp(4)$ subgroup of the $SU(4)$ flavour symmetry, as given by (A.18). Only the variation under this subgroup is relevant since the global $SU(4)$ is already broken.

The variation in the Lagrangian density is found to be

$$\delta\mathcal{L} = ie_D V_\mu \left((\Psi)^\dagger \overline{\sigma}_\mu \theta^N \left[\mathcal{Q}, T^N\right] \Psi\right), \tag{54}$$

This expression is general and not specific to a particular choice of $U(1)'$ charges. We see that the remaining flavour symmetry is spanned by those generators T^N of $Sp(4)$ that commute with $\mathcal{Q}$.

Making use of this expression allows us to identify the unbroken symmetries for any particular charge assignments. The distinct choices are outlined in table 2. We find that two diagonal assignments preserve an $SU(2) \times U(1)$ subgroup of the flavour symmetry, while all others maximally break it to $U(1) \times U(1)$. In what follows, we show that these flavour-conserving interactions lead to anomaly-free couplings between Goldstone bosons and the dark photon.

We now turn our attention to the possibility of off-diagonal couplings, i.e., allowing charge assignments $\mathcal{Q}_{ij}$, $i \neq j$ in (50). Thereby, the various Weyl flavours may couple differently to the $U(1)'$ field, allowing, for example, flavour changing processes. Since (54) is valid for any symmetric $\mathcal{Q}$, we can also see how these flavour changing assignments affect the global symmetries of the theory. We see similarities with the diagonal prescriptions; again exactly two assignments preserve a $SU(2) \times U(1)$ symmetry, while all others maximally break the flavour symmetry to $U(1) \times U(1)$. We note that from the definition of Ψ (6), it can be seen that the flavour-conserving assignments are those which couple the left- and right-handed components of the same Dirac spinors u and d. While two of the charge assignments shown in Tab. 2 are the same as those identified in [11], we also identify the existence of the flavour changing currents.

4.2 Stability of the flavour diagonal Goldstone

In the DM context, the question of the stability of the Goldstone bosons is of course of crucial importance phenomenologically. In particular, the stability of the flavour diagonal Goldstone, π^C, is important to understand. As is the case for the SM QCD neutral pion, a coupling to an external mediator (dark photon) can destabilize the particle. In order to establish the stability of particles under a particular charge assignment, it is sufficient to determine the representations in which the particles transform under the remaining flavour symmetry. In particular, when all Goldstones transform in a non-trivial representation of the preserved symmetry, they are protected from decay. The multiplet structure of Goldstones under various charge assignments are given in Tab. 2.

For all assignments discussed in the previous section which maximally break $Sp(4)$ flavour to $U(1) \times U(1)$, all off-diagonal Goldstones acquire a net $U(1)'$ charge. Since the diagonal

Goldstone state remains uncharged, it splits from the others and is made a flavour singlet. As a result, it can decay. The symmetry-preserving assignments are a different story, however. When the symmetry is instead broken as $Sp(4) \to SU(2) \times U(1)$, then only a pair of Goldstones from $\pi^{A,B,D,E}$ acquire equal and opposite $U(1)'$ charges. The remaining PNGBs form an uncharged triplet which transforms in the adjoint of the remaining $SU(2)$ flavour symmetry.

We remind the reader that our discussion of global symmetries thus far has assumed that the theory contains two degenerate Dirac flavours. In the presence of mass-splitting between the dark quarks, flavour symmetry is already broken to $SU(2) \times SU(2)$ and the π^C is always a singlet, although accidentally stable in the isolated $Sp(4)_c$ sector. Once we couple it to the dark photon, it is expected to become unstable, as it is not protected by any symmetry. Care then must be taken in ensuring that such theories, when entertained as DM scenarios, can be made consistent with constraints from the astrophysics and cosmology; we leave such exploration for future work.

Finally, we comment on the stability of the iso-singlet pseudoscalar, the η'. This particle is always a flavour singlet. This ensures no charge assignment protects its decay. As soon as the hidden sector is coupled to $U(1)'$ the η' will be destabilized, and decays through tree level processes mediated by pairs of dark photons, like the corresponding η' does in QCD.

4.3 $U(1)'$ interactions with mesons

We now turn our attention to the interactions in the dark sector with the $U(1)'$ field. To see how the light mesonic states interact with the associated gauge field, we must examine the transformation properties of the vacuum under the $U(1)'$ symmetry. Under $U \in U(1)'$, Σ transforms as

$$\Sigma \to U\Sigma U^T \sim \Sigma + i\alpha'(x)\left(\mathcal{Q}\Sigma + \Sigma\mathcal{Q}^T\right), \tag{55}$$

with α' parameterizing the local $U(1)'$ transformation. From this we can determine that the covariant derivative acting on Σ,

$$D_\mu\Sigma = \partial_\mu\Sigma + ie_D V_\mu(\mathcal{Q}\Sigma + \Sigma\mathcal{Q}^T), \tag{56}$$

In the following $\mathcal{Q}$ is taken to be diagonal and $U = U^T$. As discussed in the previous section, the presence of this coupling breaks the global flavour symmetry to some subgroup of $Sp(4)$. A subset of the PNGBs become charged under $U(1)'$ and couple directly to the dark photon.

The specifics of the interactions of the dark photon with the pion fields depend on the charge prescription $\mathcal{Q}$. An interesting aspect of this theory is that through different choices of charge assignment, we can selectively couple the vector to different pairs of off-diagonal pions. For example, for the previously mentioned $(+1,-1,-1,+1)$ prescription, we couple only to the $\pi^{A,B}$ states with interactions of the form

$$\mathcal{L}_{V-\pi} = -2ie_D V^\mu\left(\pi^A\partial_\mu\pi^B - \pi^B\partial_\mu\pi^A\right) + e_D^2 V_\mu V^\mu \pi^A\pi^B. \tag{57}$$

For a $(+1,+1,-1,-1)$ charge prescription, we couple only to the other pair of Goldstones $\pi^{D,E}$ with the same type of interaction seen above. This property distinguishes the theory from two-flavour QCD. Here, even nontrivial charge assignments can preserve stability of all Goldstones. A pair of states carry $U(1)'$ charge, while the remaining states form a flavour triplet. The above interaction Lagrangian sources two distinct interactions, a three point interaction from the first term, and four point interaction from the second. Both of these interactions must be taken into account to obtain gauge invariant results. The explicit Feynman rules are provided in Appendix C.1.

SciPost SciPost Phys. 14, 044 (2023)

In addition to the Goldstone mesons, the spin-1 mesonic states interact with V^μ. Gauge invariance of our action is preserved through the inclusion of the term

$$\mathcal{L}_{V-\rho} = -\frac{e_D}{g_\rho} V_{\mu\nu} \operatorname{Tr}(\mathcal{Q}\rho^{\mu\nu}) . \tag{58}$$

Performing a global flavour transformation of the vector multiplet (transforming in the adjoint representation of the flavour symmetry), we verify that $\mathcal{L}_{V-\rho}$ respects all symmetries not already explicitly broken by gauging the theory.

Again, the question of charge prescription is of central importance. The trace in (58) picks out only the flavour diagonal vector mesons, but, in addition, specific charge prescriptions will induce mixing among *different* flavour-diagonal vector mesons. For $Sp(4)_c$ at hand, there are two flavour diagonal vector mesons, $\rho^{N,O}$. The first (second) charge assignment in Table (2) couples only to ρ^N (ρ^O). This implies that one of these states is stable against decays into the SM, while the other is unstable for both of these assignments. This fact also highlights an interesting difference between $Sp(4)$ gauge theory and standard QCD: since the Goldstones of the former theory do not transform in the same representation as the vectors under flavour, they are not protected by the same symmetry. The flavour-diagonal ρ can decay while the flavour-diagonal Goldstone boson remains stable.

Decays of Goldstone bosons occur through processes mediated by pairs of dark photons. The relevant $\pi - V - V$ vertex is sourced by the gauged WZW action. Following the same process described in subsection 3.4, the anomalous interactions involving the dark photon can be computed by gauging the WZW term under the $U(1)'$ symmetry. The complete expression is

$$\begin{aligned}\Gamma^V_{\text{WZW}} = 5Ci \int_{M^4} & e_D V \operatorname{Tr} \mathcal{Q}\left(L^3 - R^3\right) \\ -10C \int_{M^4} & e_D^2 V dV \operatorname{Tr} \mathcal{Q}^2 (L+R) ,\end{aligned} \tag{59}$$

with $dV = \partial_\mu V dx^\mu$. For example, the term in the second line leads to the following interaction

$$\mathcal{L}_{\text{int}} \supset \frac{40iCe_D^2}{f_\pi^2} \varepsilon_{\mu\nu\alpha\beta} V^\mu \partial^\nu V^\alpha \operatorname{Tr}\left(\mathcal{Q}^2 \partial^\beta \pi\right) . \tag{60}$$

Since all the generators of $SU(4)/Sp(4)$ are traceless, it is clear that the condition $\mathcal{Q}^2 \propto \mathbb{1}$ is sufficient for this vertex to vanish for all Goldstone bosons. The two flavour-conserving charge assignments given in table 2 satisfy precisely this condition. Since these charge assignments ensure that all Goldstones transform nontrivially under flavour, this cancellation holds to all orders, and this anomalous vertex is not generated by higher order chiral terms. This is not generically the case for other gauge theories. For fermions in complex representations, the anomaly cancellation condition $\mathcal{Q}^2 \propto \mathbb{1}$, cancels this vertex only at leading order. Higher order terms facilitate this interaction [35] and so allow Goldstones to decay, highlighting another key difference between pseudo-real and complex representations.

4.4 Goldstone mass splitting through radiative corrections

In the presence of explicit symmetry breaking due to $U(1)'$ charges, the masses of our charged Goldstones are renormalized. This can be incorporated into the theory through the inclusion of an explicit term of the form

$$\mathcal{L}_{V\text{-split}} = \kappa \operatorname{Tr}\left(\mathcal{Q}\Sigma\mathcal{Q}\Sigma^\dagger\right) , \tag{61}$$

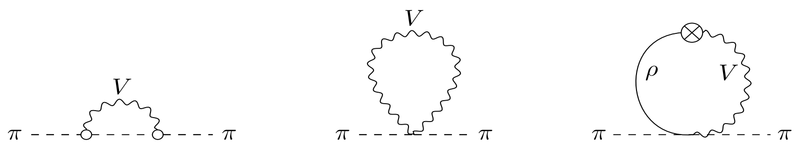

Figure 3: Diagrams contributing to the Goldstone mass-splitting due to $U(1)'$ gauge interactions. Curly lines denote $U(1)'$ gauge propagators, solid lines ρ meson propagators. Empty dots signify vertices which sum over bare couplings of the Goldstones to V^μ, as well as contributions from mixing with the ρ mesons. The crossed dot indicates oscillation between V^μ and ρ.

where κ is the associated LEC, describing the induced mass splitting due to the gauge interactions. For all charge prescriptions which preserve π^C stability (with $\mathcal{Q}^2 \propto \mathbb{1}$), Goldstones charged under $U(1)'$ acquire a correction to their masses which takes the form

$$\Delta m_\pi^2 = \frac{2\kappa e_D^2}{f_\pi^2} \,. \tag{62}$$

Any overall rescaling of the charge matrix can be absorbed into the definition of e_D. For other charge prescriptions, corrections for a given Goldstone can be acquired by multiplying the above by a factor of $Q_\pi^2/(2e_D)^2$, with Q_π the $U(1)'$ charge associated with the particle in question. With the full chiral theory, this mass splitting can be estimated through resonance contributions to the self-energy of the Goldstones, under the assumption of vector meson dominance [83].

Assuming that axial vectors are heavy enough as to be decoupled, the three diagrams of figure 3 need to be computed. Using the interactions discussed in previous sections, we may evaluate the mass corrections at leading order in m_π^2. We compute the diagrams in figure 3 with the external Goldstone lines on-shell and assume *vector meson dominance* [83], wherein the form factors of the Goldstone bosons are dominated by the spin-1 multiplet at low energies. The leading order expression is obtained by neglecting the terms proportional to the on-shell momentum squared. Expressed as a loop integral, the correction takes the form

$$\Delta m_\pi^2 = 6 e_D^2 m_\rho^4 \int \frac{d^4 q}{(2\pi)^4} \frac{1}{\left(q^2 - m_V^2\right)\left(q^2 - m_\rho^2\right)^2} \,, \tag{63}$$

with the left-hand side of the equation denoting the self-energy of the Goldstone evaluated on-shell. Such a treatment done entirely in terms of the low energy degrees of freedom of the theory hence allows us to estimate the Goldstone mass splitting. Equation (63) can be evaluated to determine the leading correction to the charged Goldstone masses, which takes the compact form

$$\Delta m_\pi^2 = \frac{6 e_D^2}{(2\pi)^2} \frac{m_\rho^4}{m_V^2 - m_\rho^2} \log\left(\frac{m_V^2}{m_\rho^2}\right) . \tag{64}$$

This result is exact in the chiral limit, and is independent of the hierarchy between V and ρ. The expression is continuous even at the crossover point $m_V = m_\rho$. Comparison with (62) lets us finally give an estimate of κ, expressed as a dimensionless ratio, at leading order

$$\frac{\kappa}{m_\rho^4} \approx \frac{3}{4\pi^2} \frac{f_\pi^2/m_\rho^2}{m_V^2/m_\rho^2 - 1} \log\left(\frac{m_V^2}{m_\rho^2}\right) . \tag{65}$$

SciPost Phys. 14, 044 (2023)

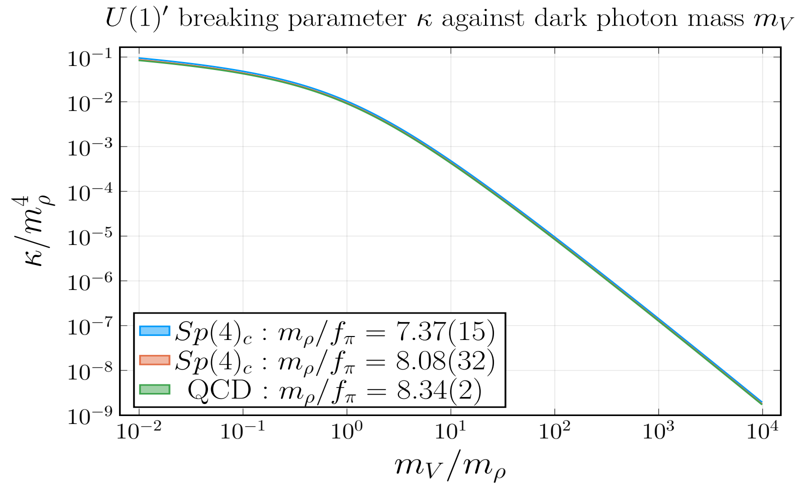

Figure 4: The low energy constant κ parameterizing the explicit symmetry breaking due to the $U(1)'$ interaction in units of m_ρ^4 as a function of m_V/m_ρ according to (65). The ratio of the dark vector meson mass to the dark Goldstone decay constant m_ρ/f_π has been constrained through the lattice results of [6]. We quote the results for two limiting cases: First, for the lattice simulation with the heaviest fermions for which leading-order chiral perturbation theory is expected to hold. This corresponds to $m_\rho/f_\pi = 7.37(15)$. Secondly, for the extrapolation to the chiral limit, where $m_\rho/f_\pi = 8.08(32)$ was found. We conclude that this relation shows only a very weak dependence on the dark quark masses. In addition, we plot (65) for the experimental value of Standard Model QCD.

Here, two different hadronic quantities of the strongly interacting theory enter: the mass of the vector mesons m_ρ and the decay constant of the (pseudo-)Goldstone bosons f_π. They are, however, not independent LECs and their ratio is constrained from lattice data [6]. Hence, once the underlying theory is fixed, κ only depends on m_V and one ratio of dark hadronic observables; see also section 6.1 for a discussion of the free parameters of the UV complete theory.

Close to the chiral limit, i.e., in a regime where $m_\rho/m_\pi > 1.4$, $m_\rho/f_\pi > 7$ always holds [6]. The heaviest fermions for which the theory was sufficiently close to chirality resulted in $m_\rho/f_\pi = 7.37(13)$. An extrapolation to the chiral limit yielded $m_\rho/f_\pi = 8.08(32)$.

In Fig. 4 we plot $\left(\kappa/m_\rho^4\right)$ as a function of m_V/m_ρ for the two aforementioned ratios of m_ρ/f_π as well as the experimental value from SM QCD. We see that the underlying gauge theory strongly constrains (65). Even for different gauge groups the results are very similar [84]. Therefore, the quantities f_π and m_ρ and even their ratio can, in general, *not* be considered as free, independent parameters. Fig. 4 also illustrates the potential for fine radiative mass splittings, independent of the splitting between Dirac flavours. m_V and e_D remain independently variable parameters, allowing a wide range of mass corrections to be obtained depending on what phenomenology is of interest. We also note that the expected behaviour of κ as a splitting between V and ρ occurs is reflected in Fig. 4, with radiative corrections diminishing as m_V becomes large.

5 Chiral Lagrangian in presence of small mass splittings in fermion masses

In this section, we study the consequences for *non-degenerate* fermion masses in the UV, $m_u \neq m_d$. Whereas this is the case for any two flavours in QCD, for the $SU(4)_c$ case of interest here, the low-energy effective theory in the presence of a fundamental mass-splitting has not yet been studied. As mentioned in Sec. 2.1, the global flavour symmetry group $SU(4)$ breaks explicitly to $Sp(2)_u \times Sp(2)_d$ for $m_u \neq m_d$ in the two flavours $u = (u_L, \tilde{u}_R)$, $d = (d_L, \tilde{d}_R)$. We may restrict ourselves to positive mass splittings $\Delta m_{du} = m_d - m_u \geq 0$; the opposite case is simply achieved by a relabelling of the fields $u \to d$ and $d \to u$ as nothing else distinguishes them. The remaining symmetry $Sp(2)_u \times Sp(2)_d$ invites us to switch to another basis where the generators are (anti-)block-diagonal given by (A.12). We denote the generators in this basis as $\tilde{T}^a$. The mass matrix can then be expressed as a sum of block-diagonal forms,

$$M = M_u + M_d = m_u \begin{pmatrix} i\sigma_2 & 0 \\ 0 & 0 \end{pmatrix} + m_d \begin{pmatrix} 0 & 0 \\ 0 & i\sigma_2 \end{pmatrix} = 2i \left(m_u \tilde{T}_u^2 + m_d \tilde{T}_d^2 \right), \tag{66}$$

where M_u, M_d are mass matrices of the respective flavours and $\tilde{T}_u^2, \tilde{T}_d^2$ are generators of $Sp(2)_u \times Sp(2)_d$.

5.1 Mass and kinetic terms in the non-degenerate case

When mass splittings are taken into account, the low energy decay constants as well as vacuum condensates will generally be modified, or, better, carry a flavour-dependence. Our choice of decay constants and vacuum condensates that enter the construction of the chiral Lagrangian is motivated by the lattice results of Sec. 6. Concretely, we make the following replacement when considering split u and d quark masses,

$$f_\pi \xrightarrow{m_u \neq m_d} \begin{cases} f_\pi & \text{for } \pi_{1,2,4,5} \\ f_{\pi_3} & \text{for } \pi_3 \end{cases}, \quad \mu^3 \xrightarrow{m_u \neq m_d} \begin{cases} \mu_u^3 = \frac{1}{2}\langle u^T \sigma_2 S E_2 u \rangle \\ \mu_d^3 = \frac{1}{2}\langle d^T \sigma_2 S E_2 d \rangle \end{cases}, \tag{67}$$

where $E_2 = i\sigma_2$ is a matrix in flavour space. The chiral condensate changes to

$$\langle q_i q_j \rangle = \begin{pmatrix} 0 & \mu_u^3 & 0 & 0 \\ -\mu_u^3 & 0 & 0 & 0 \\ 0 & 0 & 0 & \mu_d^3 \\ 0 & 0 & -\mu_d^3 & 0 \end{pmatrix} = \mu_u^3 \begin{pmatrix} E_2 & 0 \\ 0 & \frac{\mu_d^3}{\mu_u^3} E_2 \end{pmatrix} = \mu_u^3 \left(\Sigma_0^{\text{deg.}} + \Delta\Sigma_0 \right)_{ij} = \mu_u^3 (\Sigma_0)_{ij}, \tag{68}$$

where $\Sigma_0^{\text{deg.}} = \tilde{E}$ is the vacuum alignment for $m_u = m_d$; for concreteness we have chosen to pull out a factor of μ_u^3 which shall serve as overall normalization. Switching to the (anti-) block-diagonal basis given in (A.12) and denoting the change of Σ_0 in presence of different chiral condensates as $\Delta\Sigma_0$ we arrive at,

$$\Delta\Sigma_0 = \begin{pmatrix} 0 & 0 \\ 0 & \frac{\mu_d^3 - \mu_u^3}{\mu_u^3} E_2 \end{pmatrix}. \tag{69}$$

For the chiral Lagrangian for non-degenerate fermion masses in a generalization of (22) we may take the ansatz,

$$\mathcal{L} = \mathcal{L}_{\text{kin}} + \mathcal{L}_{\text{mass}} = \frac{f_\pi^2}{4} \text{Tr}\left[\partial_\mu \Sigma \partial^\mu \Sigma^\dagger \right] - \frac{1}{2} \mu_u^3 \left(\text{Tr}\left[M\Sigma \right] + \text{h.c.} \right). \tag{70}$$

The chiral field is now parameterized as follows,

$$\Sigma = \exp\left[\frac{i}{f_\pi}\sum_{k=1,2,4,5}\pi_k\tilde{T}^k + \frac{i}{f_{\pi_3}}\pi_3\tilde{T}^3\right]\Sigma_0\exp\left[\frac{i}{f_{\pi_3}}\pi_3\tilde{T}^3 + \frac{i}{f_\pi}\sum_{k=1,2,4,5}\pi_k\left(\tilde{T}^k\right)^T\right]. \tag{71}$$

In order to obtain canonical kinetic terms, a rescaling of the fields is necessary,

$$\pi_k \to \frac{2\mu_u^3}{\mu_u^3+\mu_d^3}\pi_k \;\; (k\neq 3), \quad \pi_3 \to \frac{f_{\pi_3}}{f_\pi}\frac{\sqrt{2}\mu_u^3}{\sqrt{\mu_u^6+\mu_d^6}}\pi_3\,. \tag{72}$$

In terms of the rescaled fields according to (72) and the chiral field (71) expanding (70) we may write the Lagrangian in terms of its mass-degenerate form $\mathcal{L}_{\text{kin}}^{\text{deg.}} + \mathcal{L}_{\text{mass}}^{\text{deg.}}$ plus additional terms that will vanish once the mass-degenerate limit $m_u = m_d$ is taken,

$$\begin{aligned}
\mathcal{L} &= \mathcal{L}_{\text{kin}}^{\text{deg.}} + \mathcal{L}_{\text{mass}}^{\text{deg.}} + \frac{m_\pi^2 - m_{\pi_3}^2}{2}\pi_3^2 \\
&+ \frac{1}{12f_\pi^2}\frac{\left(\mu_d^6 + 2\mu_u^3\mu_d^3 - 3\mu_d^6\right)}{(\mu_d^3+\mu_u^3)^2}\sum_{k,n=1}^{5}\left(\pi_k\pi_k\partial_\mu\pi_n\partial^\mu\pi_n - \pi_k\partial_\mu\pi_k\pi_n\partial^\mu\pi_n\right) \\
&+ \frac{1}{8f_\pi^2}\frac{\mu_u^6(\mu_d^3-\mu_u^3)^2}{(\mu_d^3+\mu_u^3)^2(\mu_d^6+\mu_u^6)}\sum_{\substack{k=1\\k\neq 3}}^{5}\left(\partial_\mu\pi_3\pi_k - \pi_3\partial_\mu\pi_k\right)\left(\partial^\mu\pi_3\pi_k - \pi_3\partial^\mu\pi_k\right) \\
&- \frac{1}{6f_\pi^2}\frac{\mu_u^6(\mu_d^3-\mu_u^3)^2}{(\mu_d^3+\mu_u^3)^2(\mu_d^6+\mu_u^6)}\sum_{\substack{k=1\\k\neq 3}}^{5}\pi_3\partial_\mu\pi_k\left(\pi_k\partial^\mu\pi_3 - \pi_3\partial^\mu\pi_k\right) \\
&- \frac{\left(\mu_d^6 + 2\mu_u^3\mu_d^3 - 3\mu_d^6\right)m_\pi^2}{48f_\pi^2(\mu_d^3+\mu_u^3)^2}\left(\sum_{k=1}^{5}\pi_k^2\right)^2 - \frac{\mu_u^6\left((\mu_d^3-\mu_u^3)^2 m_\pi^2 + 2\left(\mu_u^6+\mu_d^6\right)(m_\pi^2 - m_{\pi_3}^2)\right)}{24f_\pi^2(\mu_d^3+\mu_u^3)^2\left(\mu_u^6+\mu_d^6\right)}\pi_3^2\left(\sum_{n=1}^{5}\pi_n^2\right) \\
&+ \frac{\mu_u^6\left(\mu_d^3-\mu_u^3\right)^2\left(m_\pi^2 - m_{\pi_3}^2\right)}{24f_\pi^2(\mu_d^3+\mu_u^3)^2\left(\mu_u^6+\mu_d^6\right)}\pi_3^4 + \mathcal{O}\left(\pi^6\right).
\end{aligned} \tag{73}$$

Here, $\mathcal{L}_{\text{kin}}^{\text{deg.}}, \mathcal{L}_{\text{mass}}^{\text{deg.}}$ are found in (23) and (24) with f_π as on the R.H.S. of (67) and m_π defined through

$$m_\pi^2 \equiv m_{\pi_{1,2,4,5}}^2 = \frac{2\mu_u^6(m_u+m_d)}{f_\pi^2(\mu_u^3+\mu_d^3)}, \quad m_{\pi_3}^2 = \frac{2\mu_u^6(m_u\mu_u^3 + m_d\mu_d^3)}{f_\pi^2(\mu_u^6+\mu_d^6)}. \tag{74}$$

As can be seen, whereas $\pi_{1,2,4,5}$ remain degenerate, π_3 is now split from the other states. In other words, $\pi_{1,2,4,5}$ form a multiplet and π_3 transforms as a singlet under the symmetry $SU(2)_u \times SU(2)_d$. It should be noted, that such mass-difference only appears for $\mu_d \neq \mu_u$ and the introduction of different chiral condensates was necessary to induce such splitting. Similarly to QCD, in leading order in the chiral expansion, the Goldstone masses do not depend on the difference in decay constants $f_\pi \neq f_{\pi_3}$. Of course, once $m_u = m_d$, the Goldstone spectrum becomes degenerate and the global flavour symmetry $Sp(4)$ is restored.

5.2 WZW Lagrangian in the non-degenerate case

Next, we consider the WZW term for the PNGBs for *non-degenerate* fermion masses. Due to the correction factor in Σ_0 in (68) also the five point interaction is modified. In its compact form, the WZW term may now be written as,

$$\mathcal{L}_{\text{WZW}} = -\frac{N_c}{240\pi^2 f_\pi^5}\varepsilon^{\mu\nu\rho\sigma}\text{Tr}\left[\mathcal{A}_\Sigma\partial_\mu\mathcal{A}_\Sigma\partial_\nu\mathcal{A}_\Sigma\partial_\rho\mathcal{A}_\Sigma\partial_\sigma\mathcal{A}_\Sigma\,,\right], \tag{75}$$

SciPost | SciPost Phys. 14, 044 (2023)

where $\mathcal{A}_\Sigma := \Sigma_0\mathcal{A} = (E\mathcal{A} + \Delta\Sigma_0\mathcal{A})$, $\mathcal{A} := \left(\hat{\pi}\Sigma_0 + \Sigma_0\hat{\pi}^T\right)$ and

$$\hat{\pi} := \frac{2\mu_u^3}{\left(\mu_u^3+\mu_d^3\right)} \sum_{k=1,2,4,5} \pi_k \tilde{T}^k + \frac{\sqrt{2}\mu_u^3}{\sqrt{\left(\mu_u^6+\mu_d^6\right)}} \pi_3 \tilde{T}^3 .$$

Here, π has already been used in its rescaled form according to (72). Expanding the Lagrangian as usual, we find that the effects due to non-degeneracy yield a modified pre-factor multiplied onto the Lagrangian that is equivalent to the degenerate case $\mathcal{L}^{\text{deg.}}_{\text{WZW}}$ with f_π as on the R.H.S. of (67) ,

$$\mathcal{L}_{\text{WZW}} = \frac{\mu_d^6\sqrt{\mu_u^6+\mu_d^6}}{\sqrt{2}\mu_u^9}\mathcal{L}^{\text{deg.}}_{\text{WZW}} . \tag{76}$$

The prefactor is larger (smaller) than unity for $\mu_u < \mu_d$ ($\mu_u > \mu_d$.) The total Lagrangian including the WZW interaction is then given by the sum of (73) and (75).

5.3 Goldstone mass spectrum through partially conserved currents

We may also obtain the mass difference of the pseudo-Goldstones from the chiral Lagrangian (70) by means of current algebra instead of direct computation. We switch again to basis of generators given in Eq. (A.12), but all following quantities are also valid in the basis (A.6), replacing $\tilde{T}^a$ by T^a. Recall that under a $SU(4)$ transformation, the chiral field infinitesimally transforms as

$$\Sigma \to U\Sigma U^T \simeq \Sigma + i\theta_a\left[\tilde{T}^a\Sigma + \Sigma\left(\tilde{T}^a\right)^T\right] . \tag{77}$$

Before we derive the Goldstone masses, for completeness, we begin in the *massless* theory and establish some basic facts. The Noether currents associated with the $SU(4)$ flavour symmetry read

$$J^\mu_a\big|_{M=0} = i\frac{f_\pi^2}{2}\text{Tr}\left[\partial^\mu\Sigma^\dagger\left(\tilde{T}^a\Sigma + \Sigma\left(\tilde{T}^a\right)^T\right)\right] \equiv \begin{cases} i\frac{f_\pi^2}{2}\text{Tr}\left[\tilde{T}^a\left\{\Sigma,\partial^\mu\Sigma^\dagger\right\}\right] & a=1,3,5 \\ i\frac{f_\pi^2}{2}\text{Tr}\left[\tilde{T}^a\left[\Sigma,\partial^\mu\Sigma^\dagger\right]\right] & a=2,4 \\ 0 & a=6,\dots,15 . \end{cases} \tag{78}$$

Hence, the currents are non-vanishing for generators associated with the Goldstone bosons. Under ordinary parity P (see Eq. (14)), the currents associated with $a = 1,3,5$ and $a = 2,4$ are axial-vector and vector-currents, respectively: $PJ^\mu_{1,3,5}|_{M=0}(\vec{x},t) = -J^\mu_{1,3,5}|_{M=0}(-\vec{x},t)$ and $PJ^\mu_{2,4}|_{M=0}(\vec{x},t) = J^\mu_{2,4}|_{M=0}(-\vec{x},t)$. However, under the generalized parity D, all Goldstone bosons are pseudoscalars and the currents associated with $a = 1,\dots,5$ are indeed axial-vector currents, $DJ^\mu_a|_{M=0}(\vec{x},t) = -J^\mu_a|_{M=0}(-\vec{x},t)$. To leading order we have,

$$J^\mu_a|_{M=0} \simeq f_\pi\partial^\mu\pi_a, \quad a=1,...,5 . \tag{79}$$

As is evident, in the massless theory, these currents are conserved, $\partial_\mu J^\mu_a\big|_{M=0} = 0$, implying the masslessness of the Goldstone bosons. We now turn to the massive theory, $M \neq 0$, and establish the mass spectrum. To this end, we first note that the change of the Lagrangian upon the $SU(4)$ transformation in (77) reads,

$$\mathcal{L} \to \mathcal{L} - \frac{i\mu_u^3}{2}\theta_a\left\{\text{Tr}\left[\tilde{T}^a\left(\Sigma M - M^\dagger\Sigma^\dagger\right)\right] + \text{Tr}\left[\left(\tilde{T}^a\right)^T\left(M\Sigma - \Sigma^\dagger M^\dagger\right)\right]\right\} . \tag{80}$$

SciPost SciPost Phys. 14, 044 (2023)

From the general definition of the Noether current J_a^μ, one may use the above expression to identify the non-conserved currents for the generators associated with the Goldstone bosons,

$$\begin{aligned}\partial_\mu J_a^\mu &= \frac{i\mu_u^3}{2}\left\{\mathrm{Tr}\left[\tilde{T}^a\left(\Sigma M - M^\dagger\Sigma^\dagger\right)\right] + \mathrm{Tr}\left[\left(\tilde{T}^a\right)^T\left(M\Sigma - \Sigma^\dagger M^\dagger\right)\right]\right\}\\ &= \frac{i\mu_u^3}{2}\times\begin{cases}\mathrm{Tr}\left[\tilde{T}^a\left(\{\Sigma,M\} - \{M^\dagger,\Sigma^\dagger\}\right)\right] & \text{for } \left(\tilde{T}^a\right)^T = \tilde{T}^a,\ a=1,3,5\\ \mathrm{Tr}\left[\tilde{T}^a\left([\Sigma,M] - [M^\dagger,\Sigma^\dagger]\right)\right] & \text{for } \left(\tilde{T}^a\right)^T = -\tilde{T}^a,\ a=2,4\\ 0 & \text{for } a=6,\ldots,15\,.\end{cases}\end{aligned} \tag{81}$$

We may now use the method of *partially conserved axial currents* which posits,

$$\partial_\mu J_a^\mu\,|0\rangle \simeq m_{\pi_a}^2 f_{\pi_a}\,|\pi_a(p)\rangle\ , \tag{82}$$

and compare the masses on the right-hand-side with the ones obtained by the direct evaluation of the traces in (81). Accounting for the rescaling in (72), we obtain

$$\begin{aligned}\partial_\mu J_k^\mu\,|0\rangle &\simeq \frac{2\mu_u^6(m_u+m_d)}{f_\pi(\mu_u^3+\mu_d^3)}\,|\pi_k(p)\rangle\,,\quad k=1,2,4,5\,,\\ \partial_\mu J_3^\mu\,|0\rangle &\simeq \frac{2\mu_u^6(m_u\mu_u^3+m_d\mu_d^3)}{f_\pi(\mu_u^6+\mu_d^6)}\,|\pi_3(p)\rangle\ .\\ \partial_\mu J_n^\mu\,|0\rangle &= 0,\quad n=6,\ldots,15\,,\end{aligned} \tag{83}$$

The comparison with (82) shows that we recover the masses previously found in (74).

5.4 The pseudoscalar singlet in the non-degenerate case

Finally, we work out the role of η' in the non-degenerate fermion mass case. For this, we again perform an extra rotation on the chiral field in Eq. (71),

$$\Sigma \;\rightarrow\; \exp\left[\frac{2i}{f_{\eta'}}\eta' T^0\right]\Sigma\,. \tag{84}$$

Then, the kinetic term in the chiral Lagrangian up to fourth order in the fields is given by

$$\mathcal{L}_{\rm kin} = \frac{1}{2}\sum_{k\neq 3}\partial_\mu\pi_k\partial^\mu\pi_k + \frac{1}{2}\begin{pmatrix}\partial_\mu\pi_3 & \partial_\mu\eta'\end{pmatrix}K\begin{pmatrix}\partial^\mu\pi_3\\ \partial^\mu\eta'\end{pmatrix} + O(\pi^4)\quad , \tag{85}$$

where we have used the redefinition of the fields following (72) and, additionally rescaled η' as,

$$\eta' \rightarrow \frac{f_{\eta'}}{f_\pi}\frac{\sqrt{2}\mu_u^3}{\sqrt{\mu_u^6+\mu_d^6}}\eta'\,. \tag{86}$$

As can be seen, in the non-degenerate case, a kinetic mixing between π_3 and η' is induced by the off-diagonal elements of K,

$$K = \begin{pmatrix}1 & \frac{(\mu_u^6-\mu_d^6)}{2(\mu_u^6+\mu_d^6)}\\ \frac{(\mu_u^6-\mu_d^6)}{2(\mu_u^6+\mu_d^6)} & 1\end{pmatrix}. \tag{87}$$

We put the kinetic term into canonical form in terms of the diagonal fields,

$$\begin{pmatrix}\hat{\pi}_3\\ \hat{\eta}'\end{pmatrix} = S^{1/2}O_{\rm kin}^T\begin{pmatrix}\pi_3\\ \eta'\end{pmatrix}, \tag{88}$$

where O_{kin} is the orthogonal matrix, that diagonalizes K (mixing angle $\pi/4$) and S is composed of the eigenvalues of K in the diagonal, fulfilling $S = O_{\text{kin}}^T K O_{\text{kin}}$. The matrix S is given by

$$S = \frac{1}{2(\mu_d^6 + \mu_u^6)} \begin{pmatrix} 3\mu_d^6 + \mu_u^6 & 0 \\ 0 & \mu_d^6 + 3\mu_u^6 \end{pmatrix}. \tag{89}$$

In the new basis Eq. (88), the kinetic terms are then diagonal and canonically normalized.

We now turn to the mass term in the chiral Lagrangian after rescaling of the fields (72) and (86),

$$\mathcal{L}_{\text{mass}} = 2(m_u\mu_u^3 + m_d\mu_d^3) - \frac{\mu_u^6(m_u + m_d)}{f_\pi^2\left(\mu_u^3 + \mu_d^3\right)} \sum_{k\neq 3} \pi_k^2 - \frac{1}{2}\begin{pmatrix} \pi_3 & \eta' \end{pmatrix} M_{\pi_3\eta'}^2 \begin{pmatrix} \pi_3 \\ \eta' \end{pmatrix}, \tag{90}$$

where the squared mass matrix of π_3 and η' takes the form

$$M_{\pi_3\eta'}^2 = \frac{\mu_u^6}{f_\pi^2(\mu_u^6 + \mu_d^6)} \begin{pmatrix} 2(m_u\mu_u^3 + m_d\mu_d^3) & 2(m_u\mu_u^3 - m_d\mu_d^3) \\ 2(m_u\mu_u^3 - m_d\mu_d^3) & 2(m_u\mu_u^3 + m_d\mu_d^3) + 2\frac{\mu_d^6}{\mu_u^6}\Delta m_{\eta'}^2 f_{\eta'}^2 \end{pmatrix}. \tag{91}$$

We see that in addition to kinetic mixing there is also a mass mixing. We recall that $\Delta m_{\eta'}^2$ was introduced as an explicit breaking of the $U(1)_A$ symmetry. Switching to the new basis (88), the mass term is then diagonalized by the transformation,

$$\begin{pmatrix} \tilde{\pi}_3 \\ \tilde{\eta}' \end{pmatrix} = O_{\text{mass}}^T \begin{pmatrix} \hat{\pi}_3 \\ \hat{\eta}' \end{pmatrix}, \quad O_{\text{mass}} = \begin{pmatrix} \cos\theta_{\text{mass}} & \sin\theta_{\text{mass}} \\ -\sin\theta_{\text{mass}} & \cos\theta_{\text{mass}} \end{pmatrix}, \tag{92}$$

with the mixing angle θ_{mass} given by

$$\tan 2\theta_{\text{mass}} = \frac{f_{\eta'}^2 \Delta m_{\eta'}^2 \sqrt{\left(\mu_d^6 + 3\mu_u^6\right)\left(3\mu_d^6 + \mu_u^6\right)}}{f_{\eta'}^2 \Delta m_{\eta'}^2 \left(\mu_d^6 - \mu_u^6\right) - 2x_-}, \tag{93}$$

where $x_\pm := \frac{\mu_u^6}{\mu_d^6}\left((m_d\mu_d^3\left(\mu_d^6 + 3\mu_u^6\right) \pm m_u\mu_u^3\left(3\mu_d^6 + \mu_u^6\right)\right)$. For $\Delta m_{\eta'} = 0$, the squared mass matrix is automatically diagonal ($\theta_{\text{mass}} = 0$) after diagonalization of the kinetic term. Likewise, in the mass-degenerate case, no kinetic- and mass-mixing is induced even for $\Delta m_{\eta'} \neq 0$. The total Lagrangian in the new basis is given by,

$$\begin{aligned} \mathcal{L} = \mathcal{L}_{\text{kin}} + \mathcal{L}_{\text{mass}} &= \frac{1}{2}\sum_{k\neq 3} \partial_\mu \pi_k \partial^\mu \pi_k + \frac{1}{2}\partial_\mu \tilde{\pi}_3 \partial^\mu \tilde{\pi}_3 + \frac{1}{2}\partial_\mu \tilde{\eta}' \partial^\mu \tilde{\eta}' \\ &\quad + 2(m_u\mu_u^3 + m_d\mu_d^3) - \frac{m_\pi^2}{2}\sum_{k\neq 3}\pi_k^2 - \frac{m_{\pi_3}^2}{2}\tilde{\pi}_3^2 - \frac{m_{\eta'}^2}{2}\tilde{\eta}'^2 + O(\tilde{\pi}^4), \end{aligned} \tag{94}$$

with masses

$$\begin{aligned} m_\pi^2 \equiv m_{\pi_{1,2,4,5}}^2 &= \frac{2\mu_u^6(m_u + m_d)}{f_\pi^2(\mu_u^3 + \mu_d^3)}, \\ m_{\pi_3}^2 &= \frac{4\mu_d^6}{f_\pi^2}\left(\frac{f_{\eta'}^2 \Delta m_{\eta'}^2 \left(\mu_d^6 + \mu_u^6\right) + x_+}{\left(3\mu_d^6 + \mu_u^6\right)\left(\mu_d^6 + 3\mu_u^6\right)} - \frac{\sqrt{f_{\eta'}^4 \Delta m_{\eta'}^4 \left(\mu_d^6 + \mu_u^6\right)^2 + x_-^2 - f_{\eta'}^2 \Delta m_{\eta'}^2 \left(\mu_d^6 - \mu_u^6\right) x_-}}{\left(3\mu_d^6 + \mu_u^6\right)\left(\mu_d^6 + 3\mu_u^6\right)}\right), \\ m_{\eta'}^2 &= \frac{4\mu_d^6}{f_\pi^2}\left(\frac{f_{\eta'}^2 \Delta m_{\eta'}^2 \left(\mu_d^6 + \mu_u^6\right) + x_+}{\left(3\mu_d^6 + \mu_u^6\right)\left(\mu_d^6 + 3\mu_u^6\right)} + \frac{\sqrt{f_{\eta'}^4 \Delta m_{\eta'}^4 \left(\mu_d^6 + \mu_u^6\right)^2 + x_-^2 - f_{\eta'}^2 \Delta m_{\eta'}^2 \left(\mu_d^6 - \mu_u^6\right) x_-}}{\left(3\mu_d^6 + \mu_u^6\right)\left(\mu_d^6 + 3\mu_u^6\right)}\right). \end{aligned} \tag{95}$$

As expected, the pseudoscalar η' has a larger mass than π_3 and remains massive even in the chiral limit for $\Delta m_{\eta'} \neq 0$. The Goldstone and η' spectrum become degenerate for $\Delta m_{\eta'} = 0$, once $m_u = m_d, \mu_u = \mu_d$. For $\Delta m_{\eta'} = 0$ the masses reduce to

$$m_{\pi_3}^2 = \frac{8\mu_u^9 m_u}{f_\pi^2\left(\mu_d^6 + 3\mu_u^6\right)}, \quad m_{\eta'}^2 = \frac{8\mu_u^6\mu_d^3 m_d}{f_\pi^2\left(3\mu_d^6 + \mu_u^6\right)}. \tag{96}$$

In Sec. 3.2 we showed that at leading order η' does not appear in the WZW term in the case of degenerate fermion masses. In case of *non-degenerate* fermion masses, the iso-singlet η' enters the WZW interaction through the mixing effects between η' and π_3. In the basis in which kinetic and mass terms are diagonal, we obtain,

$$\mathcal{L}_{\rm WZW} = \frac{\mu_d^6\left(\mu_u^6+\mu_d^6\right)}{\sqrt{2}\mu_u^9}\left[\left(\frac{\cos\theta_{\rm mass}}{\sqrt{3\mu_d^6+\mu_u^6}} - \frac{\sin\theta_{\rm mass}}{\sqrt{\mu_d^6+3\mu_u^6}}\right)\mathcal{L}_{\rm WZW}^{\rm deg.,\tilde{\pi}} + \left(\frac{\cos\theta_{\rm mass}}{\sqrt{\mu_d^6+3\mu_u^6}} - \frac{\sin\theta_{\rm mass}}{\sqrt{3\mu_d^6+\mu_u^6}}\right)\mathcal{L}_{\rm WZW}^{\rm deg.,\tilde{\eta}'}\right], \tag{97}$$

Here, $\mathcal{L}_{\rm WZW}^{\rm deg.,\tilde{\pi}}$ is given in (76) where π_3 is replaced by $\tilde{\pi}_3$ and $\mathcal{L}_{\rm WZW}^{\rm deg.,\tilde{\eta}'}$ takes the same form as $\mathcal{L}_{\rm WZW}^{\rm deg.,\pi}$ in (76) with π_3 being replaced by $\tilde{\eta}'$.

6 Lattice results on $Sp(4)_c$ with $N_f = 1 + 1$

6.1 Free parameters of the microscopic Lagrangian

The chiral Lagrangian has several low-energy constants that cannot be obtained from the effective theory itself. These can be determined from the underlying UV-complete theory. As the UV theory is strongly interacting, this requires a non-perturbative method, for which we choose lattice here. This allows us to follow standard procedure for the task at hand [4]. Any potential influence of gauging under $U(1)'$ as discussed above is expected to be small, and can thus be accounted for by using perturbation theory *a posteriori*. A similar situation arises in the SM weak interactions of mesons, where the same approximation also holds very well [85].

In the following, we thus consider the strongly interacting $Sp(4)_c$ gauge theory with two fundamental Dirac fermions in isolation. The mass degenerate case was already studied in [6] and pioneering studies in $Sp(4)_c$ Yang-Mills theory and the quenched theory have been carried out in [7, 86, 87]. Since we use the $Sp(4)_c$ branch of the HiRep code [88] developed in [6, 7] for the simulations, we use the same technical framework. We briefly repeat the pertinent details in App. D.

The theory has three free parameters, the gauge coupling g and the two bare fermion masses m_u and m_d. In the context of lattice calculations, it is convenient to express the gauge coupling as $\beta = 8/g^2$. Note that both the coupling and the fermion masses are the unrenormalized bare parameters and thus unphysical.

In the continuum theory, the overall scale would be set by one of the dimensionful parameters, but in a lattice calculation it is convenient to use instead the finite lattice spacing a. Masses are then measured as a multiple of the inverse lattice spacing a^{-1} and we report here the dimensionless products am in the following. Only once some dimensionful quantity is fixed, e.g., by experimental input, explicit units become possible. Fixing the scale, and thus the lattice spacing, implies that also one of the bare lattice parameters is fixed. It is convenient to choose the gauge coupling for this fixing of the scale, leaving two dimensionless quark masses to uniquely characterize the physics. These two free parameters can be used to fix two observable quantities, e. g. properties of the dark hadrons such as masses or scattering cross-sections. All other results are then fixed.

Since a tractable way of deriving these quantities from observations requires a treatment using the effective field theory, we can only see *a posteriori* which input parameters of the microscopic theory (if any) provide viable Dark Matter candidates. In addition, we need to ensure that the effective theory is a sufficiently controlled approximation to the underlying UV theory. This will be done by comparing predictions of the EFT to first-principles results from the lattice.

Remaining agnostic about the values of the two fundamental dark quark masses, we study different combinations of them. We always start from degenerate dark quark masses, and we then incrementally increase one of them, breaking the flavour symmetry from $Sp(4)$ down to $SU(2)_u \times SU(2)_d$ explicitly. For small breaking and sufficiently light quarks, $Sp(4)$ should still be an approximate symmetry and we expect to see 5 relatively (compared to the other meson masses) light pseudo-Goldstone states of which 4 will remain degenerate. For larger breaking this will at some point no longer be the case and the system is expected to resemble a heavy-light system. For one extremely heavy dark quark we expect to see the pattern [34, 60] of a corresponding one-flavour theory for the lightest states. Since we vary the value of one of the bare quark masses to study a one-dimensional subspace of the three-dimensional parameter space and we already leave an overall scale undetermined we only have to fix one remaining bare quark mass through a suitable observable. Once this is done all other lattice observables are predictions

In Fig. 5 we depict the previously outlined workflow. We emphasize that all bare input parameters are unrenormalized and thus unphysical (this includes the bare quark masses).[10]

We fix the remaining bare quark mass (which remains unchanged when we break the flavour symmetry) through the ratio of the vector meson masses to (one of) the pseudo-Goldstones m_ρ/m_π at degeneracy. In the chiral limit, the Goldstone modes become massless and the ratio diverges, $m_\rho/m_\pi \to \infty$. In the limit of extremely heavy quarks all meson masses are dominated by the mass of the valence quarks and the ratio approaches unity, $m_\rho/m_\pi \to 1$. Thus, the larger this ratio becomes the closer we are to the chiral limit. In the Standard Model the experimental value of this is $m_\rho/m_\pi \approx 5.5-5.7$ and for the pseudo-Goldstone bosons of a three-flavour theory the K and η mesons, they are $m_\rho/m_K \approx 1.5$ and $m_\rho/m_\eta \approx 1.4$.

In this work we have studied ensembles where this ratio in the mass degenerate limits[11] are $m_\rho/m_\pi \approx 1.15, 1.25$ and 1.4. These values are slightly smaller than those suggested by existing phenomenological investigations of such theories as dark matter candidates [35]. Eventually, we also want to study ensembles with $m_\rho/m_\pi > 1.4$. However, they come at a significantly increased computational cost and we defer this to future work. We conclude, that our quark masses relate to the intrinsic scale of our theory similarly as the QCD strange quark mass relates to the QCD scale as the mass ratio is similar. Note that in all cases the aforementioned ratio is smaller than 2 and the ρ at rest cannot decay into two Goldstone bosons.

6.2 Quark masses and partially conserved axial current

In the previous section we discussed how to choose the unrenormalized bare quark masses for our lattice simulations. We stressed that these input masses are unrenormalized and thus regulator-dependent and unphysical. An obvious question is, therefore, if there is a way of calculating a "physical" quark mass. This is however *not* possible. Due to confinement there is no notion of a physical quark mass since no physical quark has ever been observed in experiment. Any definition of a quark mass is scheme-dependent and necessarily not unique. In

[10] More precisely, the lattice spacing acts as an ultraviolet cutoff $\Lambda = a^{-1}$, and the bare parameters are the ones at the cutoff. Thus, in the formal continuum limit of $a \to 0$, they will be either zero or infinite.

[11] For the degenerate case, if possible, we give results from [6], since these have been obtained on larger lattices with better statistics in comparison to ours. This will be indicated where necessary.

SciPost Phys. 14, 044 (2023)

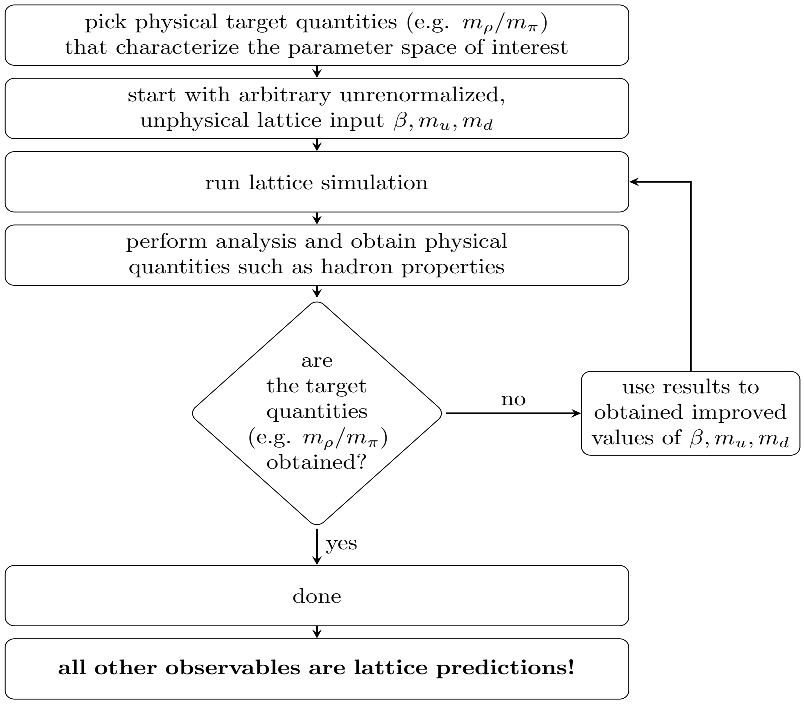

Figure 5: Workflow for choosing suitable input parameters m_u, m_d and β. These input parameters are unrenormalized and thus unphysical. They are chosen such that a set of observables has a prescribed value (in our case the ratio m_ρ/m_π). All other observables are then predictions from the lattice. Note that we do not fix the overall scale of our observables in our analysis.

the context of Standard Model QCD several ways of a defining a quark mass are being actively used. See for example the current PDG review [89] for a detailed discussion of quark masses in the SM.[12]

The scheme-dependence of any quark mass implies that quark masses are comparable only in the same scheme at the same scale μ. This implies that we need to determine the renormalization constants of the bare quark masses m_u and m_d in order to obtain the renormalized quark masses $m_u^{(r)}$ and $m_d^{(r)}$. Our discretization of the fermion fields on the lattice makes this even more challenging: The Wilson discretization of fermions breaks chiral symmetry explicitly on the lattice and results in both a multiplicative *and* additive renormalization of the bare quark mass as long as the lattice is finite, i.e. $a > 0$ [4].

We can, however, instead define a quark mass based on the *partially conserved axial current* (PCAC) equation from (82) which relates the axial current to the pion field and the *axial Ward identity* (AWI) which connects the axial current to the renormalized quark mass $m^{(r)}$. We can restrict ourselves to the AWI for the π^A pseudo-Goldstone which reads $\partial_\mu J_A^\mu = (m_u^{(r)} + m_d^{(r)})\bar{d}\gamma_5 u$. This entails that we can also define an unrenormalized quark mass through correlation functions $C_\Gamma(t)$ of the unrenormalized axial currents $\bar{u}\gamma_0\gamma_5 d$ and $\bar{u}\gamma_5 d$

[12]In fact, beyond perturbation theory the situation is even worse, and it is not settled if a concept like a quark mass can be defined in a confining theory at all. Especially, the quark propagator has not necessarily a suitable pole structure, see e. g. [90] for a discussion.

(see e.g. [91] for a detailed discussion and other equivalent definitions),

$$m^{\mathrm{PCAC}} = \lim_{t\to\infty} \frac{1}{2} \frac{\partial_t C_{\gamma_0\gamma_5,\gamma_5}(t)}{C_{\gamma_5}(t)} = \lim_{t\to\infty} \frac{1}{2} \frac{\partial_t \int d^3\vec{x} \langle (\bar{u}(\vec{x},t)\gamma_0\gamma_5 d(\vec{x},t))^\dagger \bar{u}(0)\gamma_5 d(0)\rangle}{\int d^3\vec{x} \langle (\bar{u}(\vec{x},t)\gamma_5 d(\vec{x},t))^\dagger \bar{u}(0)\gamma_5 d(0)\rangle}. \tag{98}$$

At large times t the ratio of the two correlation functions in eq. (98) tends to a constant which we identify as the PCAC-mass. In the mass-non-degenerate case this expression gives the average mass of up-type quarks and down-type quarks. In our setup we try to keep one of the quark masses fixed. This then allows us to determine the fixed mass directly in the degenerate calculations and deduce the other mass in the non-degenerate case.[13] The PCAC-mass is related to the renormalized (average) mass by a multiplicative factor

$$m^{(r)} = \frac{Z_A}{Z_P} m^{\mathrm{PCAC}}, \tag{99}$$

and is therefore an unrenormalized quantity. In order to obtain the renormalized mass the factor Z_A/Z_P needs to be determined and a scheme to be chosen. This is however quite involved and in addition a matching to other commonly used renormalization scheme is needed in order for this mass to be used in perturbative calculations (see e.g. [85]). We therefore skip this calculation in this work and point out that the renormalization factors cancel if we consider ratios of PCAC-masses such as $m_u^{\mathrm{PCAC}}/m_d^{\mathrm{PCAC}}$ since only multiplicative renormalization occurs.

Note that the PCAC relation is closely linked to chiral perturbation theory and the Gell-Mann-Oakes-Renner (GMOR) relation in particular - see section 5.3. Calculating the PCAC masses and the chiral condensate and comparing this to the GMOR relation cannot be considered to be a truly independent and quantitative test of chiral perturbation theory. We can still use it, however, as a qualitative test by examining the dependence of square of the Goldstone masses on the PCAC-masses and comparing the results to the expected linear behaviour. This can be found (although with a differently defined unrenormalized quark mass) in [6]. In this work we are primarily interested in the effects of strong isospin breaking. We will take the relation at mass-degeneracy for granted and using (74) we determine the (unrenormalized) chiral condensates. We will see that at a sufficiently large strong isospin breaking this will no longer be possible which might suggest that at this amount of strong isospin breaking the chiral Lagrangian at this order is not an adequate description of the Goldstone dynamics of the underlying theory. This is done in section 6.4.

6.3 Results: Masses, decay constants and quark masses

We have calculated the masses and decay constants of both the Goldstones and the vector mesons as well as the previously outlined unrenormalized PCAC masses. The lattice setup and the lattice action as well as the techniques used for extracting the masses and decay constants from the lattice can be found in appendix D. A detailed study of lattice systematics is given in appendix D.4. Here we present the results which we expect to give a suitable approximation of the continuum theory.

The masses for the ensembles with varying m_ρ/m_π at degeneracy are shown in Fig. 6. We see that, both for the Goldstone and vector mesons, the flavour-neutral states are the lighter states once strong isospin breaking is introduced. This makes the π^C the lightest state in the theory. The remaining 4 Goldstones are heavier and remain degenerate. At some point the 6 lighter vector mesons—among them the ρ^N—become even lighter than the heavier pseudoscalars.

[13] In principle, there is the possibility that changing one parameter can affect the other. We do not see any sign of this, but it would require further investigations to settle beyond doubt.

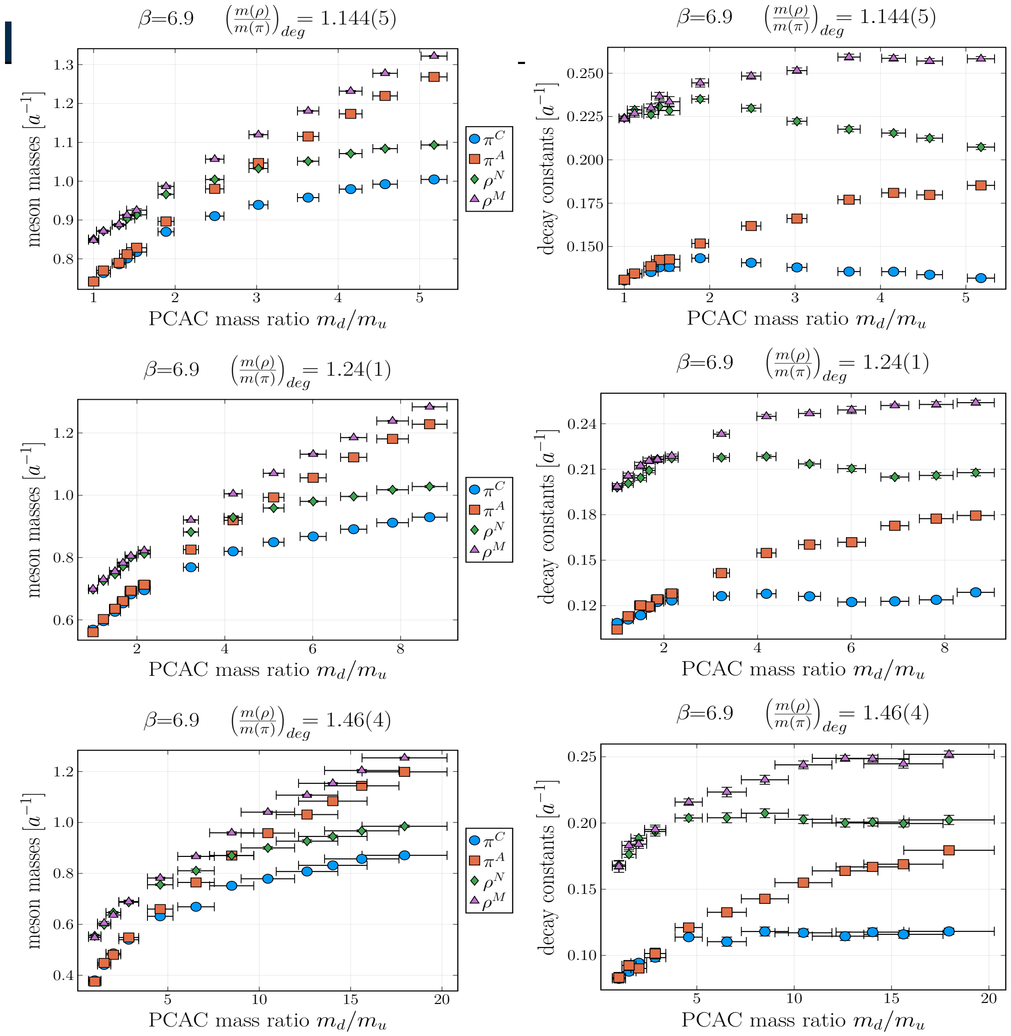

Figure 6: Masses and decay constants of the pseudo-Goldstone mesons and the vector mesons for different non-degenerate fermion masses against the ratio of the unrenormalized PCAC masses. One fermion mass is kept fixed while the other is incrementally increased. Therefore, all meson masses increase with larger fermionic mass difference. The unflavoured pseudo-Goldstone is the lightest particle in the spectrum of the isolated theory. For a larger mass difference between the fermions the unflavoured vector mesons get lighter than the flavoured pseudo-Goldstones. At this point the EFT based solely on would-be-Goldstones is certainly no longer adequate.

A similar pattern is observed for the decay constants of those dark mesons shown. The unflavoured decay constants are smaller than their flavoured counterparts. This is seen for both the Goldstone and the vector mesons. Furthermore, the unflavoured vector decay constant shows a maximum at intermediate values of the dark quark mass splitting.

Note that we observe more effects of the finite lattice extent for the lightest ensembles with $m_\rho/m_\pi \approx 1.25$ at degeneracy and in addition we see finite lattice spacing effects for heavy mesons for both $m_\rho/m_\pi \approx 1.4$ and 1.15 at degeneracy. We again refer to appendix D.4 for a discussion of lattice systematics.

We conclude that for large mass splittings the system more closely resembles a heavy-light system where the unflavoured mesons are the lightest hadronic states. At some point the mass of the second dark quark is so heavy that it decouples and the low-energy part of this theory is effectively a $N_f = 1$ theory which contains three vector mesons and one (massive) pseudoscalar [34]. In this case the theory develops a hierarchy of scales.

6.4 Validity of the Chiral Lagrangian

The chiral theory of Secs. 3 to 5 is based on the dynamics of the lightest hadronic states, which in this case are the pseudo-Goldstone bosons π. In the chiral limit, i.e., in the limit of massless dark fermions, the flavour symmetry is broken only spontaneously and the π's become massless themselves. Close to the chiral limit for degenerate quarks the GMOR relation gives the dependence of the product of Goldstone masses on the renormalized quark masses $m_q^{(r)}$ and the chiral condensate $(\mu^3)^{(r)}$

$$(f_\pi m_\pi)^2 = 2m^{(r)}(\mu^3)^{(r)}. \tag{100}$$

It can be seen that the square of the pseudo-Goldstone mass depends linearly on the average renormalized quark mass and in the chiral limit the equation is trivially fulfilled. As pointed out in section 6.2 the renormalized quark mass and the condensate are scheme-dependent. However, their product is scheme-independent since the involved renormalization constants cancel. Since we forwent a determination of the renormalization constants due to the technically involved nature of such a calculation we use the unrenormalized PCAC mass m_{PCAC} and define the chiral condensate through GMOR. This entails that also the condensate is then unrenormalized and regulator-dependent. We therefore drop the superscript $^{(r)}$ in the following. For non-degenerate quarks GMOR is given by equation (74). For convenience, we rewrite is as

$$\begin{aligned}
\mathrm{GMOR}_{\pi^A}(m_u, m_d, \mu_u, \mu_d) &= (m_{\pi^A} f_{\pi^A})^2 - \frac{2\mu_u^6(m_u + m_d)}{\mu_u^3 + \mu_d^3} = 0\,,\\
\mathrm{GMOR}_{\pi^C}(m_u, m_d, \mu_u, \mu_d) &= (m_{\pi^C} f_{\pi^C})^2 - \frac{2\mu_u^6(m_u\mu_u^3 + m_d\mu_d^3)}{\mu_u^6 + \mu_d^6} = 0\,.
\end{aligned} \tag{101}$$

We have seen that for sufficiently large UV mass difference in the dark fermions, the mass hierarchy in the mesonic spectrum changes qualitatively: the multiplet of vector mesons containing the ρ^N becomes lighter than the multiplet of flavoured pseudoscalars containing the π^A. The set of π's are then no longer the lightest hadronic states and an inclusion of the relevant vector states becomes necessary. This provides an upper limit on the amount of strong isospin breaking.

Using the aforementioned GMOR relations we can set an even stronger bound on the amount of strong isospin breaking. The validity of the GMOR relation was already studied for degenerate fermions in [6]. It was found that dependence of the square of the pseudo-Goldstone mass on a (differently defined) unrenormalized quark mass is linear for ensembles with $m_\rho/m_\pi > 1.4$, and thus chiral effective theory can be expected to work adequately latest from there on. Due to the increased computational cost of non-degenerate fermions we do not have results on ensembles that fulfil $m_\rho/m_\pi \gg 1.4$. Nevertheless, we can perform consistency tests on the GMOR relations in (101) around the threshold $m_\rho/m_\pi \approx 1.4$, see table 3 below. We use the fact that in our simulations one bare quark mass has been kept fixed and proceed as follows:

At degenerate fermion masses we take the degenerate GMOR relation (100) for granted

SciPost SciPost Phys. 14, 044 (2023)

Table 3: The point at which a change in the meson mass hierarchy occurs and the point at which the non-degenerate GMOR relation breaks down at one-sigma significance. In general, this breakdown sets a stronger bound. Note that with increased statistics the breakdown of the non-degenerate GMOR can occur at even smaller PCAC-mass-ratios.

β	$\left(\frac{m_\rho}{m_\pi}\right)_{\text{deg}}$	$\left(\frac{m_u}{m_d}\right)$ where $m_{\rho^N} = m_{\pi^A}$	$\left(\frac{m_u}{m_d}\right)$ where non-deg. GMOR breaks down
6.9	1.144(5)	2.8(3)	3.0(2)
6.9	1.25(1)	4.4(4)	1.5(1)
6.9	1.46(4)	8(1)	1.8(5)
7.05	1.16(1)	2.7(3)	2.2(2)
7.05	1.29(2)	4.7(5)	1.7(2)
7.05	1.46(4)	6.8(8)	1.7(2)
7.2	1.17(1)	2.7(4)	4(1)
7.2	1.26(2)	4.4(7)	1.7(4)
7.2	1.37(4)	6(2)	4(2)

and use it to determine the fixed chiral condensate $(\mu_u^3)^{\text{PCAC}}$ from the fixed quark mass m_u^{PCAC}.[14] Since these quantities are regulator-dependent we only compare results at the same value of the (bare) inverse gauge coupling β.[15] This determines three out of the four quantities that enter the non-degenerate GMOR relations in (101). We can then use both equations in (101) to determine $(\mu_d^3)^{\text{PCAC}}$. If the non-degenerate GMOR relation holds we expect the functions $\text{GMOR}_{\pi^{A,C}}(m_u, m_d, \mu_u, x)$ to have common roots at $x = \mu_d^{\text{PCAC}}$. Using our lattice data we find for ratios starting at $m_d/m_u \gtrsim 1.5$ that GMOR_{π^A} and GMOR_{π^C} cease to have a common root. We exemplify this in Fig. 7 for specific ensembles $\text{GMOR}_{\pi^{A,C}}(m_u, m_d, \mu_u, x)$ as a function of x. It can be seen that at larger quark-mass-ratios the functions do not share a common root. In particular GMOR_{π^C} no longer has root in this region of x.

We interpret this as a sign that at this point the description provided by the leading order chiral Lagrangian that lead to (101) no longer captures the underlying theory. This sets another upper bound on the validity of the non-degenerate GMOR relation. We might therefore hope that as long as these functions have a common root, all pseudo-Goldstone are still the lightest mesons in the spectrum and the degenerate GMOR relation holds true and the leading order Lagrangian might be an adequate description of strong isospin breaking in this theory at fixed $m_\rho/m_\pi \gtrsim 1.4$ at degeneracy. The tabulated upper limits can be found in table 3. Note that this is only an *upper bound*.

There are two reasons why the non-degenerate GMOR relation can break down: 1) The quark-mass-difference is too large in order for the system to be treated at leading order. In this case the next step would be to investigate this chiral Lagrangian at next-to-leading order in strong isospin breaking. 2) The average pseudo-Goldstone masses are in general too large to reliably use GMOR at leading order even close to the mass-degenerate limit. If this is the case we can either go to next-to-leading order in chiral perturbation theory or study the system for even lighter pseudo-Goldstones (at significantly increased computational cost).

In any case, we have shown that for small isospin breaking the non-degenerate GMOR relations do not break down immediately even for significantly heavier quarks than those used in the chiral extrapolation of [6] and also in the case of the $(m_\rho/m_\pi)_{\text{deg}} \approx 1.4$ ensemble. It will

[14] From [6] we know that the dependence of the squared Goldstone mass on the quark mass only becomes linear for $m_\rho/m_\pi \gtrsim 1.4$. However, this approach allows us to test whether the explicit introduction of isospin breaking effects cause a breakdown.

[15] In principle the regulator depends also on the bare quark masses. Experience has shown that these effects are subleading compared to the effect of β.

SciPost Phys. 14, 044 (2023)

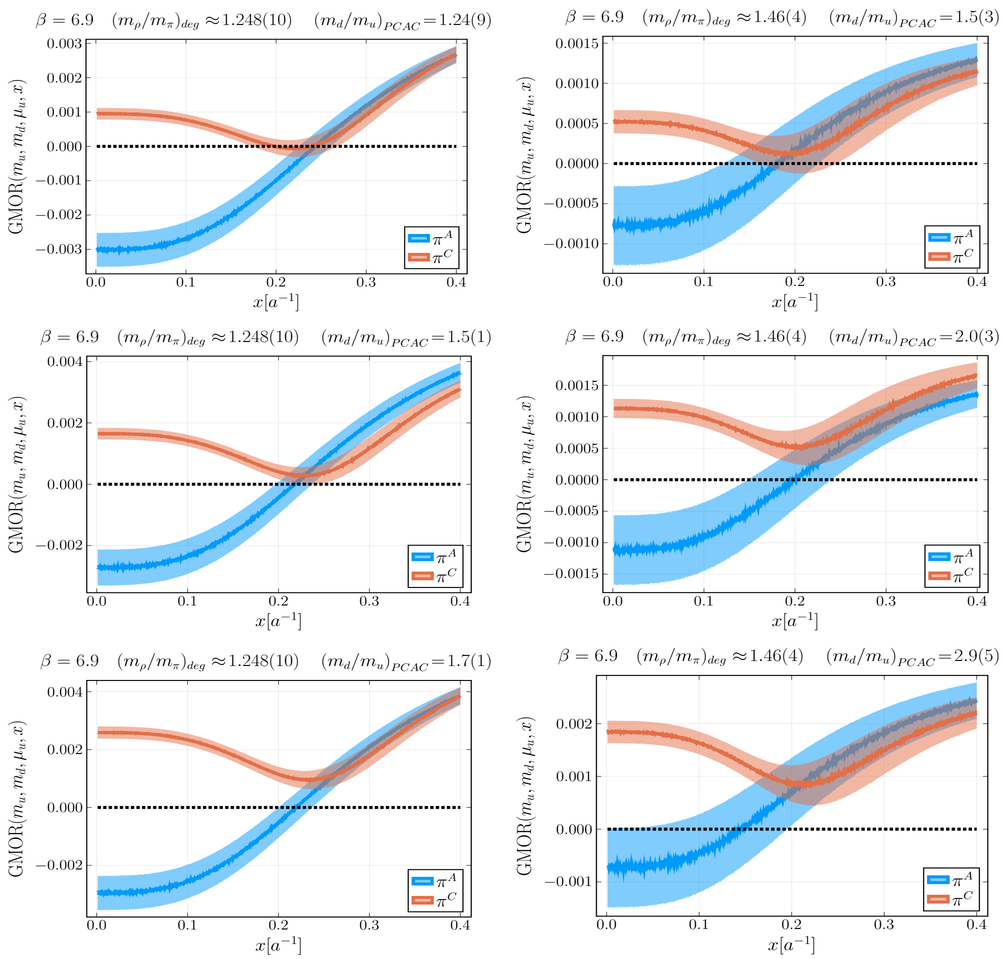

Figure 7: $\mathrm{GMOR}_{\pi^{A,C}}(m_u, m_d, \mu_u, x)$ as a function of x for an inverse gauge coupling of $\beta = 6.9$ and values of $m_\rho/m_\pi \approx 1.24$ and $m_\rho/m_\pi \approx 1.46$ at degeneracy. If the non-degenerate GMOR relation holds the condensate μ_d is given by the common root of the two functions. For small isospin breaking a common root exists. Starting at around $m_d/m_u \approx 1.5$ in both cases a tension develops. At around $m_d/m_u \approx 1.7$ for the heavier ensemble and at around $m_d/m_u \approx 2$ for the lighter ensemble the non-existence of a common root is more than one-sigma significant.

be therefore already worthwhile to study this UV complete theory and the chiral Lagrangian at leading order in this region of parameter space.

7 Conclusions

Summarizing, within this work we have laid the foundation for understanding strongly- interacting dark matter based on QCD-like symplectic gauge theories. To this end, we have constructed all possible symmetries for the non-degenerate underlying theory, including the case when gauged under a new $U(1)'$ symmetry. This yields symmetry-based constraints on absolutely stable and unstable light states.

We have constructed the chiral low-energy effective theory of the bound states, the dark hadrons, of this theory. In this process we extended previous results, see e. g. [1, 7, 11, 29, 33, 48, 60, 77, 78, 92], to include simultaneously processes mediated by the WZW term, mass-split spectra, and couplings to an Abelian gauge messenger. We fully elaborated the leading-order structure, including the Feynman rules. This comprehensive construction integrates many elements, which have been available separately in the literature, in one common framework. It therefore provides a ready-to-use effective theory to search for this type of DM at colliders and in direct detection experiments, and understand how it can fulfil astrophysical constraints. Especially, this theory can be straightforwardly extended to any QCD-like theory with a pseudo-real gauge group with two fundamental dark quarks. It will therefore serve as a versatile framework for future investigations.

The particular strength of our formulation is that it has been developed in parallel with a lattice implementation of the same theory, ensuring a coherent language and conventions. This is decisive, as effective low-energy theories require limits of validity. In the degenerate case, previous lattice results [6, 7] gave already the condition $m_\rho/m_\pi \gtrsim 1.4$. We extended this to the mass non-degenerate case, yielding the additional requirement that the PCAC dark quark masses, as defined in section 6.2, may not be split by more than a factor of 1.5 at the validity edge. We also showed how the theory at larger mass splittings is crossing over into a heavy-light system. While this requires a new low-energy effective theory, these results open interesting possibilities for strongly-interacting dark matter with split hierarchies and stable dark matter particles at different scales.

Finally, in section 4.4 we used the lattice results to determine the relevant LEC when coupling to the SM through a vector mediator. This shows how non-perturbative results can be used to reduce the number of free parameters when searching for DM by implementing constraints from the ultraviolet completion. This integration between effective theory and lattice simulations reduces substantially the number of free parameters in a pure effective theory approach, which is our ultimate aim. As figure 4 shows, the systematic comparison between different ultraviolet theories in this way yields very general constraints, making our approach predictive.

Summing up, we have created both a more comprehensive blueprint for how to construct viable low-energy theories for strongly-interacting dark matter and we have provided a particular implementation for an ultraviolet completion with a $Sp(4)$ QCD-like theory, in the spirit of e.g. [22, 30, 31, 93]. This can now be exploited to perform phenomenological calculations with a much higher degree of systematic control than previously possible. The latter can furthermore be systematically extended by going to higher orders with simultaneous lattice calculations of further LECs, just like in ordinary QCD.

Acknowledgements

This work was supported by the FWF Austrian Science Fund research teams grant STRONG-DM (FG1). SK is supported by the FWF Austrian Science Fund Elise-Richter grant project number V592-N27. MN is supported by the Austrian Science Fund FWF under the Doctoral Program W1252-N27 Particles and Interactions. We thank E. Bennett, B. Lucini, and J.-W. Lee for helpful discussions and them and the other authors of [6–8] for access to the $Sp(2N)$ HiRep code prior to publication. We are grateful to B. Lucini and M. Piai for a critical reading of the draft and helpful comments. We thank J. Pomper for his thorough proofreading and clarification on the draft and H. Kolesova for discussions on the WZW term. The lattice results presented have been obtained using the Vienna Scientific Cluster (VSC).

A $Sp(2N)$ groups: Defining properties and generators

In this section, we provide a general description of the symplectic group $Sp(2N)$. We suppress the colour and flavour indices, since all properties of the group are equivalent in the colour and flavour space and label the generators as T^a. We note, however, that all relations quoted here also apply to the colour group $Sp(4)_c$ and its generators τ^a. The fundamental representation of any $Sp(2N)$ group is pseudo-real. The representation is isomorphic to its complex conjugate representation. This can be seen from the defining property of the $Sp(2N)$ group: it is the subgroup of $SU(2N)$ that leaves

$$E = \begin{pmatrix} 0 & \mathbb{1}_N \\ -\mathbb{1}_N & 0 \end{pmatrix}, \tag{A.1}$$

invariant. It consists of all $SU(2N)$ transformations that fulfil $U^* = EUE^\dagger$. In the context of colour groups we will denote the invariant tensor as S to make the context unambiguous. For the invariant tensor E the following relations hold:

$$E^\dagger = E^{-1} = E^T = -E, \quad E^2 = -\mathbb{1}_{2N}\,. \tag{A.2}$$

On the level of the generators T^a using $U = \exp(i\alpha^a T^a)$ this is equivalent to

$$T^{a*} = -ET^aE^\dagger\,. \tag{A.3}$$

For completeness, we point out that not every representation of a $Sp(2N)$ group is pseudo-real but also real representations exist, such as the adjoint and antisymmetric representations, see e.g. [8]. However, complex representations of $Sp(2N)$ do not exist. The group $SU(4)$ has 15 generators and the subgroup $Sp(4)$ has 10 generators. From (A.3) follows the relation

$$ET^a + (T^a)^T E = 0 \quad \text{for } a = 6, \dots, 15\,, \tag{A.4}$$

for the generators of the $Sp(4)$ subgroup while the other 5 generators satisfy

$$ET^a - (T^a)^T E = 0 \quad \text{for } a = 1, \dots, 5\,. \tag{A.5}$$

The generators with normalization $\mathrm{Tr}\{T^aT^b\} = \frac{1}{2}\delta^{ab}$ are given by [94]

$$\begin{aligned}
T^1 &= \tfrac{1}{2\sqrt{2}}\begin{pmatrix} 0 & 1 & 0 & 0 \\ 1 & 0 & 0 & 0 \\ 0 & 0 & 0 & 1 \\ 0 & 0 & 1 & 0 \end{pmatrix}, &
T^2 &= \tfrac{1}{2\sqrt{2}}\begin{pmatrix} 0 & -i & 0 & 0 \\ i & 0 & 0 & 0 \\ 0 & 0 & 0 & i \\ 0 & 0 & -i & 0 \end{pmatrix}, &
T^3 &= \tfrac{1}{2\sqrt{2}}\begin{pmatrix} 1 & 0 & 0 & 0 \\ 0 & -1 & 0 & 0 \\ 0 & 0 & 1 & 0 \\ 0 & 0 & 0 & -1 \end{pmatrix}, \\
T^4 &= \tfrac{1}{2\sqrt{2}}\begin{pmatrix} 0 & 0 & 0 & -i \\ 0 & 0 & i & 0 \\ 0 & -i & 0 & 0 \\ i & 0 & 0 & 0 \end{pmatrix}, &
T^5 &= \tfrac{1}{2\sqrt{2}}\begin{pmatrix} 0 & 0 & 0 & 1 \\ 0 & 0 & -1 & 0 \\ 0 & -1 & 0 & 0 \\ 1 & 0 & 0 & 0 \end{pmatrix}, &
T^6 &= \tfrac{1}{2\sqrt{2}}\begin{pmatrix} 0 & 0 & -i & 0 \\ 0 & 0 & 0 & -i \\ i & 0 & 0 & 0 \\ 0 & i & 0 & 0 \end{pmatrix}, \\
T^7 &= \tfrac{1}{2\sqrt{2}}\begin{pmatrix} 0 & 0 & 0 & -i \\ 0 & 0 & -i & 0 \\ 0 & i & 0 & 0 \\ i & 0 & 0 & 0 \end{pmatrix}, &
T^8 &= \tfrac{1}{2\sqrt{2}}\begin{pmatrix} 0 & -i & 0 & 0 \\ i & 0 & 0 & 0 \\ 0 & 0 & 0 & -i \\ 0 & 0 & i & 0 \end{pmatrix}, &
T^9 &= \tfrac{1}{2\sqrt{2}}\begin{pmatrix} 0 & 0 & -i & 0 \\ 0 & 0 & 0 & i \\ i & 0 & 0 & 0 \\ 0 & -i & 0 & 0 \end{pmatrix}, \\
T^{10} &= \tfrac{1}{2}\begin{pmatrix} 0 & 0 & 1 & 0 \\ 0 & 0 & 0 & 0 \\ 1 & 0 & 0 & 0 \\ 0 & 0 & 0 & 0 \end{pmatrix}, &
T^{11} &= \tfrac{1}{2\sqrt{2}}\begin{pmatrix} 0 & 0 & 0 & 1 \\ 0 & 0 & 1 & 0 \\ 0 & 1 & 0 & 0 \\ 1 & 0 & 0 & 0 \end{pmatrix}, &
T^{12} &= \tfrac{1}{2}\begin{pmatrix} 0 & 0 & 0 & 0 \\ 0 & 0 & 0 & 1 \\ 0 & 0 & 0 & 0 \\ 0 & 1 & 0 & 0 \end{pmatrix}, \\
T^{13} &= \tfrac{1}{2\sqrt{2}}\begin{pmatrix} 0 & 1 & 0 & 0 \\ 1 & 0 & 0 & 0 \\ 0 & 0 & 0 & -1 \\ 0 & 0 & -1 & 0 \end{pmatrix}, &
T^{14} &= \tfrac{1}{2\sqrt{2}}\begin{pmatrix} 1 & 0 & 0 & 0 \\ 0 & -1 & 0 & 0 \\ 0 & 0 & -1 & 0 \\ 0 & 0 & 0 & 1 \end{pmatrix}, &
T^{15} &= \tfrac{1}{2\sqrt{2}}\begin{pmatrix} 1 & 0 & 0 & 0 \\ 0 & 1 & 0 & 0 \\ 0 & 0 & -1 & 0 \\ 0 & 0 & 0 & -1 \end{pmatrix}.
\end{aligned} \tag{A.6}$$

The totally antisymmetric structure constants $f^{a,b,c}$ of the $SU(4)$ group are defined as

$$\left[T^a, T^b\right] = i f^{abc} T^c \,, \tag{A.7}$$

and all non-zero structure constants are given by

$$f^{1,2,14} = f^{2,3,13} = f^{2,4,6} = f^{3,5,7} = -f^{1,3,8} = -f^{1,5,9} = -f^{3,4,11} = -f^{4,5,15} = \frac{1}{\sqrt{2}}\,, \tag{A.8}$$

$$f^{1,4,10} = f^{2,5,10} = f^{2,5,12} = -f^{1,4,12} = \frac{1}{2}\,, \tag{A.9}$$

In section 2 we found that two non-degenerate fermion masses break the global symmetry down to $SU(2)_u \times SU(2)_d$. This group has 6 generators, that are combinations of the generators of $Sp(4)$

$$T_u^1 = T^{10}, \quad T_u^2 = \frac{1}{\sqrt{2}}(T^6 + T^9), \quad T_u^3 = \frac{1}{\sqrt{2}}(T^{14} + T^{15})\,, \tag{A.10}$$

$$T_d^1 = T^{12}, \quad T_d^2 = \frac{1}{\sqrt{2}}(T^6 - T^9), \quad T_d^3 = \frac{1}{\sqrt{2}}(T^{15} - T^{14})\,. \tag{A.11}$$

Occasionally it is convenient to use another basis of the generators than the one in (A.6). A different basis of $SU(4)$ and $Sp(4)$ algebras is obtained by exchanging the second row with the third row and the second column with the third column. In this form, all generators are either block-diagonal or anti-block-diagonal where the different blocks are either the identity matrix $\mathbb{1}$ or one of the Pauli matrices σ_i,

$$\begin{aligned}
&\tilde{T}^1 = \frac{1}{2\sqrt{2}}\begin{pmatrix} 0 & \mathbb{1}_2 \\ \mathbb{1}_2 & 0 \end{pmatrix}, &&\tilde{T}^2 = \frac{1}{2\sqrt{2}}\begin{pmatrix} 0 & -i\sigma_3 \\ i\sigma_3 & 0 \end{pmatrix}, &&\tilde{T}^3 = \frac{1}{2\sqrt{2}}\begin{pmatrix} \mathbb{1}_2 & 0 \\ 0 & -\mathbb{1}_2 \end{pmatrix}, \\
&\tilde{T}^4 = \frac{1}{2\sqrt{2}}\begin{pmatrix} 0 & -i\sigma_1 \\ i\sigma_1 & 0 \end{pmatrix}, &&\tilde{T}^5 = \frac{1}{2\sqrt{2}}\begin{pmatrix} 0 & i\sigma_2 \\ -i\sigma_2 & 0 \end{pmatrix}, &&\tilde{T}^6 = \frac{1}{2\sqrt{2}}\begin{pmatrix} \sigma_2 & 0 \\ 0 & \sigma_2 \end{pmatrix}, \\
&\tilde{T}^7 = \frac{1}{2\sqrt{2}}\begin{pmatrix} 0 & \sigma_2 \\ \sigma_2 & 0 \end{pmatrix}, &&\tilde{T}^8 = \frac{1}{2\sqrt{2}}\begin{pmatrix} 0 & -i\mathbb{1}_2 \\ i\mathbb{1}_2 & 0 \end{pmatrix}, &&\tilde{T}^9 = \frac{1}{2\sqrt{2}}\begin{pmatrix} \sigma_2 & 0 \\ 0 & -\sigma_2 \end{pmatrix}, \\
&\tilde{T}^{10} = \frac{1}{2}\begin{pmatrix} \sigma_1 & 0 \\ 0 & 0 \end{pmatrix}, &&\tilde{T}^{11} = \frac{1}{2\sqrt{2}}\begin{pmatrix} 0 & \sigma_1 \\ \sigma_1 & 0 \end{pmatrix}, &&\tilde{T}^{12} = \frac{1}{2}\begin{pmatrix} 0 & 0 \\ 0 & \sigma_1 \end{pmatrix}, \\
&\tilde{T}^{13} = \frac{1}{2\sqrt{2}}\begin{pmatrix} 0 & \sigma_3 \\ \sigma_3 & 0 \end{pmatrix}, &&\tilde{T}^{14} = \frac{1}{2\sqrt{2}}\begin{pmatrix} \sigma_3 & 0 \\ 0 & -\sigma_3 \end{pmatrix}, &&\tilde{T}^{15} = \frac{1}{2\sqrt{2}}\begin{pmatrix} \sigma_3 & 0 \\ 0 & \sigma_3 \end{pmatrix}.
\end{aligned} \tag{A.12}$$

Then, the symplectic matrix E is written as

$$\tilde{E} = \begin{pmatrix} i\sigma_2 & 0 \\ 0 & i\sigma_2 \end{pmatrix}. \tag{A.13}$$

In this basis, all $SU(2)_u \times SU(2)_d$ generators and thus transformations are fully block-diagonal:

$$\begin{aligned}
&\tilde{T}_u^1 = \tilde{T}^{10} = \frac{1}{2}\begin{pmatrix} \sigma_1 & 0 \\ 0 & 0 \end{pmatrix}, &&\tilde{T}_d^1 = \tilde{T}^{12} = \frac{1}{2}\begin{pmatrix} 0 & 0 \\ 0 & \sigma_1 \end{pmatrix}, \\
&\tilde{T}_u^2 = \frac{(\tilde{T}^6 + \tilde{T}^9)}{\sqrt{2}} = \frac{1}{2}\begin{pmatrix} \sigma_2 & 0 \\ 0 & 0 \end{pmatrix}, &&\tilde{T}_d^2 = \frac{(\tilde{T}^6 - \tilde{T}^9)}{\sqrt{2}} = \frac{1}{2}\begin{pmatrix} 0 & 0 \\ 0 & \sigma_2 \end{pmatrix}, \\
&\tilde{T}_u^3 = \frac{(\tilde{T}^{14} + \tilde{T}^{15})}{\sqrt{2}} = \frac{1}{2}\begin{pmatrix} \sigma_3 & 0 \\ 0 & 0 \end{pmatrix}, &&\tilde{T}_d^3 = \frac{(\tilde{T}^{15} - \tilde{T}^{14})}{\sqrt{2}} = \frac{1}{2}\begin{pmatrix} 0 & 0 \\ 0 & \sigma_3 \end{pmatrix}.
\end{aligned} \tag{A.14}$$

SciPost SciPost Phys. 14, 044 (2023)

Another useful basis can be obtained by considering the matrix of the Goldstone bosons in (21) as well as the matrices of the spin-1 states in (36). In (29) we have rewritten the Goldstone bosons such that in every matrix element only one Goldstone field appears. Then, the Goldstone matrix takes the form

$$\pi = \sum_{i=1,\dots,5} \pi_a T^a = \sum_{N=A,\dots,E} \pi_N T^N = \frac{1}{2}\begin{pmatrix} \pi^C & \pi^B & 0 & \pi^E \\ \pi^A & -\pi^C & -\pi^E & 0 \\ 0 & -\pi^D & \pi^C & \pi^A \\ \pi^D & 0 & \pi^B & -\pi^C \end{pmatrix}, \tag{A.15}$$

which implicitly defines the generators T^N with $N = A, B, C, D, E$. In QCD this leads to the usual pion charge eigenstates $\pi^\pm$ and π^0 as shown in (30). We can extend that to the spin-1 states and by that define a new basis for the generators. It is was shown that the spin-1 states ρ_{14} and ρ_{15} correspond to the ρ^0 and ω meson of QCD [8]. Therefore, we define the other T^N by specifying the $J^D = 1^-$ matrix

$$\rho^{(J^D=1^-)} = \sum_{a=6,\dots,15} \rho_a T^a = \sum_{N=F,\dots,O} \rho_N T^N \tag{A.16}$$

$$= \frac{1}{2}\begin{pmatrix} \frac{1}{\sqrt{2}}\left(\rho^O + \rho^N\right) & \rho^M & -\rho^J & -\rho^K \\ \rho^H & \frac{1}{\sqrt{2}}\left(\rho^O - \rho^N\right) & -\rho^K & -\rho^L \\ \rho^F & \rho^G & -\frac{1}{\sqrt{2}}\left(\rho^O + \rho^N\right) & -\rho^H \\ \rho^G & \rho^I & -\rho^M & -\frac{1}{\sqrt{2}}\left(\rho^O - \rho^N\right) \end{pmatrix}. \tag{A.17}$$

All off-diagonal elements contain only one vector field and the states corresponding to the ρ^0 and ω of QCD appear on the diagonal. The generators in this basis are given by

$$\begin{aligned}
T^A &= \frac{1}{\sqrt{2}}\left(T^1 - iT^2\right), & T^B &= \frac{1}{\sqrt{2}}\left(T^1 + iT^2\right), & T^C &= T^3 \\
T^D &= \frac{1}{\sqrt{2}}\left(T^5 - iT^4\right), & T^E &= \frac{1}{\sqrt{2}}\left(T^5 + iT^4\right), & T^F &= \frac{1}{\sqrt{2}}\left(\sqrt{2}T^{10} - i\left(T^6 + T^9\right)\right), \\
T^G &= \frac{1}{\sqrt{2}}\left(T^{11} - iT^7\right), & T^H &= \frac{1}{\sqrt{2}}\left(T^{13} - iT^8\right), & T^I &= \frac{1}{\sqrt{2}}\left(\sqrt{2}T^{12} - i\left(T^6 - T^9\right)\right), \\
T^J &= \frac{1}{\sqrt{2}}\left(-\sqrt{2}T^{10} - i\left(T^6 + T^9\right)\right), & T^K &= \frac{-1}{\sqrt{2}}\left(T^{11} + iT^7\right), & T^L &= \frac{1}{\sqrt{2}}\left(-\sqrt{2}T^{12} - i\left(T^6 - T^9\right)\right), \\
T^M &= \frac{1}{\sqrt{2}}\left(T^{13} + iT^8\right), & T^N &= T^{14}, & T^O &= T^{15}.
\end{aligned} \tag{A.18}$$

Analogously, we can define the axial-vector matrix, i.e., the $J^D = 1^+$ mesons, as

$$\rho^{(J^D=1^+)} = \sum_{a=1,\dots,5} \rho_a T^a = \sum_{N=A,\dots,E} a_N T^N = \frac{1}{2}\begin{pmatrix} a^C & a^B & 0 & a^E \\ a^A & -a^C & -a^E & 0 \\ 0 & -a^D & a^C & a^A \\ a^D & 0 & a^B & -a^C \end{pmatrix}, \tag{A.19}$$

where we have given them a different name a_N in the T^N basis in order to emphasize the different parity compared to the ρ_N states. Similar relations like (29) can then be obtained from (A.18) for the vector and axial-vector matrix.

B Mesonic states and multiplets

B.1 States and $Sp(4)$ multiplets

The meson spin-0 and spin-1 fermion bilinears have already been constructed in [8]. They have the same structure as those appearing in a $N_f = 1$ theory [34]. For completeness we give in table 4 here the operators that source the $J^D = 0^-, 1^+$ and 1^- multiplets of $Sp(4)$, i.e. the pseudoscalars, axial-vectors and vectors constructed from the generators in the basis of (A.6) and (A.18), respectively. The other spin-0 and spin-1 states are the scalar 5-plet as well as the scalar flavour singlet.

B.2 Multiplet structure under $SU(2)_u \times SU(2)_d$

Because $SU(2)$ exponentials are easily calculated analytically, we may provide a general expression for $SU(2)_d \times SU(2)_u$ transformations. In the basis given by (A.12), the transformation is in block diagonal form

$$V = \begin{pmatrix} a & -b^* & 0 & 0 \\ b & a^* & 0 & 0 \\ 0 & 0 & e & -c^* \\ 0 & 0 & c & e^* \end{pmatrix}, \tag{B.1}$$

where the diagonal matrix blocks are elements of SU(2). We denote the complex coefficients of the individual $SU(2)$ by (a, b) and (e, c); they fulfil $|a|^2 + |b|^2 = 1$ and $|c|^2 + |e|^2 = 1$, respectively.It is convenient to rewrite the Dirac spinors in terms of their left- and right-handed projections

$$P_{R/L} u = u_{R/L}\,, \tag{B.2}$$
$$P_{R/L} d = d_{R/L}\,, \tag{B.3}$$
$$P_{R/L} = (1 \pm \gamma_5)/2\,. \tag{B.4}$$

Under a $SU(2)_d \times SU(2)_u$ transformation the components of Ψ transform as $\Psi \to V\Psi$, or, explicitly,

$$\begin{pmatrix} u_L \\ \tilde{u}_R \\ d_L \\ \tilde{d}_R \end{pmatrix} = \begin{pmatrix} u_L \\ -SC\bar{u}_R^T \\ d_L \\ -SC\bar{d}_R^T \end{pmatrix} \to \begin{pmatrix} au_L - b^*\tilde{u}_R \\ bu_L + a^*\tilde{u}_R \\ ed_L - c^*\tilde{d}_R \\ cd_L + e^*\tilde{d}_R \end{pmatrix}. \tag{B.5}$$

For completeness we give the following useful relations for the colour matrix S as well as the charge conjugation operator in Minkowski space and the spinors $\tilde{u}_R$ and $\tilde{d}_R$:

$$C^\dagger = C^{-1} = C^T = -C, \quad C^2 = -\mathbb{1}, \quad C\gamma_\mu C^{-1} = -\gamma_\mu^T, \tag{B.6}$$
$$(SC)^\dagger = (SC)^{-1} = (SC)^T = SC, \quad (SC)^2 = \mathbb{1}, \quad SC\gamma_\mu SC = -\gamma_\mu^T\,, \tag{B.7}$$

$$q_R = SC\bar{\tilde{q}}_R^T, \qquad q_R^T = \bar{\tilde{q}}_R SC, \tag{B.8}$$
$$\bar{q}_R = -\tilde{q}_R^T SC, \qquad \bar{q}_R^T = -SC\tilde{q}_R\,. \tag{B.9}$$

The scalar $\bar{u}d$ and vectors $\bar{u}\gamma_\mu d$ transform under $SU(2)_d \times SU(2)_u$ as

$$\begin{aligned} \bar{u}d = \bar{u}_L d_R + \bar{u}_R d_L \to \quad & a^*c^*\left(\bar{u}_L SC\bar{d}_L^T + \bar{u}_R SC\bar{d}_R^T\right) - be\left(u_L^T SCd_L + u_R^T SCd_R\right) \\ & + a^*e\left(\bar{u}_L d_R + \bar{u}_R d_L\right) - bc^*\left(u_L^T \bar{d}_R^T + u_R^T \bar{d}_L^T\right) \\ & = a^*c^*\left(\bar{u}SC\bar{d}^T\right) - be\left(u^T SCd\right) + a^*e\left(\bar{u}d\right) + bc^*\left(\bar{d}u\right), \end{aligned} \tag{B.10}$$

$$\begin{aligned} \bar{u}\gamma_\mu d = \bar{u}_L\gamma_\mu d_L + \bar{u}_R\gamma_\mu d_R \to \quad & a^*e\left(\bar{u}_L\gamma_\mu d_L + \bar{u}_R\gamma_\mu d_R\right) + bc^*\left(u_L^T\gamma_\mu^T\bar{d}_L^T + u_R^T\gamma_\mu^T\bar{d}_R^T\right) \\ & + a^*c^*\left(\bar{u}_L\gamma_\mu SC\bar{d}_R^T + \bar{u}_R\gamma_\mu SC\bar{d}_L^T\right) + be\left(u_L^T\gamma_\mu^T SCd_R + u_R^T\gamma_\mu^T SCd_L\right) \\ & = a^*e\left(\bar{u}\gamma_\mu d\right) - bc^*\left(\bar{d}\gamma_\mu u\right) + a^*c^*\left(\bar{u}\gamma_\mu SC\bar{d}^T\right) - be\left(u^T SC\gamma_\mu d\right). \end{aligned}$$

SciPost Phys. 14, 044 (2023)

Table 4: Fermion bilinears of the $J^D = 0^-, 1^\pm$ meson multiplets constructed from the generators in the basis of (A.6) (left) and (A.18) (right) respectively. In addition we give the J^P quantum numbers.

	$\Psi^T SC\gamma_5 T^n E\Psi + \bar{\Psi} E T^n SC\gamma_5 \bar{\Psi}^T$		$\Psi^T SCT^N \gamma_5 E\Psi + \bar{\Psi} E T^N SC\gamma_5 \bar{\Psi}^T$	J^P	J^D
π_1	$\frac{1}{\sqrt{2}}\left(\bar{u}\gamma_5 d + \bar{d}\gamma_5 u\right)$	π^A	$\bar{u}\gamma_5 d$	0^-	0^-
π_2	$\frac{i}{\sqrt{2}}\left(\bar{d}\gamma_5 u - \bar{u}\gamma_5 d\right)$	π^B	$\bar{d}\gamma_5 u$	0^-	0^-
π_3	$\frac{1}{\sqrt{2}}\left(\bar{u}\gamma_5 u - \bar{d}\gamma_5 d\right)$	π^C	$\frac{1}{\sqrt{2}}\left(\bar{u}\gamma_5 u - \bar{d}\gamma_5 d\right)$	0^-	0^-
π_4	$\frac{i}{\sqrt{2}}\left(\bar{d}\gamma_5 SC\bar{u}^T - d^T SC\gamma_5 u\right)$	π^D	$\bar{d}\gamma_5 SC\bar{u}^T$	0^+	0^-
π_5	$\frac{1}{\sqrt{2}}\left(\bar{d}\gamma_5 SC\bar{u}^T + d^T SC\gamma_5 u\right)$	π^E	$d^T SC\gamma_5 u$	0^+	0^-

	$\Psi^T SC\gamma_5 T^0 E\Psi + \bar{\Psi} E T^0 SC\gamma_5 \bar{\Psi}^T$		$\Psi^T SC\gamma_5 T^0 E\Psi + \bar{\Psi} E T^0 SC\gamma_5 \bar{\Psi}^T$	J^P	J^D
η'	$\frac{1}{\sqrt{2}}\left(\bar{u}\gamma_5 u + \bar{d}\gamma_5 d\right)$	η'	$\frac{1}{\sqrt{2}}\left(\bar{u}\gamma_5 u + \bar{d}\gamma_5 d\right)$	0^-	0^-

	$2\,\bar{\Psi} T^n \gamma_\mu \gamma_5 \Psi$		$2\bar{\Psi} T^N \gamma_\mu \gamma_5 \Psi$	J^P	J^D
ρ_1	$\frac{1}{\sqrt{2}}\left(\bar{u}\gamma_\mu\gamma_5 d + \bar{d}\gamma_\mu\gamma_5 u\right)$	a^A	$\bar{d}\gamma_\mu\gamma_5 u$	1^+	1^+
ρ_2	$\frac{i}{\sqrt{2}}\left(\bar{d}\gamma_\mu\gamma_5 u - \bar{u}\gamma_\mu\gamma_5 d\right)$	a^B	$\bar{u}\gamma_\mu\gamma_5 d$	1^+	1^+
ρ_3	$\frac{1}{\sqrt{2}}\left(\bar{u}\gamma_\mu\gamma_5 u - \bar{d}\gamma_\mu\gamma_5 d\right)$	a^C	$\frac{1}{\sqrt{2}}\left(\bar{u}\gamma_\mu\gamma_5 u - \bar{d}\gamma_\mu\gamma_5 d\right)$	1^+	1^+
ρ_4	$\frac{i}{\sqrt{2}}\left(\bar{d}SC\gamma_\mu\gamma_5\bar{u}^T - d^T SC\gamma_\mu\gamma_5 u\right)$	a^D	$d^T SC\gamma_\mu\gamma_5 u$	1^-	1^+
ρ_5	$\frac{1}{\sqrt{2}}\left(\bar{d}SC\gamma_\mu\gamma_5\bar{u}^T + d^T SC\gamma_\mu\gamma_5 u\right)$	a^E	$\bar{d}\gamma_\mu\gamma_5 SC\bar{u}^T$	1^-	1^+

	$2\bar{\Psi} T^n \gamma_\mu \Psi$		$2\bar{\Psi} T^N \gamma_\mu \Psi$	J^P	J^D
ρ_6	$\frac{i}{\sqrt{2}}\big(\bar{u}\gamma_\mu SCP_L\bar{u}^T + u^T SC\gamma_\mu P_L u$ $+\bar{d}\gamma_\mu SCP_L\bar{d}^T + d^T SC\gamma_\mu P_L d\big)$	ρ^F	$u^T SC\gamma_\mu P_L u$	1^+	1^-
ρ_7	$\frac{i}{\sqrt{2}}\left(\bar{u}\gamma_\mu SC\bar{d}^T + u^T SC\gamma_\mu d\right)$	ρ^G	$u^T SC\gamma_\mu d$	1^+	1^-
ρ_8	$\frac{i}{\sqrt{2}}\left(-\bar{u}\gamma_\mu d + \bar{d}\gamma_\mu u\right)$	ρ^H	$\bar{d}\gamma_\mu u$	1^-	1^-
ρ_9	$\frac{i}{\sqrt{2}}\big(\bar{u}\gamma_\mu SCP_L\bar{u}^T + u^T SC\gamma_\mu P_L u$ $-\bar{d}\gamma_\mu SCP_L\bar{d}^T - d^T SC\gamma_\mu P_L d\big)$	ρ^I	$d^T SC\gamma_\mu P_L d$	1^+	1^-
ρ_{10}	$u^T SC\gamma_\mu P_L u - \bar{u}\gamma_\mu SCP_L\bar{u}^T$	ρ^J	$\bar{u}\gamma_\mu SCP_L\bar{u}^T$	1^+	1^-
ρ_{11}	$\frac{1}{\sqrt{2}}\left(-\bar{u}\gamma_\mu SC\bar{d}^T + u^T SC\gamma_\mu d\right)$	ρ^K	$\bar{u}\gamma_\mu SC\bar{d}^T$	1^+	1^-
ρ_{12}	$d^T SC\gamma_\mu P_L d - \bar{d}\gamma_\mu SCP_L\bar{d}^T$	ρ^L	$\bar{d}\gamma_\mu SCP_L\bar{d}^T$	1^+	1^-
ρ_{13}	$\frac{1}{\sqrt{2}}\left(\bar{u}\gamma_\mu d + \bar{d}\gamma_\mu u\right)$	ρ^M	$\bar{u}\gamma_\mu d$	1^-	1^-
ρ_{14}	$\frac{1}{\sqrt{2}}\left(\bar{u}\gamma_\mu u - \bar{d}\gamma_\mu d\right)$	ρ^N	$\frac{1}{\sqrt{2}}\left(\bar{u}\gamma_\mu u - \bar{d}\gamma_\mu d\right)$	1^-	1^-
ρ_{15}	$\frac{1}{\sqrt{2}}\left(\bar{u}\gamma_\mu u + \bar{d}\gamma_\mu d\right)$	ρ^O	$\frac{1}{\sqrt{2}}\left(\bar{u}\gamma_\mu u + \bar{d}\gamma_\mu d\right)$	1^-	1^-

Here, we use the property $\left(\phi^T\Gamma\chi\right)^T = -\chi^T\Gamma^T\phi$ for Grassmann variables ϕ, χ. The pseudoscalars and axial-vectors transform similarly since the only difference is the gamma matrix γ_5.

$$
\begin{aligned}
\bar{u}\gamma_5 d &= \bar{u}_L d_R - \bar{u}_R d_L \\
&\to a^* c^*\left(\bar{u}SC\gamma_5\bar{d}^T\right) - be\left(u^T SC\gamma_5 d\right) + a^* e\left(\bar{u}\gamma_5 d\right) + bc^*\left(\bar{d}\gamma_5 u\right)\,,
\end{aligned}
\tag{B.11}
$$

$$
\begin{aligned}
\bar{u}\gamma_\mu\gamma_5 d &= \bar{u}_R\gamma_\mu d_R - \bar{u}_L\gamma_\mu d_L \\
&\to a^* e\left(\bar{u}\gamma_\mu\gamma_5 d\right) - bc^*\left(\bar{d}\gamma_\mu\gamma_5 u\right) + a^* c^*\left(\bar{u}\gamma_\mu\gamma_5 SC\bar{d}^T\right) - be\left(u^T SC\gamma_\mu\gamma_5 d\right)\,,
\end{aligned}
\tag{B.12}
$$

From this we conclude that these states form a quadruplet under $SU(2)_d \times SU(2)_u$. The remaining pseudo-scalars and scalars transform as singlets. The associated operators have the

SciPost SciPost Phys. 14, 044 (2023)

form $\bar{u}\Gamma u \pm \bar{d}\Gamma d$. The individual $SU(2)_{d,u}$ only change one of the terms, so it is sufficient to look at the transformation property of, say, $\bar{u}\Gamma u$,

$$\begin{aligned}
\bar{u}u &= \bar{u}_L u_R + \bar{u}_R u_L \to \bar{u}_L u_R + \bar{u}_R u_L = \bar{u}u\,,\\
\bar{u}\gamma_5 u &= \bar{u}_L u_R - \bar{u}_R u_L \to \bar{u}_L u_R + \bar{u}_R u_L = \bar{u}\gamma_5 u\,,\\
\bar{u}\gamma_\mu u &= \bar{u}_L\gamma_\mu u_L + \bar{u}_R\gamma_\mu u_R \to \left(|a|^2 - |b|^2\right)\left(\bar{u}\gamma_\mu u\right) + 2a^* b^*\left(\bar{u}\gamma_\mu S C P_L \bar{u}^T\right) - 2ab\left(u^T S C \gamma_\mu P_L u\right),\\
\bar{u}\gamma_\mu\gamma_5 u &= \bar{u}_R\gamma_\mu u_R - \bar{u}_L\gamma_\mu u_L \to \bar{u}\gamma_\mu\gamma_5 u\,.
\end{aligned} \tag{B.13}$$

Similar expressions for $\bar{d}\Gamma d$ are obtained by replacing $u \to d, a \to e$ and $b \to c$.

C Feynman rules

In section C.1 we provide a subset of Feynman rules which are used in this work for Goldstone bosons and the iso-singlet state η' in presence and isolation from additional, external interactions for degenerate fermions $m_u = m_d$. Additionally, we show some Feynman rules for axial- and vector states ρ_μ coupled to Goldstone bosons. In section C.2 the Feynman rules are given for non-degenerate fermions $m_u \neq m_d$. All momenta are taken as *ingoing*, with the Mandelstam variables being defined as

$$s = (p_1 + p_2)^2 = (k_1 + k_2)^2\,, \tag{C.1}$$

$$t = (p_1 + k_1)^2 = (p_2 + k_2)^2\,, \tag{C.2}$$

$$u = (p_1 + k_2)^2 = (p_2 + k_1)^2\,, \tag{C.3}$$

where $p_1 + p_2 + k_1 + k_2 = 0$.

C.1 Feynman rules for degenerate fermions $m_u = m_d$

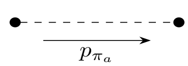

$$= \frac{1}{p_{\pi_a}^2 - m_\pi^2}\,, \tag{C.4}$$

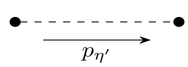

$$= \frac{1}{p_{\eta'}^2 - m_\pi^2 - \Delta m_{\eta'}^2}\,, \tag{C.5}$$

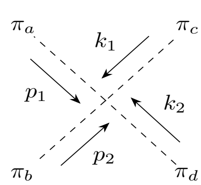

$$= \frac{1}{2f_\pi^2}\Big[\delta^{ab}\delta^{cd}(s - m_\pi^2) + \delta^{ac}\delta^{bd}(t - m_\pi^2) + \delta^{ad}\delta^{cb}(u - m_\pi^2)\Big], \tag{C.6}$$

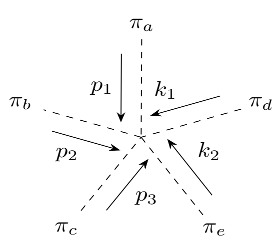

$$\begin{aligned}
= &\frac{N_c}{10\sqrt{2}\pi^2 f_\pi^5}\varepsilon^{\mu\nu\rho\sigma}\Big[\,(p_2 - p_1)_\mu\, p_{3\nu} k_{1\rho} k_{2\sigma} + \\
&+ p_{1\mu} p_{2\nu}\left(k_{1\rho} k_{2\sigma} + k_{2\rho} p_{3\sigma} + p_{3\rho} k_{1\sigma}\right)\Big],\\
&(a \neq b \neq c \neq d \neq e)
\end{aligned} \tag{C.7}$$

SciPost Phys. 14, 044 (2023)

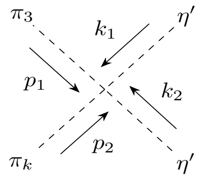

$$= \frac{m_\pi^2}{2f_\pi^2}\,, \tag{C.8}$$

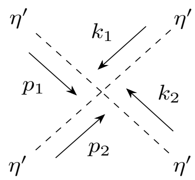

$$= \frac{m_\pi^2}{2f_\pi^2}\,, \tag{C.9}$$

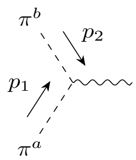

$$V^\mu = 2ie_D\,\mathrm{Tr}\big(\mathcal{Q}\big[T^a, T^b\big]\big)(p_1 - p_2)^\mu\,, \tag{C.10}$$

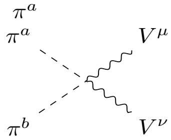

$$= 4e_D^2\,\mathrm{Tr}\big(\mathcal{Q}^2\big(T^aT^b + T^bT^a\big) - 2T^a\mathcal{Q}T^b\mathcal{Q}\big)\,\eta^{\mu\nu}\,, \tag{C.11}$$

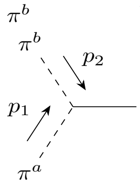

$$\rho_\mu^c = ig_\rho f^{abc}(p_1 - p_2)^\mu\,, \tag{C.12}$$

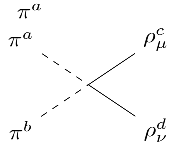

$$\begin{aligned} = \;& 2g_{\rho\pi\pi}^2\,\mathrm{Tr}(T^aT^bT^cT^d + T^bT^aT^cT^d + T^aT^bT^dT^c \\ &\qquad + T^bT^aT^dT^c - 2T^aT^cT^bT^d \\ &\qquad - 2T^aT^dT^bT^c)\eta^{\mu\nu}\,. \end{aligned} \tag{C.13}$$

C.2 Feynman rules for non-degenerate fermions $m_u \neq m_d$

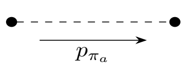

$$= \frac{1}{p_{\pi_a}^2 - m_\pi^2}\,, \tag{C.14}$$

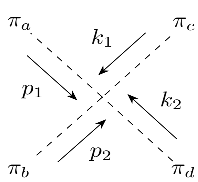

$$\begin{aligned} = \frac{2\mu_u^6}{f_\pi^2\left(\mu_u^3 + \mu_d^3\right)^2}\Big[&\delta^{ab}\delta^{cd}(s - m_\pi^2) + \delta^{ac}\delta^{bd}(t - m_\pi^2) \\ &+ \delta^{ad}\delta^{cb}(u - m_\pi^2)\Big], \qquad a, b, c, d \neq 3 \end{aligned} \tag{C.15}$$

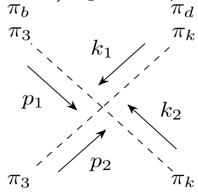

$$= \frac{\mu_u^6\left(\left(3s - 2m_{\pi_3}^2\right)\left(\mu_u^3 + \mu_d^3\right)^2 + 4\left(s - 2m_\pi^2\right)\mu_u^3\mu_d^3\right)}{4f_\pi^2\left(\mu_u^3 + \mu_d^3\right)^2\left(\mu_u^6 + \mu_d^6\right)}, (k \neq 3) \tag{C.16}$$

SciPost SciPost Phys. 14, 044 (2023)

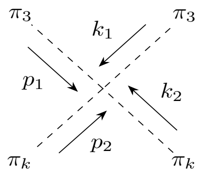

$$= \frac{\mu_u^6\left(\left(3t-2m_{\pi_3}^2\right)\left(\mu_u^3+\mu_d^3\right)^2+4\left(t-2m_\pi^2\right)\mu_u^3\mu_d^3\right)}{4f_\pi^2\left(\mu_u^3+\mu_d^3\right)^2\left(\mu_u^6+\mu_d^6\right)}, (k\neq 3) \quad \text{(C.17)}$$

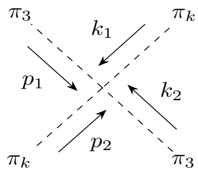

$$= \frac{\mu_u^6\left(\left(3u-2m_{\pi_3}^2\right)\left(\mu_u^3+\mu_d^3\right)^2+4\left(u-2m_\pi^2\right)\mu_u^3\mu_d^3\right)}{4f_\pi^2\left(\mu_u^3+\mu_d^3\right)^2\left(\mu_u^6+\mu_d^6\right)}, (k\neq 3)$$

(C.18)

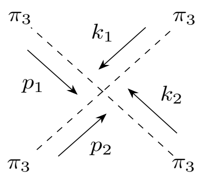

$$= \frac{\mu_u^6 m_{\pi_3}^2}{f_\pi^2\left(\mu_u^6+\mu_d^6\right)}, \quad \text{(C.19)}$$

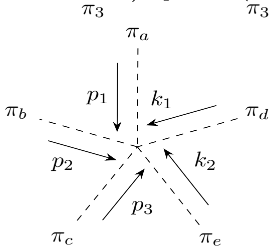

$$\begin{aligned} = &\frac{N_c\mu_d^6\sqrt{\mu_u^6+\mu_d^6}}{20\pi^2 f_\pi^5\mu_u^9}\varepsilon^{\mu\nu\rho\sigma}\times \\ &\times\Big[(p_2-p_1)_\mu p_{3\nu}k_{1\rho}k_{2\sigma}+p_{1\mu}p_{2\nu}\big(k_{1\rho}k_{2\sigma} \\ &\quad +k_{2\rho}p_{3\sigma}+p_{3\rho}k_{1\sigma}\big)\Big], \qquad (a\neq b\neq c\neq d\neq e)\,. \end{aligned} \quad \text{(C.20)}$$

C.3 Feynman rules for non-degenerate fermions $m_u \neq m_d$ with η'

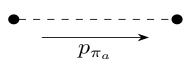

$$= \frac{1}{p_{\pi_3}^2-m_{\pi_3}^2}, \quad \text{(C.21)}$$

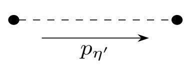

$$= \frac{1}{p_{\eta'}^2-m_{\eta'}^2}, \quad \text{(C.22)}$$

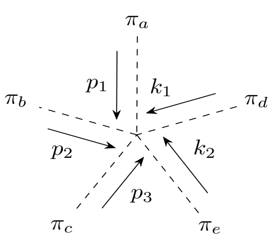

$$\begin{aligned} = &\frac{N_c\mu_d^6\sqrt{\mu_u^6+\mu_d^6}}{20\pi^2 f_\pi^5\mu_u^9}\left(\frac{\cos\theta_{\text{mass}}}{\sqrt{3\mu_d^6+\mu_u^6}}-\frac{\sin\theta_{\text{mass}}}{\sqrt{\mu_d^6+3\mu_u^6}}\right)\varepsilon^{\mu\nu\rho\sigma}\times \\ &\times\Big[(p_2-p_1)_\mu p_{3\nu}k_{1\rho}k_{2\sigma}+p_{1\mu}p_{2\nu}\big(k_{1\rho}k_{2\sigma}+k_{2\rho}p_{3\sigma}+p_{3\rho}k_{1\sigma}\big)\Big] \\ &(a\neq b\neq c\neq d\neq e)\,, \end{aligned}$$

(C.23)

SciPost | SciPost Phys. 14, 044 (2023)

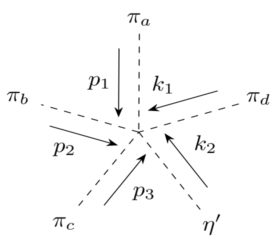

$$= \frac{N_c \mu_d^6 \sqrt{\mu_u^6 + \mu_d^6}}{20\pi^2 f_\pi^5 \mu_u^9} \left(\frac{\cos\theta_{\text{mass}}}{\sqrt{\mu_d^6 + 3\mu_u^6}} - \frac{\sin\theta_{\text{mass}}}{\sqrt{3\mu_d^6 + \mu_u^6}} \right) \varepsilon^{\mu\nu\rho\sigma} \times \\ \times \Big[(p_2 - p_1)_\mu p_{3\nu} k_{1\rho} k_{2\sigma} + p_{1\mu} p_{2\nu} \big(k_{1\rho} k_{2\sigma} + k_{2\rho} p_{3\sigma} + p_{3\rho} k_{1\sigma} \big) \Big] \\ (a \neq b \neq c \neq d \neq 3)\,. \tag{C.24}$$

D Lattice setup

D.1 Action

The HiRep code [88] is based on the Wilson gauge action

$$S_g[U] = \beta \sum_x \sum_{\mu<\nu} \left[\mathbb{1} - \frac{1}{4} \text{Re tr}\, U_{\mu\nu}(x) \right], \tag{D.1}$$

for the gauge sector, where $U_{\mu\nu}$ is the plaquette at lattice site x. For the fermionic part it uses unimproved Wilson fermions for both types of dark quarks,

$$S_F[U, \psi_u, \psi_d, \bar{\psi}_u, \bar{\psi}_d] = \sum_{f=u,d} a^4 \sum_{x,y} \bar{\psi}_f(x) D_f(x|y) \psi_f(m), \tag{D.2}$$

$$D_f(x|y) = \left(m_f + \frac{4}{a} \right) - \frac{1}{2a} \sum_\mu \Big((1-\gamma_\mu) U_\mu(x) \delta_{y,x+\hat{\mu}} + (1+\gamma_\mu) U_\mu^\dagger(x-\hat{\mu}) \delta_{y,x-\hat{\mu}} \Big). \tag{D.3}$$

This implies that chiral symmetry is explicitly broken at any finite lattice spacing, and is only recovered in the continuum limit. Furthermore, this entails an additive quark mass renormalization. Both effects are well-known, and can be controlled by analyzing the systematic effects, as is done below in appendix D.4. We simulated three different values of the inverse coupling $\beta \geq 6.9$, each of which avoids the unphysical Aoki phase that was found to exist for this theory [7]. Since we are using two distinct fermions the Wilson-Dirac determinant is not necessarily positive definite and in principle a sign problem can arise. Within our parameter range, we did not encounter any indications of a non-positive definite determinant.

D.2 Masses

We extract the masses of the mesons by determining the exponential decay of the correlation function of a suitable interpolator $O_\Gamma^f(x,y)$ where x and y are sites on the lattice. For the flavoured and unflavoured mesons we choose

$$O_\Gamma^{\bar{u}d}(x,y) = \bar{u}(x)\Gamma d(y), \tag{D.4}$$

$$O_\Gamma^0(x,y) = \bar{u}(x)\Gamma u(y) - \bar{d}(x)\Gamma d(y). \tag{D.5}$$

We only study the masses and decay constants of the mesons since they are identical to the corresponding diquark states [22]. We denote $x = (\vec{x}, t)$ and define a general correlator on a lattice of spatial extent L as

$$C_{\Gamma_1\Gamma_2}(t_x - t_y, \vec{p}) = \frac{1}{L^3} \sum_{\vec{x}\vec{y}} e^{-i\vec{p}(\vec{x}-\vec{y})} \langle O_{\Gamma_1}(\vec{x}, t_x) O_{\Gamma_2}^\dagger(\vec{y}, t_y) \rangle\,. \tag{D.6}$$

From this the meson masses can be obtained by first setting $\Gamma_1 = \Gamma_2 = \Gamma$ and projecting to zero momentum and studying the limit at large time separation.

$$\lim_{t\to\infty} C_{\Gamma\Gamma}(t, \vec{p} = 0) = \lim_{t\to\infty} \sum_n \frac{1}{2m_n} \langle 0|O_{\Gamma\Gamma}|n\rangle\langle n|O^\dagger_{\Gamma\Gamma}|0\rangle e^{-im_n\cdot t} \tag{D.7}$$

$$= \frac{1}{2m_\Gamma} |\langle 0|O_{\Gamma\Gamma}|\Gamma_{GS}\rangle|^2 e^{-im_\Gamma\cdot t}\,. \tag{D.8}$$

At large t only the contribution of the lightest state for the quantum numbers of O^f_Γ, $|\Gamma_{GS}\rangle$ survives. The mass of this state can be then extracted, by performing a fit of the lattice data. In the present case the signal-to-noise ratio is very good, and the effective mass shows well-defined plateaus, thus providing for reliable fit results.

The unflavoured mesons sourced by operators of the form (D.4) obtain so-called disconnected contributions which usually suffer from bad statistics. They are however suppressed by both the fermion masses and vanish in the limit of $m_u - m_d \to 0$ and we therefore neglect the disconnected contributions. For operators of the form

$$O_\Gamma(x, y) = \bar{u}(x)\Gamma u(y) + \bar{d}(x)\Gamma d(y)\,, \tag{D.9}$$

which source e.g. the η' and ω mesons in QCD this is no longer the case. We do not consider operators of this form in this work.

D.3 Decay constants

We define the decay constant as in [6] by the matrix elements involving the pseudoscalar $|PS\rangle$ and vector meson $|V\rangle$ ground states

$$\langle 0|O^f_{\gamma_5\gamma_\mu}|PS\rangle = f^f_{PS} p_\mu\,, \tag{D.10}$$

$$\langle 0|O^f_{\gamma_\mu}|V\rangle = f^f_V\, m_V \epsilon_\mu\,. \tag{D.11}$$

In this convention the decay constant of the π in QCD is approximately 93 MeV.

Here ϵ_μ is the polarisation vector for which $\epsilon_\mu p^\mu = 0$ and $\epsilon^*_\mu \epsilon^\mu = 1$ hold. In the rest frame the pseudoscalar matrix element is then

$$\langle 0|O^f_{\gamma_5\gamma_0}|PS\rangle = f^f_{PS} m_{PS}. \tag{D.12}$$

Inserting this expression into the corresponding correlators at large times gives

$$C^f_{\Gamma_1=\Gamma_2=\gamma_5\gamma_0}(t) = \frac{m_{PS}}{2}\left(f^f_{PS}\right)^2 \exp\left(-m_{PS}\cdot t\right), \tag{D.13}$$

$$C^f_{\Gamma_1=\Gamma_2=\gamma_\mu}(t) = \frac{m_V}{2}\left(f^f_V\right)^2 \exp\left(-m_V\cdot t\right). \tag{D.14}$$

Alternatively, the mixed correlator with $\Gamma_1 = \gamma_5\gamma_0$ and $\Gamma_2 = \gamma_5$ can be used for the pseudoscalars [6]. From this we can extract the bare decay constants which need to be renormalized. For that we follow the prescription from [6] for determining the renormalization constants defined as

$$f^{\text{ren,f}}_{\text{PS}} = Z_A f^{\text{f}}_{\text{PS}}\,, \tag{D.15}$$

$$f^{\text{ren,f}}_{\text{V}} = Z_V f^{\text{f}}_{\text{V}}\,. \tag{D.16}$$

SciPost SciPost Phys. 14, 044 (2023)

D.4 Systematics

D.4.1 Finite volume effects

The finite volume of the 4-dimensional Euclidean space introduces artefacts in the lattice results. We can obtain an estimate of the infinite volume masses by fitting the results obtain at different spatial extents L of the lattice to the known analytic form of the L-dependence of the masses. For that we use the same approach as in [6] and fit the function

$$m_{\text{meson}}(L) = m_{\text{meson}}^{\text{inf.}} \left(1 + A\frac{\exp(-m_{\text{Goldstone}}^{\text{inf}} \cdot L)}{(m_{\text{Goldstone}}^{\text{inf}} \cdot L)^{(3/2)}}\right), \tag{D.17}$$

in the almost mass-degenerate limit, since there the quark masses are the lightest in our setup and therefore the finite volume effects are the largest. We consider A as a free fitting parameter. In figures 8 and 9 we show the infinite volume extrapolation for nearly-degenerate, moderately light ensembles at $\beta = 6.9$ and 7.2 and for a nearly-degenerate ensemble with light fermions at $\beta = 7.2$. Only in the latter ensembles finite volume effects become apparent and generally the deviation from the infinite volume extrapolation stays below 10%.

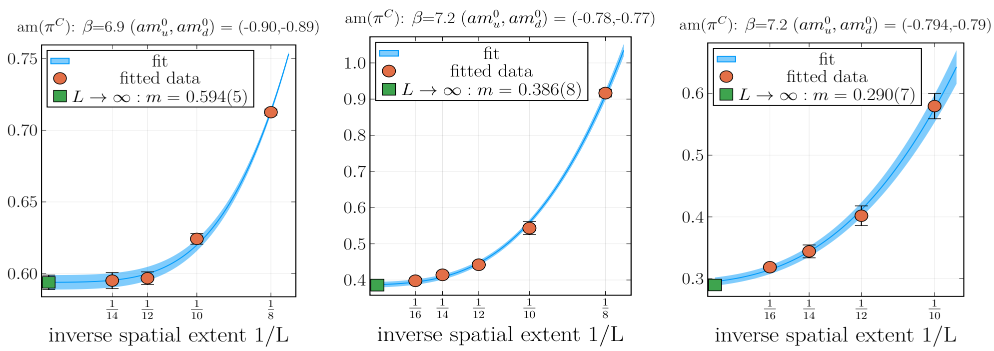

Figure 8: Finite volume extrapolation for the Goldstone mass in the almost mass-degenerate limit. It can be seen that the infinite volume mass and the mass on the largest lattices considered agree within errors. Only in the lightest ensembles on the finest lattices studied here the finite volume effects become apparent. Even in this case the deviation from the infinite volume extrapolation stays below 10%.

D.4.2 Finite spacing effects

Apart from the possible systematic errors introduced by the finite volume of the lattice, the finite distance a between two adjacent lattice points is another source of systematic errors. The physical distance a is, however, not an input parameter of simulation. In order to study the systematic effects of a we need to choose input parameters so that the results represent the same physics at different values of a. Finding these lines of constant physics in our three-dimensional parameter space is in general not straightforward.

In $SU(3)_c$ gauge theory with fermions it has been found that a depends strongly on the value of the inverse coupling β and only weakly on the masses of the fermions m_f [5]. As an first test we have chosen values of the dark fermion masses at the point of degeneracy such that at different values of β the ration of the pseudo-Goldstones and the vector mesons is reproduced. We then again increment one of the fermion masses. If the assumption of negligible effects of the fermion masses on a is correct, then the corresponding ratios of Goldstone

SciPost SciPost Phys. 14, 044 (2023)

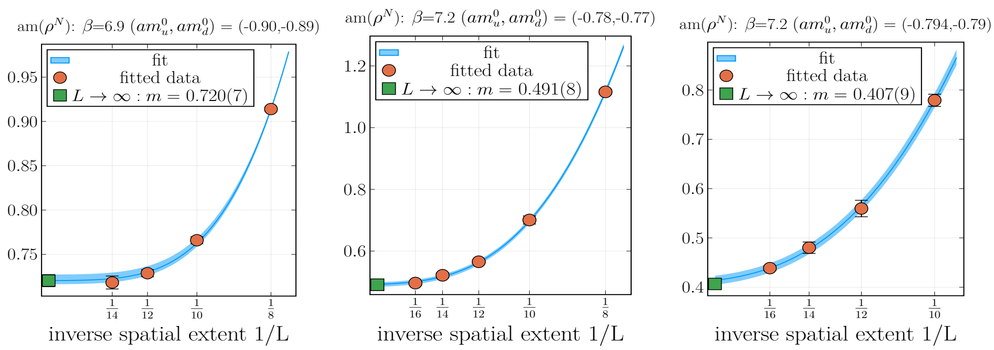

Figure 9: Finite volume extrapolation for the vector meson mass in the almost mass-degenerate limit. The vector meson masses show the same behaviour as the Goldstone bosons.

to vector masses should be the same for all values of β since we move then along lines of constant physics in parameter space. Along these lines of constant physics we can then study finite spacing effects of the other observables that do not depend on the lattice spacing, e.g. ratios.

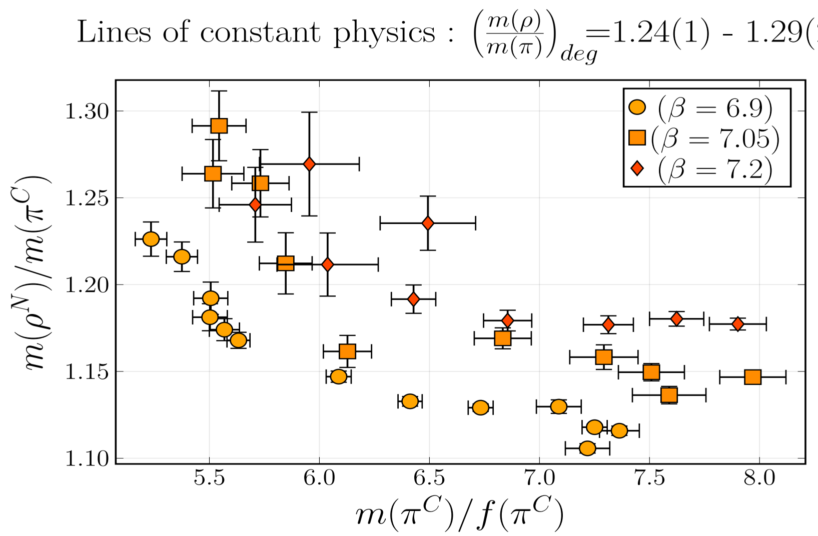

Figure 10: In order to study the effects of the finite lattice spacing we define the lines through parameter space with $m(\rho^N)/m(\pi^C)$ as the lines of constant physics. Here we plot this ratio against the mass of the lightest pseudo-Goldstone in units of its decay constant. We see that the curves at different β do not coincide. However, the deviations are only at around 10% and for the two finer lattices they almost coincide.

In figure 10 we plot the ratio of the lightest vector meson's mass to the lightest pseudo-Goldstone's mass $m(\rho^N)/m(\pi^C)$ against the lightest pseudo-Goldstone mass in units of its decay constant. We are not moving exactly along a line of constant physics. However, we

SciPost SciPost Phys. 14, 044 (2023)

find that the deviations do not significantly exceed 10%. Since this plot involves both the masses and decay constants we plot the masses and decay constants separately in figures 11 and 12 against the masses of the flavoured vector mesons — both in units of the pseudo-Goldstone mass at degeneracy. We find that at different β the masses agree within errors and we only see deviations from that behaviour most notably at $\beta = 7.2$ for large flavoured fermion masses of $m(\rho^M)/m_\pi^{\text{deg}} > 2$. For the decay constants in Fig. 12 the deviations are significantly larger and already pronounced at lower masses. For the pseudo-Goldstones the deviations are approximately 10% whereas for the vector mesons they are at around 20%.

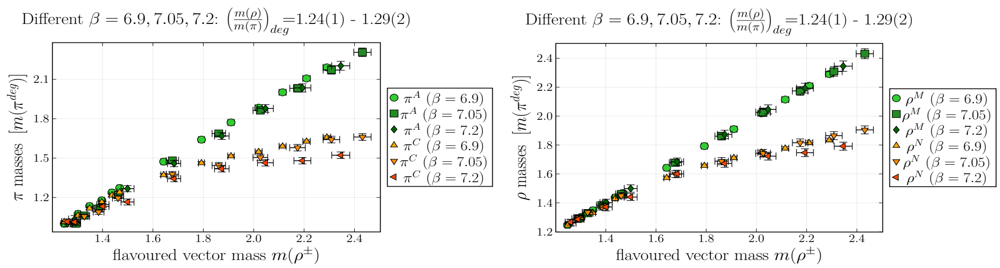

Figure 11: Masses of the pseudo-Goldstones (upper) and vector mesons (lower) for different values of the inverse coupling β in units of the pseudo-Goldstone mass degeneracy. The results at different β agree within errors except for the $\beta = 7.2$ ensembles with one relatively heavy fermion. From this we conclude that there the finite spacing effects for the meson masses are small.

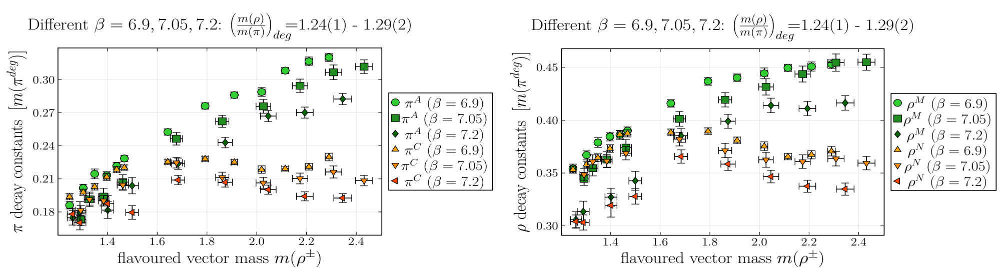

Figure 12: Decay constants of the pseudo-Goldstones (upper) and vector mesons (lower) for different values of the inverse coupling β in units of the pseudo-Goldstone mass degeneracy. The results at different β show stronger deviations than the meson masses even at very light fermion masses. For the pseudo-Goldstones the deviations are approximately 10% or smaller whereas for the vector mesons they can be as large as 20%.

D.4.3 Lattice asymmetry

In our analysis we extract the masses and decay constants from the behaviour of correlation functions at large Euclidean time t. For convenience we therefore perform simulations on lattices with larger temporal extent than spatial extent, i.e. a lattice of dimensions $L^3 \times T$ with $T > L$. This allows us to calculate the correlation functions at large t while avoiding significantly increased computation time. We have studied the effects of finite L in section D.4.1.

It is, however, still possible, that this introduces systematic error. Here we try to assess whether this has an effect on our results. For this we compare meson masses on symmetric lattices of size L^4 to the masses we have obtained for asymmetric lattices. On the symmetric lattices our time extent is substantially smaller and we expect even at the largest Euclidean times to see effects of contamination by states with higher energies. We therefore take the second lightest state into account and extract the mass from the effective mass of the correlator defined as

$$m_{\text{eff}}\left(t+\frac{1}{2}\right)=\frac{C_{O_M}(t)}{C_{O_M}(t+1)}. \tag{D.18}$$

This allows us to extract the masses from a three-parameter fit while simultaneously minimizing the effects of contamination of higher states. This comes at the cost of larger errors, since the effective mass defined this way discards some information because it as a local quantity around Euclidean time $\left(t+\frac{1}{2}\right)$. As can be seen in table 5 we don't observe any systematic effects from the use of asymmetric lattice within the errors reported.

Table 5: Comparison of meson masses extracted from both symmetric and asymmetric lattices for an inverse coupling of $\beta = 6.9$. The other two input parameters are m_1^0 and m_2^0 - the unrenormalized bare quark masses. They agree very well within errors and we conclude that there are no relevant systematic effects due to the asymmetric lattices used throughout this work.

$(-am_1^0, -am_2^0)$	$am(\pi^A)(24\times12^3)$	$am(\pi^A)(12^4)$	$am(\pi^C)(24\times12^3)$	$am(\pi^C)(12^4)$
(0.90,0.70)	0.993(7)	0.994(15)	0.83(1)	0.85(4)
(0.90,0.75)	0.917(14)	0.92(2)	0.80(2)	0.81(5)
(0.90,0.80)	0.826(11)	0.83(5)	0.76(2)	0.77(7)
(0.90,0.85)	0.712(15)	0.7(2)	0.69(2)	0.7(2)
(0.90,0.90)	0.56(4)	0.58(9)	0.56(4)	0.58(9)
$(-am_1^0, -am_2^0)$	$am(\rho^M)(24\times12^3)$	$am(\rho^M)(12^4)$	$am(\rho^N)(24\times12^3)$	$am(\rho^N)(12^4)$
(0.90,0.70)	1.070(9)	1.071(15)	0.951(14)	0.97(3)
(0.90,0.75)	1.001(14)	1.00(2)	0.92(2)	0.94(3)
(0.90,0.80)	0.921(15)	0.93(3)	0.88(2)	0.90(3)
(0.90,0.85)	0.82(2)	0.82(4)	0.81(2)	0.82(4)
(0.90,0.90)	0.70(2)	0.72(4)	0.70(2)	0.72(4

D.5 Tabulated lattice results

SciPost Phys. 14, 044 (2023)

Table 6: Tabulated results for the ensembles with $m_\rho/m_\pi \approx 1.25$. We report the input parameters the bare inverse gauge coupling β, the bare fermion masses am_u^0 and am_u^0 — a is the lattice spacing — as well as the lattice dimensions $T \times L^3$. The reported decay constants have been renormalized and in addition we give the average plaquette $\langle P \rangle$ that is used in the renormalization. In the last column we give the average PCAC-mass.

β	T	L	am_u^0	am_d^0	$\langle P \rangle$	$am(\pi^A)$	$am(\pi^C)$	$af(\pi^A)$	$af(\pi^C)$	$am(\rho^M)$	$am(\rho^N)$	$af(\rho^M)$	$af(\rho^N)$	$a\bar{m}_{\text{PCAC}}$
6.9	24	12	-0.9	-0.5	0.5333(2)	1.228(3)	0.930(3)	0.179(2)	0.129(2)	1.284(2)	1.028(3)	0.254(2)	0.208(2)	0.372(7)
6.9	24	12	-0.9	-0.55	0.5345(2)	1.181(2)	0.912(3)	0.177(2)	0.124(2)	1.239(2)	1.018(3)	0.253(2)	0.206(2)	0.340(6)
6.9	24	12	-0.9	-0.6	0.53655(8)	1.122(1)	0.891(2)	0.173(1)	0.1229(9)	1.185(1)	0.996(2)	0.252(1)	0.205(1)	0.306(3)
6.9	24	12	-0.9	-0.65	0.5386(1)	1.056(3)	0.868(3)	0.162(2)	0.122(2)	1.132(3)	0.980(3)	0.249(2)	0.210(2)	0.270(6)
6.9	24	14	-0.9	-0.7	0.54098(8)	0.993(2)	0.849(2)	0.160(1)	0.126(1)	1.070(1)	0.959(2)	0.247(1)	0.213(1)	0.236(3)
6.9	24	14	-0.9	-0.75	0.54393(8)	0.920(2)	0.820(2)	0.155(1)	0.128(1)	1.005(2)	0.929(2)	0.245(1)	0.218(1)	0.200(3)
6.9	24	14	-0.9	-0.8	0.54736(8)	0.826(2)	0.769(2)	0.142(1)	0.126(1)	0.921(2)	0.882(2)	0.233(1)	0.218(1)	0.163(3)
6.9	24	14	-0.9	-0.85	0.55163(7)	0.713(2)	0.695(2)	0.128(1)	0.123(1)	0.823(2)	0.812(2)	0.219(1)	0.217(1)	0.122(3)
6.9	24	14	-0.9	-0.86	0.5523(1)	0.694(3)	0.682(3)	0.124(2)	0.122(1)	0.805(2)	0.801(2)	0.216(2)	0.217(1)	0.110(3)
6.9	24	14	-0.9	-0.87	0.5538(1)	0.660(4)	0.653(3)	0.119(2)	0.119(2)	0.783(3)	0.771(3)	0.216(2)	0.209(2)	0.103(3)
6.9	24	14	-0.9	-0.88	0.5547(1)	0.636(4)	0.626(3)	0.120(2)	0.114(2)	0.756(3)	0.746(3)	0.212(2)	0.204(2)	0.096(3)
6.9	24	14	-0.9	-0.89	0.55582(9)	0.603(4)	0.596(3)	0.113(2)	0.111(1)	0.730(2)	0.725(2)	0.206(2)	0.201(1)	0.086(3)
6.9	24	14	-0.9	-0.9	0.5569(2)	0.560(4)	0.569(3)	0.104(2)	0.109(1)	0.699(3)	0.697(2)	0.199(2)	0.198(1)	0.077(3)
7.05	24	12	-0.835	-0.5	0.5603(1)	1.025(3)	0.738(5)	0.139(2)	0.093(2)	1.081(3)	0.847(3)	0.202(2)	0.160(2)	0.274(7)
7.05	24	12	-0.835	-0.55	0.5618(2)	0.965(4)	0.730(5)	0.136(2)	0.096(2)	1.026(3)	0.829(4)	0.202(2)	0.162(2)	0.248(6)
7.05	24	12	-0.835	-0.6	0.5636(1)	0.903(3)	0.702(5)	0.131(2)	0.094(2)	0.967(3)	0.807(3)	0.197(2)	0.160(2)	0.216(6)
7.05	24	12	-0.835	-0.65	0.5654(1)	0.828(4)	0.669(5)	0.123(2)	0.092(2)	0.901(4)	0.775(4)	0.192(2)	0.161(2)	0.182(6)
7.05	24	14	-0.835	-0.7	0.5678(1)	0.750(3)	0.642(5)	0.117(2)	0.094(2)	0.828(3)	0.751(4)	0.186(2)	0.165(2)	0.149(4)
7.05	24	14	-0.835	-0.75	0.5700(1)	0.659(4)	0.612(5)	0.110(2)	0.100(2)	0.746(4)	0.711(4)	0.178(2)	0.170(2)	0.118(4)
7.05	24	14	-0.835	-0.8	0.5731(1)	0.542(7)	0.532(4)	0.092(3)	0.091(2)	0.650(4)	0.644(4)	0.166(2)	0.164(2)	0.079(4)
7.05	24	14	-0.835	-0.82	0.5742(1)	0.496(7)	0.485(4)	0.086(3)	0.085(2)	0.615(4)	0.610(4)	0.161(2)	0.161(2)	0.064(4)
7.05	24	14	-0.835	-0.83	0.5749(1)	0.472(6)	0.469(5)	0.085(3)	0.085(2)	0.590(4)	0.593(4)	0.158(2)	0.160(2)	0.061(4)
7.05	24	14	-0.835	-0.835	0.5755(2)	0.445(6)	0.447(5)	0.077(2)	0.081(2)	0.575(4)	0.578(3)	0.153(2)	0.155(2)	0.051(3)
7.2	24	14	-0.78	-0.5	0.58108(7)	0.842(2)	0.582(4)	0.108(1)	0.074(1)	0.897(2)	0.685(2)	0.159(1)	0.128(1)	0.211(4)
7.2	24	14	-0.78	-0.55	0.58222(7)	0.778(2)	0.566(4)	0.103(1)	0.074(1)	0.838(2)	0.668(2)	0.157(1)	0.129(1)	0.181(4)
7.2	24	14	-0.78	-0.6	0.58342(7)	0.718(3)	0.560(4)	0.102(1)	0.077(1)	0.782(2)	0.659(3)	0.158(1)	0.133(1)	0.153(4)
7.2	24	14	-0.78	-0.65	0.58484(6)	0.638(3)	0.542(4)	0.093(1)	0.079(1)	0.716(2)	0.639(3)	0.153(1)	0.137(1)	0.127(3)
7.2	24	14	-0.78	-0.7	0.58634(6)	0.558(3)	0.513(4)	0.086(2)	0.080(1)	0.644(2)	0.612(3)	0.147(1)	0.140(1)	0.097(3)
7.2	32	16	-0.78	-0.73	0.58743(6)	0.484(5)	0.446(5)	0.078(3)	0.069(2)	0.573(5)	0.551(4)	0.131(3)	0.125(2)	0.078(4)
7.2	32	16	-0.78	-0.75	0.58818(6)	0.438(5)	0.433(6)	0.069(3)	0.072(3)	0.536(4)	0.524(7)	0.125(3)	0.122(4)	0.064(4)
7.2	32	16	-0.78	-0.77	0.58892(6)	0.396(8)	0.387(6)	0.069(4)	0.065(2)	0.493(5)	0.492(4)	0.120(3)	0.116(2)	0.054(4)
7.2	32	16	-0.78	-0.78	0.58923(4)	0.382(6)	0.389(5)	0.067(2)	0.068(2)	0.482(4)	0.484(3)	0.117(2)	0.116(2)	0.049(3)

SciPost SciPost Phys. 14, 044 (2023)

Table 7: Tabulated results for the ensembles with $m_\rho/m_\pi \approx 1.4$. We report the input parameters the bare inverse gauge coupling β, the bare fermion masses am_u^0 and am_u^0 — a is the lattice spacing — as well as the lattice dimensions $T \times L^3$. The reported decay constants have been renormalized and in addition we give the average plaquette $\langle P \rangle$ that is used in the renormalization. In the last column we give the average PCAC-mass.

β	T	L	am_u^0	am_d^0	$\langle P \rangle$	$am(\pi^A)$	$am(\pi^C)$	$af(\pi^A)$	$af(\pi^C)$	$am(\rho^M)$	$am(\rho^N)$	$af(\rho^M)$	$af(\rho^N)$	$a\bar{m}_{\mathrm{PCAC}}$
6.9	24	12	-0.92	-0.5	0.5349(2)	1.198(3)	0.871(5)	0.179(2)	0.118(2)	1.253(3)	0.985(4)	0.252(2)	0.202(4)	0.358(9)
6.9	24	12	-0.92	-0.55	0.5364(2)	1.144(4)	0.857(5)	0.169(3)	0.116(3)	1.204(4)	0.967(4)	0.245(3)	0.200(3)	0.314(7)
6.9	24	12	-0.92	-0.6	0.5385(2)	1.084(4)	0.832(6)	0.167(3)	0.118(3)	1.154(3)	0.945(5)	0.249(3)	0.201(3)	0.28(1)
6.9	24	12	-0.92	-0.65	0.5399(2)	1.031(4)	0.807(7)	0.164(2)	0.115(3)	1.107(3)	0.927(6)	0.249(2)	0.200(3)	0.257(8)
6.9	24	12	-0.92	-0.7	0.5427(2)	0.958(5)	0.779(7)	0.155(3)	0.117(3)	1.040(4)	0.900(5)	0.244(3)	0.203(3)	0.217(9)
6.9	24	12	-0.92	-0.75	0.5459(2)	0.870(5)	0.752(7)	0.143(3)	0.118(3)	0.959(4)	0.870(5)	0.233(3)	0.207(3)	0.180(8)
6.9	24	12	-0.92	-0.8	0.5498(2)	0.765(6)	0.669(9)	0.133(3)	0.110(3)	0.867(4)	0.810(7)	0.223(4)	0.204(4)	0.143(8)
6.9	24	14	-0.92	-0.85	0.5538(1)	0.660(5)	0.632(5)	0.121(2)	0.114(2)	0.782(4)	0.756(4)	0.216(2)	0.204(2)	0.106(4)
6.9	24	14	-0.92	-0.88	0.5572(3)	0.55(1)	0.540(7)	0.101(4)	0.098(3)	0.690(6)	0.687(6)	0.195(3)	0.194(3)	0.073(5)
6.9	24	14	-0.92	-0.9	0.5594(1)	0.480(9)	0.486(6)	0.090(3)	0.094(2)	0.637(6)	0.646(4)	0.184(3)	0.189(2)	0.057(3)
6.9	24	14	-0.92	-0.91	0.5607(1)	0.45(1)	0.441(6)	0.092(4)	0.088(3)	0.605(7)	0.598(5)	0.183(3)	0.176(2)	0.048(4)
6.9	24	14	-0.92	-0.92	0.5621(2)	0.38(1)	0.380(8)	0.083(4)	0.082(3)	0.548(9)	0.555(6)	0.167(4)	0.168(3)	0.038(4)
7.05	24	14	-0.85	-0.5	0.5614(1)	0.999(4)	0.690(4)	0.135(2)	0.086(2)	1.059(3)	0.805(4)	0.201(2)	0.155(2)	0.261(8)
7.05	24	14	-0.85	-0.55	0.5628(1)	0.943(3)	0.669(6)	0.130(2)	0.086(2)	1.001(3)	0.789(4)	0.194(2)	0.156(2)	0.233(7)
7.05	24	14	-0.85	-0.6	0.5648(1)	0.875(4)	0.662(7)	0.128(2)	0.091(2)	0.943(3)	0.772(5)	0.195(3)	0.158(2)	0.204(7)
7.05	24	14	-0.85	-0.65	0.5666(1)	0.791(5)	0.615(5)	0.118(2)	0.089(2)	0.872(4)	0.736(4)	0.188(3)	0.159(3)	0.173(6)
7.05	24	14	-0.85	-0.7	0.5685(1)	0.730(5)	0.602(5)	0.116(3)	0.088(2)	0.805(4)	0.715(4)	0.185(2)	0.160(2)	0.138(6)
7.05	24	14	-0.85	-0.75	0.5712(2)	0.620(5)	0.554(7)	0.101(2)	0.088(2)	0.717(4)	0.676(4)	0.172(2)	0.163(2)	0.106(5)
7.05	24	14	-0.85	-0.8	0.5739(1)	0.501(5)	0.481(5)	0.089(2)	0.083(2)	0.621(3)	0.606(4)	0.163(2)	0.157(2)	0.072(3)
7.05	24	14	-0.85	-0.83	0.57590(8)	0.427(8)	0.422(6)	0.078(2)	0.080(2)	0.563(5)	0.556(4)	0.155(2)	0.153(2)	0.047(3)
7.05	24	14	-0.85	-0.85	0.57736(7)	0.350(8)	0.348(6)	0.067(2)	0.066(2)	0.510(4)	0.518(3)	0.143(2)	0.145(1)	0.035(2)
7.2	24	14	-0.794	-0.45	0.5808(1)	0.874(4)	0.550(7)	0.108(2)	0.070(3)	0.925(4)	0.654(5)	0.158(2)	0.122(2)	0.227(7)
7.2	24	14	-0.794	-0.5	0.5816(1)	0.823(5)	0.535(8)	0.107(2)	0.071(2)	0.879(4)	0.647(5)	0.158(2)	0.125(2)	0.201(7)
7.2	24	14	-0.794	-0.55	0.5829(1)	0.755(4)	0.506(8)	0.100(2)	0.066(3)	0.819(3)	0.633(5)	0.155(2)	0.128(2)	0.172(7)
7.2	24	14	-0.794	-0.6	0.58408(5)	0.686(2)	0.510(4)	0.095(1)	0.070(1)	0.755(2)	0.618(3)	0.151(1)	0.126(1)	0.144(3)
7.2	24	14	-0.794	-0.65	0.58543(6)	0.613(3)	0.488(4)	0.090(1)	0.071(1)	0.693(2)	0.604(3)	0.150(1)	0.130(1)	0.117(3)
7.2	24	14	-0.794	-0.7	0.58696(6)	0.529(3)	0.460(5)	0.081(1)	0.072(1)	0.620(2)	0.577(3)	0.142(1)	0.135(1)	0.086(3)
7.2	32	16	-0.794	-0.75	0.58878(5)	0.420(4)	0.396(5)	0.071(2)	0.066(2)	0.522(9)	0.51(1)	0.124(6)	0.119(7)	0.059(2)
7.2	32	16	-0.794	-0.77	0.5895(1)	0.370(7)	0.345(6)	0.064(3)	0.058(2)	0.477(4)	0.470(4)	0.117(2)	0.117(2)	0.043(3)
7.2	32	16	-0.794	-0.78	0.58988(6)	0.324(8)	0.332(7)	0.059(3)	0.062(2)	0.433(6)	0.44(1)	0.107(3)	0.110(6)	0.039(3)
7.2	32	16	-0.794	-0.794	0.59032(6)	0.315(8)	0.317(5)	0.059(3)	0.059(2)	0.430(5)	0.426(4)	0.110(3)	0.106(2)	0.032(2)

SciPost Phys. 14, 044 (2023)

Table 8: Tabulated results for the ensembles with $m_\rho/m_\pi \approx 1.15$. We report the input parameters the bare inverse gauge coupling β, the bare fermion masses am_u^0 and am_u^0 — a is the lattice spacing — as well as the lattice dimensions $T \times L^3$. The reported decay constants have been renormalized and in addition we give the average plaquette $\langle P \rangle$ that is used in the renormalization. In the last column we give the average PCAC-mass.

β	T	L	am_u^0	am_d^0	$\langle P \rangle$	$am(\pi^A)$	$am(\pi^C)$	$af(\pi^A)$	$af(\pi^C)$	$am(\rho^M)$	$am(\rho^N)$	$af(\rho^M)$	$af(\rho^N)$	$a\bar{m}_{\text{PCAC}}$
6.9	24	12	-0.87	-0.5	0.5309(1)	1.268(2)	1.004(3)	0.185(1)	0.132(1)	1.322(2)	1.093(2)	0.258(1)	0.207(2)	0.400(5)
6.9	24	12	-0.87	-0.55	0.5326(1)	1.219(2)	0.992(2)	0.180(2)	0.134(1)	1.278(2)	1.084(2)	0.257(2)	0.213(1)	0.361(6)
6.9	24	12	-0.87	-0.6	0.5341(1)	1.173(2)	0.980(2)	0.181(2)	0.135(1)	1.232(2)	1.071(2)	0.259(2)	0.215(1)	0.334(5)
6.9	24	12	-0.87	-0.65	0.5361(1)	1.115(2)	0.958(3)	0.177(2)	0.136(1)	1.181(2)	1.051(2)	0.259(2)	0.218(2)	0.300(5)
6.9	24	12	-0.87	-0.7	0.5384(1)	1.047(2)	0.939(3)	0.166(2)	0.138(2)	1.120(2)	1.033(2)	0.251(2)	0.222(2)	0.260(5)
6.9	24	12	-0.87	-0.75	0.5411(1)	0.980(3)	0.910(3)	0.162(2)	0.141(2)	1.057(2)	1.004(2)	0.248(2)	0.230(2)	0.226(5)
6.9	24	12	-0.87	-0.8	0.5444(1)	0.896(3)	0.870(3)	0.152(2)	0.143(2)	0.986(3)	0.966(2)	0.244(2)	0.235(1)	0.187(5)
6.9	24	12	-0.87	-0.83	0.5470(2)	0.829(5)	0.818(4)	0.143(3)	0.138(2)	0.925(4)	0.913(3)	0.234(3)	0.228(3)	0.164(7)
6.9	24	12	-0.87	-0.84	0.5478(2)	0.812(3)	0.801(4)	0.142(2)	0.138(2)	0.913(2)	0.903(3)	0.237(2)	0.231(2)	0.156(5)
6.9	24	12	-0.87	-0.85	0.5485(1)	0.790(4)	0.786(3)	0.139(2)	0.135(2)	0.889(3)	0.887(2)	0.230(2)	0.226(2)	0.150(4)
6.9	24	12	-0.87	-0.86	0.5497(1)	0.770(4)	0.764(3)	0.134(2)	0.134(2)	0.872(3)	0.871(2)	0.227(2)	0.229(2)	0.137(5)
6.9	24	12	-0.87	-0.87	0.5504(2)	0.742(2)	0.743(2)	0.131(2)	0.1303(9)	0.848(2)	0.851(2)	0.224(2)	0.224(1)	0.129(3)
7.05	24	12	-0.8	-0.45	0.5566(1)	1.137(4)	0.862(4)	0.151(3)	0.108(2)	1.184(3)	0.949(3)	0.211(2)	0.171(2)	0.340(9)
7.05	24	12	-0.8	-0.5	0.5581(2)	1.080(4)	0.841(4)	0.143(2)	0.102(2)	1.132(3)	0.930(4)	0.206(2)	0.167(2)	0.304(9)
7.05	24	12	-0.8	-0.55	0.55938(9)	1.029(2)	0.833(2)	0.144(1)	0.106(1)	1.084(2)	0.918(2)	0.209(1)	0.170(1)	0.277(4)
7.05	24	12	-0.8	-0.6	0.5611(1)	0.968(3)	0.816(3)	0.139(2)	0.105(1)	1.031(2)	0.906(2)	0.207(2)	0.174(1)	0.244(5)
7.05	24	12	-0.8	-0.65	0.56321(9)	0.895(2)	0.799(2)	0.133(1)	0.112(1)	0.963(2)	0.882(2)	0.204(1)	0.180(1)	0.213(4)
7.05	24	12	-0.8	-0.7	0.56537(9)	0.819(3)	0.769(3)	0.127(1)	0.114(1)	0.893(2)	0.852(2)	0.197(1)	0.185(1)	0.178(4)
7.05	24	12	-0.8	-0.75	0.56774(9)	0.733(3)	0.723(3)	0.117(2)	0.115(1)	0.818(2)	0.809(2)	0.190(2)	0.188(1)	0.146(4)
7.05	24	12	-0.8	-0.78	0.5695(1)	0.670(3)	0.672(2)	0.111(2)	0.109(1)	0.762(3)	0.764(2)	0.184(2)	0.182(1)	0.123(4)
7.05	24	12	-0.8	-0.8	0.5708(1)	0.626(6)	0.632(3)	0.103(2)	0.106(1)	0.724(4)	0.732(3)	0.176(2)	0.183(1)	0.105(4)
7.2	24	12	-0.75	-0.45	0.5787(1)	0.950(4)	0.696(5)	0.117(2)	0.083(2)	1.002(3)	0.780(5)	0.170(2)	0.134(2)	0.262(8)
7.2	24	12	-0.75	-0.5	0.5797(2)	0.903(4)	0.681(7)	0.120(2)	0.083(2)	0.950(3)	0.763(5)	0.172(2)	0.134(2)	0.236(7)
7.2	24	12	-0.75	-0.55	0.58086(7)	0.835(2)	0.670(3)	0.112(1)	0.0846(9)	0.891(2)	0.755(2)	0.166(1)	0.1398(9)	0.203(4)
7.2	24	12	-0.75	-0.6	0.58208(6)	0.767(2)	0.653(3)	0.105(1)	0.0869(9)	0.829(2)	0.736(2)	0.1619(9)	0.1421(9)	0.174(3)
7.2	24	12	-0.75	-0.65	0.58353(6)	0.695(3)	0.638(3)	0.100(1)	0.0895(9)	0.766(2)	0.720(2)	0.159(1)	0.148(1)	0.145(3)
7.2	24	12	-0.75	-0.7	0.58512(7)	0.616(4)	0.597(3)	0.094(1)	0.090(1)	0.697(3)	0.691(2)	0.155(1)	0.154(1)	0.117(3)
7.2	24	12	-0.75	-0.72	0.58586(7)	0.582(3)	0.580(3)	0.089(1)	0.088(1)	0.674(2)	0.667(2)	0.153(1)	0.1511(9)	0.103(3)
7.2	24	12	-0.75	-0.74	0.58661(7)	0.547(4)	0.546(3)	0.086(1)	0.084(1)	0.640(2)	0.644(2)	0.150(1)	0.150(1)	0.092(3)
7.2	24	12	-0.75	-0.75	0.58690(6)	0.532(4)	0.530(3)	0.084(2)	0.0832(8)	0.624(2)	0.636(2)	0.147(1)	0.1505(8)	0.086(3)

References

[1] G. Cacciapaglia, C. Pica and F. Sannino, *Fundamental composite dynamics: A review*, Phys. Rep. **877**, 1 (2020), doi:10.1016/j.physrep.2020.07.002.

[2] S. Weinberg, *Nonlinear realizations of chiral symmetry*, Phys. Rev. **166**, 1568 (1968), doi:10.1103/PhysRev.166.1568.

[3] J. Gasser and H. Leutwyler, *Chiral perturbation theory to one loop*, Ann. Phys. **158**, 142 (1984), doi:10.1016/0003-4916(84)90242-2.

[4] T. DeGrand and C. E. Detar, *Lattice methods for quantum chromodynamics*, World Scientific, Singapore, ISBN 9789812567277 (2006), doi:10.1142/6065.

[5] C. Gattringer and C. B. Lang, *Quantum chromodynamics on the lattice*, Springer Berlin Heidelberg, Berlin, Heidelberg, ISBN 9783642018497 (2010), doi:10.1007/978-3-642-01850-3.

[6] E. Bennett, D. K. Hong, J.-W. Lee, C.-J. D. Lin, B. Lucini, M. Piai and D. Vadacchino, *$Sp(4)$ gauge theories on the lattice: $N_f = 2$ dynamical fundamental fermions*, J. High Energy Phys. **12**, 053 (2019), doi:10.1007/JHEP12(2019)053.

[7] E. Bennett, D. K. Hong, J.-W. Lee, C.-J. D. Lin, B. Lucini, M. Piai and D. Vadacchino, *$Sp(4)$ gauge theory on the lattice: Towards $SU(4)/Sp(4)$ composite Higgs (and beyond)*, J. High Energy Phys. **03**, 185 (2018), doi:10.1007/JHEP03(2018)185.

[8] E. Bennett, D. K. Hong, J.-W. Lee, C.-J. D. Lin, B. Lucini, M. Mesiti, M. Piai, J. Rantaharju and D. Vadacchino, *$Sp(4)$ gauge theories on the lattice: Quenched fundamental and antisymmetric fermions*, Phys. Rev. D **101**, 074516 (2020), doi:10.1103/PhysRevD.101.074516.

[9] E. D. Carlson, M. E. Machacek and L. J. Hall, *Self-interacting dark matter*, Astrophys. J. **398**, 43 (1992), doi:10.1086/171833.

[10] A. A. de Laix, R. J. Scherrer and R. K. Schaefer, *Constraints on self-interacting dark matter*, Astrophys. J. **452**, 495 (1995), doi:10.1086/176322.

[11] Y. Hochberg, E. Kuflik, H. Murayama, T. Volansky and J. G. Wacker, *Model for thermal relic dark matter of strongly interacting massive particles*, Phys. Rev. Lett. **115**, 021301 (2015), doi:10.1103/PhysRevLett.115.021301.

[12] Y. Hochberg, E. Kuflik, T. Volansky and J. G. Wacker, *Mechanism for thermal relic dark matter of strongly interacting massive particles*, Phys. Rev. Lett. **113**, 171301 (2014), doi:10.1103/PhysRevLett.113.171301.

[13] N. Bernal and X. Chu, *$\mathbb{Z}_2$ SIMP dark matter*, J. Cosmol. Astropart. Phys. **1**, 006 (2016), doi:10.1088/1475-7516/2016/01/006.

[14] N. Bernal, X. Chu, C. Garcia-Cely, T. Hambye and B. Zaldivar, *Production regimes for self-interacting dark matter*, J. Cosmol. Astropart. Phys. **3**, 018 (2016), doi:10.1088/1475-7516/2016/03/018.

[15] N. Bernal, C. Garcia-Cely and R. Rosenfeld, *WIMP and SIMP dark matter from the spontaneous breaking of a global group*, J. Cosmol. Astropart. Phys. **4**, 012 (2015), doi:10.1088/1475-7516/2015/04/012.

[16] E. Kuflik, M. Perelstein, N. R.-L. Lorier and Y.-D. Tsai, *Elastically decoupling dark matter*, Phys. Rev. Lett. **116**, 221302 (2016), doi:10.1103/PhysRevLett.116.221302.

[17] A. Soni and Y. Zhang, *Hidden* $SU(N)$ *glueball dark matter*, Phys. Rev. D **93**, 115025 (2016), doi:10.1103/PhysRevD.93.115025.

[18] D. Pappadopulo, J. T. Ruderman and G. Trevisan, *Dark matter freeze-out in a nonrelativistic sector*, Phys. Rev. D **94**, 035005 (2016), doi:10.1103/PhysRevD.94.035005.

[19] S. B. Gudnason, C. Kouvaris and F. Sannino, *Towards working technicolor: Effective theories and dark matter*, Phys. Rev. D **73**, 115003 (2006), doi:10.1103/PhysRevD.73.115003.

[20] T. A. Ryttov and F. Sannino, *Ultraminimal technicolor and its dark matter technicolor interacting massive particles*, Phys. Rev. D **78**, 115010 (2008), doi:10.1103/PhysRevD.78.115010.

[21] C. Kouvaris, *Dark side of strongly coupled theories*, Phys. Rev. D **78**, 075024 (2008), doi:10.1103/PhysRevD.78.075024.

[22] R. Lewis, C. Pica and F. Sannino, *Light asymmetric dark matter on the lattice:* $SU(2)$ *technicolor with two fundamental flavors*, Phys. Rev. D **85**, 014504 (2012), doi:10.1103/PhysRevD.85.014504.

[23] M. T. Frandsen, S. Sarkar and K. Schmidt-Hoberg, *Light asymmetric dark matter from new strong dynamics*, Phys. Rev. D **84**, 051703 (2011), doi:10.1103/PhysRevD.84.051703.

[24] O. Antipin, M. Redi and A. Strumia, *Dynamical generation of the weak and dark matter scales from strong interactions*, J. High Energy Phys. **01**, 157 (2015), doi:10.1007/JHEP01(2015)157.

[25] A. Hietanen, R. Lewis, C. Pica and F. Sannino, *Fundamental composite Higgs dynamics on the lattice:* $SU(2)$ *with two flavors*, J. High Energy Phys. **07**, 116 (2014), doi:10.1007/JHEP07(2014)116.

[26] R. Arthur, V. Drach, M. Hansen, A. Hietanen, C. Pica and F. Sannino, $SU(2)$ *gauge theory with two fundamental flavors: A minimal template for model building*, Phys. Rev. D **94**, 094507 (2016), doi:10.1103/PhysRevD.94.094507.

[27] R. Arthur, V. Drach, A. Hietanen, C. Pica and F. Sannino, $SU(2)$ *gauge theory with two fundamental flavours: Scalar and pseudoscalar spectrum*, (arXiv preprint) doi:10.48550/arXiv.1607.06654.

[28] F. Sannino and I. M. Shoemaker, *Asymptotically safe dark matter*, Phys. Rev. D **92**, 043518 (2015), doi:10.1103/PhysRevD.92.043518.

[29] Y. Hochberg, E. Kuflik and H. Murayama, *SIMP spectroscopy*, J. High Energy Phys. **05**, 090 (2016), doi:10.1007/JHEP05(2016)090.

[30] T. Appelquist et al., *Stealth dark matter: Dark scalar baryons through the Higgs portal*, Phys. Rev. D **92**, 075030 (2015), doi:10.1103/PhysRevD.92.075030.

[31] T. Appelquist et al., *Detecting stealth dark matter directly through electromagnetic polarizability*, Phys. Rev. Lett. **115**, 171803 (2015), doi:10.1103/PhysRevLett.115.171803.

[32] H. M. Lee and M.-S. Seo, *Communication with SIMP dark mesons via Z'-portal*, Phys. Lett. B **748**, 316 (2015), doi:10.1016/j.physletb.2015.07.013.

[33] S.-M. Choi, H. M. Lee, P. Ko and A. Natale, *Resolving phenomenological problems with strongly-interacting-massive-particle models with dark vector resonances*, Phys. Rev. D **98**, 015034 (2018), doi:10.1103/PhysRevD.98.015034.

[34] A. Francis, R. J. Hudspith, R. Lewis and S. Tulin, *Dark matter from strong dynamics: The minimal theory of dark baryons*, J. High Energy Phys. **12**, 118 (2018), doi:10.1007/JHEP12(2018)118.

[35] A. Berlin, N. Blinov, S. Gori, P. Schuster and N. Toro, *Cosmology and accelerator tests of strongly interacting dark matter*, Phys. Rev. D **97**, 055033 (2018), doi:10.1103/PhysRevD.97.055033.

[36] S.-M. Choi, H. M. Lee and B. Zhu, *Exothermic dark mesons in light of electron recoil excess at XENON1T*, J. High Energy Phys. **04**, 251 (2021), doi:10.1007/JHEP04(2021)251.

[37] A. Katz, E. Salvioni and B. Shakya, *Split SIMPs with decays*, J. High Energy Phys. **10**, 049 (2020), doi:10.1007/JHEP10(2020)049.

[38] J. M. Butterworth, X. Kong, M. Thomas, L. Corpe and S. Kulkarni, *New sensitivity of LHC measurements to composite dark matter models*, Phys. Rev. D **105**, 015008 (2022), doi:10.1103/PhysRevD.105.015008.

[39] R. Garani, M. Redi and A. Tesi, *Dark QCD matters*, J. High Energy Phys. **12**, 139 (2021), doi:10.1007/JHEP12(2021)139.

[40] G. D. Kribs and E. T. Neil, *Review of strongly-coupled composite dark matter models and lattice simulations*, Int. J. Mod. Phys. A **31**, 1643004 (2016), doi:10.1142/S0217751X16430041.

[41] A. Hietanen, R. Lewis, C. Pica and F. Sannino, *Composite Goldstone dark matter: Experimental predictions from the lattice*, J. High Energy Phys. **12**, 130 (2014), doi:10.1007/JHEP12(2014)130.

[42] R. S. Chivukula and T. P. Walker, *Technicolor cosmology*, Nucl. Phys. B **329**, 445 (1990), doi:10.1016/0550-3213(90)90151-3.

[43] S. Nussinov, *Technocosmology - could a technibaryon excess provide a "natural" missing mass candidate?*, Phys. Lett. B **165**, 55 (1985), doi:10.1016/0370-2693(85)90689-6.

[44] J. M. Cline, W. Huang and G. D. Moore, *Challenges for models with composite states*, Phys. Rev. D **94**, 055029 (2016), doi:10.1103/PhysRevD.94.055029.

[45] J. M. Cline, *B decay anomalies and dark matter from vectorlike confinement*, Phys. Rev. D **97**, 015013 (2018), doi:10.1103/PhysRevD.97.015013.

[46] J. M. Cline and J. M. Camalich, *B decay anomalies from nonabelian local horizontal symmetry*, Phys. Rev. D **96**, 055036 (2017), doi:10.1103/PhysRevD.96.055036.

[47] R. Foot, *Mirror dark matter: Cosmology, Galaxy structure and direct detection*, Int. J. Mod. Phys. A **29**, 1430013 (2014), doi:10.1142/S0217751X14300130.

[48] M. Hansen, K. Langæble and F. Sannino, *SIMP model at NNLO in chiral perturbation theory*, Phys. Rev. D **92**, 075036 (2015), doi:10.1103/PhysRevD.92.075036.

[49] W. Detmold, M. McCullough and A. Pochinsky, *Dark nuclei. II. Nuclear spectroscopy in two-color QCD*, Phys. Rev. D **90**, 114506 (2014), doi:10.1103/PhysRevD.90.114506.

[50] W. Detmold, M. McCullough and A. Pochinsky, *Dark nuclei. I. Cosmology and indirect detection*, Phys. Rev. D **90**, 115013 (2014), doi:10.1103/PhysRevD.90.115013.

[51] E. Katz, A. E. Nelson and D. G. E. Walker, *The intermediate Higgs*, J. High Energy Phys. **08**, 074 (2005), doi:10.1088/1126-6708/2005/08/074.

[52] P. Lodone, *Vector-like quarks in a 'composite' Higgs model*, J. High Energy Phys. **12**, 029 (2008), doi:10.1088/1126-6708/2008/12/029.

[53] B. Gripaios, A. Pomarol, F. Riva and J. Serra, *Beyond the minimal composite Higgs model*, J. High Energy Phys. **04**, 070 (2009), doi:10.1088/1126-6708/2009/04/070.

[54] J. A. Evans, J. Galloway, M. A. Luty and R. A. Tacchi, *Minimal conformal technicolor and precision electroweak tests*, J. High Energy Phys. **10**, 086 (2010), doi:10.1007/JHEP10(2010)086.

[55] J. Barnard, T. Gherghetta and T. S. Ray, *UV descriptions of composite Higgs models without elementary scalars*, J. High Energy Phys. **02**, 002 (2014), doi:10.1007/JHEP02(2014)002.

[56] G. Cacciapaglia and F. Sannino, *Fundamental composite (Goldstone) Higgs dynamics*, J. High Energy Phys. **04**, 111 (2014), doi:10.1007/JHEP04(2014)111.

[57] A. Arbey, G. Cacciapaglia, H. Cai, A. Deandrea, S. le Corre and F. Sannino, *Fundamental composite electroweak dynamics: Status at the LHC*, Phys. Rev. D **95**, 015028 (2017), doi:10.1103/PhysRevD.95.015028.

[58] D. Buarque Franzosi, G. Cacciapaglia, H. Cai, A. Deandrea and M. Frandsen, *Vector and axial-vector resonances in composite models of the Higgs boson*, J. High Energy Phys. **11**, 076 (2016), doi:10.1007/JHEP11(2016)076.

[59] A. Maas and F. Zierler, *Strong isospin breaking in $Sp(4)$ gauge theory*, (arXiv preprint) doi:10.48550/arXiv.2109.14377.

[60] J. B. Kogut, M. A. Stephanov, D. Toublan, J. J. M. Verbaarschot and A. Zhitnitsky, *QCD-like theories at finite baryon density*, Nucl. Phys. B **582**, 477 (2000), doi:10.1016/S0550-3213(00)00242-X.

[61] L. von Smekal, *Universal Aspects of QCD-like Theories*, Nucl. Phys. B - Proc. Suppl. **228**, 179 (2012), doi:10.1016/j.nuclphysbps.2012.06.006.

[62] V. Beylin, M. Khlopov, V. Kuksa and N. Volchanskiy, *New physics of strong interaction and dark Universe*, Universe **6**, 196 (2020), doi:10.3390/universe6110196.

[63] V. Drach, T. Janowski and C. Pica, *Update on $SU(2)$ gauge theory with $NF = 2$ fundamental flavours*, Euro. Phys. Lett. Web Conf. **175**, 08020 (2018), doi:10.1051/epjconf/201817508020.

[64] M. Shifman, *Advanced topics in quantum field theory: A lecture course*, Cambridge University Press, Cambridge, UK, ISBN 9781108885911 (2012), doi:10.1017/9781108885911.

[65] M. E. Peskin and D. V. Schroeder, *An introduction to quantum field theory*, Addison-Wesley, Reading, Pennsylvania, US, ISBN 9780367320560 (1995), doi:10.1201/9780429503559.

[66] S. Coleman, *Lectures of Sidney Coleman on quantum field theory*, World Scientific, Singapore, ISBN 9789814632539 (2018), doi:10.1142/9371.

[67] E. Witten, *Global aspects of current algebra*, Nucl. Phys. B **223**, 422 (1983), doi:10.1016/0550-3213(83)90063-9.

[68] E. Witten, *Current algebra, baryons, and quark confinement*, Nucl. Phys. B **223**, 433 (1983), doi:10.1016/0550-3213(83)90064-0.

[69] J. Wess and B. Zumino, *Consequences of anomalous ward identities*, Phys. Lett. B **37**, 95 (1971), doi:10.1016/0370-2693(71)90582-X.

[70] E. Molinaro, F. Sannino, A. E. Thomsen and N. Vignaroli, *Uncovering new strong dynamics via topological interactions at the 100 TeV collider*, Phys. Rev. D **96**, 075040 (2017), doi:10.1103/PhysRevD.96.075040.

[71] F. J. Yndurain, *The theory of quark and gluon interactions*, Springer Berlin Heidelberg, Berlin, Heidelberg, ISBN 9783540332091 (2006), doi:10.1007/3-540-33210-3.

[72] U.-G. Meissner, *Low-energy hadron physics from effective chiral Lagrangians with vector mesons*, Phys. Rep. **161**, 213 (1988), doi:10.1016/0370-1573(88)90090-7.

[73] K. Kawarabayashi and M. Suzuki, *Partially conserved axial-vector current and the decays of vector mesons*, Phys. Rev. Lett. **16**, 255 (1966), doi:10.1103/PhysRevLett.16.255.

[74] Riazuddin and Fayyazuddin, *Algebra of current components and decay widths of ρ and K^* mesons*, Phys. Rev. **147**, 1071 (1966), doi:10.1103/physrev.147.1071.

[75] V. Drach, T. Janowski, C. Pica and S. Prelovsek, *Scattering of Goldstone bosons and resonance production in a composite Higgs model on the lattice*, J. High Energy Phys. **04**, 117 (2021), doi:10.1007/JHEP04(2021)117.

[76] M. Bando, T. Kugo, S. Uehara, K. Yamawaki and T. Yanagida, *Is ρ meson a dynamical gauge boson of hidden local symmetry?*, Phys. Rev. Lett. **54**, 1215 (1985), doi:10.1103/PhysRevLett.54.1215.

[77] Z. Duan, P. S. Rodrigues da Silva and F. Sannino, *Enhanced global symmetry constraints on ϵ terms*, Nucl. Phys. B **592**, 371 (2001), doi:10.1016/S0550-3213(00)00550-2.

[78] T. Brauner and H. Kolešová, *Gauged Wess-Zumino terms for a general coset space*, Nucl. Phys. B **945**, 114676 (2019), doi:10.1016/j.nuclphysb.2019.114676.

[79] Y. Hochberg, E. Kuflik, R. McGehee, H. Murayama and K. Schutz, *Strongly interacting massive particles through the axion portal*, Phys. Rev. D **98**, 115031 (2018), doi:10.1103/PhysRevD.98.115031.

[80] J. Jaeckel and A. Ringwald, *The low-energy frontier of particle physics*, Annu. Rev. Nucl. Part. Sci. **60**, 405 (2010), doi:10.1146/annurev.nucl.012809.104433.

[81] J. Alexander et al., *Dark sectors 2016 workshop: Community report*, (arXiv preprint) doi:10.48550/arXiv.1608.08632.

[82] J. Beacham et al., *Physics beyond colliders at CERN: Beyond the Standard Model working group report*, J. Phys. G: Nucl. Part. Phys. **47**, 010501 (2019), doi:10.1088/1361-6471/ab4cd2.

[83] J. J. Sakurai, *Theory of strong interactions*, Ann. Phys. **11**, 1 (1960), doi:10.1016/0003-4916(60)90126-3.

[84] D. Nogradi and L. Szikszai, *The model dependence of m_ϱ/f_π*, Proc. Sci. **LATTICE2019**, 237 (2019), doi:10.22323/1.363.0237.

[85] Y. Aoki et al., *FLAG review 2021*, Eur. Phys. J. C **82**, 869 (2022), doi:10.1140/epjc/s10052-022-10536-1.

[86] K. Holland, M. Pepe and U.-J. Wiese, *The deconfinement phase transition of $Sp(2)$ and $Sp(3)$ Yang-Mills theories in $(2+1)$ and $(3+1)$ dimensions*, Nucl. Phys. B **694**, 35 (2004), doi:10.1016/j.nuclphysb.2004.06.026.

[87] M. Pepe and U.-J. Wiese, *Exceptional deconfinement in gauge theory*, Nucl. Phys. B **768**, 21 (2007), doi:10.1016/j.nuclphysb.2006.12.024.

[88] L. del Debbio, A. Patella and C. Pica, *Higher representations on the lattice: Numerical simulations, $SU(2)$ with adjoint fermions*, Phys. Rev. D **81**, 094503 (2010), doi:10.1103/PhysRevD.81.094503.

[89] P. A. Zyla et al., *Review of particle physics*, Prog. Theor. Exp. Phys. 083C01 (2020), doi:10.1093/ptep/ptaa104.

[90] R. Alkofer, W. Detmold, C. S. Fischer and P. Maris, *Analytic properties of the Landau gauge gluon and quark propagators*, Phys. Rev. D **70**, 014014 (2004), doi:10.1103/PhysRevD.70.014014.

[91] C. Gattringer, P. Huber and C. B. Lang, *Lattice calculation of low energy constants with Ginsparg-Wilson type fermions*, Phys. Rev. D **72**, 094510 (2005), doi:10.1103/PhysRevD.72.094510.

[92] E. Bernreuther, F. Kahlhoefer, M. Krämer and P. Tunney, *Strongly interacting dark sectors in the early Universe and at the LHC through a simplified portal*, J. High Energy Phys. **01**, 162 (2020), doi:10.1007/JHEP01(2020)162.

[93] R. C. Brower et al., *Stealth dark matter confinement transition and gravitational waves*, Phys. Rev. D **103**, 014505 (2021), doi:10.1103/PhysRevD.103.014505.

[94] J.-W. Lee, B. Lucini and M. Piai, *Symmetry restoration at high-temperature in two-color and two-flavor lattice gauge theories*, J. High Energy Phys. **04**, 036 (2017), doi:10.1007/JHEP04(2017)036.

APPENDIX A

Representation theory

A.1 Conjugate/real/pseudo-real representation of fermions

In this section we follow mostly the book by Peskin and Schroeder [112] and the book by Srednicki [113]. In QCD, fermions (quarks) are described in the fundamental representation of $SU(3)$. The fundamental representation of $SU(3)$ is the conjugate representation. In physics terms, this means that there exist quarks and antiquarks, each described by representations conjugated to each other. We can define the conjugated representation as follows. For any irreducible representation r of a symmetry group there is a conjugate representation $\bar{r}$, such that the representing matrices satisfy

$$T^A_{\bar{r}} = -(T^A_r)^\star = -(T^A_r)^T. \tag{A.1.1}$$

The above relation can be checked by taking infinitesimal transformations U that belong to representation r and to the conjugate representation $\bar{r}$,

$$\phi \to U\phi \sim (1 + i\alpha^A T^A_r)\phi, \tag{A.1.2}$$
$$\phi^\star \to U^\star\phi^\star \sim (1 - i\alpha^a (T^A_r)^\star)\phi^\star. \tag{A.1.3}$$

Then, the matrices that belong to the conjugate representation $\bar{r}$ are identified as in Eq. (A.1.1). This set of matrices form also an algebra, like T^A_r,

$$\left[T^A_{\bar{r}}, T^B_{\bar{r}}\right] = \left[-(T^A_r)^\star, -(T^B_r)^\star\right] = \left[T^A_r, T^B_r\right]^\star = -if^{ABC}T^{C\star}_r = if^{ABC}T^C_{\bar{r}}. \tag{A.1.4}$$

There exist also theories in which not only gauge bosons but also fermions are described in a real representation of the theory. For any real representation, $T^A_r = T^A_{\bar{r}}$, the generators satisfy the relation $T^A_r = -(T^A_r)^\star = -(T^A_r)^T$. In some cases, generators of a real representation do not fulfil the relation directly, but can be transformed through a unitary transformation S,

$$T^A_r \ \to \ ST^A_r S^\dagger = ST^A_r S^{-1} \tag{A.1.5}$$

such that the relation $T^a_r = -(T^a_r)^\star$ holds for every a. For a real representation the generators T^a_r are purely imaginary and S is symmetric.

However, sometimes such a unitary transformation does not exist. In this case, it is possible to find another unitary matrix $S \neq \mathbb{I}$, such that

$$T^A_{\bar{r}} = -(T^A_r)^\star = S T^A_r S^\dagger = U T^a_r S^{-1}\ \forall a. \tag{A.1.6}$$

This representation is called pseudo-real and $S = -S^T$, $SS^\star = -\mathbf{1}$ [113]. For a pseudo-real representation, the generators are not purely imaginary and S is antisymmetric. For instance, the Lie-algebra of the fundamental representation of $SU(2)$ is spanned by the Pauli-matrices $\frac{\sigma^A}{2}$. Since $-\left(\sigma^A\right)^\star \neq \sigma^A$ (not a real representation) and $-\left(\frac{1}{2}\sigma^A\right)^\star = \left(\sigma^2\right)\left(\frac{1}{2}\sigma^A\right)\left(\sigma^2\right)^{-1}$ the fundamental representation of $SU(2)$ is pseudo-real.

In summary, the generators of the Lie algebra T^A for any (pseudo-)real satisfy

$$(T^A)^T = (T^A)^\star = -ST^AS^{-1}, \quad S = (-) + S^T, SS^\star = (-) + \mathbb{I}, SS^\dagger = \mathbb{I}. \tag{A.1.7}$$

Another example of a real representation is the adjoint representation, denoted $r = G$. The generators of an adjoint representation are identified through the structure constants $(t^a_G)_{bc} = -if_{abc}$. For instance, gauge bosons in QCD are given by $A_{bc} = A^a_\mu (t^a_G)_{bc}$, where $a, b, c = 1, ..., N^2 - 1$ are group color indices. The generators (t^a_G) form also a Lie algebra,

$$([t^a_G, t^b_G])_{cd} = (t^a_G)_{ce}(t^b_G)_{ed} - (t^b_G)_{ce}(t^a_G)_{ed} = if_{abe}(t^e_G)_{cd}. \tag{A.1.8}$$

Since the structure constants f_{abc} are totally antisymmetric and real, the generators satisfy $t^a_G = -(t^a_G)^\star = (t^a_{G})$. The dimension $d(G)$ of the adjoint representation for important groups in particle physics are given by

$$d(G) = N^2 - 1 \qquad (SU(N)), \tag{A.1.9}$$

$$d(G) = N(N-1)/2 \qquad (SO(N)), \tag{A.1.10}$$

$$d(G) = N(N+1)/2 \qquad (Sp(N)). \tag{A.1.11}$$

In the end, we provide the fundamental representation for different groups in particle physics

$$SU(N): N = 2 \text{ pseudo-real representation}, N \geq 3 \text{ complex representation}, \tag{A.1.12}$$

$$SO(N): \forall N \text{ real representation}, \tag{A.1.13}$$

$$Sp(N): \forall N \text{ pseudo-real representation}. \tag{A.1.14}$$

APPENDIX B

The construction of the chiral Lagrangian in the $Sp(4)_c$ theory

B.1 From UV-theory to effective theory

The chiral Lagrangian of Nambu-Goldstone states is constructed in the following way. First, the effective theory can be defined by fluctuations of the orientation of the chiral condensate [114],

$$\Sigma = e^{i\pi/f_\pi}\Sigma_0 e^{i\pi^T/f_\pi}. \tag{B.1.1}$$

Here, Σ_0 is the vacuum alignment and f_π is the Nambu-Goldstone decay constant. The chiral field Σ has to be anti-symmetric in colour and spin indices in order to be a colour and spin singlet. As a consequence, the flavour indices have to be antisymmetric as well, $\Sigma^T = -\Sigma$.

Second, the chiral Lagrangian has to preserve the symmetries of the UV-theory [108, 111]:

- Lorentz invariance (only even number of derivatives possible)
- chiral symmetry invariance (only combinations of Σ and $\Sigma^\dagger$ allowed)
- parity invariance $P: \ \vec{x} \ \rightarrow \ -\vec{x}$,
- charge conjugation invariance $C: \ \Sigma \ \rightarrow \ \Sigma^\star$.

In our case, the chiral symmetry is the global flavour symmetry $SU(4)$. Under the action of $U \in \mathrm{SU}(4)$ the chiral condensate transforms as a $2-$index antisymmetric representation,

$$\Sigma \rightarrow U\Sigma U^T. \tag{B.1.2}$$

In addition, we require the lowest number of derivatives since we consider low-energetic Nambu-Goldstone states. Taking all requirements into account we can construct the chiral Lagrangian for massless Nambu-Goldstone fields,

$$\mathcal{L}_{\text{kin}} = \frac{f_\pi^2}{4}\mathrm{Tr}\left[\partial_\mu\Sigma\partial^\mu\Sigma^\dagger\right]. \tag{B.1.3}$$

where the prefactor is introduced in order to ensure canonically normalized kinetic terms. Terms, like $\left(\mathrm{Tr}\left[\Sigma^\dagger \partial_\mu \Sigma\right]\right)^2, \mathrm{Tr}\left[\left(\Sigma^\dagger \partial_\mu \Sigma\right)^2\right]$ do not contribute [111]. The first guess would vanish since $\Sigma^\dagger \partial_\mu \Sigma$ is proportional to a generator of $SU(4)$ and thus, traceless. The second possibility can be written in terms of Eq. (B.1.3) using the unitarity condition $\Sigma^\dagger \partial_\mu \Sigma = -\partial_\mu \Sigma^\dagger \Sigma$. Hence, we are left with one unique Lagrangian at the lowest order. The introduction of mass terms in the effective theory is already discussed in the publication [1] in Chapter 3. A higher order of the chiral Lagrangian is given in Refs. [115, 116].

APPENDIX C

The Wess-Zumino-Witten interaction in the $Sp(4)_c$ theory

C.1 Derivation of the Wess-Zumino-Witten interaction

The purpose of this section is to derive the Wess-Zumino-Witten (WZW) interaction in chiral perturbation theory [108–111]. Since the chiral Lagrangian contains only an even number of Nambu-Goldstone fields, the Wess-Zumino-Witten term is essential to describe the 5-point interaction as $K^+K^- \to \pi^+\pi^-\pi^0$ in QCD or the $3 \to 2$ interaction in the SIMP sector. First, we recap the symmetries of the kinetic Lagrangian (B.1.3):

- Lorentz symmetry
- chiral symmetry
- "naive" parity $P_0: \vec{x} \to -\vec{x}, \Sigma \to \Sigma$,
- charge conjugation $C: \Sigma \to \Sigma^\star$,
- extra symmetry $R: \Sigma \to \Sigma^\dagger$.

In terms of Nambu-Goldstone fields the last symmetry can be understood as $R: \pi \to -\pi$ and counts the number of Nambu-Goldstone boson states mod 2. Hence, we can define this symmetry as $(-1)^{N_\pi}$, where N_π is the number of Nambu-Goldstone fields. QCD as well as the $Sp(4)_c$ theory at UV-completion is not invariant under P_0 nor $(-1)^{N_\pi}$ separately, but invariant under the combination of both, $P = P_0(-1)^{N_\pi}$. This leads to the question, why the effective theory has more symmetries than the UV-complete theory. Since the effective theory contains more symmetries, we might miss a term in the chiral Lagrangian [111], which respects parity P, but violates the symmetries P_0 and $(-1)^{N_\pi}$. Such interaction term can be found through the equation of motion of the kinetic Lagrangian (B.1.3),

$$\partial_\mu \left(\frac{f_\pi^2}{2} \Sigma^\dagger \partial^\mu \Sigma \right) = 0. \tag{C.1.1}$$

We can add an extra term to the equation of motion that violates P_0, but preserves P[1],

$$\frac{1}{2} f_\pi^2 \partial_\mu \left(\Sigma^\dagger \partial^\mu \Sigma \right) + k \epsilon^{\mu\nu\rho\sigma} \Sigma^\dagger \left(\partial_\mu \Sigma \right) \Sigma^\dagger \left(\partial_\nu \Sigma \right) \Sigma^\dagger \left(\partial_\rho \Sigma \right) \Sigma^\dagger \left(\partial_\sigma \Sigma \right) = 0, \tag{C.1.2}$$

where k is a constant and can be fixed later. Now, we try to find the corresponding Lagrangian that reproduces the additional term in Eq. (C.1.2). Any simple guess like

$$\epsilon^{\mu\nu\rho\sigma} \operatorname{tr} \left(\Sigma^\dagger \left(\partial_\mu \Sigma \right) \Sigma^\dagger \left(\partial_\nu \Sigma \right) \Sigma^\dagger \left(\partial_\rho \Sigma \right) \Sigma^\dagger \left(\partial_\sigma \Sigma \right) \right) \tag{C.1.3}$$

would vanish due to the antisymmetry of the epsilon tensor. However, there is a way to find a four-dimensional Lagrangian, that respects also the global flavour symmetry $SU(4)$. Consider a four-dimensional space-time $\mathcal{M}$, where each space-time point x is mapped to an element $\Sigma(x)$ in the $SU(4)/Sp(4)$ manifold. Remember, that the global flavour symmetry $SU(4)$ is spontaneously broken to $Sp(4)$. Then, we can introduce a five-dimensional disc $\mathcal{Q}_5$, where the boundary is the space-time[2], $\partial \mathcal{Q}_5 = \mathcal{M}$. In addition, we extend the maps $\Sigma(x)$ over $\mathcal{M}$ to $\Sigma(y)$ over $\mathcal{Q}_5$. Then, the action, that reproduces Eq. (C.1.2) is given by[3]

$$\mathcal{S} = \frac{f_\pi^2}{4} \int_{\mathcal{M}} \mathrm{d}^4 x \operatorname{Tr} \partial_\mu \Sigma \partial^\mu \Sigma^\dagger + k \int_{\mathcal{Q}_5} dy^\mu dy^\nu dy^\rho dy^\sigma dy^\lambda \, \omega_{\mu\nu\rho\sigma\lambda}, \tag{C.1.4}$$

where $\omega_{\mu\nu\rho\sigma\lambda}$ is a unique fifth rank antisymmetric tensor on the $SU(4)/Sp(4)$ manifold invariant under the global flavor symmetry $SU(4)$,

$$\omega_{\mu\nu\rho\sigma\lambda} = -\frac{i}{240\pi^2} \operatorname{Tr} \left[\left(\Sigma^\dagger \partial_\mu \Sigma \right) \left(\Sigma^\dagger \partial_\nu \Sigma \right) \left(\Sigma^\dagger \partial_\rho \Sigma \right) \left(\Sigma^\dagger \partial_\sigma \Sigma \right) \left(\Sigma^\dagger \partial_\lambda \Sigma \right) \right]. \tag{C.1.5}$$

In terms of Nambu-Goldstone fields, $\Sigma^\dagger \partial_\mu \Sigma = \frac{2i}{f_\pi} \partial_\mu \pi + \mathcal{O}(\pi^2/f_\pi^2)$, we can make the Wess-Zumino-Witten interaction more transparent,

$$k \int_{\mathcal{Q}_5} dy^\mu dy^\nu dy^\rho dy^\sigma dy^\lambda \, \omega_{\mu\nu\rho\sigma\lambda} \tag{C.1.6}$$

$$= \frac{2k}{15\pi^2 f_\pi^5} \int_{\mathcal{Q}_5} dy^\mu dy^\nu dy^\rho dy^\sigma dy^\lambda \operatorname{Tr} \left[\partial_\mu \pi \partial_\nu \pi \partial_\rho \pi \partial_\sigma \pi \partial_\lambda \pi \right] + \mathcal{O}\left(\pi^6 / f_\pi^6 \right) \tag{C.1.7}$$

$$= \frac{2k}{15\pi^2 f_\pi^5} \int_{\mathcal{Q}_5} dy^\mu dy^\nu dy^\rho dy^\sigma dy^\lambda \partial_\lambda \left(\operatorname{Tr} \left[\pi \partial_\mu \pi \partial_\nu \pi \partial_\rho \pi \partial_\sigma \pi \right] \right) + \mathcal{O}\left(\pi^6 / f_\pi^6 \right) \tag{C.1.8}$$

$$= \frac{2k}{15\pi^2 f_\pi^5} \int_{\mathcal{M}} d^4 x \epsilon^{\mu\nu\rho\sigma} \operatorname{Tr} \left[\pi \partial_\mu \pi \partial_\nu \pi \partial_\rho \pi \partial_\sigma \pi \right] + \mathcal{O}\left(\pi^6 / f_\pi^6 \right). \tag{C.1.9}$$

In the last equality, we used Stoke's theorem and $dx^\mu dx^\nu dx^\rho dx^\sigma = dx^4 \epsilon^{\mu\nu\rho\sigma}$.

[1] First, we want to have the lowest number of derivatives since we consider the low-energy limit. Second, a term that violates P_0 must contain an epsilon tensor.

[2] The space-time can be extended to a five-dimensional disc if the fourth homotopy group is trivial, $\pi_4(SU(4)/Sp(4)) = 0$.

[3] There is an analogy to magnetic monopoles discussed in Witten's paper [108].

Now, we can show, that the constant k is quantized. The choice of the five-dimensional disc $\mathcal{Q}_5$ is not unique. Since we are only interested in $\exp(i\mathcal{S})$ in the Feynman path, we can also take another disc $\mathcal{Q}_5'$ with an opposite orientation, such that

$$\exp\left(ik\int_{\mathcal{Q}_5} dY^{\mu\nu\rho\sigma\lambda}\,\omega_{\mu\nu\rho\sigma\lambda}\right) = \exp\left(-ik\int_{\mathcal{Q}_5'} dY^{\mu\nu\rho\sigma\lambda}\,\omega_{\mu\nu\rho\sigma\lambda}\right), \tag{C.1.10}$$

where $dY^{\mu\nu\rho\sigma\lambda} = dy^\mu dy^\nu dy^\rho dy^\sigma dy^\lambda$. Since $\mathcal{Q}_5 \cup \mathcal{Q}_5' = \mathcal{S}^5$ is a five-dimensional sphere on the $SU(4)/Sp(4)$ manifold, we can write

$$\exp\left(ik\int_{\mathcal{S}^5} dY^{\mu\nu\rho\sigma\lambda}\,\omega_{\mu\nu\rho\sigma\lambda}\right) = 1. \tag{C.1.11}$$

The integrand characterizes maps from $\mathcal{S}^5$ to the $SU(4)/Sp(4)$ manifold by $\Sigma(y)$, which correspond exactly to the fifth homotopy group,

$$\pi_5(SU(2N_f)/Sp(2N_f)) = \mathbb{Z}, \quad N_f \geq 2. \tag{C.1.12}$$

Then, each map can be assigned to a winding number $n \in \mathbb{Z}$, such that

$$\int_{\mathcal{S}^5} dY^{\mu\nu\rho\sigma\lambda}\,\omega_{\mu\nu\rho\sigma\lambda} = 2\pi n. \tag{C.1.13}$$

Consequently, the parameter $k \in \mathbb{Z}$ [108, 111]. It can be shown, that $k = N_c$ [103, 108], where N_c is the number of colours.
In the end, the Lagrangian of the Wess-Zumino-Witten interaction for Nambu-Goldstone fields $\pi \in SU(4)/Sp(4)$ is given by

$$\begin{aligned}
\mathcal{L}_{\text{WZW}} &= \frac{2N_c}{15\pi^2 f_\pi^5}\epsilon^{\mu\nu\rho\sigma}\,\text{Tr}\left[\pi\partial_\mu\pi\partial_\nu\pi\partial_\rho\pi\partial_\sigma\pi\right] + \mathcal{O}\left(\pi^6/f_\pi^6\right) \\
&= \frac{2N_c}{15\pi^2 f_\pi^5}\epsilon^{\mu\nu\rho\sigma}\pi_i\partial_\mu\pi_j\partial_\nu\pi_k\partial_\rho\pi_l\partial_\sigma\pi_n\,\text{Tr}\left[T^iT^jT^kT^lT^n\right] + \mathcal{O}\left(\pi^6/f_\pi^6\right) \\
&= \frac{N_c}{10\sqrt{2}\pi^2 f_\pi^5}\epsilon^{\mu\nu\rho\sigma}\left(\pi_1\partial_\mu\pi_2\partial_\nu\pi_3\partial_\rho\pi_4\partial_\sigma\pi_5 - \pi_2\partial_\mu\pi_1\partial_\nu\pi_3\partial_\rho\pi_4\partial_\sigma\pi_5\right. \\
&\qquad +\pi_3\partial_\mu\pi_1\partial_\nu\pi_2\partial_\rho\pi_4\partial_\sigma\pi_5 + \pi_4\partial_\mu\pi_1\partial_\nu\pi_2\partial_\rho\pi_5\partial_\sigma\pi_3 \\
&\qquad \left.+\pi_5\partial_\mu\pi_1\partial_\nu\pi_2\partial_\rho\pi_3\partial_\sigma\pi_4\right) + \mathcal{O}\left(\pi^6/f_\pi^6\right).
\end{aligned} \tag{C.1.14}$$

The Wess-Zumino-Witten term allows only purely flavour off-diagonal interactions and is invariant under the parity symmetries P and D given in Sec. 3.

CHAPTER 4

SIMP bound states

In this chapter we discuss a project, that is work in progress. The relic abundance of SIMPs given in Chapter 3 is realized through the Wess-Zumino-Witten interaction. However, including the possibility of bound state formation, the freeze out of SIMPs may potentially change. In this project, we study the implications of the existence of dark matter bound states around the freeze-out. We consider non-relativistic bound states - SIMPonium - made of two SIMP dark matter particles described by the dark $Sp(4)_c$ theory in Chapter 3. For simplicity, we assume shallow bound states with binding energies $E_B \ll m_\pi$ that are bounded by dark strong interactions only. The authors of the publication will be Xiaoyong Chu, Marco Nikolic and Josef Pradler.

4.1 Key SIMPonium reactions

In presence of bound states $X = (\pi\pi)$ with mass $M_X = 2m_\pi - E_B$ and binding energy E_B during the epoch of freeze-out in the early universe, four reactions[1] can become relevant for $T \ll m_\pi$,

$$\begin{aligned} 3\pi &\rightleftharpoons 2\pi && \text{standard SIMP reaction,} && (4.1.1)\\ X\pi &\rightleftharpoons 2\pi && \text{bound state reduction,} && (4.1.2)\\ 3\pi &\rightleftharpoons \pi X && \text{bound state production,} && (4.1.3)\\ 2X &\rightleftharpoons 2\pi && \text{bound state annihilation.} && (4.1.4)\end{aligned}$$

Around the moment of freeze-out, the directions $\pi X \to 3\pi$, $2\pi \to \pi X$ and $2\pi \to 2X$ are suppressed by kinematics. The first reaction (4.1.1) is the standard SIMP interaction, which is generated by the Wess-Zumino-Witten action (C.1.14) and plays an important role in the SIMP paradigm (see Sec. 2.2). Including the possibility of bound state formation, three more reactions can become relevant[2]. The second reaction (4.1.2) is efficient for the reduction of the bound states X by converting X quickly to SIMPs π. The leading order of this reaction is

[1] The reaction $X \rightleftharpoons 2\pi$ is kinematically forbidden without an additional gauge boson.

[2] We consider only diagrams with π as a mediator. Diagrams with X as a mediator are sub-leading.

also mediated by the Wess-Zumino-Witten interaction and hence, only bound states with odd flavour combinations are involved. The third reaction (4.1.3) is necessary in order to create bound states. In the last reaction (4.1.4) bound states annihilate to SIMPs. The last two reactions are either generated by one 6-point or two 4-point interactions. Moreover, bound states of all flavour combinations are involved.

The Boltzmann equations for π and X including the above reactions are given by

$$\begin{aligned}\frac{dY_\pi}{dx} = \frac{xs^2}{H\left(m_\pi\right)}\Bigg[&\frac{1}{s}\langle\sigma v\rangle_{X\pi\to 2\pi}\left(Y_\pi Y_X - \frac{Y_\pi^2}{Y_\pi^{\rm eq}}Y_X^{\rm eq}\right) - 2\langle\sigma v^2\rangle_{3\pi\to\pi X}\left(Y_\pi^3 - Y_\pi(Y_\pi^{\rm eq})^2\frac{Y_X}{Y_X^{\rm eq}}\right)\\ &- \langle\sigma v^2\rangle_{3\pi\to 2\pi}\left(Y_\pi^3 - Y_\pi^2 Y_\pi^{\rm eq}\right) + \frac{2}{s}\langle\sigma v\rangle_{2X\to 2\pi}\left(Y_X^2 - \left(Y_X^{\rm eq}\right)^2\right)\Bigg],\end{aligned} \tag{4.1.5}$$

$$\begin{aligned}\frac{dY_X}{dx} = \frac{xs^2}{H\left(m_\pi\right)}\Bigg[&\langle\sigma v^2\rangle_{3\pi\to\pi X}\left(Y_\pi^3 - Y_\pi(Y_\pi^{\rm eq})^2\frac{Y_X}{Y_X^{\rm eq}}\right) - \frac{1}{s}\langle\sigma v\rangle_{\pi X\to 2\pi}\left(Y_\pi Y_X - \frac{Y_\pi^2}{Y_\pi^{\rm eq}}Y_X^{\rm eq}\right)\\ &- \frac{2}{s}\langle\sigma v\rangle_{2X\to 2\pi}\left(Y_X^2 - \left(Y_X^{\rm eq}\right)^2\right)\Bigg],\end{aligned} \tag{4.1.6}$$

where the prefactors give the change of the particle number in the interaction and $H(m_\pi) \simeq 1.67\sqrt{g_\star}\frac{m_\pi^2}{M_{\rm Pl}}$. The yield at equilibrium for π and X read

$$Y_\pi^{\rm eq} \simeq 0.145\frac{g_\pi}{g_{\star,s}}x^{3/2}e^{-x}, \tag{4.1.7}$$

$$Y_X^{\rm eq} \simeq 0.145\frac{g_X}{g_{\star,s}}x^{3/2}\left(\frac{M_X}{m_\pi}\right)^{3/2}e^{-\frac{M_X}{m_\pi}x} \tag{4.1.8}$$

$$= 0.145\frac{g_X}{g_{\star,s}}(2x)^{3/2}\left(1-\frac{E_B}{2m_\pi}\right)^{3/2}e^{-2x\left(1-\frac{E_B}{2m_\pi}\right)}, \tag{4.1.9}$$

where $x = m_\pi/T$ and g_π, g_X are degrees of freedom of π and X. In this case, the relic abundance is now a combination of Y_π and Y_X at freeze out,

$$\Omega_{\rm DM}h^2\Big|_{x\to\infty} = \frac{s_\infty}{\rho_{\rm crit}}\left(M_X Y_X(x\to\infty) + m_\pi Y_\pi(x\to\infty)\right) \tag{4.1.10}$$

$$= \frac{Y_\pi(x\to\infty)s_\infty}{\rho_{\rm crit}}\left(f_{X,\infty}M_X + m_\pi\right) \tag{4.1.11}$$

$$\overset{E_B\ll m_\pi}{\simeq} \frac{s_\infty m_\pi}{\rho_{\rm crit}}\left(2Y_X(x\to\infty) + Y_\pi(x\to\infty)\right), \tag{4.1.12}$$

where s_∞ is the entropy density at present time, $\rho_{\rm crit}$ is the critical mass density, $x = m_{\rm DM}/T$ and $f_{X,\infty} = Y_X/Y_\pi$ is the fraction of bound states X at freeze out and later. As a reminder, the mass of a bound state made of two SIMP particles is given by $M_X = 2m_\pi - E_B$, where E_B is the binding energy. In addition, the $3\pi \to 2\pi$ process needs always to be sub-leading.

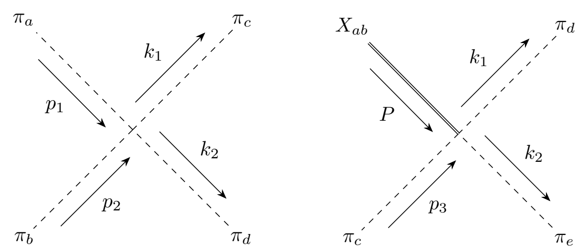

Figure 4.1: The $2\pi \to 2\pi$ and $X\pi \to 2\pi$ (right) processes. The ingoing bound state momentum is P.

Otherwise, the relic abundance of dark matter is again regulated by the SIMP mechanism. Since we are interested in the dark matter mass abundance (4.1.10), the combination of the Boltzmann equations leads to

$$\begin{aligned}\frac{d(Y_\pi + 2Y_X)}{dx} = -\frac{xs^2}{H\left(m_\pi\right)}\Bigg[&\langle\sigma v^2\rangle_{3\pi\to 2\pi}\left(Y_\pi^3 - Y_\pi^2 Y_\pi^{\mathrm{eq}}\right) + \frac{1}{s}\langle\sigma v\rangle_{\pi X\to 2\pi}\left(Y_\pi Y_X - \frac{Y_\pi^2}{Y_\pi^{\mathrm{eq}}}Y_X^{\mathrm{eq}}\right)\\ &- \frac{2}{s}\langle\sigma v\rangle_{2X\to 2\pi}\left(Y_X^2 - \left(Y_X^{\mathrm{eq}}\right)^2\right)\Bigg].\end{aligned} \tag{4.1.13}$$

Hence, the resulting relic abundance given in Eq. (4.1.10) depends on the magnitude of the thermally averaged cross sections $\langle\sigma v\rangle_{\pi X\to 2\pi}$, $\langle\sigma v^2\rangle_{3\pi\to 2\pi}$ and $\langle\sigma v\rangle_{2X\to 2\pi}$. In the next chapters, we derive the thermally averaged cross sections for $3\pi \to \pi X$ and $\pi X \to 2\pi$ explicitly.

4.2 SIMP bound states in Wess-Zumino-Witten interactions

In this section, we calculate the thermally averaged cross section for the reaction $X\pi \to 2\pi$, see Fig. 4.1 (right). For this reason, we need to derive the invariant matrix amplitude $\mathcal{M}_{X\pi\,\to\,2\pi}$ from the operator of fully connected diagrams (we follow mainly the book by Peskin and Schroeder [112])

$$\begin{aligned}\left\langle\vec{k}_1\vec{k}_2\right| T\left(i\int dx^4\mathcal{L}_{\mathrm{WZW}}\right)\left|\vec{P}, z; \vec{p}_3\right\rangle =&(2\pi)^3\delta^{(4)}(P + p_3 - k_1 - k_2)\\ &\times i\mathcal{M}_{X\pi\to 2\pi}(P, p_3 \to k_1, k_2),\end{aligned} \tag{4.2.1}$$

Here, $\vec{P}$ is the bound state momentum. The energy-momentum conservation is $P+p_3 = k_1+k_2$ in this case.

The typical momentum exchange between bound and unbound states in a scattering is

$$
\begin{aligned}
|\vec{q}\,| &\simeq \mu v_{\rm rel} && \text{unbound states,}\\
|\vec{q}\,| &\simeq \mu \alpha && \text{bound states,}
\end{aligned}
$$

where $\mu = \frac{m_\pi}{2}$ is the reduced mass and α is the effective interaction strength. Then, the energy exchange for $\alpha, v_{\rm rel} \ll 1$ is of order

$$q^0 \simeq \frac{|\vec{q}\,|^2}{2\mu} \ll |\vec{q}\,|. \tag{4.2.2}$$

Neglecting the energy exchange is known as *instantaneous approximation* [117], where the bound state is formed instantly. Hence, we can define a non-relativistic bound state with momentum $\vec{P}$ and internal quantum numbers z by

$$\left|\vec{P}, z\right\rangle = S\sqrt{2M_X}\int d^3x d^3y\, f_{\vec{P},z}\pi^\dagger_{i,+}(\vec{x}\,)\pi^\dagger_{j,+}(\vec{y}\,)\,|0\rangle\,, \tag{4.2.3}$$

where i, j are flavour indices, $M_X = 2m_\pi - E_B$ is the mass of the SIMP bound state, E_B is the binding energy, $\vec{R} = \frac{1}{2}(\vec{x} + \vec{y}\,)$ is the center of mass coordinate, $\vec{r} = \vec{x} - \vec{y}$ is the relative distance, $f_{\vec{P},z} = 2m_\pi e^{i\vec{P}\cdot\vec{R}}\psi_{X,z}(\vec{r}\,)$ and $\psi_{X,z}(\vec{r}\,)$ is a non-relativistic Schrödinger wave function, that can be found through the potential of the system. For identical particles $S = 1/\sqrt{2}$, because the system is invariant under exchanging x and y for identical states ($S = 1$ for non-identical particles). Here, $\vec{x}$, $\vec{y}$ are the positions of each SIMP and $\pi_+(\vec{x}\,)$ is the positive frequency part of a scalar field,

$$\pi_+(\vec{x}\,) = \int \frac{d^3p}{(2\pi)^3}\frac{1}{\sqrt{2E_{\vec{p}}}}e^{-ip\cdot x}a_{\vec{p}} \overset{\text{N.R.}}{\simeq} \frac{1}{\sqrt{2m_\pi}}\int\frac{d^3p}{(2\pi)^3}e^{i\vec{p}\cdot\vec{x}}a_{\vec{p}}. \tag{4.2.4}$$

In the last equality, we take the non-relativistic limit, $\sqrt{2E_{\vec{p}}} \to \sqrt{2m_\pi}$. The bound state is properly normalized as

$$\left\langle \vec{P}', z'\middle|\vec{P}, z\right\rangle = 2M_X(2\pi)^3\delta^{(3)}(\vec{P} - \vec{P}')\delta_{zz'}. \tag{4.2.5}$$

Then, the bound state can be simplified to

$$
\begin{aligned}
\left|\vec{P}, z\right\rangle &= S\sqrt{2M_X}\int d^3\vec{x}d^3\vec{y}\, f_{\vec{P},z}\int\frac{d^3p_1}{(2\pi)^3}\frac{1}{2E_{\vec{p}_1}}e^{-i\vec{p}_1\cdot\vec{x}}\int\frac{d^3p_2}{(2\pi)^3}\frac{1}{2E_{\vec{p}_2}}e^{-i\vec{p}_2\cdot\vec{y}}\,|\vec{p}_1, \vec{p}_2\rangle && (4.2.6)\\
&= S\sqrt{2M_X}\frac{m_\pi}{2}\int d^3r e^{\frac{i}{2}\vec{P}\vec{r}}\psi_{X,z}(\vec{r}\,)\int\frac{d^3p_1}{(2\pi)^3}\frac{1}{E_{\vec{p}_1}E_{\vec{P}-\vec{p}_1}}e^{-i\vec{p}_1\vec{r}}\left|\vec{p}_1, \vec{P} - \vec{p}_1\right\rangle && (4.2.7)\\
&= S\sqrt{2M_X}\frac{m_\pi}{2}\int\frac{d^3p_1}{(2\pi)^3}\tilde{\psi}_{X,z}\left(\vec{p}_1 - \vec{P}/2\right)\frac{1}{E_{\vec{p}_1}E_{\vec{P}-\vec{p}_1}}\left|\vec{p}_1, \vec{P} - \vec{p}_1\right\rangle && (4.2.8)\\
&= S\sqrt{2M_X}\frac{m_\pi}{2}\int\frac{d^3p_1}{(2\pi)^3}\frac{1}{E_{\vec{P}/2+\vec{p}_1}E_{\vec{P}/2-\vec{p}_1}}\tilde{\psi}_{X,z}\left(\vec{p}_1\right)\left|\vec{P}/2 + \vec{p}_1, \vec{P}/2 - \vec{p}_1\right\rangle && (4.2.9)\\
&\simeq \frac{S\sqrt{2M_X}}{2m_\pi}\int\frac{d^3q}{(2\pi)^3}\tilde{\psi}_{X,z}\left(\vec{q}\,\right)\left|\vec{P}/2 + \vec{q}, \vec{P}/2 - \vec{q}\right\rangle, && (4.2.10)
\end{aligned}
$$

where $\vec{q}$ can be seen as the relative momentum between particles in a bound state and $\tilde{\psi}_{X,z}$ is the Fourier transformation of $\psi_{X,z}$. In the last equality, we shifted the momentum $\vec{p}_1 \to \vec{q}+\vec{P}/2$ and renamed p_1 to q. As can be seen, the two constituents move with non-relativistic momenta $\vec{P}/2+\vec{q}$, $\vec{P}/2-\vec{q}$. In the following, we denote the momenta of constituents as $\vec{p}_1 = \vec{P}/2+\vec{q}$, $\vec{p}_2 = \vec{P}/2-\vec{q}$, the bound state momentum as $\vec{P} = \vec{p}_1+\vec{p}_2$ and the relative momentum as $\vec{q} = \frac{1}{2}(\vec{p}_1-\vec{p}_2)$. Additionally, we restrict ourselves to non-identical particles ($S=1$), since we will deal with non-identical particles in the Wess-Zumino-Witten interaction. The matrix amplitude can be extracted from Eq. (4.2.1),

$$\left\langle \vec{k}_1, \vec{k}_2 \right| T\left(i\int dx^4 \mathcal{L}_{\text{WZW}}\right)\left|\vec{P}, z; \vec{p}_3\right\rangle \tag{4.2.11}$$

$$\overset{\text{N.R.}}{\simeq} \frac{\sqrt{2M_X}}{2m_\pi}\int \frac{d^3q}{(2\pi)^3}\tilde{\psi}_{X,z}(\vec{q})\left\langle \vec{k}_1, \vec{k}_2 \right| T\left(i\int dx^4 \mathcal{L}_{\text{WZW}}\right)\left|\vec{P}/2+\vec{q}, \vec{P}/2-\vec{q}, \vec{p}_3\right\rangle \tag{4.2.12}$$

$$= (2\pi)^4\delta^{(4)}(P+p_3-k_1-k_2) \tag{4.2.13}$$

$$\times\, i\frac{\sqrt{2M_X}}{2m_\pi}\int \frac{d^3q}{(2\pi)^3}\tilde{\psi}_{X,z}(\vec{q})\,\mathcal{M}_{\text{WZW}}(P/2+q, P/2-q, p_3 \to k_1, k_2), \tag{4.2.14}$$

where $\mathcal{M}_{\text{WZW}}(p_1,p_2,p_3 \to k_1,k_2) = -\frac{N_c}{2\sqrt{2}\pi^2 f_\pi^5}\varepsilon^{\alpha\beta\mu\nu}p_{1\alpha}p_{2\beta}p_{3\mu}k_{1\nu}$ is the matrix element for the usual Wess-Zumino-Witten interaction for SIMPs with mass m_π given in App. 3. Compared to Eq. (4.2.1) the matrix amplitude for $X\pi \to 2\pi$ reads

$$\mathcal{M}_{X\pi\to 2\pi}(P,p_3 \to k_1,k_2) \overset{\text{N.R.}}{\simeq} \frac{\sqrt{2M_X}}{2m_\pi}\int \frac{d^3q}{(2\pi)^3}\tilde{\psi}_{X,z}(\vec{q})\,\mathcal{M}_{\text{WZW}}(P/2+q, P/2-q, p_3 \to k_1, k_2). \tag{4.2.15}$$

Here, we suppressed the flavour indices for π and X[3]. This matrix element agrees with the notation of Peskin and Schroeder [118] and can also be deduced with a Bethe-Salpeter equation in the non-relativistic limit [117]. Assuming that q_0 is negligible (4.2.2), the matrix amplitude can be further simplified to

$$\mathcal{M}_{X\pi\to 2\pi}(P,p_3 \to k_1,k_2) \overset{\text{N.R.}}{\simeq} \frac{\sqrt{2M_X}}{2m_\pi}\int \frac{d^3q}{(2\pi)^3}\tilde{\psi}_{X,z}(\vec{q})\,\mathcal{M}_{\text{WZW}}(P/2+q, P/2-q, p_3 \to k_1, k_2) \tag{4.2.16}$$

$$= \frac{\sqrt{M_X}N_c}{4\pi^2 m_\pi f_\pi^5}\varepsilon^{abc}P_b\,k_{1,c}\int \frac{d^3q}{(2\pi)^3}\tilde{\psi}_{X,z}(\vec{q})q_a \tag{4.2.17}$$

$$= \frac{\sqrt{M_X}N_c}{4\pi^2 m_\pi f_\pi^5}P_b\,k_{1,c}\,\varepsilon^{abc}\int d^3r\psi_{X,z}(\vec{r})\int \frac{d^3q}{(2\pi)^3}e^{-i\vec{q}\cdot\vec{r}}q_a. \tag{4.2.18}$$

One can split the wave function into a radial and angular part,

$$\psi_{X,z}(\vec{r}) = R_{nl}(r)Y_{lm}(\theta,\phi), \tag{4.2.19}$$

[3] In general, X and π have flavour indices and the matrix element is written for one specific flavour combination, $\mathcal{M}_{X_{ij}\pi_k\to\pi_l\pi_n}(P,p_3 \to k_1,k_2)$.

where n, l, m are quantum numbers and Y_{lm} are spherical harmonics normalized as $\int d\Omega Y^{\star}_{lm} Y_{l'm'} = \delta_{ll'}\delta_{mm'}$. Then, the integral in Eq. (4.2.16) yields

$$
\begin{aligned}
&\varepsilon^{abc}\int d^3r\psi_{X,z}\left(\vec{r}\right)\int \frac{d^3q}{(2\pi)^3}e^{-i\vec{q}\cdot\vec{r}}q_a = -i\varepsilon^{abc}\int d^3r\psi_{X,z}\left(\vec{r}\right)\frac{\partial\delta^{(3)}(\vec{r}\,)}{\partial r^a}\\
&= i\varepsilon^{abc}\int d^3r\frac{\partial\psi_{X,z}\left(\vec{r}\right)}{\partial r^a}\delta^{(3)}(\vec{r}\,) = \frac{i}{4\pi}\varepsilon^{abc}\int d\theta d\phi\sin\theta\left.\frac{\partial\psi_{X,z}(r,\theta,\phi)}{\partial r^a}\right|_{r=0}\\
&= \frac{i}{4\pi}\left\{\left.\frac{\partial R_{nl}(r)}{\partial r}\right|_{r=0}\int d\theta d\phi\sin\theta Y_{l,m}(\theta,\phi)\left(\varepsilon^{1bc}\sin\theta\cos\phi+\varepsilon^{2bc}\sin\theta\sin\phi+\varepsilon^{3bc}\cos\theta\right)\right.\\
&\qquad+\left.\frac{R_{nl}(r)}{r}\right|_{r=0}\int d\theta d\phi\sin\theta\frac{\partial Y_{l,m}(\theta,\phi)}{\partial\theta}\left(\varepsilon^{1bc}\cos\theta\cos\phi+\varepsilon^{2bc}\cos\theta\sin\phi-\varepsilon^{3bc}\sin\theta\right)\\
&\qquad\left.+\left.\frac{R_{nl}(r)}{r}\right|_{r=0}\int d\theta d\phi\frac{\partial Y_{l,m}(\theta,\phi)}{\partial\phi}\left(-\varepsilon^{1bc}\sin\phi+\varepsilon^{2bc}\cos\phi\right)\right\},
\end{aligned}
\tag{4.2.20}
$$

where we rewrite the delta function in spherical coordinates, $\delta^{(3)}(\vec{r}\,) = \frac{\delta(r)}{4\pi r^2}$ and evaluate the integral at $r = 0$. Here, the coordinate r^a is in the Cartesian coordinate system, but was changed to spherical coordinates in the fifth equality. Additionally, we used the relation

$$
\int\frac{d^3q}{(2\pi)^3}e^{-i\vec{q}\cdot\vec{r}}q_a = \int\frac{d^3q}{(2\pi)^3}e^{iq^kr_k}q_a = -i\frac{\partial\delta^{(3)}(\vec{r}\,)}{\partial r^a}. \tag{4.2.21}
$$

Since $-r\frac{\partial\delta(r)}{\partial r} = \delta(r)$ the radial function can be written as

$$
\left.\frac{\partial R_{nl}(r)}{\partial r}\right|_{r=0} = \left.\frac{R_{nl}(r)}{r}\right|_{r=0}. \tag{4.2.22}
$$

Then, the matrix amplitude for $l = 1$ and $m = -1, 0, 1$ is given by

$$
\begin{aligned}
&\mathcal{M}^m_{X\pi\to 2\pi}(P, p_3 \to k_1, k_2)\\
&\overset{\text{N.R.}}{\simeq} -i\frac{\sqrt{3M_X}N_c}{8\sqrt{2\pi^5}m_\pi f_\pi^5}\left.\frac{\partial R_{n1}(r)}{\partial r}\right|_{r=0}P_b\,k_{1,c}\times\begin{cases}\varepsilon^{1bc}-i\varepsilon^{2bc} & m=-1\\ \varepsilon^{3bc}\sqrt{2} & m=0\\ -\varepsilon^{1bc}-i\varepsilon^{2bc} & m=1\end{cases}.
\end{aligned}
\tag{4.2.23}
$$

The matrix element vanishes for $l = 0$ and hence, the transition $X\pi \to 2\pi$ is only possible for p-wave bound states as the lowest angular momentum state. In App. E we show an alternative way to derive the matrix element $\mathcal{M}_{X\pi\to 2\pi}$. The integrated squared matrix element in the center of mass frame[4] yields,

$$\sum_m \int d\Omega |M^m_{X\pi\to 2\pi}|^2 \overset{\text{N.R.}}{\simeq} \frac{M_X N_c^2}{8\pi^4 m_\pi^2 f_\pi^{10}} \left(\frac{\partial R_{n1}(r)}{\partial r}\bigg|_{r=0} \right)^2 s|\vec{k}_1|^2|\vec{P}|^2 \tag{4.2.24}$$

where we summed over m. We choose $P^\mu = \left(\sqrt{|\vec{P}|^2 + M_X^2}, 0, 0, |\vec{P}|\right)$ in z-direction with $|\vec{P}|^2 = \frac{1}{4s}\lambda(s, m_\pi^2, M_X^2)$ and $\vec{k}_1 = |\vec{k}_1|(\sin\theta\cos\phi, \sin\theta\sin\phi, \cos\theta)$ with $|\vec{k}_1|^2 = \frac{1}{4s}\lambda(s, m_\pi^2, m_\pi^2)$. In the case of $m = 0$ the squared matrix amplitude after angular integration is zero, provided $\vec{P}$ is taken in the z-direction. Only $m = -1, 1$ contribute to the interaction.

The cross section for one flavor combination $X_{ij}\pi_k \to \pi_l\pi_n$ for $l = 1$ is then given by

$$(\sigma v)_{(ij)k\to ln} = \frac{|\vec{k}_1|}{64\pi^2 E_P E_{p_3}\sqrt{s}} \sum_m \int d\Omega |M^m_{X\pi\to 2\pi}|^2 \tag{4.2.25}$$

$$= \frac{M_X N_c^2}{128\pi^6 f_\pi^{10} m_\pi^2} \left(\frac{\partial R_{n1}(r)}{\partial r}\bigg|_{r=0} \right)^2 \frac{s^{3/2}|\vec{k}_1|^3|\vec{P}|^2}{(s + M_X^2 - m_\pi^2)(s - M_X^2 + m_\pi^2)} \tag{4.2.26}$$

$$\overset{\text{N.R.}}{\simeq} \frac{M_X^2 N_c^2}{4096\pi^6 m_\pi f_\pi^{10}} \left(\frac{\partial R_{n1}(r)}{\partial r}\bigg|_{r=0} \right)^2 \frac{(M_X - m_\pi)^{3/2}(M_X + 3m_\pi)^{3/2}}{(M_X + m_\pi)} v_r^2, \tag{4.2.27}$$

or

$$\sigma_{(ij)k\to ln} = \frac{1}{64\pi^2 s}\frac{|\vec{k}_1|}{|\vec{P}|} \sum_m \int d\Omega |M^m_{X\pi\to 2\pi}|^2 = \frac{M_X N_c^2}{512\pi^6 f_\pi^{10} m_\pi^2} \left(\frac{\partial R_{n1}(r)}{\partial r}\bigg|_{r=0} \right)^2 |\vec{k}_1|^3|\vec{P}| \tag{4.2.28}$$

$$\overset{\text{N.R.}}{\simeq} \frac{M_X^2 N_c^2}{4096\pi^6 m_\pi f_\pi^{10}} \left(\frac{\partial R_{n1}(r)}{\partial r}\bigg|_{r=0} \right)^2 \frac{(M_X - m_\pi)^{3/2}(M_X + 3m_\pi)^{3/2}}{(M_X + m_\pi)} v_r, \tag{4.2.29}$$

where the indices in the brackets denote flavour indices of the bound state, v_r is the relative velocity $v_r = |\vec{v}_P - \vec{v}_{p_3}|$ between initial states and

$$E_P = \frac{1}{2\sqrt{s}}(s + M_X^2 - m_\pi^2), \tag{4.2.30}$$

$$E_{p_3} = \frac{1}{2\sqrt{s}}(s + m_\pi^2 - M_X^2), \tag{4.2.31}$$

$$s \simeq (M_X + m_\pi)^2 + M_X m_\pi v_r^2. \tag{4.2.32}$$

According to Refs. [43, 119], the thermally averaged cross section for one event $(ij)k \to ln$ is given by (see App. F.2 for detail calculation)

$$\langle\sigma v\rangle_{(ij)k\to ln} = \frac{\int_{(M_X+m_\pi)^2}^\infty ds\,\sigma_{(ij)k\to ln}\sqrt{s}|\vec{P}|^2 K_1\left(\frac{\sqrt{s}}{T}\right)}{2M_X^2 m_\pi^2 T K_2(M_X/T)K_2(m_\pi/T)}. \tag{4.2.33}$$

[4]The center of mass frame is given by $\vec{P} + \vec{p}_3 = 0 = \vec{k}_1 + \vec{k}_2$.

The integral above can be solved numerically or analytically in the non-relativistic regime. The thermally averaged cross section in the non-relativistic regime can then be written as an integral over the relative velocity v_r [120],

$$\langle \sigma v \rangle_{(ij)k\to ln} \overset{\text{N.R.}}{\simeq} \int_0^\infty dv_r\, v_r^2 F(v_r)\,(\sigma v_r)_{(ij)k\to ln} \tag{4.2.34}$$

where

$$F(v_r) = \sqrt{\frac{2}{\pi}}\left(\frac{\mu_{X\pi}}{T}\right)^{3/2} v_r^2 e^{-\mu_{X\pi}\frac{v_r^2}{2T}}, \tag{4.2.35}$$

$$\mu_{X\pi} = \frac{M_X m_\pi}{M_X + m_\pi}. \tag{4.2.36}$$

If we expand (σv_r) in powers of v_r, one obtains

$$\langle \sigma v \rangle_{(ij)k\to ln} \overset{\text{N.R.}}{\simeq} \frac{3N_c^2 M_X (M_X - m_\pi)^{3/2}(M_X + 3m_\pi)^{3/2}}{4096\pi^6 f_\pi^{10} m_\pi^2}\left(\left.\frac{\partial R_{n1}(r)}{\partial r}\right|_{r=0}\right)^2 T \tag{4.2.37}$$

Then, the thermally averaged cross section for $X\pi \to 2\pi$ is expressed as

$$\begin{aligned}
\langle \sigma v \rangle_{X\pi\to 2\pi} &= \frac{1}{10}\frac{1}{5}\frac{1}{2!}\sum_{(ij)knl}\langle \sigma v \rangle_{(ij)k\to ln} = \frac{1}{10}\frac{1}{5}\frac{1}{2!}\frac{1}{2}\sum_{ijknl}\langle \sigma v \rangle_{(ij)k\to ln} \\
&= \frac{1}{10}\frac{1}{5}\frac{1}{2!}\frac{1}{2}5!\langle \sigma v \rangle_{(12)3\to 45} = \frac{3}{5}\langle \sigma v \rangle_{(12)3\to 45} \\
&\overset{\text{N.R.}}{\simeq} \frac{9N_c^2 M_X (M_X - m_\pi)^{3/2}(M_X + 3m_\pi)^{3/2}}{20480\pi^6 m_\pi^2 f_\pi^{10}}\left(\left.\frac{\partial R_{n1}(r)}{\partial r}\right|_{r=0}\right)^2 T \\
&\overset{E_B \ll m_\pi}{\simeq} \frac{9\sqrt{5}N_c^2 m_\pi^2}{2048\pi^6 f_\pi^{10}}\left(\left.\frac{\partial R_{n1}(r)}{\partial r}\right|_{r=0}\right)^2 T,
\end{aligned} \tag{4.2.38}$$

where we averaged over 10 different X, 5 different π and a factor $1/2!$ is added in order to avoid double counting of the same event[5]. Since $(\sigma v)_{X\pi\to 2\pi}$ has a v^2-dependence, $\langle \sigma v \rangle_{X\pi\to 2\pi}$ scales with T in the non-relativistic regime. Moreover, the reaction $X\pi \to 2\pi$ is more efficient than $3\pi \to 2\pi$ and decouples later,

$$\frac{\Gamma_{X\pi\to 2\pi}}{\Gamma_{3\pi\to 2\pi}} = \frac{n_X \langle \sigma v \rangle_{X\pi\to 2\pi}}{n_\pi^2 \langle \sigma v^2 \rangle_{3\pi\to 2\pi}} \simeq \alpha_S^5 x_F^{5/2} e^{\frac{E_B}{m_\pi}x_F} \gg 1, \tag{4.2.39}$$

where we estimate $\left.\frac{\partial R_{n1}(r)}{\partial r}\right|_{r=0} \simeq (1/a_B)^{5/2}$ with the Bohr radius $a_B \simeq 1/(\alpha_s m_\pi)$ related to dark strong interactions with an effective coupling $\alpha_s \sim O(1)$.

[5] Like the WZW interaction, also $X\pi \to 2\pi$ has only off-diagonal flavour combinations

4.3 Higher order interactions with SIMP bound states

4.3.1 The 6-point interaction

We consider the extension of the chiral Lagrangian up to order π^6 for a gauge group $Sp(4)_c$ discussed in Ref. [103] or Sec. 3. The additional interaction is part of the bound state formation reaction $3\pi \ \to \pi X$. The Lagrangian is given by adding one more order to the chiral field $\Sigma = e^{2i\pi/f_\pi} E$,

$$\mathcal{L} = \frac{f_\pi^2}{4} \mathrm{Tr}\left[\partial_\mu \Sigma \partial^\mu \Sigma^\dagger\right] - \frac{\mu^3}{2}\left(\mathrm{Tr}\left[M\Sigma\right] + \mathrm{Tr}\left[\Sigma^\dagger M^\dagger\right]\right) \tag{4.3.1}$$

$$= \mathrm{Tr}\left[\partial_\mu \pi \partial^\mu \pi\right] - \frac{2}{3f_\pi^2}\mathrm{Tr}\left[\pi^2 \partial^\mu \pi \partial_\mu \pi - \pi \partial^\mu \pi \pi \partial_\mu \pi\right] - m_\pi^2 \mathrm{Tr}\left[\pi^2\right] + \frac{m_\pi^2}{3f_\pi^2}\mathrm{Tr}\left[\pi^4\right] + \mathcal{L}_{\mathrm{WZW}} \tag{4.3.2}$$

$$+ \frac{4}{45 f_\pi^4}\mathrm{Tr}\left[\pi^2\left(\pi^2 \partial^\mu \pi \partial_\mu \pi - \pi \partial^\mu \pi \pi \partial_\mu \pi\right)\right] - \frac{2m_\pi^2}{45 f_\pi^4}\mathrm{Tr}\left[\pi^6\right] + \mathcal{O}\left(\frac{\pi^7}{f_\pi^5}\right) \tag{4.3.3}$$

$$= \frac{1}{2}\sum_{n=1}^{5} \partial_\mu \pi_n \partial^\mu \pi_n - \frac{1}{12 f_\pi^2}\sum_{k,n=1}^{5}\left(\pi_k \pi_k \partial_\mu \pi_n \partial^\mu \pi_n - \pi_k \partial_\mu \pi_k \pi_n \partial^\mu \pi_n\right) \tag{4.3.4}$$

$$- \frac{m_\pi^2}{2}\sum_{k=1}^{5}\pi_k^2 + \frac{m_\pi^2}{48 f_\pi^2}\left(\sum_{k=1}^{5}\pi_k^2\right)^2 + \mathcal{L}_{\mathrm{WZW}} \tag{4.3.5}$$

$$+ \frac{1}{180 f_\pi^4}\sum_{j,k,n=1}^{5}\pi_j^2\left(\pi_k \pi_k \partial_\mu \pi_n \partial^\mu \pi_n - \pi_k \partial_\mu \pi_k \pi_n \partial^\mu \pi_n\right) + \frac{m_\pi^2}{2880 f_\pi^4}\left(\sum_{k=1}^{5}\pi_k^2\right)^3 + \mathcal{O}\left(\frac{\pi^7}{f_\pi^5}\right). \tag{4.3.6}$$

There is no 6-point interaction arising from the WZW action.

4.3.2 The cross section for $3\pi \to \pi X$

The relevant diagrams for the process $3\pi \to \pi X$ are given in Fig. 4.2. The last two Feynman diagrams are enhanced by the propagator when $M_X \simeq 2m_\pi$. For this reason, the contribution of the first two diagrams is negligible in the calculation for the process $3\pi \to \pi X$.

The general matrix amplitude for a four-point interaction between SIMPs is given by the Lagrangian (4.3.1),

$$\begin{aligned} M_{ab\to cd}(p_1, p_2 \to k_1, k_2) = \frac{1}{6f_\pi^2}\Big[&\delta^{ab}\delta^{cd}\left(2(p_1.p_2 + k_1.k_2) + (k_1+k_2).(p_1+p_2) + m_\pi^2\right) \\ &+ \delta^{ac}\delta^{bd}\left(-2(p_1.k_1 + p_2.k_2) - (p_2-k_2).(p_1-k_1) + m_\pi^2\right) \\ &+\delta^{ad}\delta^{cb}\left(-2(p_1.k_2 + p_2.k_1) - (p_2-k_1).(p_1-k_2) + m_\pi^2\right)\Big] \end{aligned} \tag{4.3.7}$$

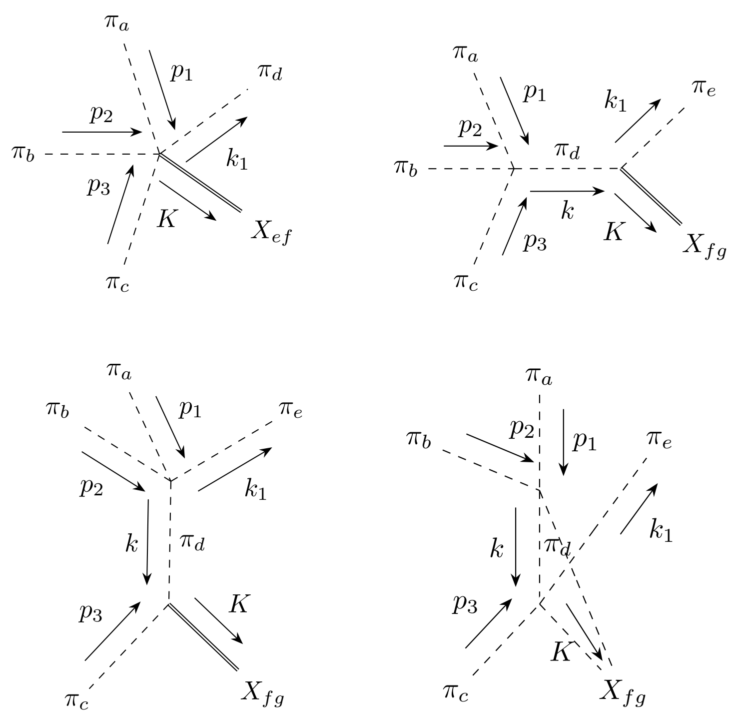

Figure 4.2: The $3\pi \to \pi X$ process, contact interaction, s-channel, t-channel, u-channel (from left to right). In each vertex, flavour indices come in pairs. The momenta p_i and k_i are ingoing and outgoing momenta, respectively. The bound state momentum is K.

where $p_1 + p_2 = k_1 + k_2$ and p_1, p_2, k_1, k_2 can be on- or off-shell. The t-channel in Fig. 4.2 has two vertices. The upper vertex is given by

$$\begin{aligned} V^t_{ab\to ed}(p_1, p_2 \to k_1, k) = \frac{1}{6f_\pi^2} \Big[& \delta^{ab}\delta^{ed} \left(4(p_1.p_2) + 2k_1.(p_1+p_2) + m_\pi^2\right) \\ & + \delta^{ae}\delta^{bd} \left(-4(p_1.k_1) - 2p_2.(p_1 - k_1) + m_\pi^2\right) \\ & + \delta^{ad}\delta^{eb} \left(-4(p_2.k_1) - 2p_1.(p_2 - k_1) + m_\pi^2\right) \Big] \end{aligned} \tag{4.3.8}$$

where $k = p_1 + p_2 - k_1$ is the momentum of the mediator and p_1, p_2, k_1 are on-shell. The lower vertex includes the bound state X with momentum K. In this case, we have to integrate over the relative momentum q of constituents,

$$V^t_{dc\to(fg)}(k, p_3 \to K) \overset{\text{N.R.}}{\simeq} \frac{S\sqrt{2M_X}}{2m_\pi} \int \frac{d^3q}{(2\pi)^3} \tilde{\psi}^\star_{X,z}(\vec{q})\, V^t_{dc\to fg}(k, p_3 \to K/2 + q, K/2 - q), \tag{4.3.9}$$

where we remind the reader, that $S = 1$ $\left(S = 1/\sqrt{2}\right)$ is the symmetry factor for non-identical (identical) constituents of the bound state and $\psi_{X,z}$ is the Schrödinger wave function. The flavour indices in the brackets denote the flavour combination of the bound state. The four-point interaction in the integral yields

$$V^t_{dc\to fg}(k,p_3\to q+K/2,K/2-q)=\frac{1}{12f_\pi^2}\Big[\delta^{dc}\delta^{fg}\left(3M_X^2-2m_\pi^2+4(K.p_3)-4(q.q)\right)$$
$$+\,\delta^{df}\delta^{cg}\frac{\left(-3M_X^2+8m_\pi^2-4(K.p_3)+12q.(2p_3-K)+4(q.q)\right)}{2}$$
$$+\delta^{dg}\delta^{cf}\frac{\left(-3M_X^2+8m_\pi^2-4(K.p_3)-12q.(2p_3-K)+4(q.q)\right)}{2}\Big],\tag{4.3.10}$$

where the momenta $k=K-p_3$, q are off-shell and K,p_3 are on-shell. Then, the integral in Eq. (4.3.9) can be solved,

$$V^t_{dc\to(fg)}(k,p_3\to K)\overset{\text{N.R.}}{\simeq}\frac{S\sqrt{2M_X}}{48\sqrt{\pi}m_\pi f_\pi^2}R_{n0}(0)\Big[\delta^{dc}\delta^{fg}\left(3M_X^2-2m_\pi^2+4(K.p_3)\right)+4E_Bm_\pi$$
$$+\delta^{df}\delta^{cg}\frac{\left(-3M_X^2+8m_\pi^2-4(K.p_3)-4E_Bm_\pi\right)}{2}+\delta^{dg}\delta^{cf}\frac{\left(-3M_X^2+8m_\pi^2-4(K.p_3)-4E_Bm_\pi\right)}{2}\Big]$$
$$-\,i\frac{S\sqrt{3M_X}}{8\sqrt{\pi}m_\pi f_\pi^2}\left.\frac{\partial R_{n1}(r)}{\partial r}\right|_{r=0}\left(\delta^{df}\delta^{cg}-\delta^{dg}\delta^{cf}\right)\times\begin{cases}(2p_3-K)^1+i(2p_3-K)^2 & m=-1\\ (2p_3-K)^3\sqrt{2} & m=0\\ -(2p_3-K)^1+i(2p_3-K)^2 & m=1\end{cases}.\tag{4.3.11}$$

In the following calculations, terms containing q are related to excited bound states. Terms proportional to q lead to $l=1$ states. Terms proportional to $(q.q)$ seem to be divergent at $\vec{r}=0$, but according to Refs. [121, 122] these terms are finite and proportional to E_B,

$$\int\frac{d^3q}{(2\pi)^3}\tilde{\psi}^\star_{X,z}(\vec{q})\,(q.q)\overset{|q^0|\ll|\vec{q}|}{\simeq}-\int\frac{d^3q}{(2\pi)^3}\tilde{\psi}^\star_{X,z}(\vec{q})\,|\vec{q}|^2=\int d^3r\frac{\partial}{\partial r^j}\frac{\partial}{\partial r^j}\psi^\star_{X,z}(\vec{r})\delta^{(3)}(\vec{r})$$
$$=\frac{1}{4\pi}\int d\phi d\theta\sin\theta\left\{\left(\left.\frac{\partial^2R(r)}{\partial r^2}\right|_{r=0}+\frac{2}{r}\left.\frac{\partial R_{nl}(r)}{\partial r}\right|_{r=0}\right)Y^\star_{lm}(\theta,\phi)\right.$$
$$\left.+\left.\frac{R_{nl}(r)}{r^2}\right|_{r=0}\left(\frac{\partial^2Y^\star_{lm}(\theta,\phi)}{\partial\theta^2}+\frac{1}{\sin^2\theta}\frac{\partial^2Y^\star_{lm}(\theta,\phi)}{\partial\phi^2}+\frac{1}{\tan\theta}\frac{\partial Y^\star_{lm}(\theta,\phi)}{\partial\theta}\right)\right\}$$
$$=\frac{1}{4\pi}\nabla^2R_{nl}(0)\int d\phi d\theta\sin\theta Y^\star_{lm}(\theta,\phi)$$
$$\overset{l=0}{\equiv}-\frac{m_\pi E_B}{2\sqrt{\pi}}R_{n0}(0),\tag{4.3.12}$$

where we used $\delta^3(\vec{r})=\frac{\delta(r)}{4\pi r^2}$. The above expression vanishes for $l=1$ states. In the first equality, we used instantaneous approximation (4.2.2). In the third line, the integral vanishes.

In the fourth line, we used $\nabla^2 R_{nl}(0) = -m_\pi E_B R_{nl}(0)$ from Refs. [121, 122] and assumed a real radial wave function $R_{nl}(0) \neq 0$. Hence, $(q.q)$ terms can be neglected in the following calculations, since we consider $E_B \ll m_\pi$. Whereas in the reaction $X\pi \to 2\pi$ p-waves are preferred, s-waves ($l = 0$) are also present in $3\pi \to \pi X$. In the end, the total matrix element is expressed as

$$\begin{aligned}M^t_{abc\to e(fg)}(p_1, p_2, p_3 \to k_1, K) &\overset{\text{N.R.}}{\simeq} V^t_{ab\to ed}(p_1, p_2 \to k_1, k)\frac{1}{k^2 - m_\pi^2} V^t_{dc\to(fg)}(k, p_3 \to K)\\ &\overset{\text{N.R.}}{\simeq} \frac{3}{2(M_X^2 - 4m_\pi^2)} V^t_{ab\to ed}(p_1, p_2 \to k_1, k) V^t_{dc\to(fg)}(k, p_3 \to K),\end{aligned} \tag{4.3.13}$$

where the propagator is approximated in the non-relativistic limit as

$$\frac{1}{k^2 - m_\pi^2} = \frac{1}{(p_3 - K)^2 - m_\pi^2} \overset{\text{N.R.}}{\simeq} \frac{1}{M_X^2 - 2m_\pi E_K} \simeq \frac{3}{2(M_X^2 - 4m_\pi^2)} \tag{4.3.14}$$

using $\sqrt{s_{45}} = E_{p_1} + E_{p_2} + E_{p_3} \simeq 3m_\pi$ and $E_K = \frac{1}{2\sqrt{s_{45}}}\left(s_{45} + M_X^2 - m_\pi^2\right)$ in the center of mass frame.

The last Feynman diagram in Fig. 4.2 is derived in a similar way and leads to

$$\begin{aligned}&M^u_{abc\to e(fg)}(p_1, p_2, p_3 \to k_1, K)\\ &\overset{\text{N.R.}}{\simeq} \frac{S\sqrt{2M_X}}{2m_\pi}\int \frac{d^3q}{(2\pi)^3}\tilde{\psi}^\star(\vec{q})_{X,z} V^u_{ab\to df}(p_1, p_2 \to K/2 + q, k)\frac{1}{k^2 - m_\pi^2} V^u_{cd\to eg}(p_3, k \to k_1, K/2 - q)\\ &\simeq -\frac{6S\sqrt{2M_X}}{m_\pi(M_X^2 - 4m_\pi^2)}\int \frac{d^3q}{(2\pi)^3}\tilde{\psi}^\star(\vec{q})_{X,z} V^u_{ab\to df}(p_1, p_2 \to K/2 + q, k) V^u_{cd\to eg}(p_3, k \to k_1, K/2 - q)\end{aligned} \tag{4.3.15}$$

where the propagator is again approximated for non-relativistic particles as

$$\frac{1}{k^2 - m_\pi^2} \simeq -\frac{12}{(M_X^2 - 4m_\pi^2)}. \tag{4.3.16}$$

The upper and lower vertices are given by

$$\begin{aligned}&V^u_{ab\to df}(p_1, p_2 \to K/2 + q, k)\\ &\quad = \frac{1}{6f_\pi^2}\Bigg[\delta^{ab}\delta^{df}\left(-\frac{M_X^2}{2} + 3m_\pi^2 + 4(p_1.p_2) + K.(p_1 + p_2) + 2q.(p_1 + p_2 - K) - 2(q.q)\right)\\ &\qquad + \delta^{ad}\delta^{bf}\left(\frac{M_X^2}{4} - 2(p_1.p_2) + K.(p_2 - 2p_1) + q.(K - 4p_1 + 2p_2) + (q.q)\right)\\ &\qquad + \delta^{af}\delta^{bd}\left(\frac{M_X^2}{4} - 2(p_1.p_2) + K.(p_1 - 2p_2) + q.(K + 2p_1 - 4p_2) + (q.q)\right)\Bigg],\end{aligned} \tag{4.3.17}$$

$$
\begin{aligned}
&V^{u}_{cd\to eg}(p_3, k \to k_1, K/2-q)\\
&\quad = \frac{1}{6f_\pi^2}\left[\delta^{dc}\delta^{eg}\left(\frac{M_X^2}{4} + 2k_1.(p_3+K) + (K.p_3) - q.(K+2p_3+4k_1) + (q.q)\right)\right.\\
&\qquad + \delta^{de}\delta^{cg}\left(-\frac{M_X^2}{2} + 3m_\pi^2 - 4(k_1.p_3) + K.(p_3-k_1) + 2q.(K-p_3+k_1) - 2(q.q)\right)\\
&\qquad \left. +\delta^{dg}\delta^{ce}\left(\frac{M_X^2}{4} - 2(p_3.K) + k_1.(2p_3-K) - q.(K-4p_3-2k_1) + (q.q)\right)\right].
\end{aligned}
\tag{4.3.18}
$$

The $3 \to 2$ cross section for the process $\pi_a\pi_b\pi_c \to \pi_e X_{fg}$ is given by (see App. F.3 for more details)

$$
\begin{aligned}
\left(\sigma v^2\right)_{abc\to e(fg)} &= \frac{|\vec{k}_1|}{128\pi^2 E_{p_1}E_{p_2}E_{p_3}s_{45}}\int d\Omega\, |\mathcal{M}_{abe\to c(fg)}|^2\\
&\overset{\text{N.R.}}{\simeq} \frac{\sqrt{M_X^4 - 20M_X^2 m_\pi^2 + 64 m_\pi^4}}{2304\pi^2 m_\pi^5}\int d\Omega\, |\mathcal{M}_{abe\to c(fg)}|^2,
\end{aligned}
\tag{4.3.19}
$$

where the matrix element can depend on angles[6]. In the following, we show exemplary the cross section for one off-diagonal ($\pi_3\pi_1\pi_2 \to \pi_3 X_{12}$) and one diagonal flavour combination $\pi_1\pi_1\pi_1 \to \pi_1 X_{11}$ for $l = 0$ bound states. All other combinations are derived in a similar way. The matrix element for the process $\pi_3\pi_1\pi_2 \to \pi_3 X_{12}$ is a sum of amplitudes of possible flavour combinations. Since in the vertices (see Fig. 4.2), π interacts in flavor pairs, interchanging the initial states π_1 and π_2, requires a change in the mediator from π_1 to π_2. In addition, two diagrams have a π_3 as a mediator. In total, we have six diagrams to add up. Then, the cross section is temperature-independent in the non-relativistic regime,

$$
(\sigma v^2)_{312->3(12)} \overset{\text{N.R.}}{\simeq} \frac{M_X R_{n0}(0)^2(3128 m_\pi^4 + 11M_X^4 - 421 m_\pi^2 M_X^2)^2}{8^6\, 9^3\pi^2 f_\pi^8 (M_X^2-4m_\pi^2)^2}\frac{\sqrt{(8m_\pi^2 - M_X^2)^2 - 4M_X^2 m_\pi^2}}{m_\pi^7}
\tag{4.3.20}
$$

$$
\simeq 1.2\times 10^{-2}\frac{R_{n0}(0)^2}{\pi^2 f_\pi^8}\left(\frac{m_\pi}{E_B}\right)^{3/2},
\tag{4.3.21}
$$

where in the second equality we expanded for $E_B \ll m_\pi$. As already discussed, the contact interaction and s-channel in Fig. 4.2 are suppressed compared to the t, u-channels. In this case, there is no s-channel for $312- > 3(12)$ with π as a mediator[7]. The enhancement is noticeable in the nominator for bound states masses close to mass $2m_\pi$ of two unbound particles. Since (σv^2) is independent of initial state momenta, $(\sigma v^2) = \langle\sigma v^2\rangle$ (up to double-counting factors).

[6]For $l = 1$ states we have to sum over magnetic quantum number m, $\sum_m |\mathcal{M}^m_{abe\to c(fg)}|^2$.

[7]There is a s-channel diagram with X as a mediator, but this interaction is realized through two Wess-Zumino-Witten interactions and is sub-leading.

Similarly, we obtain the cross section for $\pi_1\pi_1\pi_1 \to \pi_1 X_{11}$. In this case, the matrix element is given by $M_{111\to 1(11)} \simeq M^t_{111\to 1(11)} + M^u_{111\to 1(11)}$. The cross section is again temperature independent, as expected,

$$(\sigma v^2)_{111->1(11)} \overset{\text{N.R.}}{\simeq} \frac{49 m_\pi M_X R_{n0}(0)^2 \sqrt{(8m_\pi^2 - M_X^2)^2 - 4M_X^2 m_\pi^2}}{131072\pi^2 f_\pi^8 (M_X^2 - 4m_\pi^2)^2} \tag{4.3.22}$$

$$\simeq 3.3 \times 10^{-4} \frac{R_{n0}(0)^2}{\pi^2 f_\pi^8} \left(\frac{m_\pi}{E_B}\right)^{3/2} . \tag{4.3.23}$$

An enhancement of the cross section is again given for $M_X \sim 2m_\pi$. Since $\left\langle \sigma v^2 \right\rangle_{3\pi\to\pi X}$ is temperature independent and $\left\langle \sigma v^2 \right\rangle_{3\pi\to 2\pi}$ scales with T^2, the ratio $\left\langle \sigma v^2 \right\rangle_{3\pi\to\pi X} / \left\langle \sigma v^2 \right\rangle_{3\pi\to 2\pi}$ scales with $1/T^2$. For one flavor combination and $E_B \ll m_\pi$ we obtain

$$\frac{\langle \sigma v^2 \rangle_{312\to 3(12)}}{\langle \sigma v^2 \rangle_{3\pi\to 2\pi}} \overset{\text{N.R.}}{\simeq} \alpha_S^2 \frac{\pi^3 x_F^2 f_\pi^2}{(m_\pi E_B)^{3/2}} \gg 1, \tag{4.3.24}$$

where we again estimate $R_{n0}(0)^2 \simeq 1/a_B^2$ with Bohr radius $a_B \simeq 1/(\alpha_S m_\pi)$ and strong coupling $\alpha_S \sim O(1)$. Hence, $3\pi \to \pi X$ can be more efficient than $3\pi \to 2\pi$. In addition, the ratio $\langle \sigma v^2 \rangle_{3\pi\to\pi X} / \langle \sigma v \rangle_{\pi X\to 2\pi}$ scales with $1/T$.

4.4 A naive estimation of relic abundances

In Fig. 4.3 we show exemplary the relic abundances of π and X for $m_\pi = 100$ MeV and $E_B/m_\pi = 0.1$. For simplicity, we parameterize the thermally averaged cross sections entering the Boltzmann equations (4.1.5), (4.1.6) as follows:

$$\langle \sigma v^2 \rangle_{3\pi\to 2\pi} := \frac{a}{x^2}, \qquad \langle \sigma v \rangle_{X\pi\to 2\pi} := \frac{b}{x}, \tag{4.4.1}$$

$$\langle \sigma v^2 \rangle_{3\pi\to \pi X} := c \left(\frac{m_\pi}{E_B}\right)^{3/2}, \qquad \langle \sigma v \rangle_{2X\to 2\pi} := d, \tag{4.4.2}$$

where $x = m_\pi/T$ and a, b, c, d are functions of masses m_π, M_X and decay constant f_π in general. As already discussed, $l = 0$ bound states are not present in $X\pi \to 2\pi$. For our purposes of a first simplified analysis, we do not distinguish between $l = 0$ and $l = 1$ states. For further discussion, we define the rates per particle π and X:

per π	per X
$\Gamma^\pi_{3\pi\to 2\pi} = n_\pi^2 \langle \sigma v^2 \rangle_{3\pi\to 2\pi}$	
$\Gamma^\pi_{X\pi\to 2\pi} = n_X \langle \sigma v \rangle_{X\pi\to 2\pi}$	$\Gamma^X_{X\pi\to 2\pi} = n_\pi \langle \sigma v \rangle_{X\pi\to 2\pi}$
$\Gamma^\pi_{3\pi\to \pi X} = n_\pi^2 \langle \sigma v^2 \rangle_{3\pi\to \pi X}$	$\Gamma^X_{3\pi\to \pi X} = \frac{n_\pi^3}{n_X} \langle \sigma v^2 \rangle_{3\pi\to \pi X}$
$\Gamma^\pi_{2X\to 2\pi} = \frac{n_X^2}{n_\pi} \langle \sigma v \rangle_{2X\to 2\pi}$	$\Gamma^X_{2X\to 2\pi} = n_X \langle \sigma v \rangle_{2X\to 2\pi}$

(4.4.3)

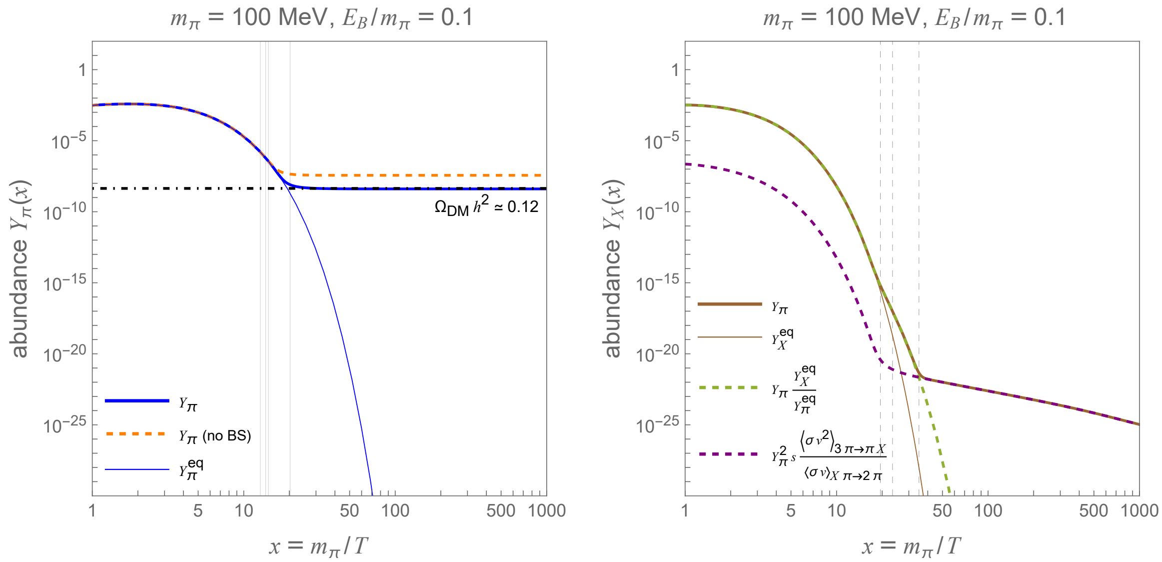

Figure 4.3: The relic abundances of SIMPs π (left) and bound states X (right) for $a = 10^7, b = 10^6, c = 10^5, d = 10^4$. The vertical lines correspond to $\Gamma \simeq H$ for each reaction from left to right: (left Fig.) $\Gamma^\pi_{3\pi\to2\pi} \simeq H, \Gamma^\pi_{2X\to2\pi} \simeq H, \Gamma^\pi_{3\pi\to\pi X} \simeq H, \Gamma^\pi_{X\pi\to2\pi} \simeq H$, (right Fig.) $\Gamma^X_{2X\to2\pi} \simeq H, \Gamma^X_{3\pi\to\pi X} \simeq H, \Gamma^X_{X\pi\to2\pi} \simeq H$.

In this framework, π do not decouple through $3\pi \to 2\pi$, but when the rate (per π) $\Gamma^\pi_{3\pi\to\pi X} \simeq H$. Since $3\pi \to \pi X$ decouples later, the particles π remain in equilibrium longer, reducing the dark matter relic abundance Y_π further (see Fig. 4.3). Increasing $\langle\sigma v^2\rangle_{3\pi\to\pi X}$ reduces the relic abundance, as expected. On the other hand, the relic abundance of bound states reduces quickly. At $x \sim 23$ the reaction rate $\Gamma^X_{3\pi\to\pi X}$ drops below the Hubble parameter, Y_X and Y_π change and reduce further, since $X\pi \to 2\pi$ is still efficient. The Boltzmann equation becomes

$$\frac{dY_\pi}{dx} \simeq -\frac{dY_X}{dx} \simeq \frac{xs}{H(m_\pi)}\left[\langle\sigma v\rangle_{\pi X\to2\pi}\left(Y_\pi Y_X - \frac{Y_\pi^2}{Y_\pi^{\rm eq}}Y_X^{\rm eq}\right) + 2\langle\sigma v\rangle_{2X\to2\pi}\left(Y_X^2 - \left(Y_X^{\rm eq}\right)^2\right)\right]. \tag{4.4.4}$$

If $\Gamma^X_{X\pi\to2\pi} > \Gamma^X_{2X\to2\pi}$, the second term on the right-hand side of Eq. (4.4.4) becomes negligible and the relic abundance of bound states follows a quasi-static equilibrium solution $Y_X \simeq Y_\pi Y_X^{\rm eq}/Y_\pi^{\rm eq}$ until $\Gamma^X_{X\pi\to2\pi} \simeq H$ (see Fig. 4.3). The abundance Y_X changes slightly between $x = 20$ and $x = 30$ when the reaction $2X \to 2\pi$ becomes relevant. As temperature decreases towards $\Gamma^X_{\pi X\to2\pi} \simeq H$, the reaction $2\pi \to \pi X$ is exponentially suppressed and the Boltzmann equation after $\Gamma^X_{\pi X\to2\pi} \simeq H$ effectively becomes[8]

$$\frac{dY_X}{dx} \simeq \frac{xs^2}{H(m_\pi)}\left[\langle\sigma_{3\pi\to\pi X}v^2\rangle Y_\pi^3 - \frac{1}{s}\langle\sigma_{\pi X\to2\pi}v\rangle Y_\pi Y_X\right]. \tag{4.4.5}$$

[8] As a reminder $3\pi \to \pi X$ already decoupled and $\pi X \to 3\pi$ is exponentially suppressed.

Then, the abundance of X follows the quasi-static equilibrium solution

$$Y_X \simeq Y_\pi^2 s \frac{\langle \sigma v^2 \rangle_{3\pi \to \pi X}}{\langle \sigma v \rangle_{\pi X \to 2\pi}}. \tag{4.4.6}$$

In summary, the strength of the reaction $3\pi \to \pi X$ regulates the freeze out of SIMPs π in the presence of bound states X.

4.5 Outlook

Since the project is still in progress, we will highlight some additional ideas and how we will proceed in the future.

First, after deriving $\langle \sigma v^2 \rangle_{abe->c(fg)}$ for all combination of flavours, we can sum over all flavours and obtain the thermally averaged cross section $\langle \sigma v^2 \rangle_{3\pi->\pi X}$, entering the Boltzmann equation. Second, once $\langle \sigma v \rangle_{2X \to 2\pi}$ is derived, the Boltzmann equations (4.1.5), (4.1.6) can be solved to determine the relic abundances of π and X precisely. This will provide some insight on the evolution of bound states in the early universe, e.g. finding the condition when bound states become relevant. Third, we can consider alternative models, like Yukawa-like theories or glueballs. Fourth, an additional $U(1)$ gauge boson V, that couples to π and X extends this project significantly. The Boltzmann equations need to be extended and the following processes become relevant in this scenario,

$$\pi X \to \pi V, \; 2\pi \to XV, \; 2\pi \to VV.$$

Bound states can now form by radiating a light vector boson or can also decay into SM particles. This opens the door to experimental exploration of dark bound states. Fifth, we can include (axial-) vector mesons and the isosinglet η' from Part II in this project. Since (axial-) vector mesons and η' interact with SIMPs, the SIMP mechanism as well as the SIMPonium mechanism change. Sixth, we can also consider mass non-degenerate SIMPs discussed in Part II. For instance, the isosinglet η' is present in the Wess-Zumino-Witten interaction with SIMPs.

APPENDIX D

Useful formulas for bound state interactions

In this appendix, we provide some useful formulas for the calculations in Chapter. 4.2. The Fourier transformation of the wave function is defined by

$$\tilde{\psi}_{X,z}(\vec{q}) = \int dr^3 \psi_{X,z}(\vec{r}) e^{-i\vec{q}\cdot\vec{r}}, \quad \tilde{\psi}^{\star}_{X,z}(\vec{q}) = \int dr^3 \psi^{\star}_{X,z}(\vec{r}) e^{i\vec{q}\cdot\vec{r}}. \tag{D.1.1}$$

In the following, we split the wave function into a radial and angular part $\Psi = R_{nl}(r)Y_{lm}(\theta,\phi)$ with quantum numbers n, $l < n$, $-l \leq m \leq l$ and used $\nabla^2 R_{nl}(0) = -m_\pi E_B R_{nl}(0)$ from Refs. [121, 122], assuming a real radial wave function $R_{nl}(0) \neq 0$. In addition, we chose $q^j = (q\sin\theta\cos\phi, q\sin\theta\sin\phi, q\cos\theta)^T$. Then, the following integrals can be expressed as

$$\int \frac{d^3q}{(2\pi)^3} \tilde{\psi}^{\star}_{X,z}(\vec{q}) = \int \frac{d^3q}{(2\pi)^3} \tilde{\psi}_{X,z}(\vec{q}) = \frac{1}{2\sqrt{\pi}} R_{n0}(0) \qquad l = m = 0, \tag{D.1.2}$$

$$\int \frac{d^3q}{(2\pi)^3} \tilde{\psi}_{X,z}(\vec{q})\; q^0 = \int \frac{d^3q}{(2\pi)^3} \tilde{\psi}^{\star}_{X,z}(\vec{q})\; q^0 \overset{\text{Eq.(4.2.2)}}{\simeq} \frac{1}{m_\pi} \int \frac{d^3q}{(2\pi)^3} \tilde{\psi}_{X,z}(\vec{q})\; |\vec{q}|^2 \tag{D.1.3}$$

$$= \frac{E_B}{2\sqrt{\pi}} R_{n0}(0) \qquad l = m = 0, \tag{D.1.4}$$

$$\int \frac{d^3q}{(2\pi)^3} \tilde{\psi}_{X,z}(\vec{q})\; q^2 = \int \frac{d^3q}{(2\pi)^3} \tilde{\psi}^{\star}_{X,z}(\vec{q})\; q^2 \overset{\text{Eq.(4.2.2)}}{\simeq} -\int \frac{d^3q}{(2\pi)^3} \tilde{\psi}_{X,z}(\vec{q})\; |\vec{q}|^2 \tag{D.1.5}$$

$$= -\frac{m_\pi E_B}{2\sqrt{\pi}} R_{n0}(0) \qquad l = m = 0, \tag{D.1.6}$$

$$A^j \int \frac{d^3q}{(2\pi)^3} \tilde{\psi}^{(\star)}_{X,z}(\vec{q})\; q_j = \underset{(-)}{+} \frac{i}{2}\sqrt{\frac{3}{2\pi}} \left.\frac{\partial R_{n1}(r)}{\partial r}\right|_{r=0} \times \begin{cases} A^1 \overset{(+)}{-} iA^2 & m = -1 \\ A^3\sqrt{2} & m = 0 \\ -A^1 \overset{(+)}{-} iA^2 & m = 1 \end{cases} \qquad l = 1, \tag{D.1.7}$$

APPENDIX E

An alternative derivation of the matrix element $\mathcal{M}_{X\pi\to 2\pi}$

Another way to calculate the result in Eq. (4.2.23), is to expand the plane wave into spherical harmonics,

$$e^{-i\vec{q}\cdot\vec{r}} = 4\pi \sum_{\ell,m} (-i)^\ell j_\ell(qr) Y^\star_{\ell m}(\hat{r}) Y_{\ell m}(\hat{q}). \tag{E.1.1}$$

Then, we can solve the integral in Eq. (4.2.20),

$$\varepsilon^{abc} \int d^3r \psi_{X,z}(\vec{r}) \int \frac{d^3q}{(2\pi)^3} e^{-i\vec{q}\cdot\vec{r}} q_a \tag{E.1.2}$$

$$= \frac{1}{2\pi^2} \varepsilon^{abc} \sum_{l',m'} (-i)^{l'} \int d^3q q_a Y_{l'm'}(\hat{q}) \underbrace{\int d^3r R_{nl}(r) j_{l'}(qr) Y_{\ell m}(\hat{r}) Y^\star_{l'm'}(\hat{r})}_{=\int drr^2 R_{nl}(r) j_{l'}(qr) \underbrace{\int d\Omega_r Y_{\ell m}(\hat{r}) Y^\star_{l'm'}(\hat{r})}_{=\delta_{ll'}\delta_{mm'}}} \tag{E.1.3}$$

$$= \frac{1}{2\pi^2} (-i)^l \varepsilon^{abc} \int d^3q q_a Y_{lm}(\hat{q}) \int drr^2 R_{nl}(r) j_l(qr) \tag{E.1.4}$$

$$\overset{l=1}{=} \frac{i}{\sqrt{6\pi^3}} \int drr^2 R_{n1}(r) \underbrace{\int dq q^3 j_1(qr)}_{=\frac{3\pi}{2r^3}\delta(r)} \times \begin{cases} \varepsilon^{1bc} - i\varepsilon^{2bc} & m=-1 \\ \varepsilon^{3bc}\sqrt{2} & m=0 \\ -\varepsilon^{1bc} - i\varepsilon^{2bc} & m=1 \end{cases} \tag{E.1.5}$$

$$= \frac{i}{2}\sqrt{\frac{3}{2\pi}} \left.\frac{\partial R_{n1}(r)}{\partial r}\right|_{r=0} \times \begin{cases} \varepsilon^{1bc} - i\varepsilon^{2bc} & m=-1 \\ \varepsilon^{3bc}\sqrt{2} & m=0 \\ -\varepsilon^{1bc} - i\varepsilon^{2bc} & m=1 \end{cases}, \tag{E.1.6}$$

where we choose $q^a = (q\sin\theta\cos\phi, q\sin\theta\sin\phi, q\cos\theta)^T$ and $\left.\frac{\partial R(r)}{\partial r}\right|_{r=0} = \left.\frac{R(r)}{r}\right|_{r=0}$. The integral in the fourth line vanishes for $l=0$. Then, the matrix amplitude is equal to Eq. (4.2.23).

APPENDIX F

Self-interactions in the DM sector

In Part II we constructed the dynamical theory of SIMPs as Nambu-Goldstone states π in a $Sp(4)_c$ theory. The dynamics of the SIMPs is captured in the chiral Lagrangian, including self-interactions, like $2\pi \rightleftharpoons 2\pi$ as well as $3\pi \rightleftharpoons 2\pi$ interactions. In this chapter, we provide the relevant self-interacting cross sections for mass degenerate SIMPs. Since the SIMP freeze-out is strongly regulated by the $3\pi \to 2\pi$ process, we also derive the thermally averaged cross section $\langle \sigma v^2 \rangle_{3\pi\to 2\pi}$, occurring in the Boltzmann equation.

F.1 The $2\pi \to 2\pi$ cross section for mass-degenerate SIMPs

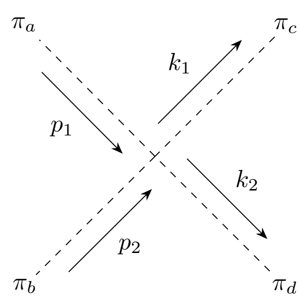

Figure F.1: The $2\pi \to 2\pi$ processes.

As already discussed in Sec. 3, the $2 \to 2$ interaction gets contribution from the kinetic and mass term of the chiral Lagrangian. The $2 \to 2$ self-interaction guarantees that the dark matter sector is at one single temperature maintaining the state of thermal equilibrium. We can determine the squared matrix element of the Feynman diagram F.1 for different combination of flavors $i, j = 1, \ldots, 5$ ($i \neq j$),

$$|M_{ii\to ii}|^2 = \frac{m_\pi^4}{4 f_\pi^4}, \tag{F.1.1}$$

$$|M_{ii\to jj}|^2 = \frac{1}{4f_\pi^2}\left(s-m_\pi^2\right)^2, \tag{F.1.2}$$

$$|M_{ij\to ij}|^2 = \frac{1}{4f_\pi^2}\left(t-m_\pi^2\right)^2. \tag{F.1.3}$$

The cross section[1] in the center of mass frame is given by the integral over the Mandelstam variable $t = (p_1 - k_1)^2 = -(\vec{p}_1 - \vec{k}_1)^2$,

$$\sigma = \frac{1}{64\pi s|\vec{p}_1|^2}\int_{t_0}^{t_1} dt|M|^2, \tag{F.1.4}$$

where p_i, k_i are ingoing and outgoing momenta in the CMS frame,

$$|\vec{p}_1|^2 = |\vec{k}_1|^2 = \frac{(s-4m_\pi^2)}{4}. \tag{F.1.5}$$

Then, the boundaries are $t_0 = -(|\vec{p}_1|+|\vec{k}_1|)^2 = -(s-4m_\pi^2)$ and $t_1 = -(|\vec{p}_1|-|\vec{k}_1|)^2 = 0$. The corresponding cross sections can now be expressed as

$$\sigma_{ij\to ij} = \frac{1}{16\pi s}\frac{1}{12f_\pi^4}\left(s^2-5sm_\pi^2+7m_\pi^4\right) \overset{\text{N.R.}}{\simeq} \frac{m_\pi^2}{32\pi f_\pi^4}\frac{1}{8}, \tag{F.1.6}$$

$$\sigma_{ii\to jj} = \frac{1}{2}\frac{1}{16\pi s}\frac{1}{4f_\pi^4}\left(s-m_\pi^2\right)^2 \overset{\text{N.R.}}{\simeq} \frac{m_\pi^2}{32\pi f_\pi^4}\frac{9}{16}, \tag{F.1.7}$$

$$\sigma_{ii\to ii} = \frac{1}{2}\frac{1}{16\pi s}\frac{m_\pi^4}{4f_\pi^2} \overset{\text{N.R.}}{\simeq} \frac{m_\pi^2}{32\pi f_\pi^4}\frac{1}{16}, \tag{F.1.8}$$

where we already assumed, that SIMPs are non-relativistic, $s \simeq 4m_\pi^2$. A factor $\frac{1}{2}$ is taken into account to avoid double counting of identical final states. The total cross section[2] is then summed up,

$$\sigma_{2\pi\to 2\pi} = \frac{1}{N_\pi^2}\sum_{i,j,k,l}\sigma_{ij\to kl} \overset{\text{N.R.}}{\simeq} \frac{225}{16}\frac{m_\pi^2}{32\pi f_\pi^4 N_\pi^2} = \frac{9m_\pi^2}{512\pi f_\pi^4}, \tag{F.1.9}$$

where the cross section is normalized with $N_\pi = 5$.

F.2 General expression of a $2 \to 2$ thermally averaged cross section

According to Refs. [43, 119], the thermally averaged cross section is derived as follows (i, j are flavor indices),

$$\langle\sigma v\rangle_{ij\to kl} = \frac{1}{n_{p_1}^{eq}n_{p_2}^{eq}}\int\frac{g_{p_1}d^3p_1}{(2\pi)^3}\frac{g_{p_2}d^3p_2}{(2\pi)^3}\left(\sigma v\right)_{ij\to kl} f_{p_1}^{eq}f_{p_2}^{eq} \tag{F.2.1}$$

[1] Here, we consider SIMPs with mass m_π.

[2] The $2\to 2$ cross section is consistent with Ref. [103] for $N_\pi = 5$, where f_π is rescaled, $f_\pi^{Ref[103]} = 2f_\pi$.

$$= \frac{1}{16\pi^2 T^2 m_1^2 m_2^2 K_2(m_1/T) K_2(m_2/T)} \int d^3p_1 d^3p_2 \, (\sigma v)_{ij\to kl} \, e^{-(E_{p_1}+E_{p_2})/T}, \quad \text{(F.2.2)}$$

where $f_i^{\rm eq}$ are Maxwell-Boltzmann distributions, p_1, p_2 are momenta of particles i, j with mass m_1, m_2 and the number density at equilibrium is given by

$$n_i^{eq} = \frac{g_i}{(2\pi)^3} \int d^3p_i f^{eq}(E_i, T) \simeq \frac{g_i}{(2\pi)^3} \int d^3p_i e^{-E_{p_i}/T} = \frac{g_i}{(2\pi)^3} 4\pi m_i^2 T K_2(m_i/T). \quad \text{(F.2.3)}$$

Here, $K_i(x)$ are modified Bessel functions of the second kind. The integral in Eq. (F.2.1) can be simplified to

$$\begin{aligned} &\int d^3p_1 d^3p_2 \, (\sigma v)_{ij\to kl} \, e^{-(E_{p_1}+E_{p_2})/T} \\ &= \left(2\pi^2\right) \int_{\sqrt{s}}^{\infty} dE_+ \int_a^b dE_- \int_{(M_X+m_\pi)^2}^{\infty} ds E_{p_1} E_{p_2} \, (\sigma v)_{ij\to kl} \, e^{-E_+/T}, \end{aligned} \quad \text{(F.2.4)}$$

where $E_\pm = E_{p_1} \pm E_{p_2}$, $s = m_1^2 + m_2^2 + 2E_{p_1}E_{p_2} - 2\sqrt{E_{p_1}^2 - m_1^2}\sqrt{E_{p_2}^2 - m_2^2}\cos\theta$, θ is the angle between $\vec{p}_1$ and $\vec{p}_2$ and $d^3p_1 d^3p_2 = 2\pi^2 E_{p_1} E_{p_2} dE_+ dE_- ds = \frac{\pi^2}{2}(E_+^2 - E_-^2) dE_+ dE_- ds$. The integral boundaries over E_- are given by

$$a = -2|\vec{p}_1|\sqrt{\frac{E_+^2 - s}{s}} + E_+ \frac{\left(m_1^2 - m_2^2\right)}{s} \quad \text{(F.2.5)}$$

$$b = 2|\vec{p}_1|\sqrt{\frac{E_+^2 - s}{s}} + E_+ \frac{\left(m_1^2 - m_2^2\right)}{s}. \quad \text{(F.2.6)}$$

Since $E_{p_1} E_{p_2} v = |\vec{p}_1|\sqrt{s}$, we can integrate over E_- directly,

$$\begin{aligned} &\int d^3p_1 d^3p_2 \, (\sigma v)_{ij\to kl} e^{-(E_{p_1}+E_{p_2})/T} \\ &\qquad = 8\pi^2 \int_{\sqrt{s}}^{\infty} dE_+ \int_{(m_1+m_2)^2}^{\infty} ds \sigma_{ij\to kl} |\vec{p}_1|^2 \sqrt{E_+^2 - s} \, e^{-E_+/T}. \end{aligned} \quad \text{(F.2.7)}$$

Since the cross section depends only on s, we can perform the integration over E_+ by substituting $E_+ = \sqrt{s}x$,

$$\int_{\sqrt{s}}^{\infty} dE_+ e^{-E_+/T} \sqrt{E_+^2 - s} = s \int_1^{\infty} dx e^{-x\sqrt{s}/T} \sqrt{x^2 - 1} = T\sqrt{s} K_1\left(\frac{\sqrt{s}}{T}\right). \quad \text{(F.2.8)}$$

In the end, we can find an analytical expression for the thermally averaged cross section,

$$\langle \sigma v \rangle_{ij\to kl} = \frac{\int_{(m_1+m_2)^2}^{\infty} ds \, \sigma_{ij\to kl} \sqrt{s} |\vec{p}_1|^2 K_1\left(\frac{\sqrt{s}}{T}\right)}{2 m_1^2 m_2^2 T K_2(m_1/T) K_2(m_2/T)}. \quad \text{(F.2.9)}$$

The Bessel function in the integral can be approximated by

$$K_1\left(\frac{\sqrt{s}}{T}\right) \simeq \sqrt{\frac{T\pi}{2s^{1/2}}} e^{-\sqrt{s}/T} \quad \text{(F.2.10)}$$

for large $\sqrt{s}/T$.

F.3 General expression of a $3 \to 2$ cross section

In this section we mainly follow the calculations from [100]. In a five-point interaction, there are five independent Mandelstam variables,

$$\begin{aligned} s_{12} &= (p_1+p_2)^2, \quad s_{13} = (p_1+k_1)^2, \quad s_{23} = (p_2+k_1)^2, \\ s_{14} &= (p_1-k_2)^2, \quad s_{24} = (p_2-k_2)^2, \end{aligned} \tag{F.3.1}$$

where p_i and k_i are ingoing and outgoing momenta, respectively. The general expression of the $3 \to 2$ cross section is defined as follows,

$$\begin{aligned} \left(\sigma v^2\right)_{ijk\to ln} = \frac{1}{(2E_{p_1})(2E_{p_2})(2E_{p_3})} \int \frac{d^3k_1}{(2\pi)^3 2E_{k_1}} \frac{d^3k_2}{(2\pi)^3 2E_{k_2}} \\ \times (2\pi)^4 \delta^4(p_1+p_2+p_3-k_1-k_2) |\mathcal{M}_{ijk\to ln}|^2. \end{aligned} \tag{F.3.2}$$

On dimensional grounds, the quantity σ is not a cross section, since it has dimension $1/E^5$. In the center of mass frame, $\vec{p}_1+\vec{p}_2+\vec{p}_3=0$, the cross section can be simplified to

$$\left(\sigma v^2\right)_{ijk\to ln} = \frac{1}{32\pi^2 E_{p_1}E_{p_2}E_{p_3}} \int \frac{d^3k_1}{2E_{k_1}} \frac{d^3k_2}{2E_{k_2}} \delta(E_{p_1}+E_{p_2}+E_{p_3}-E_{k_1}-E_{k_2}) \tag{F.3.3}$$

$$\times \delta^3\left(\vec{k}_1+\vec{k}_2\right) |\mathcal{M}_{ijk\to ln}|^2 \tag{F.3.4}$$

$$= \frac{1}{128\pi^2 E_{p_1}E_{p_2}E_{p_3}} \int \frac{d|\vec{k}_1|}{\sqrt{m_4^2+|\vec{k}_1|^2}} \frac{|\vec{k}_1|^2}{\sqrt{m_5^2+|\vec{k}_1|^2}} \tag{F.3.5}$$

$$\times \delta\left(\sqrt{s_{45}} - \sqrt{m_4^2+|\vec{k}_1|^2} - \sqrt{m_5^2+|\vec{k}_1|^2}\right) \int d\Omega\, |\mathcal{M}_{ijk\to ln}|^2, \tag{F.3.6}$$

where we are left with an integral over the angles, $d\Omega = d\varphi d\cos\theta$. In the first equality, the delta function was split into energy and momentum part

$$\delta^4(p_1+p_2+p_3-k_1-k_2) = \delta(E_{p_1}+E_{p_2}+E_{p_3}-E_{k_1}-E_{k_2})\,\delta^3(\vec{p}_1+\vec{p}_2+\vec{p}_3-\vec{k}_1-\vec{k}_2). \tag{F.3.7}$$

In the last equality, an integration over $\vec{k}_1$ was performed and the Mandelstam variable $s_{45} = E_{p_1}+E_{p_2}+E_{p_3}$ was expressed in the center of mass frame. The integral is solved by the substitution $u = \sqrt{m_4^2+|\vec{k}_1|^2} + \sqrt{m_5^2+|\vec{k}_1|^2}$,

$$\left(\sigma v^2\right)_{ijk\to ln} = \frac{1}{128\pi^2 E_{p_1}E_{p_2}E_{p_3}} \int du \frac{|\vec{k}_1|}{u} \delta(\sqrt{s_{45}}-u) \int d\Omega\, |\mathcal{M}_{ijk\to ln}|^2 \tag{F.3.8}$$

$$= \frac{|\vec{k}_1|}{128\pi^2 E_{p_1}E_{p_2}E_{p_3}\sqrt{s_{45}}} \int d\Omega\, |\mathcal{M}_{ijk\to ln}|^2. \tag{F.3.9}$$

The delta function makes $|\vec{k}_1| = \frac{1}{2\sqrt{s_{45}}}\sqrt{\lambda(s_{45}, m_4^2, m_5^2)}$ consistent with the energy conservation $E_{p_1} + E_{p_2} + E_{p_3} = E_{k_1} + E_{k_2}$ in the center of mass frame. In the non-relativistic limit, $E_i \sim m_i$, the cross section then reads,

$$\left(\sigma v^2\right)_{ijk\to ln} = \frac{|\vec{k}_1|}{128\pi^2 m_1 m_2 m_3}\frac{\int d\Omega\, |\mathcal{M}_{ijk\to ln}|^2}{(m_1+m_2+m_3)}. \tag{F.3.10}$$

F.4 General expression of the thermally averaged cross section $\left\langle\sigma v^2\right\rangle_{ijk\to ln}$

The thermally averaged cross section is written as[3]

$$\left\langle\sigma v^2\right\rangle_{ijk\to ln} = \frac{1}{n_1^{\mathrm{eq}} n_2^{\mathrm{eq}} n_3^{\mathrm{eq}}}\int \frac{g_1 d^3p_1}{(2\pi)^3 2E_{p_1}}\frac{g_2 d^3p_2}{(2\pi)^3 2E_{p_2}}\frac{g_3 d^3p_3}{(2\pi)^3 2E_{p_3}}\frac{g_d d^3k_1}{(2\pi)^3 2E_{k_1}}\frac{g_5 d^3k_2}{(2\pi)^3 2E_{k_2}} \tag{F.4.1}$$

$$\times\,(2\pi)^4\delta^4\left(p_1+p_2+p_3-k_1-k_2\right)|\mathcal{M}_{ijk\to ln}|^2\, f_1^{\mathrm{eq}} f_2^{\mathrm{eq}} f_3^{\mathrm{eq}} \tag{F.4.2}$$

$$= \frac{1}{n_1^{\mathrm{eq}} n_2^{\mathrm{eq}} n_3^{\mathrm{eq}}}\int \frac{g_1 d^3p_1}{(2\pi)^3}\frac{g_2 d^3p_2}{(2\pi)^3}\frac{g_3 d^3p_3}{(2\pi)^3}\left(\sigma v^2\right)_{ijk\to ln} f_1^{\mathrm{eq}} f_2^{\mathrm{eq}} f_3^{\mathrm{eq}}, \tag{F.4.3}$$

where $f_i^{\mathrm{eq}} \sim e^{-E_i/T}$ are Maxwell-Boltzmann distributions in the non-relativistic limit. The number density in equilibrium yields

$$n_i^{\mathrm{eq}} = \frac{g_i}{(2\pi)^3}\int d^3p_i f_i^{\mathrm{eq}} \simeq \frac{g_i}{(2\pi)^3}\left(4\pi m_i^2 T K_2(m_i/T)\right). \tag{F.4.4}$$

Here, $K_j(x)$ is the modified Bessel function of order j.

F.5 The $3\to 2$ cross section $\left(\sigma v^2\right)_{ijk\to ln}$ for mass-degenerate SIMPs

The $3\to 2$ cross section is determined by the WZW interaction in Sec. 3. For this reason, we have to derive the quantity $\int d\Omega\, |\mathcal{M}_{ijk\to ln}|^2$ for SIMPs with equal masses m_π. The matrix amplitude is given in App. 3. Since the squared matrix element is written in terms of Lorentz invariant products $(p_1.k_1), (p_2.k_1), (p_3.k_1)$, we can express those products as functions of ϕ, θ in the center of mass frame[4]

$$(p_1.k_1) = a_1 - a_2\sin\theta\cos\phi \tag{F.5.1}$$

$$(p_2.k_1) = b_1 + b_2\sin\theta\cos\phi - b_3\sin\theta\sin\phi \tag{F.5.2}$$

[3] An additional symmetry factor $1/n!$ has to be added for identical initial states.

[4] We choose the first initial state $p_1 = (E_{p_1}, |\vec{p}_1|, 0, 0)$ along the $x-$ axis in the CM frame. The second and third initial states $p_2 = (E_{p_2}, |\vec{p}_2|\cos\phi, |\vec{p}_2|\sin\phi, 0)$ and $p_3 = (E_{p_3}, -(|\vec{p}_2|\cos\phi + |\vec{p}_1|), -|\vec{p}_2|\sin\phi, 0)$ are then in the (x,y)-plane, where $|\vec{p}_1| = \frac{1}{2\sqrt{s_{45}}}\sqrt{\lambda(s_{45}, s_{23}, m_\pi^2)}$ and $|\vec{p}_2| = \frac{1}{2\sqrt{s_{45}}}\sqrt{\lambda(s_{45}, s_{13}, m_\pi^2)}$.

$$(p_3.k_1) = c_1 + c_2 \sin\theta\cos\phi + c_3 \sin\theta\sin\phi. \tag{F.5.3}$$

Here, a_i, b_i, c_i are functions, that depend on the initial momenta and on the SIMP mass m_π,

$$a_1 = \frac{1}{4}\left(m_\pi^2 - s_{23} + s_{45}\right), \quad a_2 = \frac{1}{4}\sqrt{s_{45}\left(s_{45} - 4m_\pi^2\right)}\sqrt{\lambda(m_\pi^2, s_{23}, s_{45})}, \tag{F.5.4}$$

$$b_1 = \frac{1}{4}\left(m_\pi^2 - s_{13} + s_{45}\right), \tag{F.5.5}$$

$$b_2 = \frac{\sqrt{(s_{45} - 4m_\pi^2)}}{4}\frac{\left(-m_\pi^4 + (m_\pi^2 - s_{45})(s_{13} + s_{23}) - s_{13}s_{23} + s_{45}^2\right)}{\sqrt{s_{45}\lambda(m_\pi^2, s_{23}, s_{45})}}, \tag{F.5.6}$$

$$b_3 = \frac{\sqrt{(s_{45} - 4m_\pi^2)}}{2}\frac{\sqrt{s_{13}s_{23}s_{12} - m_\pi^2\left(m_\pi^2 - s_{45}\right)^2}}{\sqrt{\lambda(m_\pi^2, s_{23}, s_{45})}}, \tag{F.5.7}$$

$$c_1 = \frac{s_{45}}{2} - a_1 - b_1, \quad c_2 = -b_2 + a_2, \quad c_3 = b_3 \tag{F.5.8}$$

The Mandelstam variable s_{45} is now given by $s_{45} = s_{12} + s_{13} + s_{23} - 3m_\pi^2$. Then, we can perform the integral over the angles and obtain

$$\int d\Omega |M_{ijk\to ln}|^2 = \frac{N_c^2(4m_\pi^2 - s_{45})(m_\pi^2(m_\pi^2 - s_{45})^2 - s_{12}s_{13}s_{23})}{96\pi^3 f_\pi^{10}}. \tag{F.5.9}$$

Thus, the $3 \to 2$ cross section is expressed in terms of Mandelstam variables,

$$\begin{aligned}
\left(\sigma v^2\right)_{ijk\to ln} &= \frac{|\vec{k}_1|}{128\pi^2 E_{p_1}E_{p_2}E_{p_3}\sqrt{s_{45}}}\int d\Omega |\mathcal{M}_{ijk\to ln}|^2 \\
&= \frac{\sqrt{s_{45} - 4m_\pi^2}}{256 E_{p_1}E_{p_2}E_{p_3}\sqrt{s_{45}}}\frac{N_c^2(4m_\pi^2 - s_{45})}{96\pi^5 f_\pi^{10}}\left(m_\pi^2(m_\pi^2 - s_{45})^2 - s_{12}s_{13}s_{23}\right) \\
&= \frac{s_{45}\sqrt{s_{45} - 4m_\pi^2}}{256}\frac{N_c^2(4m_\pi^2 - s_{45})}{12\pi^5 f_\pi^{10}}\frac{\left(m_\pi^2(4m_\pi^2 - s_{12} - s_{13} - s_{23})^2 - s_{12}s_{13}s_{23}\right)}{(m_\pi^2 - s_{12} + s_{45})(m_\pi^2 - s_{13} + s_{45})(m_\pi^2 - s_{23} + s_{45})} \\
&\overset{\text{N.R.}}{\simeq} -\frac{25N_c^2}{256\pi^4\, 72\sqrt{5}m_\pi f_\pi^{10}}\left(m_\pi^2(4m_\pi^2 - s_{12} - s_{13} - s_{23})^2 - s_{12}s_{13}s_{23}\right),
\end{aligned} \tag{F.5.10}$$

where $s_{45} \simeq 9m_\pi^2, s_{12} \simeq s_{13} \sim s_{23} \simeq 4m_\pi^2$ and the energies E_i are

$$E_{p_1} = \frac{1}{2\sqrt{s_{45}}}(m_\pi^2 - s_{23} + s_{45}), \tag{F.5.11}$$

$$E_{p_2} = \frac{1}{2\sqrt{s_{45}}}(m_\pi^2 - s_{13} + s_{45}), \tag{F.5.12}$$

$$E_{p_3} = \frac{1}{2\sqrt{s_{45}}}(m_\pi^2 - s_{12} + s_{45}). \tag{F.5.13}$$

The expression in the bracket in Eq. (F.5.10) has a velocity dependence.

F.6 The thermally averaged cross section $\langle\sigma v^2\rangle_{ijk\to ln}$ for mass-degenerate SIMPs

Since dark matter is non-relativistic, we can approximate the thermally average cross section as

$$
\begin{aligned}
\langle\sigma v^2\rangle_{ijk\to ln} &= \frac{1}{n_1^{\mathrm{eq}} n_2^{\mathrm{eq}} n_3^{\mathrm{eq}}} \int \frac{g_1 d^3p_1}{(2\pi)^3}\frac{g_2 d^3p_2}{(2\pi)^3}\frac{g_3 d^3p_3}{(2\pi)^3}\left(\sigma v^2\right)_{ijk\to ln} f_1^{eq} f_2^{eq} f_3^{eq} \\
&\overset{\text{N.R.}}{\simeq} -\frac{25N_c^2}{256\pi^4\, 72\sqrt{5}m_\pi f_\pi^{10}}\frac{1}{\left(4\pi m_\pi^2 T K_2(m_\pi/T)\right)^3} \\
&\times \int dE_{p_1} dE_{p_2} dE_{p_3} E_{p_1}E_{p_2}E_{p_3}\sqrt{E_{p_1}^2-m_\pi^2}\sqrt{E_{p_2}^2-m_\pi^2}\sqrt{E_{p_3}^2-m_\pi^2}\, e^{-(E_{p_1}+E_{p_2}+E_{p_3})/T} \\
&\times \int_0^{2\pi} d\phi_2 \int_0^{\pi} d\theta_2 \int_0^{2\pi} d\phi_3 \int_0^{\pi} d\theta_3 \left(m_\pi^2(4m_\pi^2 - s_{12} - s_{13} - s_{23})^2 - s_{12}s_{13}s_{23}\right) \\
&= \frac{25N_c^2}{16\pi^2\, 81\sqrt{5}m_\pi f_\pi^{10}}\frac{1}{\left(4\pi m_\pi^2 T K_2(m_\pi/T)\right)^3} \\
&\times \int dE_{p_1} dE_{p_2} dE_{p_3} E_{p_1}E_{p_2}E_{p_3}\sqrt{E_{p_1}^2-m_\pi^2}\sqrt{E_{p_2}^2-m_\pi^2}\sqrt{E_{p_3}^2-m_\pi^2}\, e^{-(E_{p_1}+E_{p_2}+E_{p_3})/T} \\
&\times \left(2m_\pi^4\left(E_{p_1}^2+E_{p_2}^2+E_{p_3}^2\right) - 5m_\pi^2\left(E_{p_3}^2\left(E_{p_1}^2+E_{p_2}^2\right)+E_{p_1}^2E_{p_2}^2\right) + 8E_{p_1}^2E_{p_2}^2E_{p_3}^2 + m_\pi^6\right) \\
&= \frac{25N_c^2 m_\pi^2}{1024\pi^5\, 81\sqrt{5} f_\pi^{10}\left(K_2(m_\pi/T)\right)^3} \\
&\times \Bigg\{6m_\pi^2\left(-3TK_3\left(\frac{m_\pi}{T}\right)+m_\pi K_4\left(\frac{m_\pi}{T}\right)\right)\left(K_2\left(\frac{m_\pi}{T}\right)\right)^3 \\
&- 15m_\pi\left(-3TK_3\left(\frac{m_\pi}{T}\right)+m_\pi K_4\left(\frac{m_\pi}{T}\right)\right)^2 K_2\left(\frac{m_\pi}{T}\right) \\
&+ 8\left(-3TK_3\left(\frac{m_\pi}{T}\right)+m_\pi K_4\left(\frac{m_\pi}{T}\right)\right)^3 + m_\pi^3\left(K_2\left(\frac{m_\pi}{T}\right)\right)^3\Bigg\} \\
&\overset{x=\frac{m_\pi}{T}}{=} \frac{25N_c^2 m_\pi^5}{1024\pi^5\, 81\sqrt{5} f_\pi^{10}}\Bigg\{6\left(-\frac{3}{x}\frac{K_3(x)}{K_2(x)}+\frac{K_4(x)}{K_2(x)}\right) - 15\left(-\frac{3}{x}\frac{K_3(x)}{K_2(x)}+\frac{K_4(x)}{K_2(x)}\right)^2 \\
&\qquad + 8\left(-\frac{3}{x}\frac{K_3(x)}{K_2(x)}+\frac{K_4(x)}{K_2(x)}\right)^3 + 1\Bigg\}
\end{aligned}
\tag{F.6.1}
$$

In the second equality, we pulled the pre-factor out of the integral and used the non-relativistic approximation for the Mandelstam variables $s_{45} \simeq 9m_\pi^2, s_{12} \simeq s_{13} \sim s_{23} \simeq 4m_\pi^2$. In addition, we changed the integration variable from momentum to energy by $dEE = |\vec{p}|d|\vec{p}|$. In the third equality, we chose a frame, where the first initial state p_1 is in the z-direction,

$$p_1 = (E_{p_1}, 0, 0, |\vec{p}_1|)\,, \tag{F.6.2}$$

$$p_2 = (E_{p_2}, 0, |\vec{p}_2|\sin\theta_2, |\vec{p}_2|\cos\theta_2)\,, \tag{F.6.3}$$

$$p_3 = (E_{p_3}, |\vec{p}_3|\sin\theta_3\cos\phi_3, |\vec{p}_3|\sin\theta_3\sin\phi_3, |\vec{p}_3|\cos\theta_3)\,. \tag{F.6.4}$$

Then, we expressed all Mandelstam variables in terms of $\theta_2, \theta_3, \phi_3$ and performed the integral over the angles. In the fourth equality, we integrated over the energies. In the end, we take the non-relativistic limit, $x \gg 1$ and arrive at

$$\langle \sigma v^2 \rangle_{ijk\to ln} \overset{\text{N.R.}}{\simeq} \frac{25 N_c^2 m_\pi^5}{1024\sqrt{5}\pi^5 f_\pi^{10} x^2} + O(1/x^3), \tag{F.6.5}$$

where $x = m_\pi/T$. The full $3 \to 2$ cross section is given by the sum of all combinations of Nambu-Goldstone states π,

$$\left\langle \sigma v^2 \right\rangle_{3\pi\to 2\pi} = \frac{1}{N_\pi^3}\frac{1}{3!}\frac{1}{2!}\sum_{i,j,k,l,n}\left\langle \sigma v^2 \right\rangle_{ijk\to ln} = \frac{1}{N_\pi^3}\frac{1}{3!}\frac{1}{2!}\left(5!\left\langle \sigma v^2 \right\rangle_{123\to 45}\right) = \frac{10}{N_\pi^3}\left\langle \sigma v^2 \right\rangle_{123\to 45} \tag{F.6.6}$$

$$\overset{N.R.}{=} \frac{125 N_c^2 m_\pi^5}{512\sqrt{5}\pi^5 f_\pi^{10} x^2 N_\pi^3} + O(1/x^3), \tag{F.6.7}$$

where the factor 1/3! 1/2! avoids double counting of the same event and $N_\pi = 5$. We differ by a factor 3 from the SIMPlest miracle paper [103], but agree with [123],

$$\left\langle \sigma v^2 \right\rangle_{3\pi\to 2\pi} = \frac{1}{3} \times \left\langle \sigma v^2 \right\rangle_{3\pi\to 2\pi}^{Ref[103]}\,. \tag{F.6.8}$$

Remember, that the decay constant is rescaled, $f_\pi^{Ref[103]} = 2 f_\pi$.

APPENDIX G

Constant amplitude

In this appendix we provide matrix amplitudes and cross sections of the interactions $X\pi \to 2\pi$, $3\pi \to \pi X$ and $2X \to 2\pi$ in Sec. 4.2 and 4.3.2 (up to double-counting factors), assuming a constant matrix elements $\mathcal{M}_{3\to 2}$, $\mathcal{M}_{3\to 3}$, $\mathcal{M}_{4\to 2}$ and introduced a symmetry factor $S = 1$ ($S = 1/\sqrt{2}$) for non-identical (identical) particles,

$$\mathcal{M}_{X\pi\to 2\pi}(P, p_3 \to k_1, k_2) \overset{\text{N.R.}}{\simeq} \frac{S\sqrt{2M_X}}{2m_\pi} \int \frac{d^3q}{(2\pi)^3} \tilde{\psi}_{X,z}\,(\vec{q})\,\mathcal{M}_{3\to 2} \tag{G.0.1}$$

$$\simeq \frac{S\sqrt{M_X}}{2\sqrt{2\pi}m_\pi} R_{n0}(0)\mathcal{M}_{3\to 2} \qquad l = m = 0, \tag{G.0.2}$$

$$(\sigma v)_{X\pi\to 2\pi} = \langle \sigma v \rangle_{X\pi\to 2\pi} = \frac{|\vec{k}_1|}{64\pi^2 E_P E_{p_2}\sqrt{s}} \int d\Omega |\mathcal{M}_{X\pi\to 2\pi}|^2 \tag{G.0.3}$$

$$\overset{\text{N.R.}}{\simeq} \frac{\sqrt{(M_X + m_\pi)^2 - 4m_\pi^2}}{32\pi M_X m_\pi (m_\pi + M_X)} |\mathcal{M}_{X\pi\to 2\pi}|^2 \tag{G.0.4}$$

$$\simeq \frac{\sqrt{(M_X + m_\pi)^2 - 4m_\pi^2}}{256\pi^2 m_\pi^3 (m_\pi + M_X)} S^2 R_{n0}^2(0) |\mathcal{M}_{3\to 3}|^2, \tag{G.0.5}$$

$$\mathcal{M}_{3\pi\to\pi X}(p_1, p_2, p_3 \to k_1, P) \overset{\text{N.R.}}{\simeq} \frac{S\sqrt{2M_X}}{2m_\pi} \int \frac{d^3q}{(2\pi)^3} \tilde{\psi}^\star(\vec{q})\mathcal{M}_{3\to 3} \tag{G.0.6}$$

$$\simeq \frac{S\sqrt{M_X}}{2\sqrt{2\pi}m_\pi} R_{n0}(0)\mathcal{M}_{3\to 3} \qquad l = m = 0, \tag{G.0.7}$$

$$(\sigma v^2)_{3\pi\to\pi X} = \frac{|\vec{k}_1|}{128\pi^2 E_{p_1} E_{p_2} E_{p_3}\sqrt{s_{45}}} \int d\Omega\, |\mathcal{M}_{3\pi\to\pi X}|^2 \tag{G.0.8}$$

$$\overset{\text{N.R.}}{\simeq} \frac{\sqrt{M_X^4 - 20M_X^2 m_\pi^2 + 64m_\pi^4}}{576\pi m_\pi^5} |\mathcal{M}_{3\pi\to\pi X}|^2 \tag{G.0.9}$$

$$\simeq \frac{M_X\sqrt{M_X^4 - 20M_X^2 m_\pi^2 + 64m_\pi^4}}{4608\pi^2 m_\pi^7} S^2 R_{n0}^2(0)|\mathcal{M}_{3\to 3}|^2, \tag{G.0.10}$$

$$\mathcal{M}_{2X\to 2\pi}(P_1, P_2 \to k_1, k_2) \overset{\text{N.R.}}{\simeq} \frac{S_1 S_2 M_X}{2m_\pi^2} \int \frac{d^3q}{(2\pi)^3} \frac{d^3k}{(2\pi)^3} \tilde{\psi}_{X_1,a}(\vec{q})\tilde{\psi}_{X_2,b}(\vec{k})\mathcal{M}_{4\to 2} \tag{G.0.11}$$

$$\simeq \frac{S_1 S_2 M_X}{8\pi m_\pi^2} R_{n_1 0}^{X_1}(0) R_{n_2 0}^{X_2}(0)\mathcal{M}_{4\to 2} \qquad l = m = 0, \tag{G.0.12}$$

$$(\sigma v)_{2X\to 2\pi} = \frac{|\vec{k}_1|}{64\pi^2 E_{P_1} E_{P_2}\sqrt{s}} \int d\Omega |\mathcal{M}_{2X\to 2\pi}|^2 \tag{G.0.13}$$

$$\overset{\text{N.R.}}{\simeq} \frac{\sqrt{M_X^2 - m_\pi^2}}{32\pi M_X^3} |\mathcal{M}_{2X\to 2\pi}|^2 \tag{G.0.14}$$

$$\simeq \frac{\sqrt{M_X^2 - m_\pi^2}}{2048\pi^3 m_\pi^4 M_X} S_1^2 S_2^2 |R_{n_1 0}^{X_1}(0)|^2 |R_{n_2 0}^{X_2}(0)|^2 |\mathcal{M}_{4\to 2}|^2. \tag{G.0.15}$$

Part III

Indirect measurements of dark matter through (exotic) neutrino portal

CHAPTER 5

Dark radiation from dark matter decays

Direct detection experiments searched for dark matter, especially WIMPs, for about two decades, but we have not found an undisputed dark matter signal yet. One great challenge in the future is the existence of irreducible neutrino backgrounds, that may mimic the rates of dark matter making direct detection experiments less sensitive to WIMPs. Since current experimental constraints almost reached the limit in sensitivity in the region of interest (neutrino floor), new experimental and theoretical ideas are necessary to overcome these limits. Instead of increasing the sensitivity of direct detection experiments by various methods, e.g. larger exposures or directional detection of recoil energies, we can also consider additional signatures of dark matter, e.g. through a neutrino portal, where dark matter is assumed to be unstable.

We will consider two possible scenarios:

- a multi-component dark matter model, in which a small percentage of dark matter is unstable with arbitrary lifetimes,
- the complete dark matter abundance is unstable with lifetimes much greater than the age of the universe.

Both scenarios may inject a large number of particles, that escaped detection to date. At this point, we refer to these particles as *dark radiation*. In the following, dark radiation is considered to be neutrinos, originating from dark matter two-body decays, see App. H.1. Since direct detection experiments will study irreducible neutrino backgrounds in the future, dark radiation in the form of neutrinos sourced by MeV-mass dark matter can be probed at the same time. In addition, dark radiation from sub-eV dark matter can be studied in the proposed neutrino experiment PTOLEMY, which is designed to search for relic neutrinos via neutrino capture.

In order to distinguish dark radiation signals from backgrounds, we apply Likelihood statistics and establish the minimum lifetime corresponding to the smallest dark radiation flux, where dark radiation and neutrino backgrounds are still distinguishable. For this case, we generate mock data and calculate the 3σ discovery in the parameter space $(m_{\rm DM}, \tau_{\rm DM})$, where $m_{\rm DM}, \tau_{\rm DM}$ are the mass and the lifetime of the progenitor dark matter. In addition, we explore the exclusion potential, assuming a background-free scenario. In the following publications [3, 4], we show the sensitivity of direct detection experiments and the proposed experiment PTOLEMY to dark radiation as neutrinos (Standard Model and baryonic neutrinos). The statistical procedure is explained in the following publication [3] in Sec. 6 and in App. K in more details. Moreover, we used the same statistical framework to find the 3σ discovery reach in PTOLEMY.

CHAPTER 6

Publications about dark radiation

Sensitivity of direct detection experiments to neutrino dark radiation from dark matter decay and a modified neutrino-floor
Marco Nikolic, Suchita Kulkarni & Josef Pradler

Published in: The European Physical Journal C 82, 650 (2022)
DOI: 10.1140/epjc/s10052-022-10534-3
Preprint version in arXiv: arXiv:2008.13557 [hep-ph]
Main contributions: sections $1-7$ and appendices A, B

Probing sub-eV Dark Matter decays with PTOLEMY
Kyrylo Bondarenko, Alexey Boyarsky, Marco Nikolic, Josef Pradler & Anastasia Sokolenko

Published in: Journal of Cosmology and Astroparticle Physics 03 (2021) 089
DOI: 10.1088/1475-7516/2021/03/089
Preprint version in arXiv: arXiv:2012.09704 [astro-ph.CO]
Main contributions: sections $3, 3.1, 3.2.1, 4$ and appendices A, B

Eur. Phys. J. C (2022) 82:650
https://doi.org/10.1140/epjc/s10052-022-10534-3

THE EUROPEAN PHYSICAL JOURNAL C

Regular Article -Theoretical Physics

Sensitivity of direct detection experiments to neutrino dark radiation from dark matter decay and a modified neutrino-floor

Marco Nikolic[1,a], **Suchita Kulkarni**[2,b], **Josef Pradler**[1,c]

[1] Institute of High Energy Physics, Austrian Academy of Sciences, Nikolsdorfergasse 18, 1050 Vienna, Austria
[2] Institute of Physics, NAWI Graz, University of Graz, Universitätsplatz 5, 8010 Graz, Austria

Received: 14 October 2021 / Accepted: 19 June 2022 / Published online: 27 July 2022

Abstract In this work we analyse the ultimate sensitivity of dark matter direct detection experiments to dark radiation in form of SM or semi-sterile neutrinos. This flux-component is assumed to be produced from dark matter decay. Since dark radiation may mimic dark matter signals, we perform our analysis based on likelihood statistics that allows to test the distinguishability between signals and backgrounds. Given the previous bounds from neutrino experiments, we find that xenon-based dark matter searches will not be able to probe new regions of the dark matter progenitor mass and lifetime parameter space when the decay products are SM neutrinos. In turn, if the decay instead happens to a fourth neutrino species with enhanced interactions to baryons, DR can either constitute the dominant background or a discoverable signal in direct detection experiments. In the former case, this lifts the "neutrino floor" for xenon-based experiments.

1 Introduction

The neutral current-induced coherent neutrino-nucleus scattering process [1,2] once inspired the conception of dark matter (DM) direct detection experiments [3–5]. Neutrinos with energies up to several hundred MeV elastically scatter on atomic nuclei with a cross section that is approximately enhanced by the squared number of neutrons, N^2. Similarly, the spin-independent scattering of weakly interacting massive particles (WIMPs) is enhanced by the square of the atomic number, A^2, boosting the prospects of observing an atomic recoil signal from DM in ultra-low background detectors with keV energy thresholds. Whereas DM has yet to be directly observed in the laboratory, the very process of coherent neutrino-nucleus scattering that once started the field, may also be the defining process in closing the window of opportunity in our direct searches for electroweak-scale DM. Neutrinos produced in the sun, in the atmosphere or in supernova explosions, among other sources, constitute a steady flux that cannot be shielded and, given enough observation time, detector volume, and detection sensitivity will eventually be seen as an irreducible background in DM direct detection experiments. This limits the ultimate sensitivity to discover DM of mass m_χ and nucleon cross section σ_n, and the combination of parameters where this occurs is conventionally referred to as the "neutrino floor" [6–8].

The previous years have seen steady advances in increasing the sensitivity of direct detection experiments. Besides a tremendous effort that is underway and aims at developing and operating ultra-low threshold detectors—see [9] and references therein—the classical WIMP detectors have now gone beyond the ton-year mark in exposure, reaching a sensitivity of $\sigma_n \simeq 10^{-47}\,\mathrm{cm}^2$ and better at a DM mass m_χ of several tens of GeV. Full exposure results have been reported from liquid xenon experiments LUX [10], PANDAX-II [11], and XENON1T [12], followed by results from current liquid argon detectors DEAP-3600 [13] and DarkSide-50 [14]. The next generation in these experiments, XENONnT [15] and LZ [16] is already under construction and/or commissioning and they will be sensitive enough to see a small number of neutrino background events. Finally, exposures of several hundred ton-year may be achieved with the respective liquid xenon and argon detectors DARWIN [17] and DarkSide-20k [18], and their reach in (m_χ, σ_n) will be limited by the neutrino floor.

More than 40 years after its prediction, coherent neutrino-nucleus scattering has finally been observed by the COHERENT collaboration using accelerator-based neutrino beams [19,20]; efforts to detect the process using reactors are underway [21,22]. These measurements provide valuable new insight into the interactions of Standard Model (SM) neutrinos with the constituents of atomic nuclei, thereby constrain-

[a] e-mail: marco.nikolic@oeaw.ac.at (corresponding author)
[b] e-mail: suchita.kulkarni@uni-graz.at
[c] e-mail: josef.pradler@oeaw.ac.at

ing non-standard interactions to quarks and the presence of new forces. In the context of DM direct detection, the most important neutrino source is the sun and beyond-SM neutrino physics utilizing these fluxes has been explored in [23,24]; for more recent works see [25–34] and the review [35]. A common theme in many of these studies is that new interactions of neutrinos will modify, and typically elevate the standard neutrino floor by within a factor of a few, when the new physics is subjected to complementary constraints.

In this work, we consider a principal alternative option. Rather than modifying neutrino interactions per se, we shall primarily study the presence of new neutrino fluxes, their detectability and their influence on the DM detectability. Concretely, we consider DM decay as a source of SM neutrinos; only in a second step we shall also consider the possibility of new interactions in an extended neutrino sector. Substantial fluxes of these neutrinos will originate from DM decay within our own galaxy as well as globally, by the cosmological decay of DM. Indeed, it is entirely possible that the Universe is filled in significant number with relativistic particles, *dark radiation* (DR), that may have escaped detection to date. Taking the present energy density in dark matter, $\rho_{\rm DM}$, as a calibration point, DR may contribute as much as several per cent, $\rho_{\rm DR} \lesssim 0.1\rho_{\rm DM}$, while still being allowed by gravitational cosmological probes [36]. When compared to the present number (average energy) of cosmic microwave background (CMB) photons, $n_{\rm CMB}$ ($\langle E_{\rm CMB}\rangle$), this implies that

$$\frac{\langle E_{\rm DR}\rangle}{\langle E_{\rm CMB}\rangle} \lesssim 500\frac{n_{\rm CMB}}{n_{\rm DR}}. \tag{1}$$

Hence, at the expense of having much less DR quanta than CMB photons $n_{\rm DR} \ll n_{\rm CMB}$, their typical energy may be significantly larger, $\langle E_{\rm DR}\rangle \gg \langle E_{\rm CMB}\rangle$. If the energy is in the several tens of MeV ballpark, DR neutrinos induce keV-scale nuclear recoils in direct detection experiments that are principally detectable, and, by extension, also alter the standard expectations for the neutrino floor in DM detection.

In fact, the neutrino energy range between 15–100 MeV is of particular interest because it is a window of opportunity—framed by solar and atmospheric neutrino fluxes at the respective low- and high-energy ends—to search for the diffuse supernova neutrino background (DSNB) [37,38]. Its non-observation to-date puts a limit on the flux of electron antineutrinos $\phi(\bar\nu_e) < 3\,/\mathrm{cm/s}$ [39], and an upper limit on a cosmological ν_e flux from DM decay in this window has been established with Super-Kamiokande (SK) data in [40]; see also [41].[1] In this work, we shall consider that (a component of) DM decays into neutrinos ν but not anti-neutrinos $\bar\nu$.

[1] Limits on the $\nu + \bar\nu$ flux from MeV-mass DM annihilation have been derived in [42]. Fluxes of new stable decay products, "boosted DM" from DM decay or annihilation have e.g. been considered in [43,44,44].

This possibility has been analyzed in some generality in a previous work by some of us [45], where constrains on the combination of lifetime and progenitor mass from neutrino and direct detection experiments have been derived.[2] In this work we explore in detail the DR detectability and the consequences on the DM neutrino floor in the allowed regions of parameter space.

The paper is organized as follows: in Sect. 2 we establish the principal DR fluxes from DM decay, in Sect. 3 we introduce the neutrino-induced event rates at direct detection experiments and list the standard neutrino fluxes, in Sect. 4 we establish the statistical tools for quantifying the principal reach for DM or DR discovery. The main results are then presented in Sect. 5 before concluding in Sect. 7.

2 Dark radiation from DM decay

We consider the possibility that non-thermal DR is made of neutrinos, either from the Standard Model (SM) or of a new type, that originate from the decay of an unstable DM progenitor X. Due to cosmological constraints [36,47,48], we restrict ourselves to DR scenarios, where only a fraction f_X of the total DM abundance injects monochromatic neutrinos via two body decays of a lepton-number carrying Majoron-type scalar relic $X \to \nu\nu$; a description of such asymmetric model is provided in the original paper [45]. As we are principally interested in neutral current processes, the flavor evolution of injected neutrinos is of no relevance.

The DR flux arriving at the Earth is by and large a combination of two components, the galactic flux $\Phi_{\nu,\rm gal}$ and the extra-galactic flux $\Phi_{\nu,\rm e.gal}$. Assuming no directional sensitivity, for a DM particle X with lifetime τ_X and mass m_X decaying within the Milky Way, the differential galactic flux is given by,

$$\frac{d\Phi_{\nu,\rm gal}}{dE_\nu} = \frac{N_\nu\, f_X}{\tau_X m_X}\, e^{-\frac{t_0}{\tau_X}}\, r_\odot \rho_\odot \langle J_{\rm dec}\rangle \delta(E_\nu - E_{\rm in}), \tag{2}$$

where $t_0 = 13.787 \pm 0.020$ Gyr is the age of the universe, $N_\nu = 2$ is the number of neutrinos in final state, $E_{\rm in} = m_X/2$ is the injection energy, $r_\odot = 8.33$ kpc is the distance between the observer at the Earth and the galactic center, $\rho_\odot = 0.3\ \mathrm{GeV/cm^3}$ is the local DM density and $\langle J_{\rm dec}\rangle \approx 2.19$ is the angular averaged J-factor obtained from an NFW profile [49]. Compared to t_0, Eq. (2) probes the amount of DM that is decaying "today." For staying in line with [45], we largely present results for $f_X = 0.1$, but explore smaller, cosmologically better compatible fractions as well.

[2] DR-induced direct detection signals from sterile neutrino decay have recently been studied in [46], however these predictions are challenged by existing experimental limits [45].

In contrast, DR that arrives from cosmological distances probes the decaying DM fraction at a time $t_{\rm dec} \le t_0$, or, in terms of redshift, at $z \ge 0$. Hence, the extra-galactic flux is assembled by contributions from all redshifts. To estimate this flux, remember that neutrinos arriving at the Earth with relativistic energy $E_\nu = |\vec{p}_\nu|$ were emitted with higher energy $E_\nu^{\rm em} = E_\nu(1+z)$. The energy-differential extra-galactic flux is then obtained via a redshift integral, which for monochromatic injection can be resolved [45],

$$\frac{d\Phi_{\nu,\rm e.gal}}{dE_\lambda} = N_\nu \frac{f_X\, \Omega_{\rm dm}\rho_{\rm crit}}{H_0 m_X \tau_X} \frac{1}{|\vec{p}_\nu|} \times \frac{1}{\sqrt{\alpha^3\Omega_M + \Omega_\Lambda}} e^{-\frac{t(\alpha-1)}{\tau_X}} \Theta(\alpha - 1), \tag{3}$$

where $\alpha = E_{\rm in}/E_\nu \ge 1$. We set the density parameters $\Omega_{\rm dm}h^2 = 0.12$, $\Omega_M = 0.315$, $\Omega_\Lambda = 1 - \Omega_M$ consistent with the ΛCDM model of a flat Universe. $H_0 = 100h$ km/s/Mpc and $\rho_{\rm crit} = 3H^2/(8\pi G)$ are the Hubble parameter and critical density at the present time with $h = 0.674$ [50].[3] Considering DM lifetimes such that its decay proceeds after matter-radiation equality, we are allowed to neglect the radiation content of the Universe and may find an analytic expression for the cosmic time $t(z)$,

$$t(z) = \int_z^\infty \frac{dz'}{(1+z')H(z')} = \frac{1}{3H_0\sqrt{\Omega_\Lambda}} \ln \left| \frac{\sqrt{1+(1+z)^3\frac{\Omega_M}{\Omega_\Lambda}} + 1}{\sqrt{1+(1+z)^3\frac{\Omega_M}{\Omega_\Lambda}} - 1} \right|, \tag{4}$$

where $H(z) = H_0\sqrt{(1+z)^3\Omega_M + \Omega_\Lambda}$ is the Hubble rate at redshift z. In this way, a connection between the elapsed time and the redshift is established. Equations (2) and (3) are also applicable for any two body massive final states with replacement $E_\nu \to \sqrt{m_\nu^2 + |\vec{p}_\nu|^2}$, where m_ν, p_ν are the mass and momenta of the massive species [45].

The total DR flux $\Phi_{X2\nu} = \Phi_{\nu,\rm gal.} + \Phi_{\nu,\rm e.gal}$, a sum of the galactic and extra-galactic component, is obtained by integration over E_ν. The galactic flux reads,

$$\Phi_{\nu,\rm gal} = N_\nu \frac{f_X}{\tau_X m_X} e^{-\frac{t_0}{\tau_X}} r_\odot \rho_\odot \langle J_{\rm dec}(\theta)\rangle. \tag{5}$$

One may in fact also obtain a useful analytic expression for the extra-galactic flux for the two-body decay with relativistic final states (see Appendix A),

$$\Phi_{\nu,\rm e.gal} = N_\nu \frac{f_X\, \Omega_{\rm dm}\rho_{\rm crit}}{m_X} \times \left[1 - \left(\frac{\sqrt{\Omega_M/\Omega_\Lambda + 1} + 1}{\sqrt{\Omega_M/\Omega_\Lambda + 1} - 1} \right)^{-\frac{1}{3H_0\sqrt{\Omega_\Lambda}\tau_X}} \right] \simeq N_\nu \frac{f_X\, \Omega_{\rm dm}\rho_{\rm crit}}{m_X} \times \begin{cases} 1 & \tau_X \ll t_0 \\ (H_0\tau_X)^{-1} & \tau_X \gg t_0 \end{cases}, \tag{6}$$

where $\rho_{\rm crit}$ is the Universe's critical energy density today. In the last relation we show the asymptotic scaling for short and long lifetimes, respectively. For $\tau_X \gg t_0$ the coefficient is close to unity within 5% because of a numerical cancellation of the value of a logarithm with its prefactor once Ω_M and Ω_Λ are plugged in. The extra-galactic flux hence asymptotically approaches a maximum for lifetimes $\tau_X \lesssim t_0$, and can be parametrised as

$$\Phi_{\nu,\,\rm e.gal}^{\rm max} \simeq 1.5 \times 10^5 \left(\frac{f_X}{0.1}\right)\left(\frac{50\,\rm MeV}{m_X}\right) \rm cm^{-2}\, s^{-1}. \tag{7}$$

In Fig. 1, we exemplify the DR fluxes originating from galactic (dashed lines) and extra-galactic (solid lines) components for various progenitor masses m_X assuming a 10% mass-fraction of decaying DM, i.e. $f_X = 0.1$. As both fluxes are inversely proportional to progenitor mass, for a fixed progenitor lifetime the flux decreases as progenitor mass increases. For large lifetime, both galactic and extra-galactic fluxes fall as $1/\tau_X$, for small lifetime, the galactic flux diminishes exponentially, whereas the extra-galactic flux asymptotes to a constant value $N_\nu f_X \Omega_{DM}\rho_{crit}/m_X$. This is manifest from (6) and is easily understood: a *complete* decay of X at some early redshift z corresponds to a mere transferal from one particle species (X) to another (2ν) with the comoving number of their sum being conserved. "Early DR" originates from a cosmological DM density that is larger by a factor $(1+z)^3$, hence compensating for the flux dilution by a factor $(1+z)^{-3}$ from area expansion and increase in the time-interval of subsequent particle arrivals. For $\tau_X \ll t_0$, the total extragalactic flux becomes hence independent of progenitor lifetime. Nevertheless, given the finite energy thresholds of any experiment, the number of "active" neutrinos in a detector diminishes for ν originating at high redshift, because of their redshifting in energy. The maximum flux (as the sum of galactic and extragalactic contributions) is attained when $\tau_X \sim t_0$. Finally, it is interesting to note that the galactic flux is a double-valued function in m_X: for a fixed progenitor mass, the same flux is attained for two different progenitor lifetimes. As we will see later this feature leads to interesting consequences for the experimental sensitivity to DR.

[3] There is a well-known current discrepancy between the CMB-inferred value of H_0 and the distance ladder estimates from SNIa [51] (among other, more recent local measurements). Our results only depend mildly on the adopted value of H_0, but we note that decaying DM scenarios such as the one considered here can alleviate this tension [52,53].

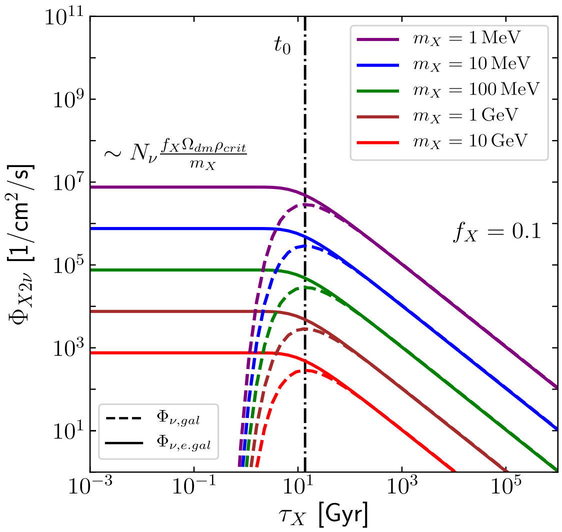

Fig. 1 The integrated neutrino flux originating from galactic (dashed lines) and extra-galactic (solid lines) components for different DM masses m_X as a function of DM lifetime. The flux has the general $1/m_X$ scaling, is inversely proportional to progenitor lifetime for $\tau_X \lesssim t_0$ and the extragalactic component asymptotes to a constant in the converse limit. The maximum DR flux as the sum of solid and dashed lines is obtained for $\tau \sim t_0$

3 Signatures of DR at direct detection experiments

Dark radiation in the form of neutrinos produced by unstable progenitors as described in the previous section can potentially be detected at direct detection experiments at the Earth via neutrino-nucleus coherent scattering. Even in absence of such DR neutrinos, the neutrino-nucleus scattering at direct detection takes place due to neutrino fluxes arising from standard ambient neutrino sources. These include solar, atmospheric and supernova-generated neutrinos. We shall refer to those fluxes as the "standard" ones.

The standard neutrino fluxes adopted in this work together with their standard errors are listed in Table 1. For solar neutrinos we use the ones based on the chemical composition determination of [54].[4] While solar neutrinos dominate for $E_\nu \lesssim 20\,\mathrm{MeV}$, atmospheric and supernova neutrinos are otherwise the most important fluxes. There are no measurements of the atmospheric flux below 100 MeV and we use the results from a FLUKA simulation [57]. The DSNB neutrinos originate from Type II supernovae and their largest emission in all flavours takes place during the Kelvin–Helmholtz cooling phase. The prediction depends crucially on the star formation rate [58] as a function of redshift and in this work we use the analytical fit provided in [59]. The emission spectrum is expected to be thermal [60], with each neutrino component being assigned a specific temperature, $T_{\nu_e} \approx 4\,\mathrm{MeV}$, $T_{\bar{\nu}_e} \approx 5\,\mathrm{MeV}$, $T_x \approx 8\,\mathrm{MeV}$ ($x = \nu_\mu, \bar{\nu}_\mu, \nu_\tau, \bar{\nu}_\tau$). Finally, we note in passing that reactor- and geo-neutrinos are location dependent and relatively small, and we neglect them in this work.

The second relevant aspect is the differential recoil cross section of neutrinos on atomic nuclei. Within SM, the process is mediated by neutral current interactions for spin-independent scattering and can be written as

$$\frac{d\sigma_{N\nu}(E_\nu, E_R)}{dE_R} = \frac{Q_W^2 G_F^2\, m_N F^2(|\vec{q}\,|)}{4\pi}\left[1 - \frac{E_R m_N}{2E_\nu^2}\right], \tag{8}$$

where $G_F = 1.1663787(6) \times 10^{-5}\,\mathrm{GeV}^{-2}$ is the Fermi constant, $Q_W = (4\sin^2\theta_W - 1)Z + N$ is the weak charge of the nucleus and E_ν is the neutrino energy. The differential cross section is primarily a function of number of Neutrons (N) because of a near cancellation in the charge (Z) dependent part of Q_W; $\sin^2\theta_W \approx 0.23$ is the weak angle. The degree of coherence is given by the Helm form factor $F(|\vec{q}|)$ [64] where $\vec{q}$ is the three-momentum transfer to the nucleus.

As a second possibility we shall consider the case that X decays into a pair of new neutrinos ν_B which interact with baryon number through a new vector particle of mass m_V and gauge coupling g_B [65]. The effective description amounts to a four-fermion interaction $\mathcal{L} = -G_B(\bar{\nu}_B\gamma_\mu\nu_B)J_B^\mu$ where $J_\mu^B = \bar{n}\gamma^\mu n + \bar{p}\gamma^\mu p$ is the baryon current and $G_B = q_\nu g_B^2/m_V^2$ with q_ν being the charge of ν_B under $U(1)_B$. In the following we shall only be concerned with relativistic states and we may take the mass of the new neutrino to zero, $m_\nu \to 0$, so that $|\vec{p}_\nu| = E_\nu$. The nuclear recoil cross section is coherently enhanced with atomic number A^2 and then reads [45,65],

$$\frac{d\sigma_{N\nu}(E_\nu, E_R)}{dE_R} = \frac{A^2 q_\nu^2 g_B^4}{2\pi}\frac{m_N F^2(|\vec{q}|)}{(m_V^2 + 2m_N E_R)^2}\left[1 - \frac{m_N E_R}{2E_\nu^2}\right]. \tag{9}$$

For the sake of presentation, we shall only consider the case of a mediator that is heavy compared to the typical momentum transfer $|\vec{q}| = \sqrt{2E_R m_N}$, implying $m_V \gtrsim 100\,\mathrm{MeV}$ in practice. The phenomenology of this model has been explored in [66–70], and in this work we shall consider values $G_B \simeq G_F$ as a possibility to boost the direct detection phenomenology

[4] The results of this work are only mildly dependent on the solar opacity problem: the more recent determination [55] primarily affects the O, N, and F fluxes in addition to a 20% downward shift of the ^{8}B flux. We note in passing that for the last flux, being the most relevant in this context, the measurement [56] lies in between both low and metallicity determinations of [55] and [54], respectively.

Table 1 Adopted neutrino fluxes in this work; we follow [61–63] in their compilation of the fluxes (original works are referenced in the main text). Beside the fluxes, the endpoint or the maximally used energy together with the corresponding maximal nuclear recoil energies on a xenon target are given

Source	Flux Φ_ν [cm^{-2} s^{-1}]	$E_\nu^{\max}$ [MeV]	$E_{R,\nu}^{\max}$ [keV]
Solar			
pp	$5.98\,(1 \pm 0.006) \times 10^{10}$	0.42	2.9×10^{-3}
hep	$8.04\,(1 \pm 0.3) \times 10^{3}$	1.88	5.8
^{17}F	$5.52\,(1 \pm 0.17) \times 10^{6}$	1.74	5.0×10^{-2}
^{15}O	$2.23\,(1 \pm 0.15) \times 10^{8}$	1.73	4.9×10^{-2}
^{13}N	$2.96\,(1 \pm 0.14) \times 10^{8}$	1.20	2.4×10^{-2}
^{8}B	$5.58\,(1 \pm 0.14) \times 10^{6}$	16.6	4.5
^{7}Be (line 1)	$4.50\,(1 \pm 0.07) \times 10^{8}$	0.384	2.4×10^{-3}
^{7}Be (line 2)	$5.00\,(1 \pm 0.07) \times 10^{9}$	0.861	1.2×10^{-2}
pep (line)	$1.44\,(1 \pm 0.012) \times 10^{8}$	1.44	3.4×10^{-2}
Atmospheric			
ν_e	$1.27\,(1 \pm 0.2)$	10^3	> 100
$\bar{\nu}_e$	$1.17\,(1 \pm 0.2)$	10^3	> 100
ν_μ	$2.46\,(1 \pm 0.2)$	10^3	> 100
$\bar{\nu}_\mu$	$2.45\,(1 \pm 0.2)$	10^3	> 100
DSNB			
ν_e (fid)	$22.12\,(1 \pm 0.5)$	100	> 100
$\bar{\nu}_e$ (fid)	$17.69\,(1 \pm 0.5)$	100	> 100
ν_x (fid)	$11.06\,(1 \pm 0.5)$	100	> 100

of DR.[5] Current limits on G_B arise from rare meson and Z-decays such as $K \to \pi V$, $B \to KV$ and $Z \to V\gamma$ [68,71], respectively, monojet searches [72,73], as well as from neutrino facilities [67,74]. For example, for $m_V = 300\,\text{MeV}$ the most stringent guaranteed constraints come from MiniBooNe, requiring $G_B \lesssim 500 G_F$. The limits significantly tighten by an enhancement of longitudinal V emission when baryon-number is broken by the chiral anomaly, essentially ruling out $G_B > G_F$ [68,71]. Although those limits are fairly robust, they may also be evaded depending on the anomaly-canceling UV completion of the model [68], and, $G_B > G_F$ remains a possibility that we entertain as the most optimistic case in this work. The differential recoil rate introduced by neutrinos of source i is therefore given by

$$\frac{dR_i(E_R)}{dE_R} = N_T \int_{E_{\nu,\min}}^{E_\nu^{\max}} dE_\nu \, \frac{d\Phi_{\nu,i}(E_\nu)}{dE_\nu} \frac{d\sigma_{N\nu}(E_\nu, E_R)}{dE_R}. \tag{10}$$

where $E_{\nu,\min} = \sqrt{E_R m_N/2}$ is the minimum neutrino energy to produce a recoil on a target of mass m_N; $E_\nu^{\max}$ is the maximum energy neutrinos of source i can have. In case of DR, $E_\nu^{\max}$ is given by endpoint energy of the source $E_{in} = m_X/2$. The number of target nuclei per unit mass of detector material is denoted by N_T. The total rate in a detector will then be the sum over all isotopic compositions of relevant elements and over all neutrino sources i. We shall denote by $dR_\nu(E_R)/dE_R$ the total rate over all "standard" sources and by $dR_{X2\nu}(E_R)/dE_R$ the DR-induced non-standard recoil rate. The latter carries two contributions, from galactic and extragalactic fluxes, respectively. An analytic expression for the differential recoil rate for the extragalactic flux can be obtained and is given in Appendix A.

The maximum nuclear recoil energy from DR is derived from kinematics and depends on the mass of the progenitor,

$$E_{R,X2\nu}^{\max} = \frac{2(E_\nu^{\max})^2}{2E_\nu^{\max} + m_N} \simeq \frac{m_X^2}{2m_N} \quad (m_X \ll m_N), \tag{11}$$

where $E_\nu^{\max} = E_{\text{in}}$ is the neutrino energy at injection. It is worth noticing that the end point of recoil energy is directly proportional to the square of progenitor mass.

[5] Besides DM decay, ν_b can be generated from oscillation or through direct production. The former contribution is rendered unimportant when $\theta_b^2 G_B \ll G_F$ where θ_b is the new (small) mixing angle or by virtue of an astronomical oscillation length that prevents their appearance in terrestrial or solar fluxes [24]. The direct production of ν_b may likewise be neglected for the purpose of this study: any atmospheric ν_b-yield competes with the QCD production of mesons and is much smaller; any thermal solar ν_b flux (e.g. through proton–proton bremsstrahlung) is undetectable on the account of keV-scale energies, as is its SM counterpart. Finally, a DSNB in ν_b is an interesting possibility, but the final spectrum is expected to be suppressed both in energy and overall flux because of a very efficient trapping inside the supernova. Out of these reasons we expect little to none interference with the DR fluxes and therefore neglect those additional contributions.

The expected recoil rate is then given by the integral over the recoil energy,

$$\mu_{X2\nu} = \sum_{i=\text{gal,e.gal}} \int_{E_{R_{\text{thr}}}}^{E^{\max}_{R,X2\nu}} dE_R \, \frac{dR_i}{dE_R}, \tag{12}$$

where $E_{R_{\text{thr}}}$ is the threshold of the detector.

As an example, consider the recoil rate induced by a progenitor of 100 MeV mass decaying to SM neutrinos in a liquid xenon detector with negligible nominal 1 eV threshold. Notwithstanding a general dependence on recoil energy, saturating the possible DR fluxes, we find that the differential rate is bounded from above by

$$\frac{dR_{X2\nu}}{dE_R} \lesssim \left(\frac{100\,\text{MeV}}{m_X}\right) \begin{cases} 11 \text{ keV}^{-1} \text{ ton}^{-1} \text{ year}^{-1} & \text{(gal.)} \\ 18 \text{ keV}^{-1} \text{ ton}^{-1} \text{ year}^{-1} & \text{(e.g.)} \end{cases}.$$

This implies for the total detectable rate,

$$\mu_{X2\nu} \lesssim \left(\frac{100\,\text{MeV}}{m_X}\right) \begin{cases} 80 \text{ ton}^{-1} \text{ year}^{-1} & \text{(gal.)} \\ 124 \text{ ton}^{-1} \text{ year}^{-1} & \text{(e.g.)} \end{cases},$$

and demonstrates that for a given progenitor mass, there is a natural ceiling on the event rate when considering DR in form of SM neutrinos.

In Fig. 2, we show exemplary differential recoil rates in xenon introduced by DR in form of SM neutrinos for a progenitor mass of 60 MeV in comparison with the differential recoil rate due to standard neutrino fluxes. The progenitor lifetime takes on values from 10^{-3} Gyr to 10^4 Gyr. Heavier progenitor particles introduce larger recoil energies at direct detection experiments, as the recoil endpoint energy is controlled by m_X. Generally speaking, $m_X \gtrsim 30$ MeV is required to exceed solar neutrino-induced events—in particular the ones induced by ^{8}B neutrinos—because of the principal limitations in the magnitude of incident DR flux.

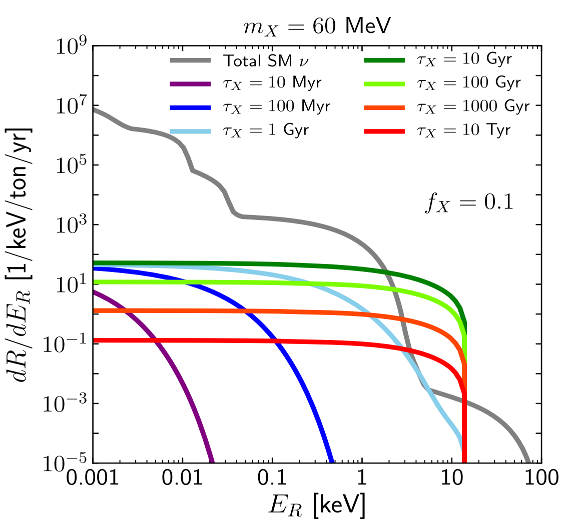

Fig. 2 Energy differential recoil rate on xenon induced by standard fluxes (gray line) and induced by DR originating from a progenitor with $m_X = 60$ MeV and various lifetimes as labeled (colored lines)

The latter point is further exacerbated by the fact that for a percent-level decaying fraction of DM we find that there is *no* combination of (τ_X, m_X) such that the total DR-induced event rate in xenon is larger than the one from ^{8}B neutrinos,

$$R(\text{DR}) < R(^8\text{B}) \quad (E_{R_{\text{thr}}} \ll 1\,\text{keV},\ m_X > 1\,\text{MeV}). \tag{13}$$

While it is well known that approximately 6 GeV mass WIMP recoils mimic ^{8}B neutrino recoils, we find that DR induced neutrino recoils from 2-body DM decay can neither mimic nor exceed the latter. This puts a principal limitation on the detectability/influence of DR in direct detection experiments: any set of prospective parameters must be such that the DR flux has a component that exceeds the ^{8}B flux in energy, hence pointing to $m_X \gtrsim 30$ MeV.[6]

Before discussing the employed statistical framework, for completeness, we close this section by reviewing the DM (χ) signal hypothesis, which has not been discussed so far. The total event rate of DM recoils at the direct detection experiments, integrated over the differential recoil spectrum dR_χ/dE_R reads

$$\begin{aligned} \mu_\chi &= \int_{E_{\text{thr}}} \frac{dR_\chi}{dE_R} \, dE_R \\ &= N_T \sigma_n \frac{\rho_\chi}{m_\chi} \frac{m_N}{2m^2_{\chi,n}} A^2 \int_{E_{\text{thr}}} dE_R \, F^2(|\vec{q}\,|) \int_{|\vec{v}\,| \geq v_{\min}} d^3\vec{v} \, \frac{f(\vec{v}\,)}{v}. \end{aligned} \tag{14}$$

In the second equality, we make the assumption of a standard spin-independent DM-nucleus interaction of contact type. The local DM mass density is $\rho_\chi \simeq 0.3\,\text{GeV/cm}^3$ and m_χ ($\mu_{\chi,n}$) is the DM (reduced DM-nucleon) mass and σ_n is the DM-nucleon scattering cross-section with equal coupling to protons and neutrons. At last, $f(\vec{v}\,)$ is the normalized galactic Maxwell–Boltzmann velocity distribution with $v_0 = 220$ km/s, truncated at the escape velocity $v_{\text{esc}} = 544$ km/s and boosted into the detector frame with $v_{\text{lab}} = 232$ km/s. Detector specifics are only entering via the recoil threshold energy E_{thr} and assume 100% efficiency of detection for $E_R \geq E_{\text{thr}}$, ignoring finite energy resolution effects. Furthermore, for our purposes it is sufficient to integrate the

[6] More precisely, if the statistical error bar on the ^{8}B-induced events becomes smaller than the DR-induced event rate, one may actually subtract the ^{8}B background and DR becomes detectable. This is seen by the extra island at $m_X \simeq 10$ MeV in left Fig. 5 for the futuristic exposure of 100 ton-year (see below).

differential recoil rate up to a recoil energy of 100 keV. It should be noted that μ_χ, μ_ν, and $\mu_{X2\nu}$ represent recoil rates per detector mass and live-time and need to be multiplied by detector exposure ε to get the total number of observed events.

We now introduce the formalism to make quantitative statements on sensitivity of direct detection experiments to DR and its influence on the observation of a potential WIMP signal.

4 The principle reach of direct detection experiments

To forecast sensitivity of an experiment, there are two seemingly similar, yet distinct questions to address: the first regards the ability to exclude the presence of a signal and the second regards the ability to discover the signal. The exclusion and discovery exercises can in turn be performed either assuming no backgrounds or in the presence thereof.

The purpose of this work is to see to what extent direct detection experiments can discover DR. Furthermore, we like to quantify the reach of direct detection experiments to a DM signal in presence of DR in addition to the standard neutrino background. We therefore deal with two different signal and background hypotheses, one which involves DR recoils as signal and standard neutrino sources as background and one which involves a DM signal and DR plus standard neutrino sources as backgrounds. In each case, we are interested in understanding the exclusion potential and discovery reach. The methodology we outline below closely follows previous work on the neutrino floor in direct detection [7]; for an alternative approach see e.g. [75].

4.1 DR exclusion potential of direct detection experiments

In this part, we set up the formalism to obtain the potential of direct detection experiments to exclude a DR signal for as long as backgrounds remain absent. This situation can be dealt with easily, and we outline it below; the signal hypothesis in the presence of background will be dealt with using the likelihood approach as in Sect. 4.2.

For a single channel counting experiment, the probability to observe n events, when λ events are expected is given by the Poisson distribution $\mathrm{Pois}(n|\lambda) = \lambda^n e^{-\lambda}/n!$. In general, λ can be the expected number of signal events $\varepsilon\mu_{X2\nu}$, background events, or their sum. For zero observed events, $n = 0$, and zero expected background, the 90% CL upper limit on λ is obtained from a p-value $p_\lambda = 0.1$, corresponding to a 10% probability that the outcome of an experiment is at least as extreme as observed. It is then related to the confidence level via $p_\lambda \leq 1-\mathrm{CL}$. Solving $p_\lambda = \mathrm{Pois}(0|\lambda)$ for λ yields $\lambda = 2.3$ as usual.

In a background-free experiment with threshold energy E_{thr} and exposure ε, the 90% CL exclusion contour in the (m_X, τ_X)-plane is found by evaluating (12) under the condition $\varepsilon\mu_{X2\nu} = 2.3$. The strongest exclusion that can be obtained in such background-free scenario, is the one where the exposure grows to the level that the first irreducible neutrino background event is seen,

$$1 \stackrel{!}{=} \varepsilon(E_{\mathrm{thr}})\,\mu_\nu = \varepsilon(E_{\mathrm{thr}}) \int_{E_{\mathrm{thr}}} dE_R\, \frac{dR_\nu}{dE_R}. \tag{15}$$

Here we have highlighted the threshold-dependence of the required exposure, $\varepsilon(E_{\mathrm{thr}})$; the neutrino-induced recoil rate is given by the sum over all "standard sources" in Eq. (10).

Later we shall also consider the possibility that DR is present as additional "background," and we wish to understand how it impacts the standard literature results on the DM neutrino floor [7]. The condition for when background starts limiting the DM in the presence of DR search reads $1 \stackrel{!}{=} \varepsilon(E_{\mathrm{thr}})\,[\mu_\nu + \mu_{X2\nu}]$ in an obvious modification to (15).

4.2 DR discovery potential of direct detection experiments

While the procedure described above is applicable in the zero background scenario, the upcoming/ongoing ton scale direct detection experiments with large exposures will not remain background free. These backgrounds which originate from standard neutrino recoils suffer from uncertainties in the measured neutrino fluxes (see Table 1) and which need to be taken into account when charting out the discovery reach of an experiment.

We assume that observed spectra of events are composed from signal and background sources. As such, they enter the generalized Poisson likelihood,

$$\mathcal{L}_{\mathrm{events}}(\vec{\theta}|\mathrm{H}) = \frac{e^{-\varepsilon \sum_\alpha \mu_\alpha(\vec{\theta})}}{N_{\mathrm{obs}}!} \prod_{i=1}^{N_{\mathrm{obs}}} \varepsilon \sum_\alpha \frac{dR_\alpha(E_{R_i}, \vec{\theta})}{dE_R}, \tag{16}$$

where the sum over sources α depends on the hypothesis under question; model parameters such as m_X and τ_X are part of the vector $\vec{\theta}$. In our simulations, the individual recoil events E_{R_i} are random numbers, a total N_α of them drawn for each source α from the probability density function (PDF) $\mu_\alpha^{-1} dR_\alpha/dE_R$. Note that N_α itself is a Poisson random number with mean value $\epsilon\mu_\alpha$. Finally, $N_{\mathrm{obs}} = \sum_\alpha N_\alpha$ is the total number of observed events.

When a source of events is declared a background under the considered hypothesis their associated fluxes become a nuisance parameter. Concretely, we model the flux uncertainties as Gaussians with mean $\langle\phi_\beta\rangle$ and variance σ_β^2,

$$\mathcal{L}_{\mathrm{bg-flux}}(\vec{\theta}) = \prod_\beta \mathrm{gauss}(\phi_\beta | \langle\phi_\beta\rangle, \sigma_\beta^2). \tag{17}$$

Here, the product is over all background sources β and the random variables ϕ_β are part of $\vec{\theta}$. For the standard neutrino sources the mean values $\langle\phi_\beta\rangle$ together with their standard errors are listed in Table 1. When DR is considered as a background, we take $\langle\phi_{X2\nu}\rangle = \Phi_{\nu,\text{e.gal}} + \Phi_{\nu,\text{gal}}$ and assume $\sigma_{X2\nu} = 0.3$. The assignment of a 30% uncertainty is somewhat arbitrary, but meant to be conservatively reflective of overall astrophysical uncertainties concerning DM-induced DR fluxes. Taken together, the total likelihood becomes,

$$\mathcal{L}(\vec{\theta}|\text{H}) = \mathcal{L}_{\text{events}}(\vec{\theta}|\text{H}) \times \mathcal{L}_{\text{bg-flux}}(\vec{\theta}) \tag{18}$$

For a given threshold energy E_{thr} and exposure ε and for every point $\vec{\theta}$ in the parameter space, we then generate several hundred mock realizations to build a statistical sample. Each of these realisations we refer to as an "experiment".

We now spell out the signal and background hypotheses that we are considering in this work:

(1) DR signal with standard neutrino backgrounds: The first step is to explore the DR discovery potential of direct detection experiments. Hence, we treat the DR recoils as signal in the presence of standard neutrino backgrounds but in absence of DM-induced events. The null hypothesis is H_0: $\sigma_n = 0$ and $\tau_X \to \infty$ and the alternative hypothesis becomes H_1: $\sigma_n = 0$ and finite τ_X. We therefore take the sums in Eqs. (16) and (17) $\alpha = X2\nu,\ \nu_j$ and $\beta = \nu_j$, respectively. In the baryonic neutrino scenario, we fix G_B to an exemplary value.

(2) WIMP signal/no DR background: As a validation procedure we may also consider the complete absence of any DR. This allows us to recover the standard result on the neutrino floor in the (σ_n, m_χ)-plane [7]. In order to *discover* a WIMP signal, the background only hypothesis H_0: $\sigma_n = 0$ must rejected; the alternative hypothesis is H_1: $\sigma_n > 0$. We take $\alpha = \text{DM}, \nu_j$ in Eq. (16) and $\beta = \nu_j$ in Eq. (17) to minimize the likelihood ratio (19).

(3) WIMP signal with DR background: The final alternative is to switch on DR as an additional source of background and study the influence on the WIMP discovery region. The background only hypothesis remains H_0: $\sigma_n = 0$ and the alternative hypothesis is again H_1: $\sigma_n > 0$, but now we take the sums in Eqs. (16) and (17) to include DR, i.e. $\alpha = \text{DM},\ X2\nu,\ \nu_j$ and $\beta = X2\nu,\ \nu_j$, respectively. We fix progenitor mass and lifetime for this procedure.

Once H_0 and its alternative H_1 are chosen, one may then proceed in standard fashion and use the negative log-likelihood as test statistic for each experiment [76],

$$q = -2\ln\frac{\mathcal{L}(\hat{\hat{\vec{\theta}}}|\text{H}_0)}{\mathcal{L}(\hat{\vec{\theta}}|\text{H}_1)}, \tag{19}$$

where $\hat{\hat{\vec{\theta}}}$ maximizes the likelihood under the background-only hypothesis H_0 and $\hat{\vec{\theta}}$ maximizes $\mathcal{L}$ for signal plus background, H_1. The distribution of q under H_0 asymptotically follows a χ^2-distribution with one degree of freedom as per Wilk's theorem [77]. The p_0-value then characterizes the probability that the background-only hypothesis H_0 is excluded if the q-value is greater than the "observed value" q_{obs},

$$p_0 = \text{P}(q \geq q_{\text{obs}}|\,\text{H}_0) = \int_{q_{\text{obs}}}^{\infty} dq\ f(q|\,\text{H}_0), \tag{20}$$

where $f(q|\,\text{H}_0)$ is the PDF of q under H_0. We obtain the latter by Monte Carlo generation of mock data. In terms of significance $Z = \sqrt{q}$, given in units of standard deviations, the p_0-value is obtained by the cumulative standard normal distribution $\Phi(x)$,

$$p_0 = \text{P}(Z \geq \text{Z}_{\text{obs}}|\,\text{H}_0) \simeq 1 - \Phi(\text{Z}_{\text{obs}}). \tag{21}$$

For a discovery with 3σ significance the corresponding p_0-value is given by $p_0 = 0.00135$. If data is observed in the critical region $Z \geq Z_{\text{obs}}$ the hypothesis H_0 is rejected. For the 3σ significance that we are interested in, $Z_{\text{obs}} = 3$. We have verified, that our generated background data satisfies $f(q|\,\text{H}_0) \sim \chi^2$.

In turn, the probability β for H_1 being rejected is defined by,

$$\beta = \text{P}(Z \leq \text{Z}_{90}|\,\text{H}_1) = \int_0^{\text{Z}_{90}} dZ\ f(Z|\,\text{H}_1), \tag{22}$$

where f is now the PDF of Z under H_1 and Z_{90} represents the significance that can be at least obtained 90% of the time in an experiment with data generated under H_1. Conversely, H_1 is accepted at a confidence level $1-\beta$. Assuming a confidence level of 90% the alternative hypothesis H_1 is excluded for $\beta = 0.1$. It is thus possible to find a value of signal with $1 - \beta = 0.9$, which leads to $Z_{90} \geq 3$. For this case, an experiment has a 90% probability to detect at least a 3σ signal.

Concretely, we generate between 250 and 500 Monte-Carlo data sets for the signal plus background hypothesis H_1 for each value of progenitor mass m_X or DM mass m_χ and for each lifetime τ_X or cross section σ_n. These data sets determine the significance distribution. The procedure is repeated for a range of lifetimes or cross sections until we obtain $Z_{90} = 3$ for $\beta = 0.1$ which corresponds to a 3σ discovery potential at 90% CL. We repeat this procedure until the entire parameter space is mapped out.

The formalism described above is not specific to any particular detector. As was shown above, DR fluxes from DM decay can compete with standard solar neutrino fluxes only above the ^{8}B endpoint energy. Dark radiation introduces changes to the standard picture in the recoil energy region where the large WIMP detectors have ample sensitivity and ultra-low thresholds are of little benefit. In the following, we will hence explore the formalism on the basis of ton-scale xenon experiments like the ones mentioned in the introduction.

5 DR exclusion and discovery

5.1 DR exclusion limits

We first establish the exclusion potential for DR in the presence of standard neutrino backgrounds. In the remainder of the paper we shall focus on the example of a liquid xenon detector. The operational procedure is then as follows: given the presence of standard neutrino fluxes, we first compute the DR limit at a fixed threshold by finding the exposure for which one background event as explained in Sect. 4.1 is seen. In a second step, the threshold is varied and the hull of all exclusion curves is obtained. The resulting contour in the (m_X, τ_X) plane then represents the optimal DR exclusion potential of the experiment when irreducible backgrounds are not dealt with.

Figure 3 shows the results of the procedure, i.e., the exclusion potentials for DR in form of SM neutrinos (left) and baryonic neutrinos (right) for threshold energies ranging from 0.01 keV up to 50 keV. In the region $\tau_X > t_0$ they are determined by the galactic and extra-galactic components whereas in the region $\tau_X < t_0$ only the extra-galactic flux contributes. The prospective regions are hence centered around t_0: for $\tau_X \gg t_0$ the flux is too small and for $\tau_X \ll t_0$ the extra-galactic flux becomes too soft. It is interesting to note that in the right panel of Fig. 3 below the *minimum* assumed threshold of 1.2 keV, DR in from of SM neutrinos cannot be excluded, as their induced events are superseded by solar neutrinos, especially the ones originating from the ^{8}B reaction. On the flip side, as the threshold increases, the experiment becomes more sensitive to higher energy recoils generated by larger m_X. Hence, in contrast to the WIMP case, and because of the general limitations in the DR flux in form of SM neutrinos, ever lower thresholds as they are sought in many direct detection experiments are not a beneficiary factor.

So far, for simplicity, we assumed $f_X = 0.1$ throughout. At this point, it is worthwhile exploring the impact of smaller values of f_X that remain cosmologically unconstrained. This is shown in Fig. 4, and one should bear in mind that the exclusion limits are iso-contour lines of 2.3 DR events at the optimal threshold-dependent exposure where a SM neutrino background starts to be seen. In the large lifetime region $\tau_X \gg t_0$, f_X only changes the overall flux normalization: a decrease in f_X hence demands a decrease in τ_X for a fixed progenitor mass m_X to attain the same number of events. In the small lifetime regime $\tau_X \ll t_0$, events are due to the extra-galactic component. Here the position of curves is rather determined by the fraction of flux that has not been redshifted below the relevant threshold value that is associated with the model-point (m_X, τ_X). Overall, it is a combination of factors that implies that the discovery reach is more slowly deteriorating with decreasing f_X. Finally, in the right panel, one additionally observes the strong decrease in sensitivity for $\tau_X \sim t_0$ with falling f_X. It happens because the ^{8}B background becomes visible before 2.3 DR events can be attained with smaller f_X at the associated exposure; this is the situation all along in the SM case (left panel) which does not have such "nose" feature even for $f_X = 0.1$. Similar conclusions with respect to a decrease in f_X will also hold for the discovery potentials discussed in the next section.

The exclusion potentials have to be put in perspective with the current sensitivity of multi-ton scale neutrino experiments. This has been explored previously in Ref. [45] and the gray shaded regions in Fig. 3 show the excluded regions in the DR progenitor plane (m_X, τ_X) from Super-Kamiokande and Borexino. The constraints included in the left panel of the Fig. 3 were derived from measurements of solar- and atmospheric fluxes [78,79], and from searches of DSNB neutrinos [39]. In the right panel of Fig. 3 the constraint was obtained by re-purposing a Borexino solar-axion search [80] to ν_B-induced elastic proton recoils; for further details on both cases see [45].[7] The inside of the curves labeled according to the assumed threshold correspond to a combination of parameters where we find that DR sourced by a DM progenitor is discoverable in a direct detection experiment.

In summary, except for relatively small regions located in the quadrant $m_X \lesssim 100$ MeV and $\tau_X > t_0$, neutrino experiments carry stronger current constraining power to SM DR than DM direct detection experiments will every have.

On the other hand, when we are to entertain new physics in the DR itself (in form of ν_B), direct detection sensitive to lower masses $m_X \lesssim 20$ GeV is gained as the threshold drops below 1 keV. But even with higher threshold values, and expanded region in τ_X at a given m_X can be covered.

5.2 DR discovery potential

We now turn our attention to the prospects of making a discovery of DR in the presence of irreducible backgrounds which are to be faced in the coming generation of direct detection experiments. Charting out the discovery regions will be achieved using the likelihood approach outlined in Sect. 4.2. Similarly to the previous section, we attempt at discovering DR recoils in presence of standard neutrino backgrounds.

[7] A bug in the derivation of the Borexino result lead to an erroneous area of exclusion in [45] which we correct here.

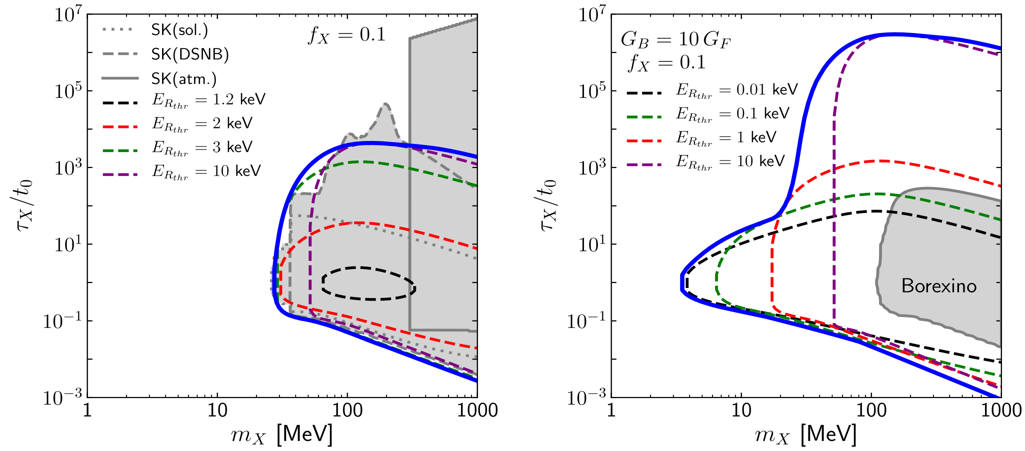

Fig. 3 Obtainable exclusion limits, for DR in form of SM neutrinos (baryonic neutrinos) in the left (right) panel, assuming $f_X = 0.1$. The various dashed curves assume different nuclear recoil energies as labeled. The thick blue line is the maximum of all curves. The gray areas in the left (right) panel show excluded regions from SK (Borexino) and are taken from [45]

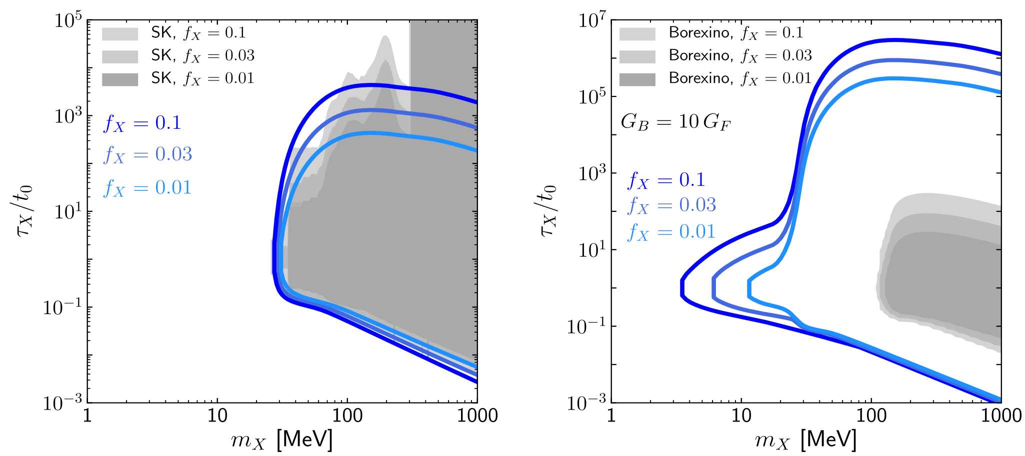

Fig. 4 Obtainable exclusion limits, for DR in form of SM neutrinos (baryonic neutrinos) in the left (right) panel, assuming $f_X = 0.1, 0.03, 0.01$. The gray areas in the left (right) panel show excluded regions from SK (Borexino) for different f_X and are taken from [45]

Importantly, such exercise requires specification of an experiment's exposure and threshold and is hence specific to these assumptions. In the following we choose $\varepsilon = 1$ ton-year and $E_{\rm thr} = 0.1$ keV to normalize on current collected data sets combined with an aggressive assumption on nuclear recoil threshold.

Figure 5 shows the result. We consider exposures up to 100 ton-year for a threshold of 0.1 keV for DR in form of SM neutrinos (left panel) and baryonic neutrinos (right panel). For the extreme case of 100 ton-year exposure, reflective of the sensitivity of future multi-ton xenon detectors such as DARWIN [17], we switch to a binned likelihood approach with $N_{\rm bin} = 50$. The limiting factors for the reach can be understood by analysing the most dominant background fluxes. In the bulk of the (m_X, τ_X) parameter space, hep neutrinos constitute the dominant background to DR. This is because hep neutrinos generate a large range of recoil energies with appreciable flux. Around 20 MeV progenitor mass, the ^{8}B neutrinos become the limiting factor. As can be seen in the left panel of Fig. 5, it is not possible to make a 3σ discovery of DR in form of SM neutrinos, unless a 100 ton-year exposure is assumed (and paralleling progress with neutrino detectors is neglected.) When ν_B are invoked

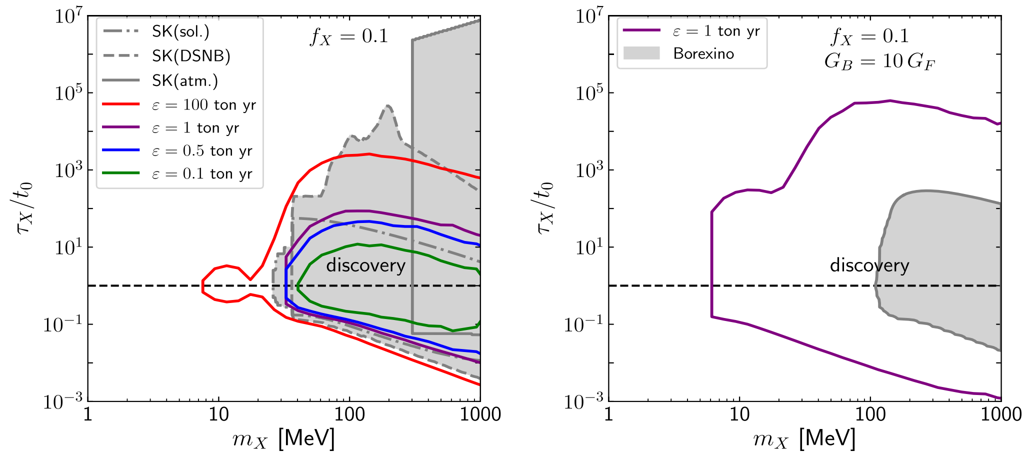

Fig. 5 Discovery limits at a 90% CL for a threshold $E_{R_{\rm thr}} = 0.1$ keV. Left panel: for DR in form of SM neutrinos. Right panel: for DR in form of baryonic neutrinos

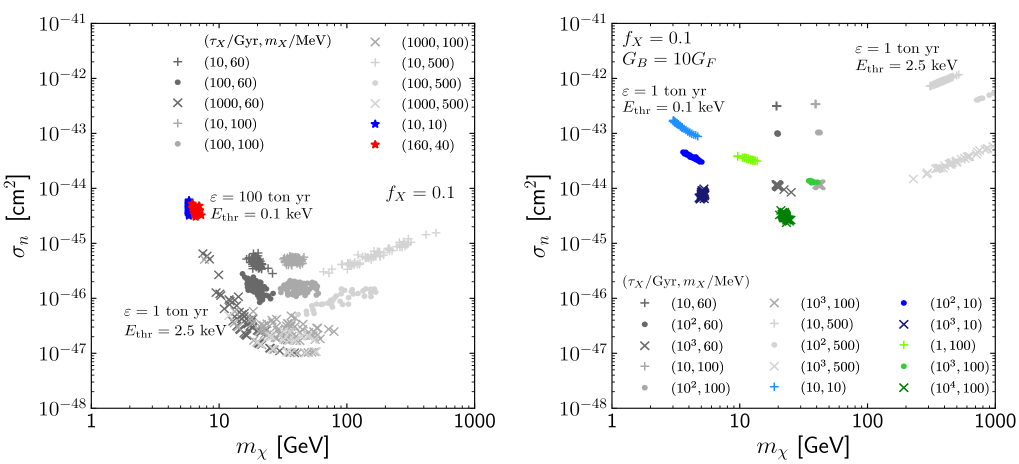

Fig. 6 The distribution of maximum likelihood parameters σ_n, m_χ under the DM hypothesis when they originate from DR with various combinations of (τ_X, m_X) in form of SM neutrinos (left panel) and baryonic neutrinos (right panel) instead. The gray points as labeled show excluded combinations of (τ_X, m_X) for an exposure of 1 ton year and threshold of $E_{\rm thr} = 2.5$ keV. The colored points show allowed combinations of (τ_X, m_X) for an exposure of 100 ton year and threshold of $E_{\rm thr} = 0.1$ keV

(right panel), they can still be discovered in a wide mass range with only 1 ton-year exposure.

6 DM direct detection in the presence of DR

6.1 Dark matter vs. dark radiation

Here we shall first consider the scenario in which a signal of DR origin is interpreted as DM. For this purpose, we generate one hundred mock-data sets where we inject a DR signal on top of the usual neutrino background. In order to study how such a false positive DM signal is seen, we fit the mock-data by a binned version of the DM-only likelihood for $\alpha =$ DM and find the best fit parameters σ_n, m_χ. The results of this procedure are shown in Fig. 6 where in the left (right) panel we consider SM (baryonic) neutrino DR. The gray dots and crosses show otherwise disfavored parameter points in (τ_X, m_X) that are within the discovery reach for a threshold of $E_{\rm thr} = 2.5$ keV but avoid the large ^{8}B background. In turn, the colored points and crosses are for allowed parameter combinations, but require a low threshold $E_{\rm thr} = 0.1$ keV for discovery and hence face a large solar neutrino background.

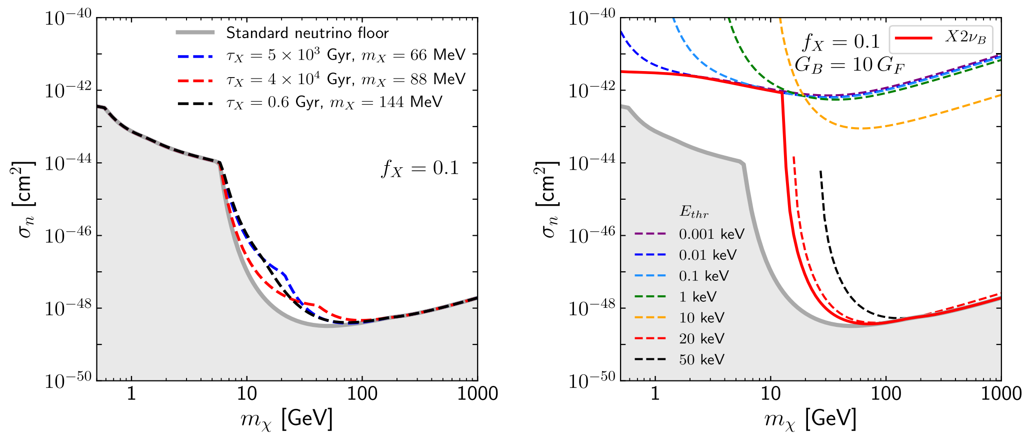

Fig. 7 The DM exclusion potential in the presence of DR in form of SM neutrinos for various exemplary currently allowed combinations of (m_X, τ_X) in the left panel and for ν_B with $m_X = 60$ MeV, $\tau_X = 10$ Gyr and $G_B = 10 G_F$ in the right panel; the gray region shows the standard result without DR. The various dashed lines show the limits for varying threshold energy for DR. The thick blue (red) curve as the minimum of all curves is the modified neutrino floor

The general trend in both panels is, that for larger progenitor masses m_X, mock-data is fitted by larger DM mass m_χ. The lifetime dependence of DR is primarily imprinted into a linear scaling of the cross section σ_n and the highest fitted cross section is given for $\tau_X \sim t_0$, when the DR flux is maximal. For some combinations (τ_X, m_X) for DR in form of baryonic neutrinos, the cross section is even higher due to the enhancement $A^2 G_B^2$ in the neutrino cross section. For SM DR (left panel) the most important feature in the misidentification is that when the DR flux diminishes, the fitted points start tracing out the boundary of the neutrino floor. When the smaller threshold is considered, all fits indeed center in on the ^{8}B tip, at $(\sigma_n, m_\chi) \sim (4 \times 10^{-45}$ cm^2, 6 GeV), of the neutrino floor. This shows that although SM DR can be discovered with 3σ significance in an experiment with exposure $\varepsilon = 100$ ton year as shown in the previous section, it requires a careful statistical analysis that goes beyond the naive fits presented in this section, for which one would rather make the erroneous conclusion of only facing the neutrino floor. For the baryonic case (right panel) the prospects are better in the sense, that a naive fitting would largely point to a new physics signal (even if misinterpreted in term of its origin.)

6.2 DM exclusion potential in presence of DR

Next we consider the modifications to the exclusion potential for DM when DR neutrinos become a source of additional background. The procedure is similar to before: given the presence of an anomalous neutrino flux, we first compute the best DM limit at a fixed threshold by finding the exposure for which one background event is seen. Varying the threshold, the minimum value of σ_n for each m_χ, is obtained.

In the left panel of Fig. 7, the results for various currently allowed (m_X, τ_X) combinations are shown. In the right panel, a progenitor mass of 60 MeV, and lifetime of 10 Gyr decaying into ν_B with $G_B = 10 G_F$ is shown. The various dashed curves show the best limit on σ_n for various assumed thresholds, from 1 eV to 50 keV, as labeled. The blue (red) solid thick line is the minimum of all curves and represents the optimal exclusion potential. The curves are to be compared with the gray line and shaded region which represents the standard exclusion potential.

In the left panel, only modest modifications to the standard result are obtained in the regions between 6–50 GeV WIMP mass. In the right panel, the sizable new coupling boosts the DR-induced nuclear recoil rate above the ^{8}B neutrino recoil rate, weakening the minimal excludable DM-nucleon cross section by few orders of magnitude once $m_\chi < 50$ GeV.

The general trend in both panels of Fig. 7 is that the exclusion potential is shifted to the right off the standard ^{8}B shoulder. How far that shift goes, depends on kinematics. For a progenitor mass of $m_X = 60$ MeV, DR neutrinos induce recoils that compete with DM only below $m_\chi \lesssim 50$ GeV. The exclusion potential for heavier DM is then only challenged by the standard, more energetic atmospheric fluxes. Only if we were to entertain the possibility of $m_X \gg 100$ MeV into the GeV-regime (generally challenged from neutrino experiments), the floor would be lifted by several orders of magnitude in the electroweak scale DM mass regime.

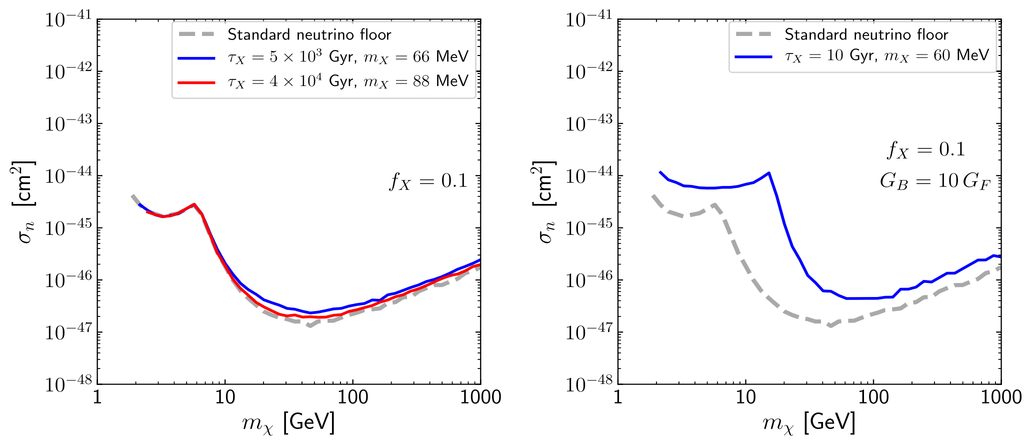

Fig. 8 The modified neutrino floor at 90% CL in case of $X2\nu_{SM}$ (left) and $X2\nu_B$ (right) and for a threshold $E_{R_{\rm thr}} = 0.1$ keV, exposure of 1 ton-year, and exemplary allowed combinations (m_X, τ_X)

6.3 DM discovery potential in presence of DR

Finally, in Fig. 8, we show the DM discovery potential in the presence of SM neutrino DR (left panel) and ν_B DR (right panel) for currently allowed exemplary parameter points. As in the previous sections, modifications to the standard result (dashed line) appear for $m_\chi \gtrsim 6$ GeV, when DR fluxes come to dominate the event rates. The modification of discovery limits are seen up to DM masses of 1 TeV. As can be seen in the left panel, the maximal allowed DR signal is at most comparable to the SM neutrino backgrounds and only mildly alters the standard neutrino floor (gray dashed). In the right panel, because of large statistics, we switch to a binned likelihood approach with $N_{\rm bin} = 50$. Owing to the increased strength of interaction, the neutrino floor is also raised in the low mass region left of the ^{8}B shoulder ($m_\chi \lesssim 6$ GeV).

In both panels of Fig. 8, the modification of discovery limits are seen up to the largest shown DM masses of 1 TeV. This is in contrast to the exclusion potentials of the previous section. For the latter, only the number of events for varying threshold (up to 50 keV) enter, but not their detailed spectral shape. In this section, we fix the threshold to $E_{\rm thr} = 0.1$ keV so that DR spills into the standard induced events at any rate, also affecting the discovery potential for $m_\chi \gtrsim 50$, GeV.

7 Conclusions

In the foreseeable future, DM direct detection experiments will face irreducible background in the form of neutrino-nucleus elastic scattering. The responsible neutrino fluxes originate from the sun and to a smaller degree from the atmosphere or from the cosmological SN history. In this work, we first study the detectability of neutrino DR, sourced by a percent fraction of DM that may decay with arbitrary lifetime after recombination. We consider either SM or baryonic neutrinos ν_B as DR. The latter designate a semi-sterile fourth species that interacts through gauged baryon number. In a next step, we also explore the impact on the DM discovery and exclusion potential at next generation direct detection searches in the presence of new, anomalous neutrino fluxes.

The DR fluxes principally fall into two categories, either constituting neutrinos that travel cosmological distances or neutrinos that originate from DM decay in the galaxy. Whereas the latter requires $\tau_X \gtrsim t_0$ as otherwise the DR-generating sub-component of DM would have already decayed, the former contributes for any τ_X and we provide a new closed-form expression for its total flux. In the detector, the neutrinos then interact coherently with the nucleus, with a cross section that approximately scales as $(A-Z)^2$ and A^2 for SM and baryonic neutrinos, respectively. The benefit of DR in form of SM neutrinos is that its interactions are known. In turn, DR in form of ν_B allows for effective interactions that can be stronger than in the SM, $G_B > G_F$, boosting the principal importance of the DR signal.

After establishing the exclusion potential of DR, we then address the more important question of detectability of DR on the example of a ton-scale liquid xenon detector. Here, standard neutrino sources act as the irreducible background. Given that the signal might be salient in the data, we employ a profile-likelihood analysis to reach robust statistical conclusions about the various assumed hypotheses. For various combinations of detection threshold and exposure, we build a statistical sample by Monte-Carlo generating a large set of mock recoil spectra that are subsequently used in the maximization of the likelihood function. Through this numerically expensive procedure we are able to obtain the discovery reach to DR as well as a DR-modified "neutrino floor", i.e. the boundary in the (m_χ, σ_n) parameter space for the ability to detect DM with 3σ significance when neutrino backgrounds cannot be rejected.

Concretely, we find that SM DR cannot be discovered in direct detection experiments unless a futuristic exposure of 100 ton-year is assumed. The coverage in new parameter space is modest (and neglects the paralleling advances in neutrino detectors). In contrast, direct detection experiments bear better potential to discover non-standard neutrino interactions of DR, as exemplified in the ν_B case, see Fig. 5. Here progenitor masses down to $m_X = 10\,\mathrm{MeV}$ and lifetimes as large as $10^5\,t_0$ can be discovered.

In a next step, we turn to the potential DR-induced interference for the DM searches. Here we study the confusion potential between DR and DM and establish the DM exclusion and discovery potential in the presence DR in future WIMP searches. For DR in form of SM neutrinos, we find that the best sensitivity to the DM-nucleon cross section is weakened by less than an order of magnitude once the scenario is subjected to existing constraints from SK data. Considering ν_B as DR with $G_B > G_F$ we find that the entire region $m_\chi \lesssim 50$, GeV can be strongly affected, and the DM exclusion or discovery potential can be modified substantially.

With the advance of multi-ton scale direct detection experiments, we are entering the "end-game" of WIMP detection. Neutrinos from standard sources will become an irreducible background and ultimately limit our ability to push for ever smaller event rates and better DM sensitivity. It is hence only timely to ask, what other signals and irreducible backgrounds there could be. Here we investigated the perfect possibility that our Universe is filled with MeV-scale DR that traces back to the instability of (a component of) DM. We find that standard expectations can be altered, and—in the presence of new particles and interactions—in a significant manner. In the latter case, DM direct detection experiments may then be turned into DR detectors instead.

Acknowledgements We thank Y. Perez-Gonzalez, and W. Waltenberger for useful discussions. MN is supported by the FWF Research Group grant FG1. JP is supported through the New Frontiers Program by the Austrian Academy of Sciences. SK is supported by Elise-Richter grant project number V592-N27.

Data Availability Statement This manuscript has no associated data or the data will not be deposited. [Authors' comment: The data can be easily generated by random Monte Carlo experiments as described in Section 4 and consist of random recoil energies from the signal and background hypotheses].

Funded by SCOAP[3]. SCOAP[3] supports the goals of the International Year of Basic Sciences for Sustainable Development.

Appendix A: Analytic form of $dR_{X2\nu}/dE_R$

For 2-body decays into massless neutrino DR, the energy-differential recoil rate given in Eq. (10) can be integrated analytically. For the extragalactic signal with the flux given in (3) we split the integral over neutrino energy into the two terms that comprise the cross section (8),

$$\frac{dR^{\text{e.gal}}_{X2\nu}}{dE_R} = N_T \frac{Q_W^2 G_F^2 m_N F(q)^2}{4\pi} \left(\int_{E_{\min}}^{E_{\text{in}}} dE_\nu \, \frac{d\Phi_{\nu,\text{e.g.}}}{dE_\nu} - \frac{E_R m_N}{2} \int_{E_{\min}}^{E_{\text{in}}} dE_\nu \, \frac{d\Phi_{\nu,\text{e.g.}}}{dE_\nu} \frac{1}{E_\nu^2} \right), \tag{23}$$

where $E_{\text{in}} = \frac{m_X}{2}$ is the injection energy and $E_{\min} = \sqrt{\frac{E_R m_N}{2}}$ is the minimum energy to produce a recoil E_R. The integrals are solved by substitution,

$$u = \sqrt{\left(\frac{E_{\text{in}}}{E_{\min}}\right)^3 \frac{\Omega_M}{\Omega_\Lambda} + 1}, \quad w = \frac{u+1}{u-1}, \tag{24}$$

and we obtain the expression,

$$\frac{dR^{\text{e.gal}}_{X2\nu}}{dE_R} = N_T \frac{Q_W^2 G_F^2 m_N F(|\vec{q}\,|)^2}{4\pi} N_\nu \frac{f_X \Omega_{\text{dm}} \rho_{\text{crit}}}{m_X} \times \left(x_{\min}^d - x_{\max}^d - 3d \left(\frac{\sqrt{2}\,\Omega_\Lambda}{\Omega_M}\right)^{\frac{2}{3}} \times \frac{E_R m_N}{E_{\text{in}}^2} \frac{{}_2F_1\left(-\frac{1}{3}, \frac{1}{3}-d, \frac{2}{3}; 1-x\right)}{\sqrt[3]{-1+x}} \Bigg|_{x_{\min}}^{x_{\max}} \right). \tag{25}$$

where

$$d = -\frac{1}{3H_0\sqrt{\Omega_\Lambda}\,\tau_X}, \quad x_{\min} = \frac{\sqrt{\frac{E_{\text{in}}^3}{E_{\min}^3}\frac{\Omega_M}{\Omega_\Lambda}+1}+1}{\sqrt{\frac{E_{\text{in}}^3}{E_{\min}^3}\frac{\Omega_M}{\Omega_\Lambda}+1}-1},$$
$$x_{\max} = \frac{\sqrt{\frac{\Omega_M}{\Omega_\Lambda}+1}+1}{\sqrt{\frac{\Omega_M}{\Omega_\Lambda}+1}-1}. \tag{26}$$

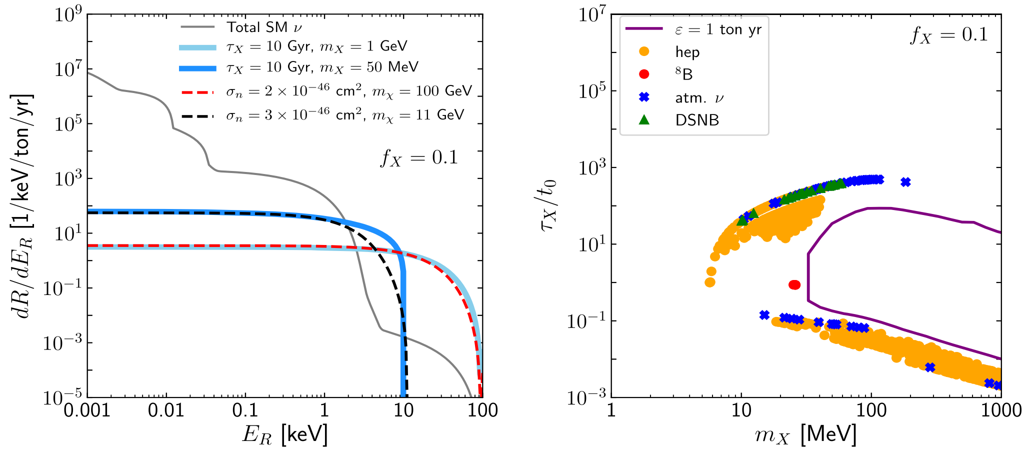

Fig. 9 Left: Best fit WIMP recoil spectra (dashed lines) which mimic the DR recoils (cyan solid lined) with progenitor lifetime of 10 Gyr and progenitor mass of 50 MeV (left) and 1 GeV. The total standard neutrino recoil rates are also overlaid (solid grey). Right: Contributions from each neutrino source (best fits) shown by the points as labeled and determining the shape of the discovery limit for threshold $E_{R_{\rm thr}} = 0.1$ keV and exposure of $\epsilon = 1$ ton-year

The total flux $\Phi_{X2\nu}$ in Eq. (6) is obtained from the first two terms in the bracket of (25) by setting $x_{\rm min} = 1$. For the galactic component the integral with the flux given in (2) can be evaluated directly,

$$\frac{dR^{\rm gal.}_{X2\nu}}{dE_R} = N_T \frac{Q_W^2 G_F^2 m_N F(|\vec{q}\,|)^2}{4\pi} N_\nu \times \frac{f_X\, e^{-\frac{t_0}{\tau_X}}}{\tau_X m_X} r_\odot \rho_\odot \langle J_{\rm dec}(\theta)\rangle \left(1 - \frac{2E_R m_N}{m_X^2}\right). \tag{27}$$

The DR rate is then the sum of both, galactic and extragalactic contributions. The baryonic neutrino rate is calculated in the same way replacing $Q_W^2 G_F^2/4\pi$ by $A^2 G_B^2/2\pi$.

Appendix B: Details on discovery and exclusion potentials

Here we show some examples of exclusion and discovery limits, where SM neutrinos may mimic potential DR and DM signals in direct detection experiments. The reach of an experiment for a signal depends on the shape of the recoil rate and the number of events in relation to backgrounds. In this appendix we study cases where DR neutrinos exhibit some degree of similarity with DM-induced events.

In the left panel of Fig. 9 we show two examples where DM and DR yield similar differential recoil spectra for two different progenitor masses 50 MeV and 1 GeV and DM masses as labeled such that the recoil endpoint energies match. For the lighter progenitor—and which is most prospective with respect to existing constraints (see above)—the DM and DR spectra are well distinguishable, with DR-induced events exhibiting a harder spectrum. For GeV-scale progenitors, the spectrum is cut off by the nuclear form factor $|F(q)|^2$ explaining thee similarity in the rate with an electroweak-scale mass DM particle. We note in passing, that in the latter case, additional inelastic nuclear channels are possible as the CM energy is in the tens of MeV regime.

In the right panel of Fig. 9 we follow our usual procedure and simulate several thousand Monte-Carlo experiments for each neutrino source ν_j and calculate the distribution of best parameters (m_X, τ_X) by minimizing the likelihood from Eq. (16) for $\alpha = X2\nu$. The discovery limit to SM DR neutrinos for an exposure of 1 ton-year and threshold $E_{R_{\rm thr}} = 0.1$ keV is shown. In addition, the dots as labeled are indicative of the standard neutrino fluxes that limit a further extended reach.

References

1. D.Z. Freedman, Phys. Rev. D **9**, 1389 (1974). https://doi.org/10.1103/PhysRevD.9.1389
2. V. Kopeliovich, L. Frankfurt, JETP Lett. **19**, 145 (1974)
3. A. Drukier, L. Stodolsky, Phys. Rev. D **30**, 395 (1984). https://doi.org/10.1103/PhysRevD.30.2295
4. B. Cabrera, L.M. Krauss, F. Wilczek, Phys. Rev. Lett. **55**, 25 (1985). https://doi.org/10.1103/PhysRevLett.55.25
5. M.W. Goodman, E. Witten, Phys. Rev. D **31**, 3059 (1985). https://doi.org/10.1103/PhysRevD.31.3059
6. L.E. Strigari, New J. Phys. **11**, 105011 (2009). https://doi.org/10.1088/1367-2630/11/10/105011 arXiv:0903.3630 [astro-ph.CO]

7. J. Billard, L. Strigari, E. Figueroa-Feliciano, Phys. Rev. D **89**, 023524 (2014). https://doi.org/10.1103/PhysRevD.89.023524 arXiv:1307.5458 [hep-ph]
8. J. Monroe, P. Fisher, Phys. Rev. D **76**, 033007 (2007). https://doi.org/10.1103/PhysRevD.76.033007 arXiv:0706.3019 [astro-ph]
9. M. Battaglieri et al. (2017). arXiv:1707.04591 [hep-ph]
10. D.S. Akerib et al. (LUX), Phys. Rev. Lett. **118**, 021303 (2017). https://doi.org/10.1103/PhysRevLett.118.021303. arXiv:1608.07648 [astro-ph.CO]
11. X. Cui et al. (PandaX-II), Phys. Rev. Lett. **119**, 181302 (2017). https://doi.org/10.1103/PhysRevLett.119.181302. arXiv:1708.06917 [astro-ph.CO]
12. E. Aprile et al. (XENON), Phys. Rev. Lett. **121**, 111302 (2018). https://doi.org/10.1103/PhysRevLett.121.111302. arXiv:1805.12562 [astro-ph.CO]
13. R. Ajaj et al. (DEAP), Phys. Rev. D **100**, 022004 (2019). https://doi.org/10.1103/PhysRevD.100.022004. arXiv:1902.04048 [astro-ph.CO]
14. P. Agnes et al. (DarkSide), Phys. Rev. D **98**, 102006 (2018). https://doi.org/10.1103/PhysRevD.98.102006. arXiv:1802.07198 [astro-ph.CO]
15. E. Aprile et al. (XENON), JCAP **1604**, 027 (2016). https://doi.org/10.1088/1475-7516/2016/04/027. arXiv:1512.07501 [physics.ins-det]
16. D.S. Akerib et al. (LUX-ZEPLIN), Phys. Rev. D **101**, 052002 (2020). https://doi.org/10.1103/PhysRevD.101.052002. arXiv:1802.06039 [astro-ph.IM]
17. J. Aalbers et al. (DARWIN), JCAP **1611**, 017 (2016). https://doi.org/10.1088/1475-7516/2016/11/017. arXiv:1606.07001 [astro-ph.IM]
18. C.E. Aalseth et al., Eur. Phys. J. Plus **133**, 131 (2018). https://doi.org/10.1140/epjp/i2018-11973-4 arXiv:1707.08145 [physics.ins-det]
19. D. Akimov et al. (COHERENT), Science **357**, 1123 (2017). https://doi.org/10.1126/science.aao0990. arXiv:1708.01294 [nucl-ex]
20. D. Akimov et al. (COHERENT), Phys. Rev. Lett. **126**, 012002 (2021). arXiv:2003.10630 [nucl-ex]
21. G. Angloher et al. (NUCLEUS), Eur. Phys. J. C **79**, 1018 (2019). https://doi.org/10.1140/epjc/s10052-019-7454-4. arXiv:1905.10258 [physics.ins-det]
22. J. Hakenmüller et al., Eur. Phys. J. C **79**, 699 (2019). https://doi.org/10.1140/epjc/s10052-019-7160-2 arXiv:1903.09269 [physics.ins-det]
23. R. Harnik, J. Kopp, P.A.N. Machado, JCAP **07**, 026 (2012). https://doi.org/10.1088/1475-7516/2012/07/026 arXiv:1202.6073 [hep-ph]
24. M. Pospelov, J. Pradler, Phys. Rev. D **85**, 113016 (2012). https://doi.org/10.1103/PhysRevD.85.113016. arXiv:1203.0545 [hep-ph] [Erratum: Phys. Rev. D **88**, 039904 (2013)]
25. J. Billard, L.E. Strigari, E. Figueroa-Feliciano, Phys. Rev. D **91**, 095023 (2015). https://doi.org/10.1103/PhysRevD.91.095023 arXiv:1409.0050 [astro-ph.CO]
26. B. Dutta, S. Liao, L.E. Strigari, J.W. Walker, Phys. Lett. B **773**, 242 (2017). https://doi.org/10.1016/j.physletb.2017.08.031 arXiv:1705.00661 [hep-ph]
27. E. Bertuzzo, F.F. Deppisch, S. Kulkarni, Y.F. Perez Gonzalez, R. Zukanovich Funchal, JHEP **04**, 073 (2017). https://doi.org/10.1007/JHEP04(2017)073. arXiv:1701.07443 [hep-ph]
28. D. Aristizabal Sierra, N. Rojas, M. Tytgat, JHEP **03**, 197 (2018). https://doi.org/10.1007/JHEP03(2018)197 arXiv:1712.09667 [hep-ph]
29. I.M. Shoemaker, J. Wyenberg, Phys. Rev. D **99**, 075010 (2019). https://doi.org/10.1103/PhysRevD.99.075010 arXiv:1811.12435 [hep-ph]
30. C. Bœhm, D. Cerdeño, P. Machado, A. Olivares-Del Campo, E. Perdomo, E. Reid, JCAP **01**, 043 (2019). https://doi.org/10.1088/1475-7516/2019/01/043 arXiv:1809.06385 [hep-ph]
31. M. Gonzalez-Garcia, M. Maltoni, Y.F. Perez-Gonzalez, R. Zukanovich Funchal, JHEP **07**, 019 (2018). https://doi.org/10.1007/JHEP07(2018)019 arXiv:1803.03650 [hep-ph]
32. D. Aristizabal Sierra, B. Dutta, S. Liao, L.E. Strigari, JHEP **12**, 124 (2019). https://doi.org/10.1007/JHEP12(2019)124 arXiv:1910.12437 [hep-ph]
33. W. Chao, J.-G. Jiang, X. Wang, X.-Y. Zhang, JCAP **08**, 010 (2019). https://doi.org/10.1088/1475-7516/2019/08/010 arXiv:1904.11214 [hep-ph]
34. S. Sadhukhan, M.P. Singh, Phys. Rev. D **103**, 015015 (2021). https://doi.org/10.1103/PhysRevD.103.015015
35. B. Dutta, L.E. Strigari, Annu. Rev. Nucl. Part. Sci. **69**, 137 (2019). https://doi.org/10.1146/annurev-nucl-101918-023450 arXiv:1901.08876 [hep-ph]
36. V. Poulin, P.D. Serpico, J. Lesgourgues, JCAP **1608**, 036 (2016). https://doi.org/10.1088/1475-7516/2016/08/036 arXiv:1606.02073 [astro-ph.CO]
37. J.F. Beacom, Annu. Rev. Nucl. Part. Sci. **60**, 439 (2010). https://doi.org/10.1146/annurev.nucl.010909.083331 arXiv:1004.3311 [astro-ph.HE]
38. J.F. Beacom, M.R. Vagins, Phys. Rev. Lett. **93**, 171101 (2004). https://doi.org/10.1103/PhysRevLett.93.171101 arXiv:hep-ph/0309300
39. K. Bays et al. (Super-Kamiokande), Phys. Rev. D **85**, 052007 (2012). https://doi.org/10.1103/PhysRevD.85.052007. arXiv:1111.5031 [hep-ex]
40. S. Palomares-Ruiz, Phys. Lett. B **665**, 50 (2008). https://doi.org/10.1016/j.physletb.2008.05.040 arXiv:0712.1937 [astro-ph]
41. C. Garcia-Cely, J. Heeck, JHEP **05**, 102 (2017). https://doi.org/10.1007/JHEP05(2017)102 arXiv:1701.07209 [hep-ph]
42. S. Palomares-Ruiz, S. Pascoli, Phys. Rev. D **77**, 025025 (2008). https://doi.org/10.1103/PhysRevD.77.025025 arXiv:0710.5420 [astro-ph]
43. J. Huang, Y. Zhao, JHEP **02**, 077 (2014). https://doi.org/10.1007/JHEP02(2014)077 arXiv:1312.0011 [hep-ph]
44. K. Agashe, Y. Cui, L. Necib, J. Thaler, JCAP **10**, 062 (2014). https://doi.org/10.1088/1475-7516/2014/10/062 arXiv:1405.7370 [hep-ph]
45. Y. Cui, M. Pospelov, J. Pradler, Phys. Rev. D **97**, 103004 (2018). https://doi.org/10.1103/PhysRevD.97.103004 arXiv:1711.04531 [hep-ph]
46. O. Seto, T. Shimomura, Phys. Lett. B **811**, 135880 (2020). https://doi.org/10.1016/j.physletb.2020.135880. arXiv:2007.14605 [hep-ph]
47. K. Enqvist, S. Nadathur, T. Sekiguchi, T. Takahashi, JCAP **09**, 067 (2015). https://doi.org/10.1088/1475-7516/2015/09/067 arXiv:1505.05511 [astro-ph.CO]
48. A. Nygaard, T. Tram, S. Hannestad, JCAP **05**, 017 (2021). https://doi.org/10.1088/1475-7516/2021/05/017. arXiv:2011.01632 [astro-ph.CO]
49. J.F. Navarro, C.S. Frenk, S.D.M. White, Astrophys. J. **462**, 563 (1996). https://doi.org/10.1086/177173 arXiv:astro-ph/9508025
50. N. Aghanim et al. (Planck), Astron. Astrophys. **641**, A6 (2020), [Erratum: Astron. Astrophys. **652**, C4 (2021)]. https://doi.org/10.1051/0004-6361/201833910e. arXiv:1807.06209 [astro-ph.CO]
51. A.G. Riess, S. Casertano, W. Yuan, L.M. Macri, D. Scolnic, Astrophys. J. **876**, 85 (2019). https://doi.org/10.3847/1538-4357/ab1422 arXiv:1903.07603 [astro-ph.CO]
52. K.L. Pandey, T. Karwal, S. Das, JCAP **07**, 026 (2020). https://doi.org/10.1088/1475-7516/2020/07/026. arXiv:1902.10636 [astro-ph.CO]

53. K. Vattis, S.M. Koushiappas, A. Loeb, Phys. Rev. D **99**, 121302 (2019). https://doi.org/10.1103/PhysRevD.99.121302 arXiv:1903.06220 [astro-ph.CO]
54. N. Grevesse, A.J. Sauval, Space Sci. Rev. **85**, 161 (1998). https://doi.org/10.1023/A:1005161325181
55. M. Asplund, N. Grevesse, A.J. Sauval, P. Scott, Annu. Rev. Astron. Astrophys. **47**, 481 (2009). https://doi.org/10.1146/annurev.astro.46.060407.145222 arXiv:0909.0948 [astro-ph.SR]
56. N. Vinyoles, A.M. Serenelli, F.L. Villante, S. Basu, J. Bergström, M.C. Gonzalez-Garcia, M. Maltoni, C. Peña-Garay, N. Song, Astrophys. J. **835**, 202 (2017). https://doi.org/10.3847/1538-4357/835/2/202 arXiv:1611.09867 [astro-ph.SR]
57. G. Battistoni, A. Ferrari, T. Montaruli, P. Sala, Astropart. Phys. **23**, 526 (2005). https://doi.org/10.1016/j.astropartphys.2005.03.006
58. T. Totani, K. Sato, Y. Yoshii, Astrophys. J. **460**, 303 (1996). https://doi.org/10.1086/176970 arXiv:astro-ph/9509130
59. H. Yuksel, M.D. Kistler, J.F. Beacom, A.M. Hopkins, Astrophys. J. **683**, L5 (2008). https://doi.org/10.1086/591449 arXiv:0804.4008 [astro-ph]
60. D. Hartmann, S. Woosley, Astropart. Phys. **7**, 137 (1997)
61. G.B. Gelmini, V. Takhistov, S.J. Witte, JCAP **1807**, 009 (2018). https://doi.org/10.1088/1475-7516/2018/07/009. arXiv:1804.01638 [hep-ph] [Erratum: JCAP **1902**, E02 (2019). https://doi.org/10.1088/1475-7516/2019/02/E02]
62. G. Battistoni, A. Ferrari, T. Montaruli, P.R. Sala, Astropart. Phys. **23**, 526 (2005). https://doi.org/10.1016/j.astropartphys.2005.03.006
63. S. Horiuchi, J.F. Beacom, E. Dwek, Phys. Rev. D **79**, 083013 (2009). https://doi.org/10.1103/PhysRevD.79.083013 arXiv:0812.3157 [astro-ph]
64. J.D. Lewin, P.F. Smith, Astropart. Phys. **6**, 87 (1996). https://doi.org/10.1016/S0927-6505(96)00047-3
65. M. Pospelov, Phys. Rev. D **84**, 085008 (2011). https://doi.org/10.1103/PhysRevD.84.085008 arXiv:1103.3261 [hep-ph]
66. M. Pospelov, J. Pradler, Phys. Rev. D **89**, 055012 (2014). https://doi.org/10.1103/PhysRevD.89.055012 arXiv:1311.5764 [hep-ph]
67. B. Batell, P. deNiverville, D. McKeen, M. Pospelov, A. Ritz, Phys. Rev. D **90**, 115014 (2014). https://doi.org/10.1103/PhysRevD.90.115014 arXiv:1405.7049 [hep-ph]
68. J.A. Dror, R. Lasenby, M. Pospelov, Phys. Rev. Lett. **119**, 141803 (2017). https://doi.org/10.1103/PhysRevLett.119.141803 arXiv:1705.06726 [hep-ph]
69. J.A. Dror, R. Lasenby, M. Pospelov, Phys. Rev. D **96**, 075036 (2017). https://doi.org/10.1103/PhysRevD.96.075036 arXiv:1707.01503 [hep-ph]
70. A. Aguilar-Arevalo et al. (MiniBooNE DM), Phys. Rev. D **98**, 112004 (2018). https://doi.org/10.1103/PhysRevD.98.112004. arXiv:1807.06137 [hep-ex]
71. J.A. Dror, R. Lasenby, M. Pospelov, Phys. Rev. D **99**, 055016 (2019). https://doi.org/10.1103/PhysRevD.99.055016 arXiv:1811.00595 [hep-ph]
72. I.M. Shoemaker, L. Vecchi, Phys. Rev. D **86**, 015023 (2012). https://doi.org/10.1103/PhysRevD.86.015023 arXiv:1112.5457 [hep-ph]
73. H. An, X. Ji, L.-T. Wang, JHEP **07**, 182 (2012). https://doi.org/10.1007/JHEP07(2012)182 arXiv:1202.2894 [hep-ph]
74. A.A. Aguilar-Arevalo et al. (MiniBooNE DM), Phys. Rev. D **98**, 112004 (2018). https://doi.org/10.1103/PhysRevD.98.112004. arXiv:1807.06137 [hep-ex]
75. C.A.J. O'Hare, Phys. Rev. Lett. **127**, 251802 (2021). https://doi.org/10.1103/PhysRevLett.127.251802. arXiv:2109.03116 [hep-ph]
76. G. Cowan, *Statistical Data Analysis* (Oxford University Press, New York, 1998)
77. S.S. Wilks, Ann. Math. Stat. **9**, 60 (1938). https://doi.org/10.1214/aoms/1177732360
78. E. Richard et al. (Super-Kamiokande), Phys. Rev. D **94**, 052001 (2016). https://doi.org/10.1103/PhysRevD.94.052001. arXiv:1510.08127 [hep-ex]
79. K. Abe et al. (Super-Kamiokande), Phys. Rev. D **83**, 052010 (2011). https://doi.org/10.1103/PhysRevD.83.052010. arXiv:1010.0118 [hep-ex]
80. G. Bellini et al. (Borexino), Phys. Rev. D **85**, 092003 (2012). https://doi.org/10.1103/PhysRevD.85.092003. arXiv:1203.6258 [hep-ex]

Journal of Cosmology and Astroparticle Physics
An IOP and SISSA journal

Probing sub-eV Dark Matter decays with PTOLEMY

Kyrylo Bondarenko,[a,b] **Alexey Boyarsky,**[c] **Marco Nikolic,**[d] **Josef Pradler**[d] **and Anastasia Sokolenko**[d]

[a]Theoretical Physics Department, CERN,
1 Esplanade des Particules, Geneva 23, CH-1211, Switzerland
[b]L'Ecole polytechnique fédérale de Lausanne,
Route Cantonale, 1015 Lausanne, Switzerland
[c]Intituut-Lorentz, Leiden University,
Niels Bohrweg 2, 2333 CA Leiden, The Netherlands
[d]Institute of High Energy Physics, Austrian Academy of Sciences,
Nikolsdorfergasse 18, 1050 Vienna, Austria

E-mail: kyrylo.bondarenko@cern.ch, boyarsky@lorentz.leidenuniv.nl, marco.nikolic@oeaw.ac.at, josef.pradler@oeaw.ac.at, anastasia.sokolenko@oeaw.ac.at

Received January 11, 2021
Accepted February 10, 2021
Published March 26, 2021

Abstract. When the Dark Matter mass is below the eV-scale, its cosmological occupation number exceeds the ones of photons from the cosmic microwave background as well as of relic neutrinos. If such Dark Matter decays to pairs of neutrinos, it implies that experiments that seek the detection of the cosmic neutrino background may as well be sensitive to this additional form of "dark radiation". Here we study the prospects for detection taking into account various options for the forecasted performance of the future PTOLEMY experiment. From a detailed profile likelihood analysis we find that Dark Matter decays with lifetime as large as 10^4 Gyr or a sub-% Dark Matter fraction decaying today can be discovered. The prospects are facilitated by the distinct spectral event shape that is introduced from galactic and cosmological neutrino dark radiation fluxes. In the process we also clarify the importance of Pauli-blocking in the Dark Matter decay. The scenarios presented in this work can be considered early physics targets in the development of these instruments with relaxed demands on performance and energy resolution.

Keywords: cosmological neutrinos, neutrino experiments, dark matter experiments

ArXiv ePrint: 2012.09704

 https://doi.org/10.1088/1475-7516/2021/03/089

Contents

1 Introduction

Besides the cosmic microwave background (CMB), the prediction of the cosmic neutrino background (CνB) is the second, unequivocal key signature of a hot Big Bang. The Universe must have passed through a stage of billions degrees of Kelvin in order to enable the fusion of light elements from protons and neutrons. At this temperature neutrinos become the main actors balancing the relative abundance of nucleons. However, whereas the measurements of the CMB have elevated Big Bang cosmology to a precision science, the relic radiation of neutrinos from the nucleosynthesis era remains undetected to date.

The observation of relic neutrinos would provide a window into the first second after the Big Bang, and its detection is an important task in cosmology. Today's observed CMB radiation temperature of $T = 2.73$ K implies that there are 411 relic photons per cm^3. Assuming a standard cosmological history, it then follows that the average cosmic CνB number density is 336 cm^{-3} (see e.g. [1]). Relic neutrinos hence constitute the largest of neutrino fluxes at Earth [2]. However, whereas microwave photons are readily detected, "infrared" neutrinos have exceedingly small cross section, making them literally inert under any ordinary laboratory scheme. Among the various other ideas for detection [3–7], the most prospective way appears to leverage the energy release in the threshold-free electron-neutrino capture reactions of beta-decaying nuclei [8, 9]. Here, the capture on tritium atoms,

$$\nu_e + \mathrm{T} \to {}^3\mathrm{He} + e^-, \tag{1.1}$$

is one of the best candidate reactions. The relatively low Q-value of the associated super-allowed beta-decay, $Q_\beta = 18.529(2)$ keV, allows for schemes that achieve the required sub-eV energy resolution in electron energy, while its half-life $t_{1/2} = 12.32(2)$ yrs implies a sensible experimental timescale where sufficient statistics can be collected.

Because of the minute cross section for neutrino absorption, $\sigma v_\nu \sim 10^{-44}\,\mathrm{cm}^2$, detecting relic neutrinos takes extremely large amounts of tritium. The PTOLEMY experiment [10, 11] proposes to use 100 g of tritium, which is 10^6 times more than the best current experiment KATRIN [12] employs.[1] Even with this amount of tritium, the expected detection rate is ~ 4 or ~ 8 relic neutrinos per year, with a dependence if neutrinos are Dirac or Majorana particles [6, 14]. Both experiments use or plan to use sophisticated schemes that filter electron energies with (sub-)eV precision. Neglecting the recoil of the daughter nucleus, the electron kinetic energy in reaction (1.1) is given by

$$E_e = Q + E_\nu. \tag{1.2}$$

Any experiment that aims at detecting the neutrino capture (1.1) in the electron over the common beta background $\mathrm{T} \to {}^3\mathrm{He} + \mathrm{e}^- + \bar{\nu}_\mathrm{e}$ must hence resolve an amount E_ν at the beta-endpoint energy. For the CνB— which is guaranteed to be partially composed of massive, non-relativistic neutrinos today — this implies that a successful detection of relic neutrinos is tantamount to measuring neutrino mass.

Given the long road ahead that the efforts in CνB detection face, it is only just to ask what other kind of physics can be probed with such experiment. For example, it has been proposed that neutrino capture experiments such as PTOLEMY can be used to detect light sterile neutrinos [15], constrain the neutrino lifetime, lepton-asymmetry or thermal history [14], or act as directional Dark Matter (DM) direct detectors [11, 16, 17]. In this work, we consider yet another possibility, namely, the detection of neutrino "dark radiation" (DR). Here, the potentially largest source can be the decay of a fraction κ_{DM} of DM of mass m_{DM}.[2] To see, if this is prospective at all, we may saturate the cosmological DR flux by assuming the fraction κ_{DM} has already decayed (or is currently decaying at an unsuppressed rate) into N_ν neutrinos — typically $N_\nu = 1, 2$ in simple models — to estimate the ratio of DR to CνB neutrino absorption,

$$\frac{R_{\mathrm{DR}}}{R_{\mathrm{C}\nu\mathrm{B}}} \sim \frac{N_\nu \kappa_{\mathrm{DM}} \Omega_{\mathrm{DM}} \rho_{\mathrm{crit}}}{m_{\mathrm{DM}} n_{\mathrm{C}\nu\mathrm{B}}} \frac{(\sigma c)}{(\sigma v_\nu)} \sim \mathcal{O}(10)\kappa_{\mathrm{DM}} \left(\frac{1\ \mathrm{eV}}{m_{\mathrm{DM}}}\right). \tag{1.3}$$

The first factor is the ratio of the cosmological DM number density over the number density $n_{\mathrm{C}\nu\mathrm{B}}$ of the CνB. The second factor is the ratio of absorption cross section times the typical velocity of the incoming neutrino; the latter product is to good approximation velocity independent and hence a number close to unity. This rough estimate neglects the flavor and helicity composition of the CνB as well as additional contributions that may arise from local DM decays,[3] but already demonstrates that if DM with mass below the eV-scale decays, it may be detected in a CνB experiment [23, 24].

The mass-scale of the decaying DM in (1.3) implies that the only channels of decay into Standard Model (SM) particles are photons and neutrinos. Moreover, when $\kappa_{\mathrm{DM}} = \mathcal{O}(1)$ the estimate (1.3) implies that we are to consider bosonic light DM. Fermionic DM

[1] Tritium has the life-time $t_{1/2} \sim 12$ years, therefore, the amount of tritium that decays during the experiment will not significantly change, see e.g. [13].

[2] The possibility of more energetic neutrino DR and its signature in DM direct detection and neutrino experiments was considered in [18–22].

[3] The *total* DR flux is independent of DM lifetime τ_{DM} for $\tau_{\mathrm{DM}} \lesssim t_0$, where t_0 is the age of the Universe, and for as long as DR remains relativistic [22].

needs to satisfy the Tremaine-Gunn bound $m_{\rm DM} \gtrsim 300\,{\rm eV}$ [25–27] and sub-eV fermionic DM cannot comprise its dominant component.[4] There are then several possibilities for a concrete realization of this scenario. A particularly well motivated one is that of a Majoron DM candidate [28], for which the decay DM $\to \nu\nu(\bar\nu\bar\nu)$ is a defining feature. The decay rate is linear in DM mass, $\Gamma_{{\rm DM}\to\nu\nu} \propto g^2 m_{\rm DM}$, and the required smallness of the effective parameter $g \sim 10^{-17}{\rm eV}/m_{\rm DM}$ to achieve a cosmological lifetime arises from the global breaking of lepton number at some UV scale $\langle\Phi\rangle$ that provides neutrino with mass, $g \sim m_\nu/\langle\Phi\rangle$. This possibility was considered in [23, 24].

In this work, we build on these previous proposals and, first, study the prospects of an enhanced signature when considering the non-relativistic injection regime, and, second, present a detailed sensitivity study that takes into account the projected performance of PTOLEMY. A Majoron is of course not the only possibility to source low-energy neutrinos. One may equally well consider vector DM particle, associated with a gauged combination of lepton-number and/or baryon minus lepton number, or an eV-scale sterile neutrino with $\kappa_{\rm DM} < 1$ and enhanced decays to three Standard Model neutrinos through mixing. In this work, we will not go into these various options, but rather choose a phenomenological approach, studying the concrete detectability of decaying sub-eV DM; an exploration of models is left for future work.

The paper is organized as follows: in section 2 we introduce the neutrino DR signal in the neutrino capture reactions with a focus on PTOLEMY. In section 3 we predict the neutrino DR signal for PTOLEMY, considering various cases. In section 4 we forecast the sensitivity of PTOLEMY to detect DR from DM decay, taking into account the backgrounds from beta-decay and relic neutrinos. In section 5 we summarize our results and conclude.

2 PTOLEMY neutrino detection rate

The overall capture rate (per tritium atom) is given by a product of neutrino flux $n_\nu v_\nu$ times the capture cross section σ. Importantly, for as long as the incoming neutrino energy satisfies $E_\nu \ll Q$, the product σv_ν is a constant, with its only dependence on the helicity composition of the incoming flux [14],

$$n_\nu \sigma v_\nu = \left[(1-v_\nu) n_{\nu_{h_R}} + (1+v_\nu) n_{\nu_{h_L}}\right] (\sigma v)_0, \tag{2.1}$$

with $(\sigma v)_0 \approx 3.7 \cdot 10^{-45}\ {\rm cm}^2$ and where $n_{\nu_{h_L}} (n_{\nu_{h_R}})$ denote the number density left-helical (right-helical) active neutrinos. This dependence leads to a twice larger event rate when CνB neutrinos are Majorana rather than Dirac. For simplicity, in the following we assume that DM decays into equal amounts of right- and left-helical states, which is indeed the case for Majoron decay [24]. By making this assumption, the dependence on helicity composition drops out, simplifying the discussion.

Neutrinos propagate as mass-eigenstates ν_i and enter as such the detector in an incoherent mixture of flavor states as they have traveled astronomical distances from the source. The reaction to consider is then $\nu_i + {\rm T} \to {}^3{\rm He} + {\rm e}^-$ and the probability of capture is modulated by their electron-flavor content, given by the squared PMNS-matrix element $|U_{ei}|^2$. The total rate of neutrino capture in an experiment with a mass M_T of tritium (PTOLEMY

[4] If $\kappa_{\rm DM} \ll 1$ the decaying DM can be fermionic for as long it is only light enough to boost its occupation number by $1/\kappa_{\rm DM}$ to retain an $\mathcal{O}(1)$ number in the estimate (1.3).

plans to use $M_{\rm T} = 100$ g [10]) is given by

$$\Gamma = \frac{M_{\rm T}}{m_{\rm T}} \sum_{i=1}^{3} |U_{ei}|^2 \int dE_{\nu,i}\, \sigma\, v_{\nu,i} \frac{dn_{\nu,i}}{dE_{\nu_i}} \approx \frac{M_{\rm T}}{m_{\rm T}} (\sigma v)_0 \sum_{i=1}^{3} |U_{ei}|^2 n_{\nu,i}. \tag{2.2}$$

Here, $m_{\rm T}$ is the mass of one tritium atom, $dn_{\nu,i}/dE_{\nu_i}$ is the energy spectrum of the i-th mass eigenstate; dE_{ν_i} is the total neutrino energy and $v_{\nu,i}$ the associated velocity. For the remainder of this paper, we shall always consider the kinematic regime of low-energy neutrinos where $\sigma_c v_{\nu,i}$ is a constant, and the local number density $n_{\nu,i}$ alone becomes the figure of merit that informs us about the overall rate. Applied to the CνB, the number density of relic neutrinos can be written as $n_{\nu,i} = f_{c,i} n_0$, where $n_0 \approx 56$ cm^{-3} is the average number density per neutrino state today, and $f_{c,i}$ is a clustering factor in our Galaxy that ranges from 1 to 1.1 for neutrino masses below 50 meV [29, 30].[5] The detection rate of relic neutrinos by PTOLEMY is therefore (cf. [32])

$$\Gamma_{\rm CNB} \approx (4\,\text{or}\,8)\ \text{yr}^{-1} \left(\frac{M_{\rm T}}{100\ \text{g}}\right). \tag{2.3}$$

Here we have taken $f_{c,i} = 1$ and used unitarity of the PMNS matrix, $1 = \sum_{i=1}^{3} |U_{ei}|^2$.

The energy spectrum of electrons emitted in the capture is immediately obtained from (2.2) together with (1.2),

$$\frac{d\Gamma}{dE_e}(E_e) = \frac{M_{\rm T}}{m_{\rm T}} (\sigma v)_0 \sum_{i=1}^{3} |U_{ei}|^2 \frac{dn_{\nu,i}}{dE_{\nu,i}}(E_e - Q). \tag{2.4}$$

The detectability of a signal depends on its intrinsic shape, the values of neutrino masses and on the energy resolution Δ of the experiment. We follow [32] and model the latter by a Gaussian with full-width-at-half-maximum (FWHM) given by Δ to obtain the observed rate,

$$\frac{d\widetilde{\Gamma}}{dE_e}(E_e) = \frac{1}{\sqrt{2\pi}(\Delta/\sqrt{8\ln 2})} \int \frac{d\Gamma}{dE_e}(E') \exp\left(-\frac{(E'-E_e)^2}{2(\Delta/\sqrt{8\ln 2})^2}\right) dE'. \tag{2.5}$$

For the PTOLEMY forecasts below, we shall take $\Delta = 10 \ldots 100\,$eV as a representative range covering the optimal to pessimistic range.

3 Neutrino dark radiation from Dark Matter decay

As we have seen in the previous section, when we consider the additional sources of neutrinos with energies $E_\nu \ll Q$, the relative local number densities inform us about the absolute rates. The rate of DR-induced capture events is hence related to the CνB prediction via,

$$\Gamma_{\rm DR} = \frac{n_{\nu_e}^{\rm DR}}{n_{\nu_e}^{{\rm C}\nu{\rm B}}} \Gamma_{{\rm C}\nu{\rm B}}, \tag{3.1}$$

where $n_{\nu_e}^{{\rm C}\nu{\rm B}} \equiv n_0 \sum_i |U_{ei}|^2 f_{c,i}$ is an effective number density of electron neutrinos in the CνB and $n_{\nu_e}^{\rm DR} \equiv \sum_i |U_{ei}|^2 n_{\nu,i}^{\rm DR}$ is an effective number density of electron neutrinos in DR originating from DM decay.

[5]The absolute neutrino mass scale is unknown; the best current limit on the sum of neutrino masses is from cosmology, $\sum_i m_{\nu_i} \leq 0.12$ eV [31]. Therefore, using 50 meV in the estimate of the clustering factor is already close to the limit for an inverted hierarchy, and clustering is almost negligible.

There are then two principal components that source the contributions to $n_{\nu_e}^{\rm DR}$:

1. *DM decay at cosmological distances* — the averaged neutrino background from DM decays outside of our Galaxy and over the course of history;
2. *DM decay in the Galaxy* — neutrinos from DM decays from the DM halo of our Galaxy at present.

As is turns out, for $\tau_{\rm DM} \gtrsim t_0$, where t_0 is the age of the Universe, these contributions happen to be of almost identical size in total flux. However, the principal difference is that in the former category the neutrinos experience redshifting of their momenta, whereas in the second category, they do not. This has important consequences for the prediction of the event spectra, and in the following we obtain the respective concentration and energy distribution of both DR components.

3.1 Neutrino DR from cosmological DM decay

We first consider the cosmological contribution to the local DR number density. Denoting by $\kappa_{\rm DM} n_{\rm DM,0} = \kappa_{\rm DM}\Omega_{\rm DM}\rho_{\rm crit}/m_{\rm DM}$ the average number density the decaying DM-component would have today in the limit of infinite lifetime, the number density of the ith neutrino mass state can be estimated as[6]

$$n_{\nu,i}^{\rm cosm} \approx {\rm BR}_i \left(1 - e^{-t_0/\tau_{\rm DM}}\right) N_\nu \kappa_{\rm DM} n_{\rm DM,0} \sim {\rm BR}_i \frac{t_0}{\tau_{\rm DM}} N_\nu \kappa_{\rm DM} n_{\rm DM,0}, \qquad \tau_{\rm DM} \gg t_0, \tag{3.2}$$

where ${\rm BR}_i$ is the branching ratio of DM decay into ith neutrino mass state; in the last expression we have exposed the scaling in the limit of long lifetime, $\tau_{\rm DM} \gg t_0$.

Of course, gravity alone already constrains the lifetime of DM, e.g. from CMB physics. Here, the statement is that either 4% of all of DM could have decayed between recombination and today, or $\kappa_{\rm DM}/\tau_{\rm DM} < 6.3 \times 10^{-3}\,$Gyr for lifetimes larger than the age of the Universe. The latter implies that $\tau_{\rm DM} \gtrsim 12 t_0$ if $\kappa_{\rm DM} = 1$ [33]. For simplicity, we either use $\tau_{\rm DM} = 10 t_0$ with $\kappa_{\rm DM} = 1$ for the long lifetime regime, or $\kappa_{\rm DM} = 0.05$ for the short (arbitrary) lifetime regime, even if it implies that we slightly slip into the disfavoured region.

Using eq. (3.2) we obtain the effective number density of cosmological electron neutrinos as,

$$n_{\nu_e}^{\rm cosm} = \sum_{i=1}^{3} |U_{ei}|^2 n_{\nu,i}^{\rm cosm} \approx 46~{\rm cm}^{-3}\xi \left(\frac{10 t_0}{\tau_{\rm DM}}\right)\left(\frac{1~{\rm eV}}{m_{\rm DM}}\right), \qquad \xi = 3N_\nu \sum_{i=1}^{3} |U_{ei}|^2 {\rm BR}_i, \tag{3.3}$$

where we have again taken the limit of long lifetime. For equal branching ratios, ${\rm BR}_i = 1/3$, the factor $\xi = N_\nu$. Substituting this result into eq. (2.2) the total PTOLEMY detection rate for cosmologically sourced neutrino DR reads

$$\Gamma_{\rm DR}^{\rm cosm} \approx 3.2~{\rm yr}^{-1}\xi \left(\frac{M_{\rm T}}{100~{\rm g}}\right)\left(\frac{10 t_0}{\tau_{\rm DM}}\right)\left(\frac{1~{\rm eV}}{m_{\rm DM}}\right). \tag{3.4}$$

We see that for sub-eV DM mass the detection rate of cosmological neutrinos can be higher than for relic neutrinos, see eq. (2.3). The scenario can hence become another target for PTOLEMY. It is, however, beyond the reach of KATRIN which uses $M_{\rm T} = 100~\mu$g.

[6] This estimate neglects the effects of the Universe's expansion. The exact expression is given in [22] and it makes a 50% downward correction to the estimate for $\tau_{\rm DM} \gtrsim t_0$.

To obtain the differential event rate in PTOLEMY, we now turn to the energy spectrum of the cosmological DR component. For simplicity, we shall only consider the case of 2-body decay, DM $\to \nu\bar{\nu}$ or DM $\to \nu\nu$. With the initial DM kinetic energy being negligible in comparison to its mass, the neutrinos are initially injected with energy $m_{\rm DM}/2$. The associated neutrino momentum then redshifts, and the continuous decay of DM during the cosmic history accumulates to the following spectrum [21],

$$\frac{dn^{\rm cosm}_{\nu,i}}{dE_{\nu,i}}(E_{\nu,i}) = \frac{N_\nu}{p_{\nu,i} v_{\nu,i}} \frac{{\rm BR}_i \kappa_{\rm DM} n_{\rm DM,0}}{H(z_{\rm dec})\tau_{\rm DM}} e^{-t(z_{\rm dec})/\tau_{\rm DM}}, \tag{3.5}$$

where $z_{\rm dec}$ is the decay redshift obtained from the redshift of the initial momentum to the momentum at arrival, $p_{\nu,i} = \sqrt{E^2_{\nu,i} - m^2_{\nu,i}}$,

$$z_{\rm dec} = \sqrt{\frac{\frac{m^2_{\rm DM}}{4} - m^2_{\nu,i}}{p^2_{\nu,i}}} - 1. \tag{3.6}$$

In the above formula, $t(z)$ is the cosmic look-back time evaluated at $z_{\rm dec}$; for $\tau_{\rm DM} \gtrsim t_0$ the exponential factor can be neglected. The energy differential flux itself is given by multiplying (3.5) by the neutrino velocity $v_{\nu,i}$.

Examples of the signal for different values of neutrino masses and different assumptions about PTOLEMY energy resolutions are shown (together with the galactic component of the signal that is discussed below) in figure 1 as well as figure 4 in appendix B.

3.2 Neutrino DR from galactic DM decay

Let us now estimate the contribution to neutrino DR from DM decay inside the Galaxy. For such an estimate it is important to specify the ratio v_ν/c as it defines the resulting neutrino concentration around us. We will discuss below the two principal cases: neutrinos that escape upon injection and neutrinos that are injected with a speed below the escape speed and are hence retained in the Galaxy.

3.2.1 Escaping neutrinos

If neutrinos are injected at velocities v_ν that exceed the escape speed $v_{\rm esc} \simeq 550\,{\rm km\,s^{-1}} \simeq 2\times10^{-3}c$, they will escape the Galaxy in a time $t_{\rm esc} \sim r_\odot/v_\nu \sim 10^{12}\,{\rm s}\,(c/v_\nu) \ll t_0$, where $r_\odot = 8.3$ kpc is the distance from the center of the Galaxy to the Sun. A Galactic contribution with $v_\nu \geq v_{\rm esc}$ is only present for $\tau_{\rm DM} \gtrsim t_0$. Taking the long-lifetime limit, an order of magnitude estimate for the local neutrino number density is hence,

$$n^{\rm gal}_{\nu,i} \approx {\rm BR}_i \frac{t_{\rm esc}}{\tau_{\rm DM}} N_\nu \kappa_{\rm DM} n_{\rm DM,\odot} \sim 0.4 \left(\frac{c}{v_\nu}\right)\left(\frac{{\rm BR}_i}{1/3}\right) n^{\rm cosm}_{\nu,i} \quad (\tau_{\rm DM} \gtrsim t_0). \tag{3.7}$$

For this estimate we used the local DM density $\rho_{\rm DM,\odot} \sim 0.3$ GeV/cm^3 as a representative value. From this estimate we see that the Galactic DR contribution can be comparable with the cosmological one and it can be even larger if the DM mass is such that galactic neutrinos are only semi-relativistic. The Galactic flux that takes into account the DM density profile then reads,

$$n^{\rm gal}_{\nu,i} = {\rm BR}_i \frac{r_\odot}{v_{\nu,i}\tau_{\rm DM}} N_\nu \kappa_{\rm DM} n_{\rm DM,\odot} \langle D\rangle \quad (v_{\nu,i} > v_{\rm esc}), \tag{3.8}$$

where $\langle D \rangle$ is the whole sky average of the line-of-sight integral as seen from Earth over the galactic DM density distribution (see e.g. [34]),

$$\langle D \rangle = \frac{1}{4\pi}\int D d\Omega, \qquad D = \frac{1}{r_\odot \rho_{\mathrm{DM},\odot}} \int_{\mathrm{l.o.s.}} \rho(r) ds. \tag{3.9}$$

The value of the averaged D-factor normalised in this way describes how much our naive eq. (3.7) underestimates the local concentration of galactic neutrinos. We adopt $\langle D \rangle = 2.19$ obtained from an NFW profile with a mild dependence on other canonical profiles.[7] Similarly to the cosmological case, we may obtain effective number density of electron neutrinos

$$n_{\nu_e}^{\mathrm{gal}} = \sum_{i=1}^{3} |U_{ei}|^2 n_{\nu,i}^{\mathrm{gal}} \approx 43~\mathrm{cm}^{-3} \xi \kappa_{\mathrm{DM}} \left(\frac{c}{v_\nu}\right)\left(\frac{10t_0}{\tau_{\mathrm{DM}}}\right)\left(\frac{1~\mathrm{eV}}{m_{\mathrm{DM}}}\right) \quad (\tau_{\mathrm{DM}} \gtrsim t_0), \tag{3.10}$$

where ξ is given by eq. (3.3). Using eq. (2.2) we estimate the PTOLEMY detection rate of galactic DR neutrinos,

$$\Gamma_{\mathrm{gal}} \approx 3.0~\mathrm{yr}^{-1} \xi \kappa_{\mathrm{DM}} \left(\frac{c}{v_\nu}\right)\left(\frac{M_{\mathrm{T}}}{100~\mathrm{g}}\right)\left(\frac{10t_0}{\tau_{\mathrm{DM}}}\right)\left(\frac{1~\mathrm{eV}}{m_{\mathrm{DM}}}\right). \tag{3.11}$$

Comparing eqs. (3.4) and (3.11) we see that once the D-factor is taken into account the contributions from Galactic neutrinos and from cosmological neutrinos sourced by DM decay are almost equal in the long-lifetime regime.

We may at this point check whether we stay clear from any suppression factors that arise from Pauli blocking. The maximum occupation number in a Fermi-Dirac gas is attained from $dn_\nu^{\max} = g_\nu/(8\pi^3) d^3\vec{p}_\nu$ where $g_\nu = 2$ are the active neutrino degrees of freedom of each massive state. In this section, we consider a kinematic situation where every neutrino, once injected, is on a straight trajectory escaping the Galaxy. In the 2-body decay, a small momentum spread $\Delta p_\nu/p_\nu \sim 10^{-3}$ is inherited from the non-relativistic bound motion of the galactic DM. Integration yields $n_{\nu,\mathrm{gal}}^{\max} \approx g_\nu/(2\pi^2) p_\nu^3 \times (\Delta p_\nu/p_\nu)$. Taking the ratio with the concentration obtained above yields

$$\frac{n_{\nu,\mathrm{gal}}^{\max}}{n_{\nu,\mathrm{gal}}|_{\mathrm{eq.}~(3.8)}} \approx \frac{10^7}{\kappa_{\mathrm{DM}}}\left(\frac{v_\nu}{c}\right)^4 \left(\frac{\tau_{\mathrm{DM}}}{10t_0}\right)\left(\frac{m_{\mathrm{DM}}}{\mathrm{eV}}\right)^4, \tag{3.12}$$

and where we have taken the same estimate on the escape time t_{esc} as above. There is a steep dependence on m_{DM} and v_ν, and the ratio may drop below unity, signaling that the naive concentration (3.8) is affected by Pauli blocking issues. We take this effect into account by multiplying the relevant rates by a phase-space suppression factor,

$$\mathrm{ps} \approx \frac{n_{\nu,\mathrm{gal}}^{\max}}{n_{\nu,\mathrm{gal}}|_{\mathrm{eq.}~(3.8)}} \leq 1 \tag{3.13}$$

whenever this ratio drops below unity. We note that this kind of blocking is mitigated in a decay with more than 2 final states, as neutrinos then assume a broader distribution in momentum.

[7]For the NFW profile we use $r_s = 24.4$ kpc, $\rho_s = 0.18\,\mathrm{GeV/cm}^3$; for an Einasto profile with the core radius $r_c = 1$kpc and $\rho_{\mathrm{DM},\odot} \sim 0.4~\mathrm{GeV/cm}^3$ one obtains $\langle D \rangle = 2.96$. One may of course entertain the possibility of a core and/or spike at the Galactic center [35–37], amplifying the Galactic DR contribution; the effect is milder than for annihilating DM and we will not go into such possibilities here.

Finally, we may find the optimum injection velocity where the concentration saturates $n^{\max}_{\nu,\mathrm{gal}}(v_{\nu,\mathrm{optimal}}) = n_{\nu,\mathrm{gal}}(v_{\nu,\mathrm{optimal}})$; for this, note that $n^{\max}_{\nu,\mathrm{gal}} \propto v_\nu^2$ whereas $n_{\nu,\mathrm{gal}} \propto 1/v_\nu$ on the account of t_{esc}. Therefore, the "optimal" velocity is

$$\frac{v_{\nu,\mathrm{optimal}}}{c} \approx 4 \cdot 10^{-3} \kappa_{\mathrm{DM}}^{1/3} \left(\frac{10t_0}{\tau_{\mathrm{DM}}}\right)^{1/3} \left(\frac{1\ \mathrm{eV}}{m_{\mathrm{DM}}}\right)^{4/3}. \tag{3.14}$$

As can be seen, the number can fall below the escape speed. In this case, the estimate is revised; see following section. The maximal galactic event rate for escaping neutrinos reads,

$$\Gamma_{\mathrm{gal,max}} \approx 750\ \mathrm{yr}^{-1} |U_{e1}|^2 \left(\frac{M_{\mathrm{T}}}{100\ \mathrm{g}}\right) \kappa_{\mathrm{DM}}^{2/3} \left(\frac{10t_0}{\tau_{\mathrm{DM}}}\right)^{2/3} \left(\frac{m_{\mathrm{DM}}}{1\ \mathrm{eV}}\right)^{1/3}, \ \text{for } m_{\mathrm{DM}} \approx 2m_{\nu,\mathrm{lightest}}. \tag{3.15}$$

This shows that although Pauli-blocking may severely constrain the absolute numbers, in the optimal case the galactic contribution can far exceed the cosmological one.

DR neutrinos from 2-body decay are created with a fixed energy $E_\nu = m_{\mathrm{DM}}/2$ in the DM rest frame. In the laboratory frame they will have some energy distribution due to random velocities of DM particles with the width $\Delta E_\nu / E_\nu \sim v_{\mathrm{DM}}/c \sim 10^{-3}$. This scatter in energy can be neglected compared to the energy resolution of the PTOLEMY detector. Therefore, we may take the Galactic DR neutrino energy distribution as a delta-function,

$$\frac{dn^{\mathrm{gal}}_{\nu,i}}{dE_{\nu,i}}(E_{\nu,i}) = n^{\mathrm{gal}}_{\nu,i}\ \mathrm{ps}\ \delta\left(E_{\nu,i} - \frac{m_{\mathrm{DM}}}{2}\right). \tag{3.16}$$

The Galactic component hence produces a peak at the highest possible energy for neutrino capture signal, $E_e = Q + m_{\mathrm{DM}}/2$, see figure 1. Assuming an optimistic energy resolution of $\Delta = 10$ meV this peak can be resolved from the cosmological contribution and serves as another signature of the DR scenario.

3.2.2 Non-escaping neutrinos

Let us now consider the special case that neutrinos from DM decay are injected at non-relativistic speeds with $v_\nu \ll v_{\mathrm{esc}} \sim 10^{-3}c$. In this case, neutrinos accumulate (and saturate in number) rather than escape. In the 2-body decay benchmark case considered here, it happens when the mass of the lightest neutrino is close to the mass of DM, $m_{\mathrm{DM}} \approx 2m_{\nu,1}$. This kinematic arrangement to yield $v_\nu \leq v_{\mathrm{esc}}$ in the decay, requires fine-tuning,

$$\frac{m_{\mathrm{DM}} - 2m_\nu}{m_{\mathrm{DM}}} \lesssim 10^{-6}. \tag{3.17}$$

Despite the severeness of the condition, it may nevertheless be a natural property in some models for the origin of neutrino masses; see e.g. [38, 39]. On the other hand, if DM were to decay into an n-body final state with $n > 2$, there will always neutrinos with $v_\nu \leq v_{\mathrm{esc}}$. Unless the differential decay rate is strongly IR-biased in the neutrino-energy, the efficiency to inject slow neutrinos is directly proportional to the related phase-space volume, which, again will be a small number. Despite these, at first sight unpalatable circumstances, we shall work out this special case below.

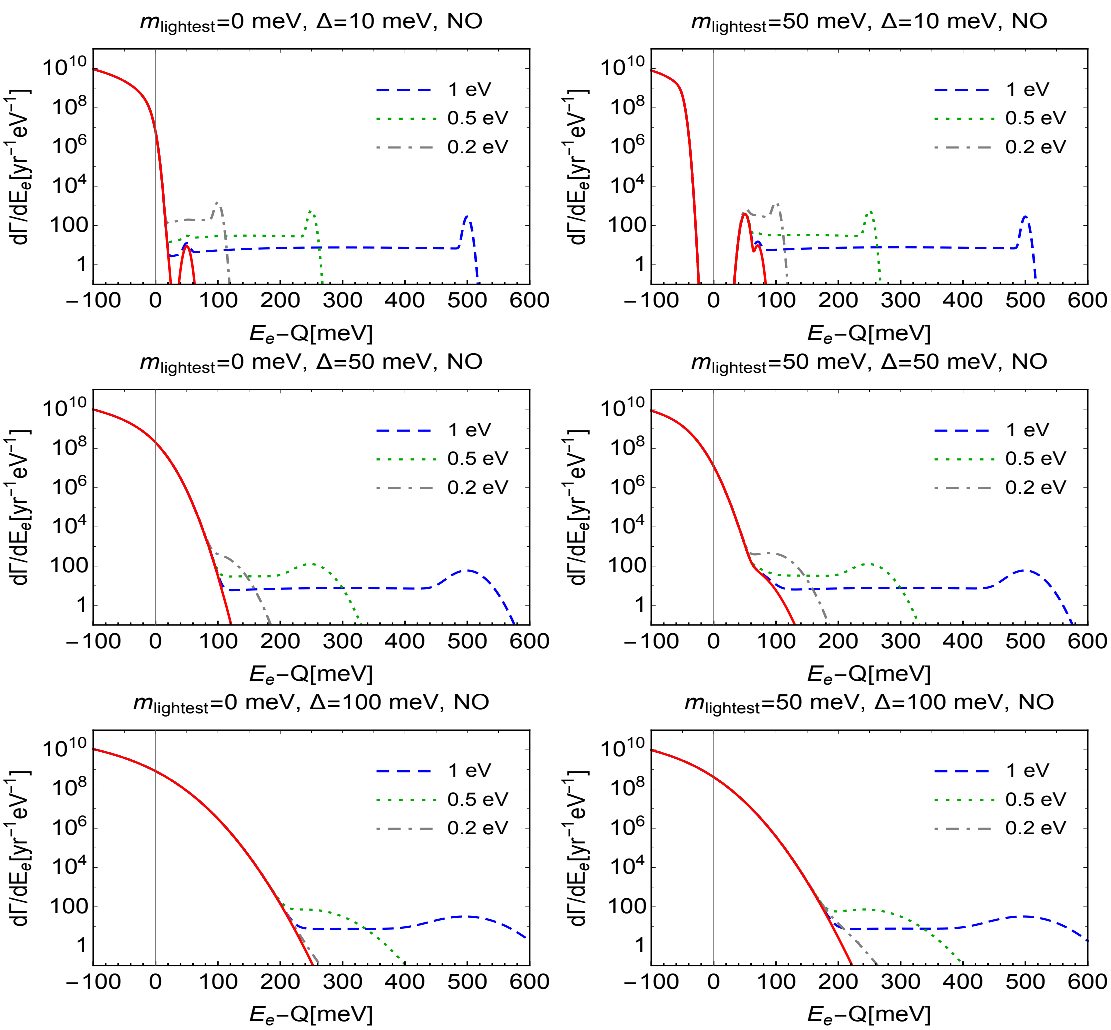

Figure 1. Electron spectra from neutrino DR capture sourced by DM decay with $m_{\rm DM} = 1, 0.5$ and $0.2\,$eV and normal neutrino mass ordering (NO) with the mass of the lightest neutrino $m_1 = 0$ (left panel) and 50 meV (right panel) and $\xi = 1$. The DM lifetime is taken $\tau_{\rm DM} = 10t_0$ and the detector energy resolution is varied from $\Delta = 10$ meV, $\Delta = 50$ meV, to $\Delta = 100$ meV from top to bottom.

If v_ν is smaller than the escape velocity from our Galaxy, $v_\nu \ll v_{\rm esc} \sim 10^{-3}c$, neutrinos rather accumulate than escape. In this case the local neutrino density is[8]

$$n_\nu^{\rm gal} \approx \frac{t_0}{\tau_{\rm DM}} N_\nu \kappa_{\rm DM} n_{{\rm DM},\odot} \times {\rm ps}, \tag{3.18}$$

[8]Gravitationally bound neutrinos can change their helicity when momenta are reversed but spins are not (see e.g. [6]). However, as for such neutrinos $v_\nu \ll 1$, we can neglect each of the velocity-dependent terms in eq. (2.1).

where the escape time is now replaced by the age of the Galaxy, that we have taken as t_0 for simplicity. If we neglect the phase space factor "ps", eq. (3.18) suggests a concentration in excess of (3.7) by a factor $t_0/t_{\rm esc}$ which would be enormous.

Again, when we are sourcing fermionic DR from a bosonic parent with $\kappa_{\rm DM} = O(1)$, we need to include the restriction on phase space density by the factor "ps". To estimate its importance, let us consider for the parent DM phase space distribution function a non-truncated Maxwellian, for concreteness again using the local value $n_{{\rm DM},\odot}$,

$$f_{\rm DM}(|\vec{p}|) = \kappa_{\rm DM} n_{{\rm DM},\odot} \left(\frac{1}{2\pi m_{\rm DM}^2 \sigma^2}\right)^{3/2} \exp\left(-\frac{\vec{p}^2}{2\sigma^2 m_{\rm DM}^2}\right), \tag{3.19}$$

such that $\int d^3\vec{p}\, f_{\rm DM} = \kappa_{\rm DM} n_{{\rm DM},\odot}$; σ is the one-dimensional velocity dispersion. The maximum value is attained for $|\vec{p}| = 0$ which we denote by $f_{\rm DM}^{\rm max} \equiv f_{\rm DM}(0)$. In turn, the precise distribution function of the created non-relativistic neutrinos is difficult to know, because the neutrino spends significant time in the Galaxy and is subject to the same thermalization processes as DM. However, if we are to consider a strictly non-relativistic injection with $v_\nu \ll v_{\rm esc}$, which is possible in the finely-tuned 2-body decay, it is not unreasonable to assume that the DM phase space density is largely inherited. Irrespective of the detailed functional form $f_\nu(|\vec{p}|)$, however, we may particularly expect that $\tilde{f}_\nu^{\rm max} \approx f_{\rm DM}^{\rm max}$ holds well, if Pauli-blocking can be neglected.

As mentioned in the previous section, Fermi-Dirac statistics tells us that the maximum phase space density is $f_\nu^{\rm max} = f_\nu/(8\pi^3)$, and Pauli-blocking in the decay needs to be taken into account, whenever this density becomes saturated. Therefore, we may evaluate the "in-medium" phase space suppression factor from the ratio

$$\text{ps} \approx \frac{f_\nu^{\rm max}}{f_{\rm DM}^{\rm max}} = \frac{g_\nu}{8\pi^3} \frac{(2\pi\sigma^2)^{3/2} m_{\rm DM}^4}{\kappa_{\rm DM}\rho_{{\rm DM},\odot}} \approx 4\times 10^{-6} \frac{g_\nu}{\kappa_{\rm DM}} \left(\frac{m_{\rm DM}}{\rm eV}\right)^4. \tag{3.20}$$

On the right hand side we have used $\sigma = v_c/\sqrt{2}$ where $v_c \simeq 220\,{\rm km/s}$ is the circular velocity of the solar system. This is a punishing factor and implies that the enhancement in the local concentration is at best moderate for $m_{\rm DM} \simeq 1$ eV, and even turns into a suppression factor for lower DM mass when neutrinos are not evacuated from the galaxy like in the relativistic case above. The arguments above are similar in the spirit that underlie the ones leading to the Gunn-Tremaine bound [25] and essentially a manifestation of Liouville's theorem; see also [26] and the recent update in [27].

Since the solar mass splitting is $\sqrt{|\Delta m_\odot^2|} \simeq 10^{-2}$ eV, the degeneracy condition (3.17) can only hold for one of the three neutrino mass eigenstates. If the degeneracy holds for the lightest of neutrino states, ν_1, it remains the only kinematically allowed decay channel and $v_\nu \lesssim v_{\rm esc}$ is guaranteed. If the degeneracy is with a heavier state, then the branching ratio into the "slow channel" will be suppressed by a model-dependent factor $\sim (v_\nu/c)^n$, $n \geq 1$ as a lighter final state is available. In our numerical results, we will assume for simplicity that the fine-tuning happens for the lightest neutrino in which case the branching fraction of DM decay into the lightest neutrino mass state $i = 1$ is equal to one.

4 PTOLEMY sensitivity

We now proceed to forecast the sensitivity to neutrino DR on the concrete example of PTOLEMY. The canonical event shape for CνB detection is a large beta-background until the endpoint energy that needs to get filtered in order to detect the small capture signals that are offset by a small amount given by their neutrino masses. In the current context, both constitute backgrounds to a DR search. However, as we argued above, the DR signal can extend in energy up to ~ 1 eV above the endpoint, into an essentially background free region.

To treat both cases simultaneously, we use a binned profile likelihood and simulate the experiment with assumed 1 yr and 5 yr exposures and a target mass of 100 g by generating Monte Carlo mock representations. We consider the neutrino-induced capture events from sources $\alpha = \beta, \mathrm{C}\nu\mathrm{B}$, and DR together with their associated energy spectra $d\widetilde{\Gamma}_\alpha(E_e, \vec{\theta})/dE_e$ that are obtained by folding the theoretical rates with an Gaussian energy resolution Δ according to (2.5). The model parameters that enter these predictions are τ_{DM} and m_{DM} for DR with $\vec{\theta} = \tau_{\mathrm{DM}}$; for $\alpha = \beta, \mathrm{C}\nu\mathrm{B}$ $\vec{\theta}$ there are no fit parameters and $\vec{\theta}$ is null. The likelihood function under the hypothesis H for fixed neutrino mass hierarchy (NO, IO), fixed DM mass m_{DM} and absolute neutrino mass scale given by m_{ν_1} reads,

$$\mathcal{L}(\vec{\theta}|\mathrm{H}) = \prod_{i=1}^{N_{\mathrm{bin}}} \frac{e^{-\varepsilon \sum_\alpha \mu_\alpha^i(\vec{\theta})}}{N_{\mathrm{obs}}^i!} \left[\sum_\alpha \mu_\alpha^i(\vec{\theta}) \right]^{N_{\mathrm{obs}}^i}. \tag{4.1}$$

For our analysis, we divide the signal region in $E_e - Q$ from $-25, -75, -150$ meV (for $\Delta = 10, 50, 100$ meV, respectively) to 300 meV into $N_{\mathrm{bin}} = 100$ equidistant bins and from 0.3 eV to 30 eV into $N_{\mathrm{bin}} = 50$ logarithmic bins. The reason for such division is owed to computational efficiency, since at higher energies we enter the background-free region. The expected number of events in each bin i of source α is denoted by μ_α^i and N_α^i is the associated random number of observed events in each bin that is drawn from a Poisson distribution; $N_{\mathrm{obs}}^i = \sum_\alpha N_\alpha^i$.

A discovery of a DR signal in presence of backgrounds then amounts to a rejection of the background-only hypothesis H_0 for sources $\alpha = \beta, \mathrm{C}\nu\mathrm{B}$. Here, the negative log-likelihood then serves as test statistic for the hypothesis test, $q = -2 \ln \mathcal{L}(\hat{\hat{\vec{\theta}}}|\mathrm{H}_0)/\mathcal{L}(\hat{\vec{\theta}}|\mathrm{H}_1)$, where $\hat{\hat{\vec{\theta}}}$ maximizes the likelihood under the background-only hypothesis H_0: $\tau_{\mathrm{DM}} \to \infty$ and $\hat{\vec{\theta}}$ maximizes $\mathcal{L}$ for signal plus background, H_1: $\tau_{\mathrm{DM}} \neq 0$. A distribution in q under H_1 is obtained by generating 10^3 mock data-sets for each combination of $(\tau_{\mathrm{DM}}, m_{\mathrm{DM}})$, until the entire parameter space is scanned; in turn, the distribution in q with mock-data generated under H_0 we verified that it follows a χ^2 distribution with one degree of freedom as per Wilk's theorem [40]. The significance distributions are then given by $Z = \sqrt{q}$. The discovery criterion at 3σ significance implies that H_0 is rejected with 99.865% probability (p-value $p_0 = 0.00135$). For a chosen confidence level of 90% we require that a given experiment has a 90% probability to detect at least a signal with 3σ significance. Hence, this leads to a detection of the signal, if 90% of the mock-data sets generated under H_1 lie above the discovery criterion $Z \geq 3\sigma$, where H_1 is accepted and where at the same time H_0 is rejected; see [22, 41] for further details on this procedure.

The resulting discovery potentials are shown in the left (right) panel of figure 2 for normal (inverted) neutrino mass hierarchy; we additionally take the lightest neutrino as massless, $m_{\nu_1} = 0$ ($m_{\nu_3} = 0$). We assume that DR is sourced from $X \to \nu\bar{\nu}$, i.e. $N_\nu = 1$ with a decaying DM fraction of 100%, $\kappa_{\mathrm{DM}} = 1$. The blue and green sets of lines are associated with exposures of 100 g yr and 500 g yr, respectively. The solid, dashed, and dash-dotted lines correspond to progressively worsening assumptions on the energy resolution, $\Delta = 10$, 50 and 100 meV, respectively. The thin vertical lines show the kinematic thresholds for the decays into the heavier neutrino mass eigenstates $m_{\nu_{2,3}}$. The gray shaded region shows the

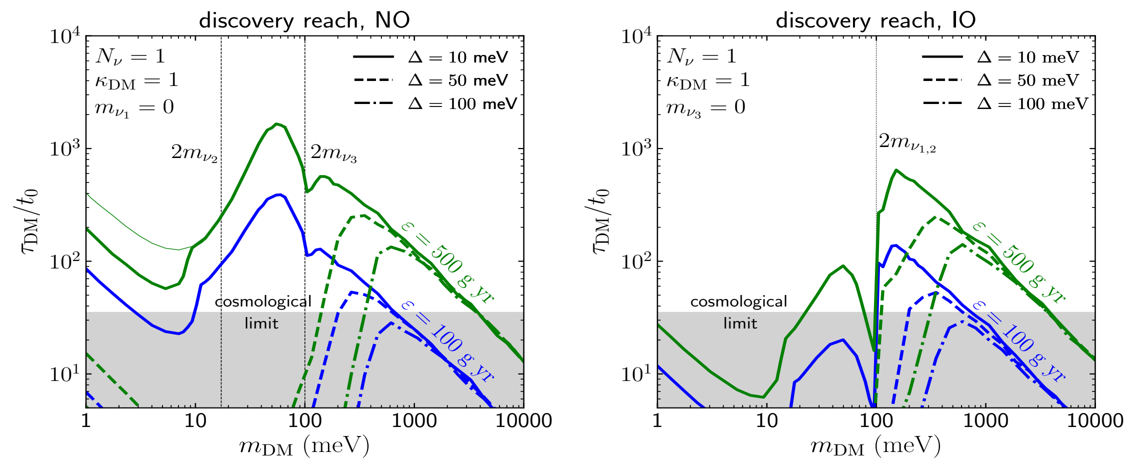

Figure 2. Discovery reach of PTOLEMY as a function of progenitor mass $m_{\rm DM}$ and lifetime in units of the age of the Universe, $\tau_{\rm DM}/t_0$. An exposure of 100 g yr (blue lines) and 500 g yr (green lines) has been assumed for various projected performances on the electron energy resolution Δ as labeled, with 10 eV (100 eV) being the optimal (most conservative) case. All of DM is assumed to be decaying $\kappa_{\rm DM} = 1$. The mass of the lightest neutrino is $m_{\nu_1} = 0$. In the left (right) panel The mass of the lightest neutrino is $m_{\nu_1} = 0$ ($m_{\nu_3} = 0$) and a normal (inverted) hierarchy is assumed.

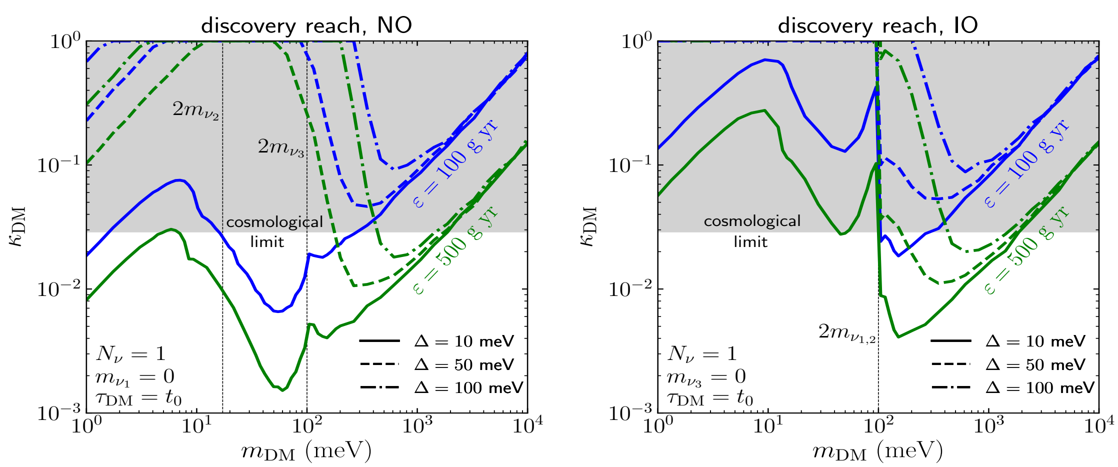

Figure 3. Sensitivity of PTOLEMY to the decaying fraction of DM, $\kappa_{\rm DM}$, as a function of DM mass; same labeling as in figure 2.

cosmological limit on the decaying cold DM lifetime, $\tau_{\rm DM} \gtrsim 35 t_0$ [42]; see also [33, 43, 44]. Finally, the thin green line in the left panel is obtained when Pauli-blocking is neglected.

Both panels establish the sensitivity to the maximum DM lifetime, directly related to the minimum detectable DR flux (a 3σ significance in the general presence of the CνB background. In the high mass region $m_{\rm DM} \gtrsim 100$ meV, the discovery potential is almost independent on the neutrino mass hierarchy and a general $1/m_{\rm DM}$ scaling can be seen. At around 100 meV progenitor mass, this trend is broken by the presence of the CνB peak generated by the heaviest neutrino, $m_{\nu_3} = 50$ meV ($m_{\nu_{1,2}} \simeq 50$ meV) assuming normal (inverted) hierarchy. In the left panel, the sensitivity for $\Delta = 10$ meV reaches its optimum at $m_{\rm DM} \sim 50$ meV, whereas in the inverted hierarchy scenario (right panel) the lightest neutrino has a smaller contribution to the DR signal due to the smaller squared PMNS-matrix element $|U_{e3}|^2$. Therefore, smaller lifetimes, i.e. a larger DR flux, are necessary to discover the signal in comparison to the right panel. For $m_{\rm DM} \lesssim 40$ meV, the continuous tritium beta background starts playing a role, suppressing the lifetime reach in both panels. However, this is eventually counterbalanced by the growing decaying DM number density with $1/m_{\rm DM}$ and the sensitivity is again improved for diminishing DM mass. However, only for the NO the lines extend above the cosmological limit.

We conclude that a discovery of decaying DM with $m_{\rm DM} \gtrsim 100$ meV is possible with rather relaxed assumptions on energy resolution. For lighter DM mass, an optimum energy resolution is critical to suppress the bleeding of the beta background into the signal region, and decaying DM with neutrino final states is discoverable in the normal ordering across the entire conceivable mass range.

Finally, we may consider the possibility that a fraction $\kappa_{\rm DM}$ of DM decays with arbitrary lifetime and ask for the sensitivity of PTOLEMY to $\kappa_{\rm DM}$. For this, we saturate the flux by choosing an optimal lifetime, $\tau_{\rm DM} = t_0$, so that the fraction $\kappa_{\rm DM}$ decays today with an unsuppressed rate. The model parameters that enter in the likelihood in eq. (4.1) are now $\kappa_{\rm DM}$ and $m_{\rm DM}$ for DR with $\vec{\theta} = \kappa_{\rm DM}$. Figure 3 presents the 3σ discovery sensitivity to $\kappa_{\rm DM}$ as a function of progenitor mass as above. As expected, the discovery potentials in the $(\kappa_{\rm DM}, m_{\rm DM})$-plane exhibit an inverse behaviour with respect to the contours in the $(\tau_{\rm DM}, m_{\rm DM})$-plane in figure 2. The discoverable region is hence affected by the same limiting factors as were discussed above. We conclude that with an exposure of 100 g yr (500 g yr) PTOLEMY is capable to detect a decaying fraction of $\sim 1\%$ ($\sim 0.1\%$) with an optimal energy resolution of $\Delta = 10$ meV. For the pessimistic case $\Delta = 100$ meV it takes the larger of assumed exposures to compete with cosmological limits with a mild prospect to detect DR originating from a decay with progenitor mass $0.1 \lesssim m_{\rm DM}/{\rm eV} \lesssim 2$.

5 Conclusions

PTOLEMY is a visionary and ambitious experiment. Its main science goal — the detection of relic neutrinos — would mark a resounding success for a key prediction of hot Big Bang cosmology, but will require significant breakthroughs in experimental technology. When entering such unexplored areas we are not safe from unexpected difficulties and obstacles. In this work we demonstrate through a detailed profile likelihood study that even before PTOLEMY reaches the level of performance (first of all, energy resolution and statistics) it can potentially detect a signal from new physics that can accede the SM relic neutrino signal, namely, the detection of neutrino DR. Such DR may be sourced by the decay of (a component of) DM with sub-eV mass. The potential signal in PTOLEMY can then be classified as follows:

- In the most generic case (see figure 1) DM decays into a 2-body neutrino final state which results in an additional peak located at $E_{\rm peak} = Q + m_{\rm DM}/2$. The number of events in this signal may be equal or larger than in the signal from the CνB for the

DM mass range $2m_{\nu_1} \leq m_{\rm DM} \lesssim 1\,\text{eV}$. This peak comes from DM decay in our Galaxy. Additionally, extragalactic DM decays give rise to a second component of the signal, similar in overall magnitude but with events almost equally distributed in electron energy between Q and $Q + m_{\rm DM}/2$.

- There is a special case when neutrinos are efficiently released at semi- or non-relativistic velocities, either in a suitably arranged decay with more than two final states, or when $m_{\rm DM}/2 \simeq m_{\nu_1}$ in the 2-body decay. The local concentration of neutrinos can then be enhanced by Galactic DM decays, reaching a maximum when the injection velocity is in the vicinity of the Milky Way's escape speed.

There is a number of avenues to explore further in our proposal. First of all, concrete models of sub-eV DM should be explored and how they embed themselves into the bigger scheme of things, such as relic density generation; such program has already started in [23, 24]. Is it possible to find well-motivated or natural cases where the non-relativistic injection boosts the detection prospects? On the signal side, we may quantitatively address the question to what degree it is possible to discriminate between early ($\tau_{\rm DM} \lesssim t_0$) and late ($\tau_{\rm DM} \gtrsim t_0$) decays by virtue of the Galactic peak. In summary, there is a scientific case for relic neutrino searches such as PTOLEMY that is connected to another pressing topic in modern physics, namely, the quest in understanding the most basic properties of DM, such as its lifetime and mass-scale. A detection of DR in a future CνB experiment may shed light on these questions.

Acknowledgments

MN and AS are supported by the FWF Research Group grant FG1. JP is supported through the New Frontiers Program by the Austrian Academy of Sciences. KB and AB are supported by the European Research Council (ERC) Advanced Grant "NuBSM" (694896).

A A solar neutrino basin?

Another intense local source of neutrinos is the Sun. Here, one may first wonder if the most prominent of fluxes, the *pp*-flux may constitute a background for PTOLEMY. However, it is easy to see that the falling statistical beta spectrum with decreasing energy yields a small flux, e.g. at $E_\nu = 1$ eV it is $dF_{pp}/dE_\nu \simeq 10^{-2}\,\text{cm}^{-2}\,\text{s}^{-1}\,\text{keV}^{-1}$. Overall, the spectrum translates into a minute local concentration $n_{\nu,\rm pp} \sim 10^{-16}$ of *pp*-neutrinos below 1 eV energy. In fact, the low energy region is largely dominated by the flux from plasmon decay [45]. From figure 2 in [46] one finds a differential flux value $dF/dE = 10$ cm^{-2} s^{-1} keV^{-1} at a neutrino energy of 1 eV, still falling significantly short for an interesting instantaneous concentration.

The above arguments neglect neutrino mass. Neutrinos produced in the Sun may, however, also be gravitationally trapped within the solar system because of their finite masses. Such possibility has recently been proposed in [47] as an amplification scheme for probing light new physics that may be produced in Sun. We may take a quick estimate to demonstrate, that for neutrinos this mechanism is negligible to obtain a reasonable neutrino concentration at Earth.

Let the flux of neutrinos that reaches Earth but do not escape the solar system be ΔF. On dimensional grounds, the number density of neutrinos at Earth is then of order,

$$n_{\nu,\rm solar} \sim \frac{\Delta F t_\odot}{r_E}, \tag{A.1}$$

where $t_\odot \approx 4.5 \times 10^9$ yr is the age of the solar system and $r_E = 1\,\mathrm{AU}$ is the distance between Sun and Earth. To estimate the neutrino flux we may take the above quoted value of 10 cm^{-2} s^{-1} keV^{-1} at 1 eV energy from [46], hence overestimating the relevant non-relativistic portion at even lower energy.[9] Neutrinos that reach Earth but do not escape the solar system have a narrow energy distribution with a width

$$\Delta E = \frac{G M_\odot m_\nu}{r_E} \approx 10^{-8}\ \mathrm{eV} \left(\frac{m_\nu}{1\ \mathrm{eV}}\right). \tag{A.2}$$

We may then limit the associated flux of such neutrinos from above,

$$\Delta F \lesssim \frac{dF}{dE}(E = 1\ \mathrm{eV}) \Delta E \approx 10^{-10}\ \mathrm{cm}^{-2}\ \mathrm{s}^{-1} \left(\frac{m_\nu}{1\ \mathrm{eV}}\right) \tag{A.3}$$

Substituting this value into (A.1) we arrive at

$$n_{\nu,\mathrm{solar}} \sim 10^{-6}\ \mathrm{cm}^{-3}. \tag{A.4}$$

This number is already overestimation of the trapped neutrino density at Earth and it is eleven orders of magnitude smaller than for relic neutrinos. This means that solar neutrinos do not constitute a background for relic neutrino searches.

B Inverse ordering

In this appendix figure 4 presents the pendant to figure 1 for an inverted neutrino mass ordering with two heavier states split by the smaller solar mass difference.

C Discovery potential for $m_{\nu_1} = 50$ meV ($m_{\nu_3} = 50$ meV)

In figures 5, 6 we present the discovery potentials for $m_{\nu_1} = 50$ meV ($m_{\nu_3} = 50$ meV) for normal (inverted) mass hierarchy. In this case, the minimum allowed DM mass is 100 meV and the tritium beta background does not play a role. Hence, the CνB is the only background that enters in the analysis and only alters the limits around $m_{\mathrm{DM}} = 100$ meV compared to the figures 2, 3.

[9] It appears that finite neutrino masses were not taken into account in the numerical results of [46], but their inclusion would render the neutrino flux even smaller.

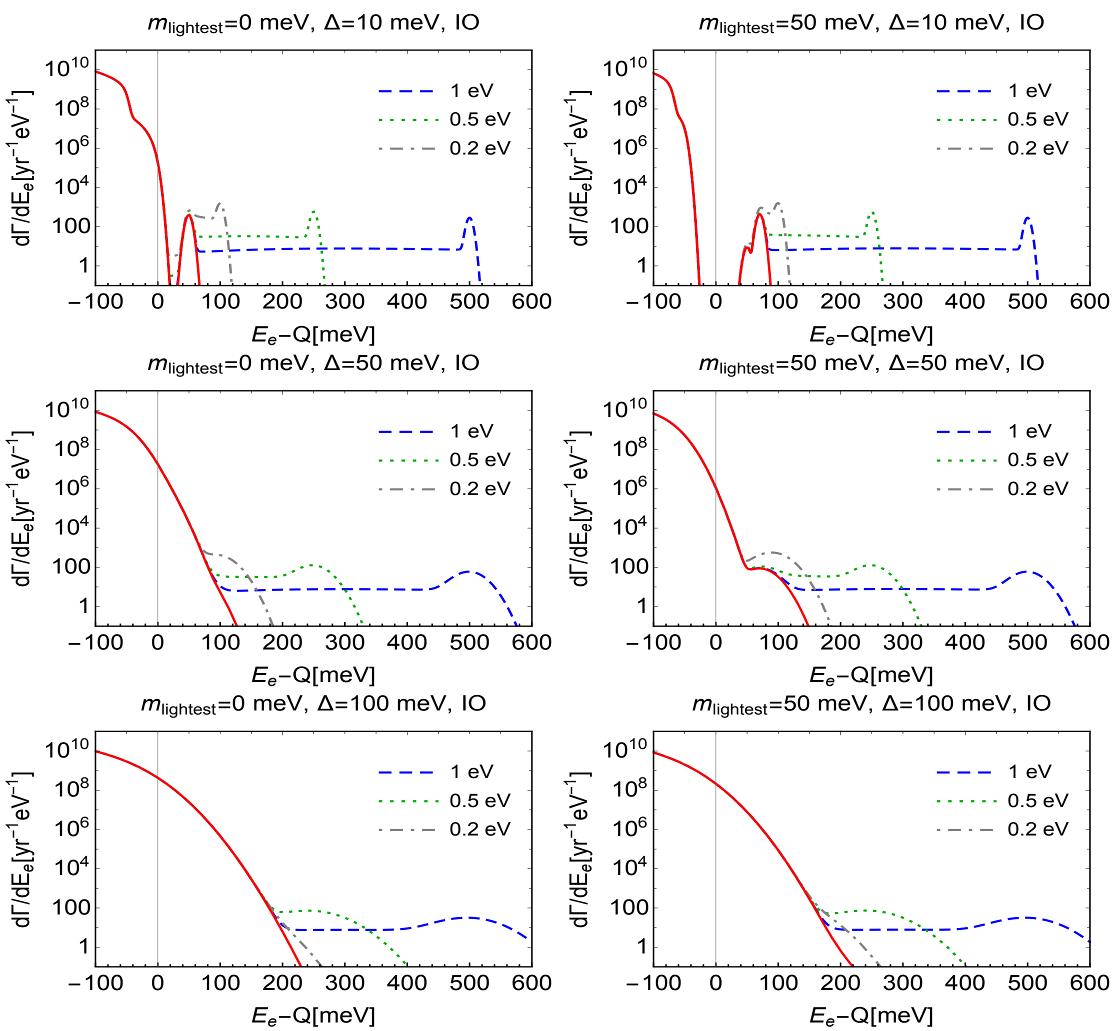

Figure 4. Examples of the DR neutrino signals from DM decay with $m_{\rm DM} = 1, 0.5$ and $0.2\,$eV and inverse neutrino mass ordering (IO) with $m_{\nu_1} = 0$ (left panel) and 50 meV (right panel). The DM lifetime is taken as $\tau_{\rm DM} = 10t_0$ and the detector energy resolution is assumed to be $\Delta = 10$ meV, 50 meV, and 100 meV from top to bottom.

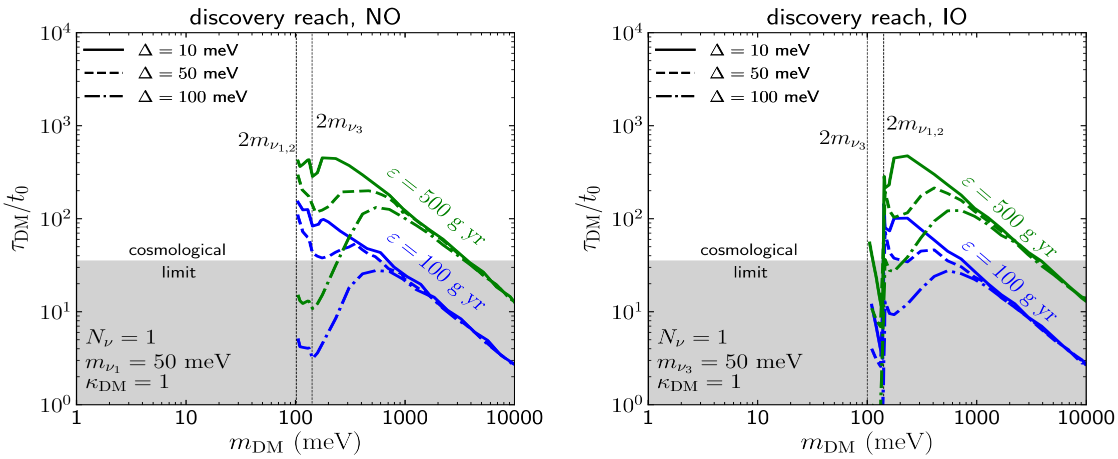

Figure 5. Reach of PTOLEMY at 3σ significance as a function of progenitor mass m_{DM} and lifetime in units of the age of the Universe, τ_{DM}/t_0. An exposure of 100 g yr (blue lines) and 500 g yr (green lines) has been assumed for various projected performances on the electron energy resolution Δ as labeled, with 10 eV (100 eV) being the optimal (most conservative) case. All of DM is assumed to be decaying $\kappa_{\mathrm{DM}} = 1$. In the left (right) panel the mass of the lightest neutrino is $m_{\nu_1} = 50$ meV ($m_{\nu_3} = 50$ meV) and a normal (inverted) hierarchy is assumed.

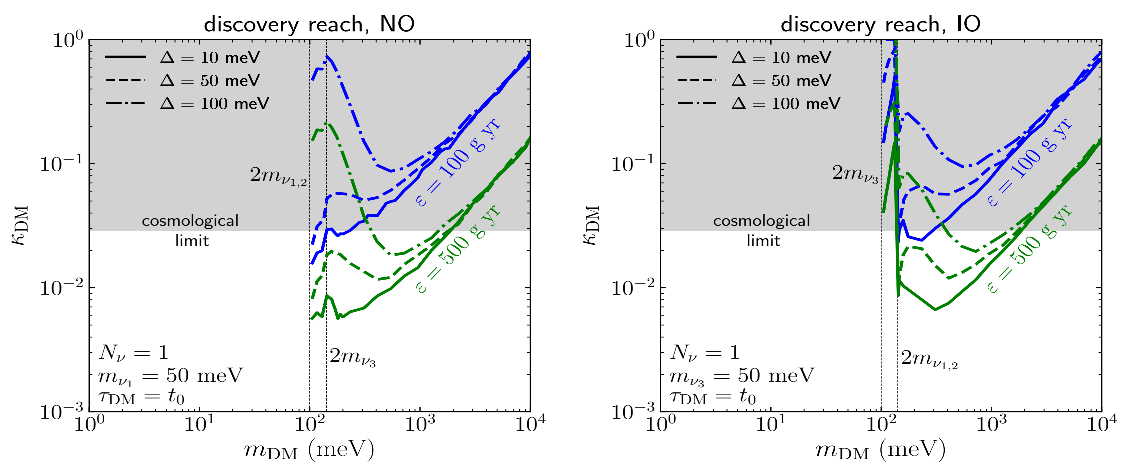

Figure 6. Reach of PTOLEMY at 3σ significance to the decaying fraction of DM, κ_{DM}, as a function of DM mass. The mass of the lightest neutrino is $m_{\nu_1} = 50$ meV ($m_{\nu_3} = 50$ meV); a normal (inverted) hierarchy is assumed.

References

[1] V.A. Rubakov and D.S. Gorbunov, *Introduction to the Theory of the Early Universe: Hot big bang theory*, World Scientific, Singapore, (2017).

[2] E. Vitagliano, I. Tamborra and G. Raffelt, *Grand Unified Neutrino Spectrum at Earth: Sources and Spectral Components*, *Rev. Mod. Phys.* **92** (2020) 045006 [arXiv:1910.11878] [INSPIRE].

[3] L. Stodolsky, *Speculations on Detection of the Neutrino Sea*, *Phys. Rev. Lett.* **34** (1975) 110 [*Erratum ibid.* **34** (1975) 508] [INSPIRE].

[4] B.F. Shvartsman, V.B. Braginsky, S.S. Gershtein, Y.B. Zeldovich and M.Y. Khlopov, *Possibility of detecting relict massive neutrinos*, *JETP Lett.* **36** (1982) 277 [*Pisma Zh.Eksp.Teor.Fiz.* **36** (1982) 224] [INSPIRE].

[5] P. Langacker, J.P. Leveille and J. Sheiman, *On the Detection of Cosmological Neutrinos by Coherent Scattering*, *Phys. Rev. D* **27** (1983) 1228 [INSPIRE].

[6] G. Duda, G. Gelmini and S. Nussinov, *Expected signals in relic neutrino detectors*, *Phys. Rev. D* **64** (2001) 122001 [hep-ph/0107027] [INSPIRE].

[7] V. Domcke and M. Spinrath, *Detection prospects for the Cosmic Neutrino Background using laser interferometers*, *JCAP* **06** (2017) 055 [arXiv:1703.08629] [INSPIRE].

[8] J.m. Irvine and R. Humphreys, *Neutrino masses and the cosmic neutrino background*, *J. Phys. G* **9** (1983) 847 [INSPIRE].

[9] A.G. Cocco, G. Mangano and M. Messina, *Probing low energy neutrino backgrounds with neutrino capture on beta decaying nuclei*, *JCAP* **06** (2007) 015 [hep-ph/0703075] [INSPIRE].

[10] S. Betts et al., *Development of a Relic Neutrino Detection Experiment at PTOLEMY: Princeton Tritium Observatory for Light, Early-Universe, Massive-Neutrino Yield*, in *Community Summer Study 2013: Snowmass on the Mississippi*, (2013) [arXiv:1307.4738] [INSPIRE].

[11] PTOLEMY collaboration, *PTOLEMY: A Proposal for Thermal Relic Detection of Massive Neutrinos and Directional Detection of MeV Dark Matter*, arXiv:1808.01892 [INSPIRE].

[12] KATRIN collaboration, *KATRIN: A next generation tritium beta decay experiment with sub-eV sensitivity for the electron neutrino mass. Letter of intent*, hep-ex/0109033 [INSPIRE].

[13] Y.F. Li and Z.-z. Xing, *Possible Capture of keV Sterile Neutrino Dark Matter on Radioactive β-decaying Nuclei*, *Phys. Lett. B* **695** (2011) 205 [arXiv:1009.5870] [INSPIRE].

[14] A.J. Long, C. Lunardini and E. Sabancilar, *Detecting non-relativistic cosmic neutrinos by capture on tritium: phenomenology and physics potential*, *JCAP* **08** (2014) 038 [arXiv:1405.7654] [INSPIRE].

[15] Y.F. Li, Z.-z. Xing and S. Luo, *Direct Detection of the Cosmic Neutrino Background Including Light Sterile Neutrinos*, *Phys. Lett. B* **692** (2010) 261 [arXiv:1007.0914] [INSPIRE].

[16] Y. Hochberg, Y. Kahn, M. Lisanti, C.G. Tully and K.M. Zurek, *Directional detection of dark matter with two-dimensional targets*, *Phys. Lett. B* **772** (2017) 239 [arXiv:1606.08849] [INSPIRE].

[17] J.A. Dror, G. Elor and R. Mcgehee, *Absorption of Fermionic Dark Matter by Nuclear Targets*, *JHEP* **02** (2020) 134 [arXiv:1908.10861] [INSPIRE].

[18] S. Palomares-Ruiz, *Model-Independent Bound on the Dark Matter Lifetime*, *Phys. Lett. B* **665** (2008) 50 [arXiv:0712.1937] [INSPIRE].

[19] S. Palomares-Ruiz and S. Pascoli, *Testing MeV dark matter with neutrino detectors*, *Phys. Rev. D* **77** (2008) 025025 [arXiv:0710.5420] [INSPIRE].

[20] C. Garcia-Cely and J. Heeck, *Neutrino Lines from Majoron Dark Matter*, *JHEP* **05** (2017) 102 [arXiv:1701.07209] [INSPIRE].

[21] Y. Cui, M. Pospelov and J. Pradler, *Signatures of Dark Radiation in Neutrino and Dark Matter Detectors*, *Phys. Rev. D* **97** (2018) 103004 [arXiv:1711.04531] [INSPIRE].

[22] M. Nikolic, S. Kulkarni and J. Pradler, *The neutrino-floor in the presence of dark radiation*, arXiv:2008.13557 [INSPIRE].

[23] D. McKeen, *Cosmic neutrino background search experiments as decaying dark matter detectors*, *Phys. Rev. D* **100** (2019) 015028 [arXiv:1812.08178] [INSPIRE].

[24] Z. Chacko, P. Du and M. Geller, *Detecting a Secondary Cosmic Neutrino Background from Majoron Decays in Neutrino Capture Experiments*, *Phys. Rev. D* **100** (2019) 015050 [arXiv:1812.11154] [INSPIRE].

[25] S. Tremaine and J.E. Gunn, *Dynamical Role of Light Neutral Leptons in Cosmology*, *Phys. Rev. Lett.* **42** (1979) 407 [INSPIRE].

[26] A. Boyarsky, O. Ruchayskiy and D. Iakubovskyi, *A lower bound on the mass of Dark Matter particles*, *JCAP* **03** (2009) 005 [arXiv:0808.3902] [INSPIRE].

[27] J. Alvey et al., *New constraints on the mass of fermionic dark matter from dwarf spheroidal galaxies*, *Mon. Not. Roy. Astron. Soc.* **501** (2021) 1188 [arXiv:2010.03572] [INSPIRE].

[28] Y. Chikashige, R.N. Mohapatra and R.D. Peccei, *Are There Real Goldstone Bosons Associated with Broken Lepton Number?*, *Phys. Lett. B* **98** (1981) 265 [INSPIRE].

[29] A. Ringwald and Y.Y.Y. Wong, *Gravitational clustering of relic neutrinos and implications for their detection*, *JCAP* **12** (2004) 005 [hep-ph/0408241] [INSPIRE].

[30] K. Akita, S. Hurwitz and M. Yamaguchi, *Precise Capture Rates of Cosmic Neutrinos and Their Implications on Cosmology*, arXiv:2010.04454 [INSPIRE].

[31] Planck collaboration, *Planck 2018 results. VI. Cosmological parameters*, *Astron. Astrophys.* **641** (2020) A6 [arXiv:1807.06209] [INSPIRE].

[32] PTOLEMY collaboration, *Neutrino physics with the PTOLEMY project: active neutrino properties and the light sterile case*, *JCAP* **07** (2019) 047 [arXiv:1902.05508] [INSPIRE].

[33] V. Poulin, P.D. Serpico and J. Lesgourgues, *A fresh look at linear cosmological constraints on a decaying dark matter component*, *JCAP* **08** (2016) 036 [arXiv:1606.02073] [INSPIRE].

[34] M. Cirelli et al., *PPPC 4 DM ID: A Poor Particle Physicist Cookbook for Dark Matter Indirect Detection*, *JCAP* **03** (2011) 051 [*Erratum ibid.* **10** (2012) E01] [arXiv:1012.4515] [INSPIRE].

[35] P. Gondolo and J. Silk, *Dark matter annihilation at the galactic center*, *Phys. Rev. Lett.* **83** (1999) 1719 [astro-ph/9906391] [INSPIRE].

[36] P. Ullio, H. Zhao and M. Kamionkowski, *A dark matter spike at the galactic center?*, *Phys. Rev. D* **64** (2001) 043504 [astro-ph/0101481] [INSPIRE].

[37] A.A. Dutton and A.V. Macciò, *Cold dark matter haloes in the Planck era: evolution of structural parameters for Einasto and NFW profiles*, *Mon. Not. Roy. Astron. Soc.* **441** (2014) 3359 [arXiv:1402.7073] [INSPIRE].

[38] G. Dvali, S. Folkerts and A. Franca, *How neutrino protects the axion*, *Phys. Rev. D* **89** (2014) 105025 [arXiv:1312.7273] [INSPIRE].

[39] G. Dvali and L. Funcke, *Small neutrino masses from gravitational θ-term*, *Phys. Rev. D* **93** (2016) 113002 [arXiv:1602.03191] [INSPIRE].

[40] S.S. Wilks, *The Large-Sample Distribution of the Likelihood Ratio for Testing Composite Hypotheses*, *Annals Math. Statist.* **9** (1938) 60 [INSPIRE].

[41] J. Billard, L. Strigari and E. Figueroa-Feliciano, *Implication of neutrino backgrounds on the reach of next generation dark matter direct detection experiments*, *Phys. Rev. D* **89** (2014) 023524 [arXiv:1307.5458] [INSPIRE].

[42] DES collaboration, *Constraints on Decaying Dark Matter with DES-Y1 and external data*, arXiv:2011.04606 [INSPIRE].

[43] K. Enqvist, S. Nadathur, T. Sekiguchi and T. Takahashi, *Decaying dark matter and the tension in* σ_8, *JCAP* **09** (2015) 067 [arXiv:1505.05511] [INSPIRE].

[44] A. Nygaard, T. Tram and S. Hannestad, *Updated constraints on decaying cold dark matter*, arXiv:2011.01632 [INSPIRE].

[45] G. Raffelt, *Stars as laboratories for fundamental physics: The astrophysics of neutrinos, axions, and other weakly interacting particles*, Chicago University Press, Chicago, U.S.A. (1996) [INSPIRE].

[46] E. Vitagliano, J. Redondo and G. Raffelt, *Solar neutrino flux at keV energies*, *JCAP* **12** (2017) 010 [arXiv:1708.02248] [INSPIRE].

[47] K. Van Tilburg, *Stellar Basins of Gravitationally Bound Particles*, arXiv:2006.12431 [INSPIRE].

APPENDIX H

Galactic and extragalactic dark radiation flux

H.1 Dark radiation from two body decays

In this appendix, we derive the galactic and extragalactic fluxes of dark radiation used in Ref. [3] in Sec. 6. Dark matter may decay in the galaxy or at cosmological distances. The magnitude of these flux components depends on the lifetime and the mass of the progenitor, assuming no directional sensitivity.

The galactic flux component is derived in the following way, see [30, 124–126] for more details. The total number of decay products per energy E_{DR} in a volume element dV at distance s is given by

$$\frac{dN}{dE_{\mathrm{DR}}}\frac{f_{\mathrm{DM}}\rho_{\mathrm{DM}}(r)e^{-\frac{t_0}{\tau_{\mathrm{DM}}}}}{\tau_{\mathrm{DM}}m_{\mathrm{DM}}}dV, \tag{H.1.1}$$

where $\rho_{\mathrm{DM}}(r(s,\theta))$ is the dark matter density expressed in galactic coordinates for an observer at distance s and for an observation angle θ, $t_0 \simeq 13.8$ Gyr [6] is the age of the universe, f_{DM} is the fraction of decaying dark matter with mass m_{DM} and lifetime τ_{DM} and dN/dE_{DR} is the dark radiation energy spectrum. Then, the differential galactic flux through an area $A = 4\pi s^2$ is given by the integration over the line of sight (l.o.s) and angles θ, ϕ of a sphere,

$$\frac{d\Phi_{\mathrm{DR,\ gal}}}{dE_{\mathrm{DR}}} = \frac{1}{4\pi}\frac{dN}{dE_{\mathrm{DR}}}\frac{f_{\mathrm{DM}}e^{-\frac{t_0}{\tau_{\mathrm{DM}}}}}{\tau_{\mathrm{DM}}m_{\mathrm{DM}}}\int_0^{2\pi}\int_0^{\pi}\int_{\mathrm{l.o.s}}\rho_X(r(s,\theta))\sin\theta\, ds\, d\theta d\phi \tag{H.1.2}$$

$$= \frac{dN}{dE_{\mathrm{DR}}}\frac{f_{\mathrm{DM}}e^{-\frac{t_0}{\tau_{\mathrm{DM}}}}}{\tau_{\mathrm{DM}}m_{\mathrm{DM}}}r_\odot\rho_\odot\left\langle J_{\mathrm{dec}}\right\rangle, \tag{H.1.3}$$

where $r_\odot = 8.33$ kpc is the distance between the galactic center and the observer at the Earth, $\rho_\odot = 0.3\ \mathrm{GeV/cm}^3$ is the local dark matter density. For a NFW-profile (1.3.3), the J-factor averaged over angles yields

$$\langle J_{\mathrm{dec}}\rangle = \frac{1}{4\pi\rho_\odot r_\odot}\int_0^{2\pi}\int_0^{\pi}\int_{\mathrm{l.o.s}}\rho_X(r(s,\theta))\sin\theta\, ds\, d\theta d\phi \simeq 2.19, \tag{H.1.4}$$

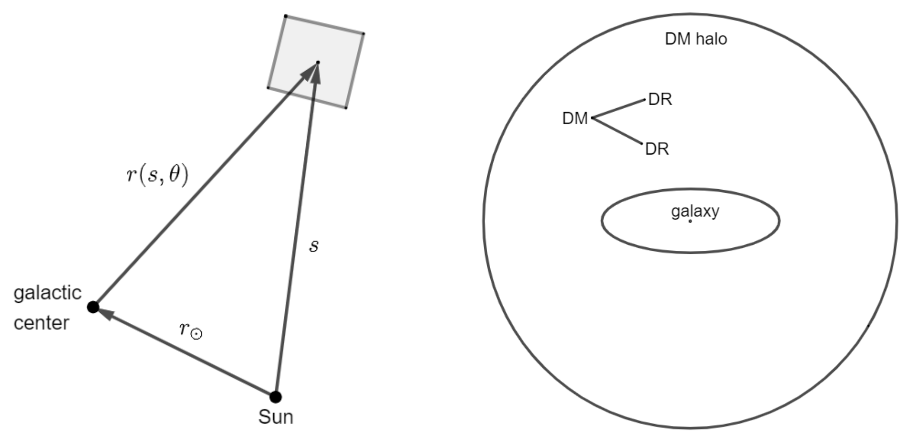

Figure H.1: Galactic coordinates (left) and galactic decays (right).

where $r(s,\theta) = \sqrt{s^2 + r_\odot^2 - 2sr_\odot \cos\theta}$, see Fig. H.1.

Similarly, we can derive the extragalactic flux [125]. Since dark matter decays also happen at extragalactic distances, dark radiation is redshifted and has a momentum $|\vec{p}_{\rm DR}|_{\rm em} = (1+z)|\vec{p}_{\rm DR}|$, where $|\vec{p}_{\rm DR}|_{\rm em}$, $|\vec{p}_{\rm DR}|$ are momenta at emission and observation, respectively. The total number of decay products at redshift z is

$$\frac{dN(E_{\rm em})}{dE_{\rm DR}} \frac{f_{\rm DM}\rho_{\rm DM,0}\, e^{-\frac{t(z)}{\tau_{\rm DM}}}}{\tau_{\rm DM} m_{\rm DM}} \chi^2 d\chi d\Omega, \tag{H.1.5}$$

where χ is the comoving distance, $\rho_{\rm DM,0}$ is the dark matter density at present time and the number spectrum depends on the energy at emission. Then, the differential extragalactic flux at observation is given by

$$\frac{d\Phi_{\rm DR,\ e.g.}}{dE_{\rm DR}} = \int d\chi \frac{dN\,(E_{\rm em})}{dE_{\rm DR}} \frac{f_{\rm DM}\rho_{\rm DM,0}\, e^{-\frac{t(z)}{\tau_{\rm DM}}}}{\tau_{\rm DM} m_{\rm DM}}. \tag{H.1.6}$$

Assuming a flat universe, the extragalactic flux component can be further reduced to an integral over the redshift,

$$\frac{d\Phi_{\rm DR,\ e.gal}}{dE_{\rm DR}} = \frac{f_{\rm DM}\rho_{\rm DM,0}}{\tau_{\rm DM} m_{\rm DM}} \int_0^{z_f} \frac{dz}{H(z)} \frac{dN\,(E_{\rm em})}{dE_{\rm DR}} v_{\rm em}(z)\, e^{-\frac{t(z)}{\tau_{\rm DM}}}, \tag{H.1.7}$$

where $v_{\rm em}(z)$ is the velocity of dark radiation particles at emission. Here, we changed the integral over the comoving distance to a redshift integral by

$$\int d\chi = \int \frac{dz}{H(z)} v_{\rm em}(z). \tag{H.1.8}$$

Since we consider dark matter decays in the matter-dominated universe, the upper bound $z_f < z_{\text{eq}} \simeq 10^4$ is a good approximation. We can find an analytic expression for the cosmic time

$$t(z) = \int_z^\infty \frac{dz'}{(1+z')\,H\,(z')} = \frac{1}{3H_0\sqrt{\Omega_\Lambda}} \ln \left| \frac{\sqrt{1+(1+z)^3\frac{\Omega_M}{\Omega_\Lambda}}+1}{\sqrt{1+(1+z)^3\frac{\Omega_M}{\Omega_\Lambda}}-1} \right|. \tag{H.1.9}$$

Then, the total dark radiation flux is a combination of both components,

$$\frac{d\Phi_{\text{DR}}}{dE_{\text{DR}}} = \frac{d\Phi_{\text{DR, gal}}}{dE_{\text{DR}}} + \frac{d\Phi_{\text{DR, e.gal}}}{dE_{\text{DR}}}. \tag{H.1.10}$$

The simplest case of dark radiation are two-body decays of dark matter[1]. Dark radiation is injected with energies $E_{\text{in}} = m_{\text{DM}}/2$ described by the spectrum,

$$\frac{dN}{dE_{\text{DR}}} = N_{\text{DR}}\delta(E_{\text{em}} - E_{\text{in}}). \tag{H.1.11}$$

For two-body decays, $N_{\text{DR}} = 2$. Then, the galactic flux reads

$$\frac{d\Phi_{\text{DR, gal}}}{dE_{\text{DR}}} = N_{\text{DR}} \frac{f_{\text{DM}} e^{-\frac{t_0}{\tau_{\text{DM}}}}}{\tau_{\text{DM}} m_{\text{DM}}} r_\odot \rho_\odot \left\langle J_{\text{dec}} \right\rangle \delta(E_{\text{em}} - E_{\text{in}}). \tag{H.1.12}$$

The extragalactic flux has an integral over the redshift, that can be evaluated due to the delta function

$$\delta(E_{em} - E_{\text{in}}) = \delta\left(\sqrt{|\vec{p}_{\text{DR}}|^2(1+z)^2 + m_{\text{DR}}^2} - \frac{m_{\text{DM}}}{2}\right) \tag{H.1.13}$$

$$= \frac{m_{\text{DM}}}{|\vec{p}_{\text{DR}}|\sqrt{m_{\text{DM}}^2 - 4m_{\text{DR}}^2}} \delta\left(z - \alpha + 1\right), \tag{H.1.14}$$

where $\alpha = \frac{\sqrt{m_{\text{DM}}^2 - 4m_{\text{DR}}^2}}{2|\vec{p}_{\text{DR}}|}$. Then, we perform the redshift integral and we are left with

$$\frac{d\Phi_{\text{DR, e.gal}}}{dE_{\text{DR}}} = \frac{m_{\text{DM}}}{|\vec{p}_{\text{DR}}|\sqrt{m_{\text{DM}}^2 - 4m_{\text{DR}}^2}} \frac{N_{\text{DR}} f_{\text{DM}} \rho_{\text{DM},0}}{H_0 \tau_{\text{DM}} m_{\text{DM}}} \frac{v_{\text{em}}(\alpha-1)\, e^{-\frac{t(\alpha-1)}{\tau_{\text{DM}}}}}{\sqrt{\alpha^3\Omega_M + \Omega_\Lambda}} \theta(\alpha-1)\theta(z_f - \alpha + 1), \tag{H.1.15}$$

where $H(z)^2 = H_0^2\left((1+z)^3\Omega_M + \Omega_\Lambda\right)$ is the Hubble parameter. The theta function $\theta(z_f - \alpha + 1)$ is always satisfied, since $z_f > \alpha - 1$. The velocity at emission is given by

$$v_{\text{em}}(\alpha - 1) = \frac{|\vec{p}_{\text{DR}}|_{\text{em}}}{E_{\text{em}}} = \frac{\sqrt{m_{\text{DM}}^2 - 4m_{\text{DR}}^2}}{m_{\text{DM}}}. \tag{H.1.16}$$

[1] For our purposes, dark matter decays at rest and velocity dispersions are negligible [126].

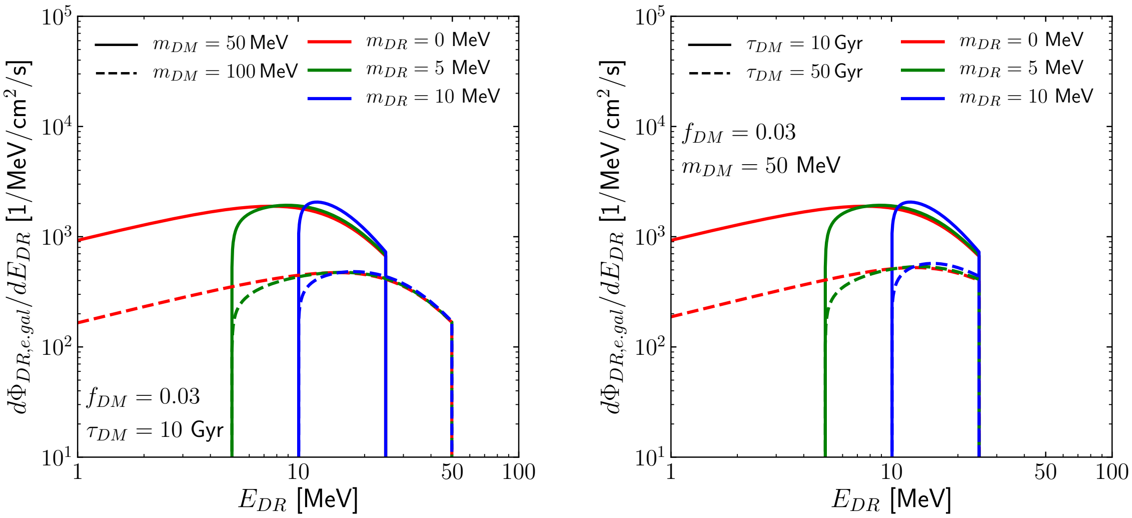

Figure H.2: The differential extragalactic flux for several progenitor masses and lifetimes. Dark radiation is produced by two body dark matter decays with injection energy $E_{\text{in}} = \frac{m_{\text{DM}}}{2}$.

In the end, the extragalactic flux reads

$$\frac{d\Phi_{\text{DR, e.gal}}}{dE_{\text{DR}}} = \frac{N_{\text{DR}} f_{\text{DM}} \rho_{\text{DM},0}}{H_0 \tau_{\text{DM}} m_{\text{DM}}} \frac{e^{-\frac{t(\alpha-1)}{\tau_{\text{DM}}}}}{|\vec{p}_{\text{DR}}| \sqrt{\alpha^3 \Omega_M + \Omega_\Lambda}} \theta(\alpha - 1). \tag{H.1.17}$$

The theta function guarantees that the injected energy is larger than the observed energy, $E_{\text{in}} \geq E_{\text{DR}}$. Exemplary, we show the extragalactic flux for several masses and lifetimes in Fig. H.2.

APPENDIX I

Irreducible neutrino backgrounds

I.1 Backgrounds in direct detection experiments

In this appendix, we explain the neutrino backgrounds in direct detection experiments in more detail, that enter in the analysis in Sec. 6. These backgrounds are irreducible and decrease the sensitivity on dark matter, since neutrinos may mimic dark matter events [127]. Hence, it is important to understand the origin of each component of the neutrino background.

The three main sources of neutrinos, that are relevant in direct detection experiments are solar, atmospheric and supernova neutrinos. The origin of solar neutrinos is the Sun. Nuclear fusion reactions produce a large amount of electron neutrinos with MeV-energies, that escape the inner layers of the Sun and stream freely to the Earth. In Fig. I.1 we show the evolution of fusion processes in the Sun. For instance, pp fusion leads to the highest flux on earth, but these neutrinos have small energies [128, 129]. On the other hand, ^8B neutrinos have a broad range of energies. The following reactions create monochromatic neutrinos[1],

$$
\begin{aligned}
p + e^- + p &\to {}^2H + \nu_e && \text{(I.1.1)}\\
{}^7Be + e^- &\to {}^7Li + \nu_e. && \text{(I.1.2)}
\end{aligned}
$$

The latter reaction emits monochromatic neutrinos with energies 861.3 keV and 384.3 keV when beryllium captures electrons. In the Sun, the CNO cycle contributes only $\sim 1\%$ to the heating [129, 130].

Atmospheric neutrinos are produced when cosmic rays hit the atmosphere of the Earth and interact with nuclei in the atmosphere [131, 132]. The resulting pions, muons and a smaller abundance of kaons create a large number of electron and muon neutrinos,

$$\pi^- \to \mu^- + \bar{\nu}_\mu, \quad \pi^+ \to \mu^+ + \nu_\mu, \tag{I.1.3}$$

[1]The reaction $p + e^- + p \to {}^2H + \nu_e$ creates almost monochromatic neutrinos since tiny energy smearing in neutrino energy is caused by the recoil of the deuterium [129].

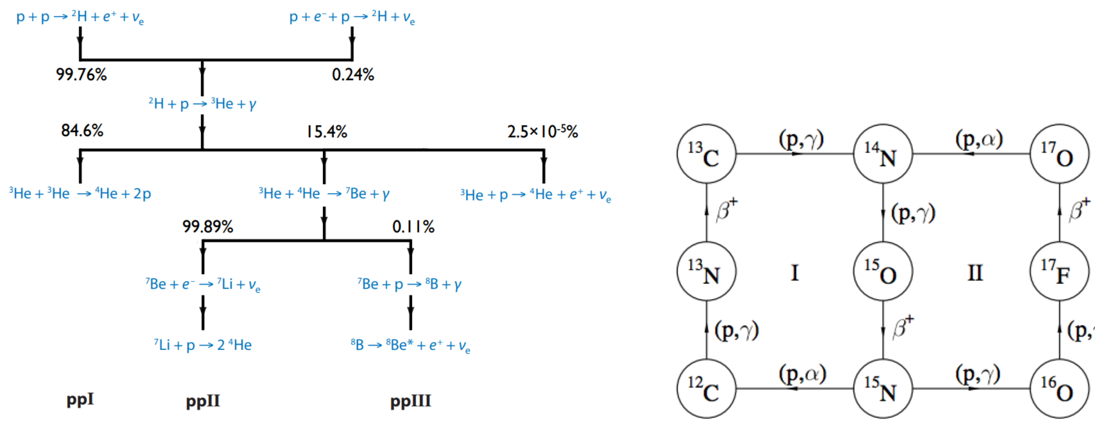

Figure I.1: The ppI, ppII, ppII cycles (left) [128] and the CNO cycle reactions (right) [130].

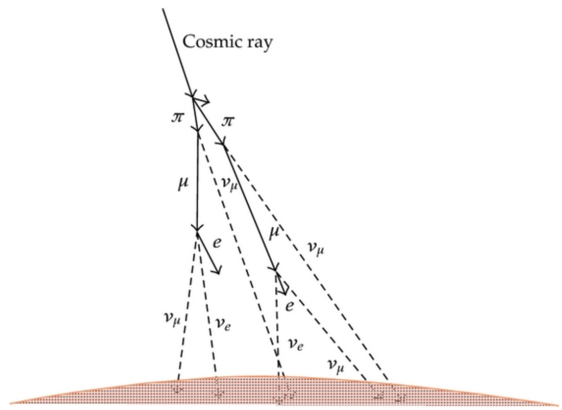

Figure I.2: The dominant reactions contributing to the production of atmospheric neutrinos. The figure is taken from Ref. [131].

$$K^- \rightarrow \mu^- + \bar{\nu}_\mu, \quad K^+ \rightarrow \mu^+ + \nu_\mu, \tag{I.1.4}$$
$$\mu^- \rightarrow e^- + \bar{\nu}_e + \nu_\mu, \quad \mu^+ \rightarrow e^+ + \nu_e + \bar{\nu}_\mu. \tag{I.1.5}$$

In Fig. I.2 we show the dominant neutrino production in the atmosphere of the Earth. When all muons decay before hitting the surface of the Earth, the fluxes are related to each other as

$$\phi(\nu_\mu + \bar{\nu}_\mu) \simeq 2\phi(\nu_e + \bar{\nu}_e), \quad \phi(\nu_\mu) \simeq \phi(\bar{\nu}_\mu). \tag{I.1.6}$$

Solar and atmospheric neutrinos were detected by the experiments, like HOMESTAKE [133], GALLEX [134], SAGE [135], Super-Kamiokande [136, 137], just to name a few.

Last but not least, the diffuse supernova neutrino background (DSNB) are neutrinos from distant core collapse supernovae of Type II [138, 139]. These neutrinos have several tens of

MeV energy and have not yet been observed. The averaged DSNB detection rate is estimated to be 3 events per year [138]. The only detection of supernova neutrinos at 0.05 Mpc close to the Milky Way galaxy was announced by two experiments: Kamiokande II [140–142] and Irvine-Michigan-Brookhaven experiment [143, 144], observing the supernova SN1987A in the Large Magellanic Cloud. Although SN1987A is not part of the DSNB, these reported events are a milestone in the study of supernovae.

There are different sources of supernova neutrinos [139]. Supernova neutrinos are produced when electrons and protons are forced to merge due to the high density and high temperature in the core. Moreover, they cannot escape the ultra dense core and are trapped by coherent neutral current scatterings. The neutrinos are then released during the explosion. Additionally, there is also a prompt ν_e burst originating from protons of dissociated nuclei merging with electrons during the explosion. However, the dominant neutrino emission is during Helmholtz cooling, when the neutron star cools down. The amount of gravitational binding energy during a supernova is released through neutrinos of all flavors[2],

$$E_{\nu_{\rm tot}} \simeq E_B \simeq 2\times 10^{52} \times \left(\frac{M_{\rm NS}}{1.4 M_\odot}\right)^2 \times \left(\frac{10\ {\rm km}}{R_{\rm NS}}\right)\ {\rm TeV}. \tag{I.1.7}$$

The DSNB flux [145] is given by the star formation rate and thermal emission spectrum [146, 147] associated to a specific temperature for each neutrino species, $T_{\nu_e} \simeq 4$ MeV, $T_{\bar\nu_e} \simeq 5$ MeV, $T_x \simeq 8$ MeV ($x = \nu_\mu, \bar\nu_\mu, \nu_\tau, \bar\nu_\tau$). The temperature hierarchy $T_{\nu_e} < T_{\bar\nu_e} < T_x$ is related to the radius at which the neutrinos decouple[3]. The DSNB flux is given by (for more details see [145])

$$\frac{d\phi_{\rm DSNB}}{dE_\nu} = \frac{1}{H_0}\int_0^{z_{\rm max}} \frac{dz}{\sqrt{(1+z)^3\Omega_M + \Omega_\Lambda}} R_{\rm SN}(z)\frac{dN(E_\nu^{\rm em})}{dE_\nu}, \tag{I.1.8}$$

where $R_{\rm SN}(z)$ is the supernova rate and $dN(E_\nu)/dE_\nu$ is the thermal spectrum at emission given by

$$\frac{dN(E_\nu^{\rm em})}{dE_\nu} = \frac{120}{7\pi^4}\frac{E_{\nu_{\rm tot}}}{6}\frac{(E_\nu^{\rm em})^2}{T_\nu^4}\left(1+\exp\left(\frac{E_\nu^{\rm em}}{T_\nu}\right)\right)^{-1}. \tag{I.1.9}$$

We assume, that the first supernovae occurred at $z_{\rm max} \sim 5$. The supernova rate is related to the star formation rate by the fraction of stars ending in a Type II supernova. In Fig. I.3 we show the neutrino flux for different sources.

In the end, we show the nuclear recoil spectrum of each neutrino background in units [1/keV/ton/yr] arising in direct detection experiments from Sec. 6,

$$\frac{dR_\nu(E_R)}{dE_R} = N_T \int_{E_\nu^{\rm min}} dE_\nu \frac{d\Phi_\nu}{dE_\nu}\frac{d\sigma_{N\nu}}{dE_R}, \tag{I.1.10}$$

[2] Approximately 1% of the energy is emitted through photons.

[3] The neutrinos ν_μ, ν_τ and their antiparticles don't have enough energy to produce their corresponding leptons and can only interact via neutral currents making it faster to decouple. Whereas ν_μ, ν_τ are coupled only through neutral interactions, electron neutrinos interact through weak and neutral currents and decouple later at lower temperature ($T_x > T_{\nu_e}$) [138].

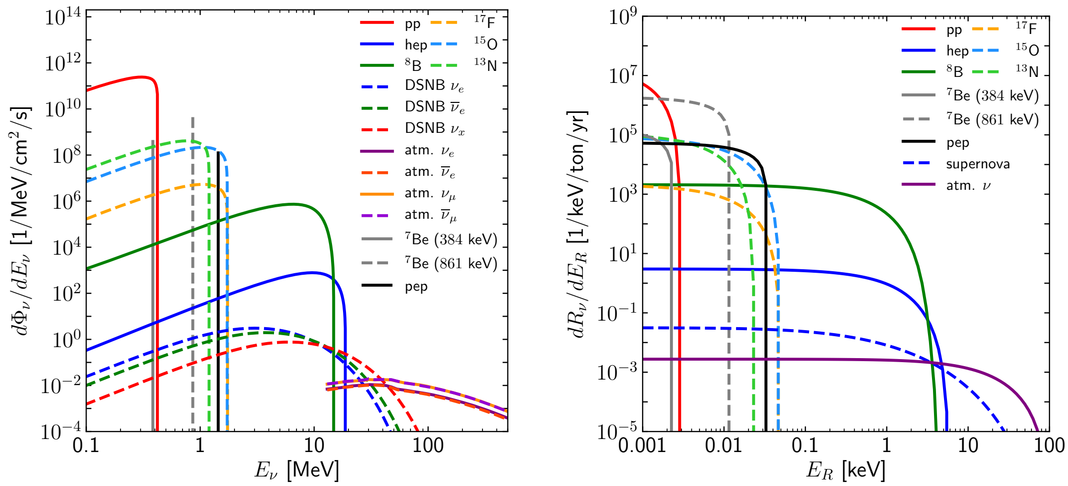

Figure I.3: The neutrino flux (right) and nuclear recoil rates (left) for various sources in a xenon-based direct detection experiment. Whereas solar neutrinos are dominant in the low-energetic region, atmospheric neutrinos and DSNB are highly energetic. The data were taken from Refs. [148, 149].

where the differential neutrino flux $\frac{d\Phi_\nu}{dE_\nu}$ of each component is shown in Fig. I.3, $\frac{d\sigma_{N\nu}}{dE_R}$ is the coherent neutrino-nucleus cross section given in Sec. 6, $E_\nu^{\min} = \sqrt{E_R m_N/2}$ is the minimum neutrino energy to produce a recoil and N_T is the number of target nuclei per kg detector mass. The differential neutrino flux depends on the neutrino energy spectrum and its total flux,

$$\frac{d\Phi_\nu}{dE_\nu} = \Phi_\nu \frac{dN_\nu}{dE_\nu}. \tag{I.1.11}$$

The energy spectra are taken from Refs. [148, 149]. Since neutrinos have energies of several tens of MeV, nuclear recoil energies from neutrinos are of order keV, see Fig. I.3 for a xenon-based direct detection experiment. The range of recoil energies of each neutrino source is given in Sec. 6,

$$E_R^{\max} = \frac{2\,(E_\nu^{\max})^2}{2E_\nu^{\max} + m_N}, \tag{I.1.12}$$

where m_N is the mass of the nucleus and $E_\nu^{\max}$ is the maximum neutrino energy.

I.2 The neutrino experiment PTOLEMY

In this section we discuss the signals in the neutrino experiment PTOLEMY, that enter as backgrounds in the analysis in Sec. 6 of the publication [4]. The neutrino signal in the PTOLEMY experiment is not an irreducible background per se, but it makes the search on dark radiation in the form of Standard Model neutrinos more challenging. The goal of the PTOLEMY experiment [150, 151] is to discover signals of the cosmic neutrino background via the threshold-free neutrino capture of beta-decaying nuclei, $(A, Z) + \nu_e \;\to\; (A, Z+1) + e^-$.

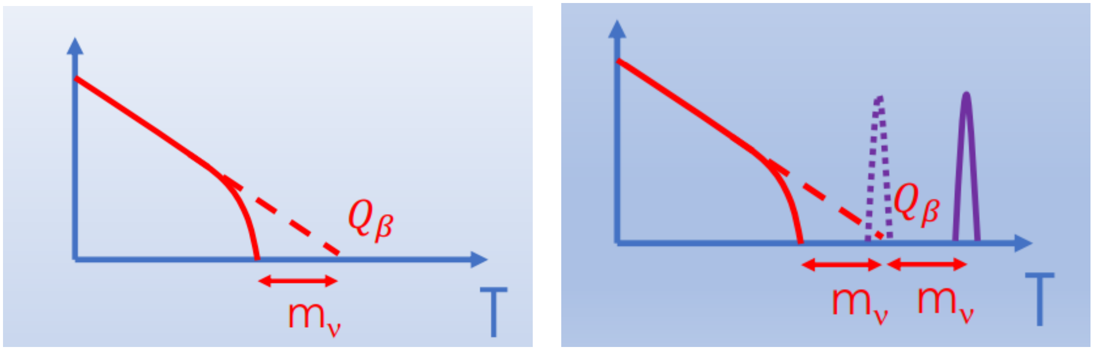

Figure I.4: The β spectrum (left) and the cosmic neutrino background (right). The x-axis denotes the kinetic energy of electrons. The figures are taken from the talk [152].

In this case, the β spectrum acts as a background, but can be distinguished from neutrino capture by kinematics, see Fig. I.4. The signal peak of the cosmic neutrino background arises above the endpoint energy of the β spectrum. The challenge of PTOLEMY is to resolve the energies of electrons originating from the β decay and neutrino capture [153]. One of the best candidates as a target is tritium decaying to helium,

$$^3\mathrm{H} \;\rightarrow\; ^3\mathrm{He} + e^- + \bar{\nu}_e \tag{I.2.1}$$
$$\nu_e +^3\mathrm{H} \;\rightarrow\; ^3\mathrm{He} + e^-. \tag{I.2.2}$$

It has three benefits, a low Q-value $Q = 18.6$ keV[4], a half-life $t_{1/2} \simeq 12.32$ yr and a large neutrino capture cross section $\langle\sigma v\rangle_0 \simeq 3.7 \times 10^{-45}$ cm^2.

The β spectrum [155] is a combination of neutrino mass eigenstates,

$$\frac{d\Gamma_\beta}{dE_e} = N_T \frac{\langle\sigma v\rangle_0}{\pi^2} \sum_{i=1}^{3} |U_{ei}|^2 H(E_e, m_i), \tag{I.2.3}$$

where

$$H(E_e, m_i) = \frac{1 - \frac{m_e^2}{E_e m_T}}{\left(1 - 2\frac{E_e}{m_T} + \frac{m_e^2}{m_T^2}\right)^2} \sqrt{y\left(y + \frac{2m_i m_{\mathrm{He}}}{m_T}\right)} \left(y + \frac{m_i}{m_T}(m_{\mathrm{He}} + m_i)\right), \tag{I.2.4}$$

$y = E_{\mathrm{end},0} - m_i - E_e$ and $E_{\mathrm{end},0}$ is the endpoint energy of electrons in the β spectrum for massless neutrinos [156],

$$E_{\mathrm{end},0} = \frac{m_{^3\mathrm{H}}^2 + m_e^2 - m_{^3\mathrm{He}}}{2m_{^3\mathrm{H}}}. \tag{I.2.5}$$

[4]It is easier to resolve sub-eV with lower Q-values, $\frac{\mathrm{eV}}{18\ \mathrm{keV}} \simeq 10^{-4}$. The spectrum of electrons emitted by β-decaying tritium, that is deposited on graphene sheets becomes smeared [154]. The tritium nucleus bound to graphene experiences a Heisenberg uncertainty in momentum and cannot be seen at rest. The uncertainty is estimated to be $0.3 - 0.7$ eV, making tritium attached to graphene an ineffective target to detect CνB. There is a discussion about the best β-emitter and best graphene structure for PTOLEMY.

Here, $m_{^3\mathrm{H}} \simeq 2808.921$ MeV and $m_{^3\mathrm{He}} \simeq 2808.391$ MeV are nuclear masses of tritium and helium. The β spectrum is smeared with a Gaussian distribution with full width at half maximum given by the energy resolution Δ. Taking an energy resolution into account, the spectrum reads

$$\frac{d\tilde{\Gamma}_\beta}{dE_e} = \frac{1}{\sqrt{2\pi}(\Delta/\sqrt{8\ln 2})} \int_{-\infty}^{\infty} dE' \frac{d\Gamma_\beta}{dE_e}\left(E'\right) \exp\left(-\frac{(E'-E_e)^2}{2(\Delta/\sqrt{8\ln 2})^2}\right). \tag{I.2.6}$$

The smeared spectrum of the cosmic neutrino background is given by

$$\frac{d\widetilde{\Gamma}_{\mathrm{C}\nu\mathrm{B}}}{dE_e}\left(E_e\right) = \frac{1}{\sqrt{2\pi}(\Delta/\sqrt{8\ln 2})} \sum_{i=1}^{3} \Gamma_i \exp\left(-\frac{\left(E_e - (E_{\mathrm{end},0} - m_i)\right)^2}{2(\Delta/\sqrt{8\ln 2})^2}\right), \tag{I.2.7}$$

where its signal peak is around $E_{\mathrm{end},0} - m_i$. Here, $\Gamma_i = N_T |U_{ei}|^2 \langle \sigma v \rangle_0 f_{c,i} n_0$ is the capture rate for each neutrino mass eigenstate, N_T is the number of tritium nuclei in the experiment and $f_{c,i}$ is the gravitational clustering factor, describing an enhancement of the local density of neutrinos. PTOLEMY would ideally use 100 g of tritium to detect a few cosmic neutrinos per year. For instance, KATRIN [157] is limited to $\sim 100\ \mu$g of tritium and therefore, not able to detect the cosmic neutrino background ($\sim 10^{-6}$ events/yr). If PTOLEMY achieves a small energy resolution and resolves energies of the signals between the β spectrum and the cosmic neutrino background, an accurate measurement of the neutrino mass is possible.

APPENDIX J

Baryonic neutrinos

The Standard Model predicts the existence of three generations of neutrinos. However, sterile neutrinos are still a possible scenario given the current constraints on the effective number of neutrino species $N_{\text{eff}} = 2.99 \pm 0.34$ [6]. Here, we introduce quasi-sterile neutrinos, also known as baryonic neutrinos ν_B, that couple to baryons (we will mainly follow the paper [158]). Baryonic neutrinos do not interact through neutral nor weak currents of the Standard Model and hence, do not scatter elastically on leptons. However, they can couple to baryonic currents through a new gauge boson, enhancing neutral currents on baryons. It was shown in Refs. [126, 158, 159] that inelastic scatterings (break-up or excitation of nuclei) are suppressed by the factor $(E_\nu R_N)^4$ for neutrino energies $E_\nu \sim O(10\text{ MeV})$ and a nuclear radius $R_N \simeq 2$ fm, making direct detection essential for baryonic neutrino detection. In the following, we restrict ourselves to models without kinetic mixing with the SM photon, since we are only interested in nuclear recoils (for models with kinetic mixing see [160, 161]).

J.1 The baryonic model

The new neutrino ν_B is introduced by an Abelian gauge group $U(1)_B$, where all quarks under $U(1)_B$ have a charge $g_B/3$ and leptons are neutral. The neutrino is left-handed with a charge g_l under $U(1)_B$ and uncharged under any SM gauge group. Then, the relevant Lagrangian is given by

$$\mathcal{L} \supset i\bar{\nu}_B\gamma^\mu(\partial_\mu - ig_l V_\mu)\nu_B + \frac{g_B}{3}\sum_q \bar{q}\gamma^\mu V_\mu q - \frac{1}{4}V_{\mu\nu}V^{\mu\nu} + \frac{m_V^2}{2}V_\mu + \mathcal{L}_M + \mathcal{L}_q^{\text{SM}}, \tag{J.1.1}$$

where $\mathcal{L}_M$ is relevant for mass generation of neutrinos (neutrino mixing with ν_B [159]), $\mathcal{L}_q^{\text{SM}}$ are standard SM interactions of quarks. The mass of the gauge boson V_μ is generated by spontaneous breaking of $U(1)_B$. An introduction of right-handed neutrinos and heavy fermion fields can cancel gauge anomalies [158]. For our purpose, we can consider massless ν_B that elastically scatter off nucleons as discussed in the Sec. 6. Since we consider small momentum transfers, we switch to the effective theory with nucleons,

$$\frac{g_B}{3}\sum_q \bar{q}\gamma^\mu V_\mu q \simeq g_B V_\mu J^\mu, \tag{J.1.2}$$

where $J^\mu = \bar{p}\gamma^\mu p + \bar{n}\gamma^\mu n$ is the nucleon current. Thus, V_μ couples equally to protons and neutrons. In the end, one can compute the coherent ν_B-nucleus cross section given in Sec. 6 for $m_\nu = 0$,

$$\frac{d\sigma_{\nu_B N}}{dE_R} \simeq \frac{A^2 G_B^2 m_N F^2(|\vec{q}\,|)}{2\pi}\left(1 - \frac{E_R m_N}{E_\nu^2}\right), \tag{J.1.3}$$

where $G_B = \zeta G_F$ is related to the Fermi constant G_F, m_N is the nucleus mass and $F^2(|\vec{q}\,|)$ is the Helm-Form factor, a measure for coherence. Here, we take the contact limit $q^2 \ll m_V^2$. If we replace $G_B^2 A^2$ by $G_F^2 Qw^2/2$ we obtain the usual elastic scattering between a Standard Model neutrino and a nucleus.

APPENDIX K

Statistical framework

K.1 Likelihood statistics

A likelihood function [162] can be seen as the "inverse" of a probability density function (PDF) f,

$$x \mapsto f(x|\theta), \tag{K.1.1}$$

$$\theta \mapsto L(\theta|x), \tag{K.1.2}$$

where x are observed or simulated data and θ are parameters defining the PDF. The likelihood function is not a PDF, since it is not normalized. Given the data of an experiment, the likelihood can be fitted for θ. The best fit is found by maximum likelihood estimation, where the likelihood function L is maximized for the parameters θ of a PDF given the data x. In practice, the log-likelihood $-\ln L$ is minimized. This is allowed since the log-function is a monotonously increasing function and $\max_\theta L = \min_\theta(-\ln L)$.

K.2 Hypotheses testing with profile likelihood ratio test

Hypotheses tests are a general way to test one hypothesis or theoretical model against another one [163]. Here, we show hypotheses testing in the case of dark radiation vs. neutrino backgrounds in direct detection experiments. As a reminder, dark radiation are neutrinos for us, that originate from two-body decays of dark matter with mass m_{DM} and lifetime τ_{DM}. The null hypothesis $H_0 : \tau_{\mathrm{DM}} \to \infty$ characterizes neutrino backgrounds only (solar, atmospheric, DSNB), that is tested against the alternative hypothesis H_1 : finite τ_{DM} (dark radiation signal + neutrino backgrounds). The standard neutrino backgrounds given in Sec. 6 are characterized by their fluxes ϕ_ν. These fluxes are nuisance parameters in the statistical framework, that are part of the theory, but are not of main interest.

The most used test in particle physics in order to discriminate between H_0 and H_1 is the likelihood ratio test. In that case, given the data x, we have

$$q = \begin{cases} -2\ln\frac{L(\tau_{\rm DM}\to\infty,\hat{\phi}_\nu\,|x)}{L(\tilde{\tau}_{\rm DM},\tilde{\phi}_\nu\,|x)} & \text{for finite } \tau_{\rm DM} \\ \\ 0 & \text{for } \tau_{\rm DM}\to\infty, \end{cases}, \tag{K.2.1}$$

where $\hat{\phi}_\nu$ are the best fit neutrino fluxes under the hypothesis H_0 and $\tilde{\tau}_{\rm DM}, \tilde{\phi}_\nu$ are the best fit parameters under hypothesis H_1. We simulated the data x containing the dark radiation signal for various combinations of ($\tau_{\rm DM}$, $m_{\rm DM}$) and neutrino backgrounds. The data is generated by the distributions within the likelihood function. Larger q-values correspond to a larger discrepancy between H_0 and H_1.

K.3 Discovery of dark radiation

In order to discover a signal, we have to reject the null hypothesis H_0. For this case, we define the probability p_0, when H_0 is rejected, and the confidence level [162, 164].

First, the p_0-value defines the probability, when H_0 is excluded,

$$p_0 = P(q \geq q_{\rm obs}|{\rm H}_0) = \int_{q_{\rm obs}}^{\infty} dq\ f(q\,|{\rm H}_0), \tag{K.3.1}$$

where $f(q\,|{\rm H}_0)$ is the distribution of q-values, that follows a χ^2-distribution with one degree of freedom in the asymptotic limit (see Wilk's theorem [163]). The background-only hypothesis H_0 is therefore rejected when the likelihood ratio q is greater than some "observed" value $q_{\rm obs}$. In particle physics, we often work with significances in terms of standard deviations σ, $Z = \sqrt{q}$. In this case, we can define a probability p_0 in terms of significances,

$$p_0 = P(Z \geq Z_{\rm obs}|H_0) = \int_{Z_{\rm obs}}^{\infty} dZ\ f(Z\,|{\rm H}_0), \tag{K.3.2}$$

where $f(Z\,|{\rm H}_0)$ is a Gaussian distribution ${\rm No}(0,1)$ with expectation value $\mu = 0$ and standard deviation $\sigma = 1$. Here, we take $Z_{\rm obs} = 3$ corresponding to a discovery with 3σ ($p_0 = 0.00135$). Hence, for a 3σ discovery the background-only hypothesis H_0 is rejected when $p_0 \lesssim 0.00135$.

Second, the p_1-value characterizes the probability, when H_1 is excluded,

$$p_1 = P(q \leq q_{\rm obs}|{\rm H}_1) = \int_{-\infty}^{q_{\rm obs}} dq\ f(q\,|{\rm H}_1) \tag{K.3.3}$$

$$p_1 = P(Z \leq Z_{\rm obs}|{\rm H}_1) = \int_{-\infty}^{Z_{\rm obs}} dZ\ f(Z\,|{\rm H}_1). \tag{K.3.4}$$

Then, the confidence level is given by

$$\text{CL} = 1 - p_1 = \int_{Z_{\rm obs}}^{\infty} dZ\ f(Z\,|{\rm H}_1) \tag{K.3.5}$$

and quantifies the probability, that H_1 is accepted. For a confidence level of 90% a 3σ discovery of a signal is given, when 90% of experiments reach the region $Z_{\mathrm{obs}} \geq 3$. In this case, the only-background H_0 and signal+background hypotheses H_1 are distinguishable.

Part IV

Conclusion

CHAPTER 7

Discussion

In this thesis, we investigated two broader topics: 1) the viability of strongly interacting massive particles (SIMPs) in dark $Sp(4)_c$ gauge theories, including effects when SIMP bound states are present and, 2) dark radiation from dark matter decay in the form of Standard Model or baryonic neutrinos.

First, we constructed the effective field theory of SIMPs in a dark $Sp(4)_c$ gauge theory with $N_f = 2$ fundamental mass-degenerate dark fermions, including the Wess-Zumino-Witten interaction, the axial anomaly, the $U(1)'$ gauge coupling and additional spin-1 states. In Ref. [1] we showed that SIMPs are composite states and Nambu-Goldstone bosons that arise by chiral symmetry breaking when a global flavour symmetry group $Sp(2N_f = 4)$ breaks spontaneously to $Sp(2N_f = 4)$. The 10 vector and 5 axial-vector mesons were introduced as gauge fields of a $SU(4)$ symmetry and can also interact with SIMPs. We identified the axial-vector states being heavier than the vector mesons and assumed them to be decoupled from the theory. In addition, we introduced the iso-singlet η', which is associated with the axial anomaly. We discussed the consequences of explicit breaking in the presence of a $U(1)'$ gauge boson and in the case of massive dark fermions in the UV-Lagrangian. The former allows e.g. SIMPs to connect to the Standard Model, but can make spin-1 states as well as one SIMP state unstable, depending on the charge assignments. The latter makes SIMPs and other particle states massive. In the second part of Ref. [1] we provided the effective description of $Sp(4)_c$ theories, including mass splittings in the dark fermion sector. In this case, the global flavour symmetry $SU(4)$ breaks explicitly to a smaller group $SU(2)_u \times SU(2)_d$ and SIMPs become non-degenerate in mass. For instance, the SIMP multiplet splits into a quadruplet and a singlet. It turns out, that the singlet is the lightest state in this theory and mixes with the pseudoscalar singlet η', implying a small change in the mass. The effective description of the theory was linked to lattice simulations, providing decay constants, mass hierarchies and tested the validity of the theory. It was shown, that small mass splittings in the fermion sector are allowed and a change in the meson mass hierarchy occurs for larger splittings. This construction of the effective theory provides a framework that can be used for further dark matter research.

Second, we investigated the implications of SIMPonium made of two SIMP states with equal mass m_π, that can change the freeze-out mechanism of free SIMPs. We found that the relevant processes, involving SIMP bound states without additional gauging are the reactions $X\pi \rightleftharpoons 2\pi$, the annihilation $2X \rightleftharpoons 2\pi$ and the bound state production $3\pi \rightleftharpoons \pi X$, requiring $3\pi \to 2\pi$ to be sub-leading. We provided the Boltzmann equations for free SIMPs and for bound states and derived the thermally averaged cross sections for $3\pi \to 2\pi$, $X\pi \to 2\pi$ and $3\pi \to \pi X$. We showed that the reaction $X\pi \to 2\pi$ is realized through the Wess-Zumino-Witten interaction at leading order, whereas the bound state formation $3\pi \to \pi X$ is achieved by two four-point or one six-point interaction at leading order. Finally, for the first analysis, we parameterized the cross sections and illustrated the evolution of the relic abundances of free SIMPs and bound states. We found that the relic abundance of free SIMPs is primarily affected by the magnitude of the reaction $3\pi \to \pi X$. This work is ongoing and can be extended by including additional gauging, spin-1 states and mass non-degeneracy, as discussed in the Outlook 4.5.

In the last topic, we studied the detectability of dark radiation in the form of Standard Model neutrinos and baryonic neutrinos. We analyzed the sensitivity of dark radiation in xenon-based direct detection experiments and in the neutrino experiment PTOLEMY. For this case, we established the minimum lifetime corresponding to the smallest dark radiation flux for each progenitor mass, where backgrounds and dark radiation are still distinguishable. In addition, we explored the background-free exclusion potential of dark radiation for various fractions f_X in Ref. [3]. We introduced the dark radiation flux sourced by two-body decays of unstable dark matter and derived its rates in both experiments. On the one hand, in Ref. [3], we considered a small percentage of unstable MeV dark matter. On the other hand, in Ref. [4], we assumed, that the complete or a small abundance of sub-eV dark matter is unstable. Given the constraints from Super-Kamiokande, dark radiation in the form of Standard Model neutrinos is not detectable in direct detection experiments for exposures $\varepsilon \lesssim 1$ ton yr. However, futuristic exposures $\varepsilon \sim 100$ ton yr increase the sensitivity of dark radiation beyond the ^{8}B neutrino shoulder since more statistics allow a better discrimination between signals and backgrounds. For this case, we switched to a binned Likelihood in order to handle large statistical data. The discovery potential for baryonic neutrinos is larger than for Standard Model neutrinos since the recoil rates are boosted by a factor $G_B^2 A^2$. Given the constraints imposed by Borexino, a large parameter space of dark matter can be explored with baryonic neutrinos in xenon-based direct detection experiments. The sensitivity of direct detection experiments could be improved by measuring the direction of recoil events or by reducing the uncertainties of the Standard Model neutrino background. Other dark radiation sources that could be probed are e.g. dark radiation from evaporating black holes or from supernova explosions.

In Ref. [4], it was demonstrated, that dark radiation can also be probed in the future experiment PTOLEMY. Since PTOLEMY is designed to search for the cosmic neutrino background, sub-eV dark matter may induce Standard Model neutrinos, that can be detected. For this reason, we explored discovery limits of dark radiation in the presence of the cosmic neutrino background and the β-decay spectrum of tritium. We analyzed the sensitivity for exposures $\varepsilon = 100, 500$ g yr and energy resolutions $\Delta = 10, 50, 100$ meV, assuming a normal and inverse ordering of massive neutrinos. The discovery reach of PTOLEMY shows that the experiment is sensitive to dark radiation from sub-eV dark matter, even for a poor energy resolution of 100 meV. The increase of the exposure to 500 g yr improves the sensitivity by at least 20%.

In summary, dark matter is an important field of research that needs to be explored further. Both the exploration of dark matter models as well as their experimental exploration are necessary to understand the particle nature of dark matter and its connection to the Standard Model. Whether dark matter is a particle or not will hopefully be clarified in the future.

Bibliography

[1] S. Kulkarni, A. Maas, S. Mee, M. Nikolic, J. Pradler and F. Zierler, *Low-energy effective description of dark Sp(4) theories*, *SciPost Phys.* **14** (2023) 044 [2202.05191].

[2] X. Chu, M. Nikolic and J. Pradler*, in preperation* .

[3] M. Nikolic, S. Kulkarni and J. Pradler, *Sensitivity of direct detection experiments to neutrino dark radiation from dark matter decay and a modified neutrino-floor*, *Eur. Phys. J. C* **82** (2022) 650 [2008.13557].

[4] K. Bondarenko, A. Boyarsky, M. Nikolic, J. Pradler and A. Sokolenko, *Probing sub-eV Dark Matter decays with PTOLEMY*, *JCAP* **03** (2021) 089 [2012.09704].

[5] M. Nikolic, *The ultimate sensitivity in dark matter direct detection experiments in the presence of an anomalous neutrino source*, 2019.

[6] Planck collaboration, *Planck 2018 results. VI. Cosmological parameters*, *Astron. Astrophys.* **641** (2020) A6 [1807.06209].

[7] V.C. Rubin and W.K. Ford, Jr., *Rotation of the Andromeda Nebula from a Spectroscopic Survey of Emission Regions*, *Astrophys. J.* **159** (1970) 379.

[8] A. Collaboration, "ATLAS Standard Model." 2021.

[9] J.H. Chang, R. Essig and S.D. McDermott, *Supernova 1987A Constraints on Sub-GeV Dark Sectors, Millicharged Particles, the QCD Axion, and an Axion-like Particle*, *JHEP* **09** (2018) 051 [1803.00993].

[10] J.L. Feng, *Dark Matter Candidates from Particle Physics and Methods of Detection*, *Ann. Rev. Astron. Astrophys.* **48** (2010) 495 [1003.0904].

[11] M. Battaglieri et al., *US Cosmic Visions: New Ideas in Dark Matter 2017: Community Report*, in *U.S. Cosmic Visions: New Ideas in Dark Matter*, 7, 2017 [1707.04591].

[12] XENON collaboration, *Projected WIMP sensitivity of the XENONnT dark matter experiment*, *JCAP* **11** (2020) 031 [2007.08796].

[13] CRESST collaboration, *First results from the CRESST-III low-mass dark matter program*, *Phys. Rev. D* **100** (2019) 102002 [1904.00498].

[14] LUX collaboration, *The Large Underground Xenon (LUX) Experiment*, *Nucl. Instrum. Meth. A* **704** (2013) 111 [1211.3788].

[15] Particle Data Group collaboration, *Review of Particle Physics*, *PTEP* **2022** (2022) 083C01.

[16] E. Aubourg et al., *Cosmological implications of baryon acoustic oscillation measurements*, *Phys. Rev. D* **92** (2015) 123516 [1411.1074].

[17] G.C.F. Chen et al., *A SHARP view of H0LiCOW: H_0 from three time-delay gravitational lens systems with adaptive optics imaging*, *Mon. Not. Roy. Astron. Soc.* **490** (2019) 1743 [1907.02533].

[18] V. Bonvin et al., *H0LiCOW – V. New COSMOGRAIL time delays of HE 0435−1223: H_0 to 3.8 per cent precision from strong lensing in a flat ΛCDM model*, *Mon. Not. Roy. Astron. Soc.* **465** (2017) 4914 [1607.01790].

[19] K.C. Wong et al., *H0LiCOW – IV. Lens mass model of HE 0435−1223 and blind measurement of its time-delay distance for cosmology*, *Mon. Not. Roy. Astron. Soc.* **465** (2017) 4895 [1607.01403].

[20] S. Birrer et al., *H0LiCOW - IX. Cosmographic analysis of the doubly imaged quasar SDSS 1206+4332 and a new measurement of the Hubble constant*, *Mon. Not. Roy. Astron. Soc.* **484** (2019) 4726 [1809.01274].

[21] A.G. Riess et al., *A 2.4% Determination of the Local Value of the Hubble Constant*, *Astrophys. J.* **826** (2016) 56 [1604.01424].

[22] A.G. Riess, S. Casertano, W. Yuan, L. Macri, J. Anderson, J.W. MacKenty et al., *New parallaxes of galactic cepheids from spatially scanning theihubble space telescope/i: Implications for the hubble constant*, *The Astrophysical Journal* **855** (2018) 136.

[23] A.G. Riess, S. Casertano, W. Yuan, L.M. Macri and D. Scolnic, *Large Magellanic Cloud Cepheid Standards Provide a 1% Foundation for the Determination of the Hubble Constant and Stronger Evidence for Physics beyond ΛCDM*, *Astrophys. J.* **876** (2019) 85 [1903.07603].

[24] W.L. Freedman, *Cosmology at a Crossroads*, *Nature Astron.* **1** (2017) 0121 [1706.02739].

[25] T. Wrase, "Lecture notes: Cosmology and particle physics." http://hep.itp.tuwien.ac.at/~wrasetm/cosmology2015.html.

[26] H. Kurki-Suonio, "Lecture Notes: Cosmology I." http://www.courses.physics.helsinki.fi/teor/cosmology/, 2022.

[27] A.H. Guth, *The Inflationary Universe: A Possible Solution to the Horizon and Flatness Problems*, *Phys. Rev. D* **23** (1981) 347.

[28] L. Kofman, A. Linde and A.A. Starobinsky, *Reheating after inflation*, *Physical Review Letters* **73** (1994) 3195.

[29] A. Knebe, "Thermal history of the universe." http://popia.ft.uam.es/Cosmology/files/03ThermalHistory.pdf.

[30] E.W. Kolb and M.S. Turner, *The Early Universe*, vol. 69 (1990), 10.1201/9780429492860.

[31] S. Dodelson, *Modern Cosmology*, Academic Press, Amsterdam (2003).

[32] M. Kunz, "A brief thermal history of the universe." https://indico.cern.ch/event/104126/contributions/23554/attachments/14281/20797/kunz_thermal_history.pdf, 2019.

[33] E. Krause, "Week 3: Thermal history of the universe." https://kamion.pha.jhu.edu/Ay127/home.html, Cosmology, Ay127, Spring 2008.

[34] A. Knebe, "Big bang nucleosynthesis." http://popia.ft.uam.es/Cosmology/files/04BBN.pdf.

[35] B.D. Fields, *The primordial lithium problem*, *Ann. Rev. Nucl. Part. Sci.* **61** (2011) 47 [1203.3551].

[36] P.J.E. Peebles, *Recombination of the Primeval Plasma*, *Astrophys. J.* **153** (1968) 1.

[37] R. Barkana and A. Loeb, *In the beginning: The First sources of light and the reionization of the Universe*, *Phys. Rept.* **349** (2001) 125 [astro-ph/0010468].

[38] J. Miralda-Escude, *The dark age of the universe*, *Science* **300** (2003) 1904 [astro-ph/0307396].

[39] H. Ewen and E.M. Purcell, *Observation of a Line in the Galactic Radio Spectrum: Radiation from Galactic Hydrogen at 1,420 Mc./sec*, *Nature* **168** (1951) 356.

[40] S.R. Furlanetto, *The 21-cm Line as a Probe of Reionization*, 1511.01131.

[41] J.D. Bowman, A.E.E. Rogers, R.A. Monsalve, T.J. Mozdzen and N. Mahesh, *An absorption profile centred at 78 megahertz in the sky-averaged spectrum*, *Nature* **555** (2018) 67 [1810.05912].

[42] S. Singh, J. Nambissan T., R. Subrahmanyan, N. Udaya Shankar, B.S. Girish, A. Raghunathan et al., *On the detection of a cosmic dawn signal in the radio background*, *Nature Astron.* **6** (2022) 607 [2112.06778].

[43] P. Gondolo and G. Gelmini, *Cosmic abundances of stable particles: Improved analysis*, *Nucl. Phys. B* **360** (1991) 145.

[44] Y. Hochberg, E. Kuflik, T. Volansky and J.G. Wacker, *Mechanism for Thermal Relic Dark Matter of Strongly Interacting Massive Particles*, *Phys. Rev. Lett.* **113** (2014) 171301 [1402.5143].

[45] F. Zwicky, *Die Rotverschiebung von extragalaktischen Nebeln*, *Helv. Phys. Acta* **6** (1933) 110.

[46] T.S. van Albada, J.N. Bahcall, K. Begeman and R. Sancisi, *Distribution of dark matter in the spiral galaxy NGC 3198.*, **295** (1985) 305.

[47] K.A. Olive and J.A. Peacock, *Big-Bang Cosmology*, *Particle Data Group* (2021) .

[48] M. Pettini, "Fluctuations in the cosmic microwave background." https://people.ast.cam.ac.uk/~pettini/Intro%20Cosmology/Lecture10.pdf.

[49] D. Clowe, M. Bradac, A.H. Gonzalez, M. Markevitch, S.W. Randall, C. Jones et al., *A direct empirical proof of the existence of dark matter*, *Astrophys. J. Lett.* **648** (2006) L109 [astro-ph/0608407].

[50] X-ray: NASA/CXC/CfA/ M. Markevitch et al., Lensing Map: NASA/STScI; ESO WFI; Magellan/U.Arizona/ D.Clowe et al., Optical: NASA/STScI; Magellan/U.Arizona/D.Clowe et al., "The Matter of the Bullet Cluster." https://apod.nasa.gov/apod/ap170115.html, 2017.

[51] J.S. Bullock, *Notes on the missing satellites problem*, 2010.

[52] A.A. Klypin, A.V. Kravtsov, O. Valenzuela and F. Prada, *Where are the missing Galactic satellites?*, *Astrophys. J.* **522** (1999) 82 [astro-ph/9901240].

[53] B. Moore, S. Ghigna, F. Governato, G. Lake, T.R. Quinn, J. Stadel et al., *Dark matter substructure within galactic halos*, *Astrophys. J. Lett.* **524** (1999) L19 [astro-ph/9907411].

[54] G. Kauffmann, S. White and B. Guiderdoni, *The formation and evolution of galaxies within merging dark matter haloes*, *mnras* **264** (1993) 201.

[55] S. Tulin and H.-B. Yu, *Dark Matter Self-interactions and Small Scale Structure*, *Phys. Rept.* **730** (2018) 1 [1705.02358].

[56] J.D. Simon and M. Geha, *The Kinematics of the Ultra-Faint Milky Way Satellites: Solving the Missing Satellite Problem*, *Astrophys. J.* **670** (2007) 313 [0706.0516].

[57] M. Boylan-Kolchin, J.S. Bullock and M. Kaplinghat, *Too big to fail? The puzzling darkness of massive Milky Way subhaloes*, *Mon. Not. Roy. Astron. Soc.* **415** (2011) L40 [1103.0007].

[58] W.J.G. de Blok, *The core-cusp problem*, *Advances in Astronomy* **2010** (2010) 1.

[59] J.F. Navarro, C.S. Frenk and S.D.M. White, *The Structure of cold dark matter halos*, *Astrophys. J.* **462** (1996) 563 [astro-ph/9508025].

[60] K.A. Oman et al., *The unexpected diversity of dwarf galaxy rotation curves*, *Mon. Not. Roy. Astron. Soc.* **452** (2015) 3650 [1504.01437].

[61] A. Kamada, M. Kaplinghat, A.B. Pace and H.-B. Yu, *How the Self-Interacting Dark Matter Model Explains the Diverse Galactic Rotation Curves*, *Phys. Rev. Lett.* **119** (2017) 111102 [1611.02716].

[62] D.N. Spergel and P.J. Steinhardt, *Observational evidence for selfinteracting cold dark matter*, *Phys. Rev. Lett.* **84** (2000) 3760 [astro-ph/9909386].

[63] J. Zavala, M. Vogelsberger and M.G. Walker, *Constraining self-interacting dark matter with the milky way's dwarf spheroidals*, *Monthly Notices of the Royal Astronomical Society: Letters* **431** (2013) L20.

[64] M. Vogelsberger, J. Zavala and A. Loeb, *Subhaloes in self-interacting galactic dark matter haloes*, *Monthly Notices of the Royal Astronomical Society* **423** (2012) 3740.

[65] S.W. Randall, M. Markevitch, D. Clowe, A.H. Gonzalez and M. Bradac, *Constraints on the Self-Interaction Cross-Section of Dark Matter from Numerical Simulations of the Merging Galaxy Cluster 1E 0657-56*, *Astrophys. J.* **679** (2008) 1173 [0704.0261].

[66] M. Kaplinghat, S. Tulin and H.-B. Yu, *Dark Matter Halos as Particle Colliders: Unified Solution to Small-Scale Structure Puzzles from Dwarfs to Clusters*, *Phys. Rev. Lett.* **116** (2016) 041302 [1508.03339].

[67] A. Arbey and F. Mahmoudi, *Dark matter and the early Universe: a review*, *Prog. Part. Nucl. Phys.* **119** (2021) 103865 [2104.11488].

[68] S. Cebrián, *Review on dark matter searches*, in *10th Symposium on Large TPCs for Low-Energy Rare Event Detection*, 5, 2022 [2205.06833].

[69] AMS 02 collaboration, *The antimatter spectrometer (AMS-02): A particle physics detector in space*, *Nucl. Instrum. Meth. A* **588** (2008) 227.

[70] M. Casolino et al., *Launch of the Space experiment PAMELA*, *Adv. Space Res.* **42** (2008) 455 [0708.1808].

[71] J. Cortina, F. Goebel and T. Schweizer, *Technical performance of the magic telescopes*, 2009.

[72] T.C. Weekes et al., *VERITAS: The Very energetic radiation imaging telescope array system*, *Astropart. Phys.* **17** (2002) 221 [astro-ph/0108478].

[73] HESS collaboration, *Search for γ-Ray Line Signals from Dark Matter Annihilations in the Inner Galactic Halo from 10 Years of Observations with H.E.S.S.*, *Phys. Rev. Lett.* **120** (2018) 201101 [1805.05741].

[74] W.B. Atwood, A.A. Abdo, M. Ackermann, W. Althouse, B. Anderson, M. Axelsson et al., *THE LARGE AREA TELESCOPE ON THE FERMI GAMMA-RAY SPACE TELESCOPE MISSION*, *The Astrophysical Journal* **697** (2009) 1071.

[75] HAWC collaboration, *A Search for Dark Matter in the Galactic Halo with HAWC*, *JCAP* **02** (2018) 049 [1710.10288].

[76] CTA Consortium collaboration, B.S. Acharya et al., *Science with the Cherenkov Telescope Array*, WSP (11, 2018), 10.1142/10986, [1709.07997].

[77] ANTARES collaboration, *Search for dark matter towards the Galactic Centre with 11 years of ANTARES data*, *Phys. Lett. B* **805** (2020) 135439 [1912.05296].

[78] IceCube collaboration, *Search for neutrino lines from dark matter annihilation and decay with IceCube*, 2303.13663.

[79] Super-Kamiokande collaboration, *Indirect search for dark matter from the Galactic Center and halo with the Super-Kamiokande detector*, *Phys. Rev. D* **102** (2020) 072002 [2005.05109].

[80] M. Ibe, W. Nakano, Y. Shoji and K. Suzuki, *Migdal Effect in Dark Matter Direct Detection Experiments*, *JHEP* **03** (2018) 194 [1707.07258].

[81] XENON collaboration, *Search for Light Dark Matter Interactions Enhanced by the Migdal Effect or Bremsstrahlung in XENON1T*, *Phys. Rev. Lett.* **123** (2019) 241803 [1907.12771].

[82] LUX collaboration, *Results of a Search for Sub-GeV Dark Matter Using 2013 LUX Data*, *Phys. Rev. Lett.* **122** (2019) 131301 [1811.11241].

[83] N.F. Bell, J.B. Dent, J.L. Newstead, S. Sabharwal and T.J. Weiler, *Migdal effect and photon bremsstrahlung in effective field theories of dark matter direct detection and coherent elastic neutrino-nucleus scattering*, *Phys. Rev. D* **101** (2020) 015012 [1905.00046].

[84] C. Kouvaris and J. Pradler, *Probing sub-GeV Dark Matter with conventional detectors*, *Phys. Rev. Lett.* **118** (2017) 031803 [1607.01789].

[85] SENSEI collaboration, *SENSEI: Direct-Detection Results on sub-GeV Dark Matter from a New Skipper-CCD*, *Phys. Rev. Lett.* **125** (2020) 171802 [2004.11378].

[86] PandaX-II collaboration, *Results of dark matter search using the full PandaX-II exposure*, *Chin. Phys. C* **44** (2020) 125001 [2007.15469].

[87] ATLAS collaboration, *The ATLAS Experiment at the CERN Large Hadron Collider*, *JINST* **3** (2008) S08003.

[88] CMS collaboration, *CMS Physics: Technical Design Report Volume 1: Detector Performance and Software*, .

[89] LHCb collaboration, *The LHCb Detector at the LHC*, JINST **3** (2008) S08005.

[90] BaBar collaboration, *The BaBar detector*, Nucl. Instrum. Meth. A **479** (2002) 1 [hep-ex/0105044].

[91] Belle-II collaboration, *Belle II Technical Design Report*, 1011.0352.

[92] DAMA collaboration, *The DAMA/LIBRA apparatus*, Nucl. Instrum. Meth. A **592** (2008) 297 [0804.2738].

[93] COSINE-100 collaboration, *An induced annual modulation signature in COSINE-100 data by DAMA/LIBRA's analysis method*, Sci. Rep. **13** (2023) 4676 [2208.05158].

[94] J. Amaré et al., *First Results on Dark Matter Annual Modulation from the ANAIS-112 Experiment*, Phys. Rev. Lett. **123** (2019) 031301 [1903.03973].

[95] J. Amare et al., *Annual modulation results from three-year exposure of ANAIS-112*, Phys. Rev. D **103** (2021) 102005 [2103.01175].

[96] XENON collaboration, *Excess electronic recoil events in XENON1T*, Phys. Rev. D **102** (2020) 072004 [2006.09721].

[97] XENON collaboration, *Search for New Physics in Electronic Recoil Data from XENONnT*, Phys. Rev. Lett. **129** (2022) 161805 [2207.11330].

[98] AMS collaboration, *First Result from the Alpha Magnetic Spectrometer on the International Space Station: Precision Measurement of the Positron Fraction in Primary Cosmic Rays of 0.5–350 GeV*, Phys. Rev. Lett. **110** (2013) 141102.

[99] Y. Hochberg, *SIMP Dark Matter*, SciPost Phys. Lect. Notes (2022) 59.

[100] S. Bhattacharya, P. Ghosh and S. Verma, *SIMPler realisation of Scalar Dark Matter*, JCAP **01** (2020) 040 [1904.07562].

[101] M. Lisanti, *Lectures on Dark Matter Physics*, in *Theoretical Advanced Study Institute in Elementary Particle Physics: New Frontiers in Fields and Strings*, pp. 399–446, 2017, DOI [1603.03797].

[102] D.G. Cerdeño, *Dark matter 101 dark matter 101 from production to detection*, 2016.

[103] Y. Hochberg, E. Kuflik, H. Murayama, T. Volansky and J.G. Wacker, *Model for Thermal Relic Dark Matter of Strongly Interacting Massive Particles*, Phys. Rev. Lett. **115** (2015) 021301 [1411.3727].

[104] E.D. Carlson, M.E. Machacek and L.J. Hall, *Self-interacting dark matter*, Astrophys. J. **398** (1992) 43.

[105] A.A. de Laix, R.J. Scherrer and R.K. Schaefer, *Constraints of selfinteracting dark matter*, Astrophys. J. **452** (1995) 495 [astro-ph/9502087].

[106] Y. Hochberg, E. Kuflik and H. Murayama, *SIMP Spectroscopy*, JHEP **05** (2016) 090 [1512.07917].

[107] D.B. Kaplan, *Five lectures on effective field theory*, 10, 2005 [nucl-th/0510023].

[108] E. Witten, *Global Aspects of Current Algebra*, Nucl. Phys. B **223** (1983) 422.

[109] E. Witten, *Current Algebra, Baryons, and Quark Confinement*, *Nucl. Phys. B* **223** (1983) 433.

[110] J. Wess and B. Zumino, *Consequences of anomalous Ward identities*, *Phys. Lett. B* **37** (1971) 95.

[111] D. Tong, "Lecture Notes: Gauge Theory." http://www.damtp.cam.ac.uk/user/tong/gaugetheory.html, 2018.

[112] M.E. Peskin and D.V. Schroeder, *An Introduction to quantum field theory*, Addison-Wesley, Reading, USA (1995).

[113] M. Srednicki, *Quantum Field Theory*, Cambridge University Press (2007), 10.1017/CBO9780511813917.

[114] J.B. Kogut, M.A. Stephanov, D. Toublan, J.J.M. Verbaarschot and A. Zhitnitsky, *QCD - like theories at finite baryon density*, *Nucl. Phys. B* **582** (2000) 477 [hep-ph/0001171].

[115] J. Gasser and H. Leutwyler, *Chiral Perturbation Theory: Expansions in the Mass of the Strange Quark*, *Nucl. Phys. B* **250** (1985) 465.

[116] G. Cacciapaglia, C. Pica and F. Sannino, *Fundamental Composite Dynamics: A Review*, *Phys. Rept.* **877** (2020) 1 [2002.04914].

[117] K. Petraki, M. Postma and M. Wiechers, *Dark-matter bound states from Feynman diagrams*, *JHEP* **06** (2015) 128 [1505.00109].

[118] M.E. Peskin, *The Alignment of the Vacuum in Theories of Technicolor*, *Nucl. Phys. B* **175** (1980) 197.

[119] J. Edsjo and P. Gondolo, *Neutralino relic density including coannihilations*, *Phys. Rev. D* **56** (1997) 1879 [hep-ph/9704361].

[120] M. Cannoni, *Relativistic* $<\sigma v_{rel}>$ *in the calculation of relics abundances: a closer look*, *Phys. Rev. D* **89** (2014) 103533 [1311.4494].

[121] N. Brambilla, D. Eiras, A. Pineda, J. Soto and A. Vairo, *Inclusive decays of heavy quarkonium to light particles*, *Phys. Rev. D* **67** (2003) 034018 [hep-ph/0208019].

[122] S. Biondini and V. Shtabovenko, *Bound-state formation, dissociation and decays of darkonium with potential non-relativistic Yukawa theory for scalar and pseudoscalar mediators*, *JHEP* **03** (2022) 172 [2112.10145].

[123] A. Kamada, S. Kobayashi and T. Kuwahara, *Perturbative Unitarity of Strongly Interacting Massive Particle Models*, 2210.01393.

[124] M. Cirelli, G. Corcella, A. Hektor, G. Hutsi, M. Kadastik, P. Panci et al., *PPPC 4 DM ID: A Poor Particle Physicist Cookbook for Dark Matter Indirect Detection*, *JCAP* **03** (2011) 051 [1012.4515].

[125] P. Ullio, L. Bergstrom, J. Edsjo and C.G. Lacey, *Cosmological dark matter annihilations into gamma-rays - a closer look*, *Phys. Rev. D* **66** (2002) 123502 [astro-ph/0207125].

[126] Y. Cui, M. Pospelov and J. Pradler, *Signatures of Dark Radiation in Neutrino and Dark Matter Detectors*, *Phys. Rev. D* **97** (2018) 103004 [1711.04531].

[127] J. Billard, L. Strigari and E. Figueroa-Feliciano, *Implication of neutrino backgrounds on the*

reach of next generation dark matter direct detection experiments, Phys. Rev. D **89** (2014) 023524 [1307.5458].

[128] W.C. Haxton, R.G. Hamish Robertson and A.M. Serenelli, *Solar Neutrinos: Status and Prospects*, Ann. Rev. Astron. Astrophys. **51** (2013) 21 [1208.5723].

[129] V.A. Naumov, *Solar neutrinos. Astrophysical aspects*, Phys. Part. Nucl. Lett. **8** (2011) 683.

[130] M. Wiescher, J. Görres, E. Uberseder, G. Imbriani and M. Pignatari, *The cold and hot cno cycles*, Annual Review of Nuclear and Particle Science **60** (2010) 381.

[131] T. Kajita, *Atmospheric neutrinos*, New J. Phys. **6** (2004) 194.

[132] T.K. Gaisser and M. Honda, *Flux of atmospheric neutrinos*, Ann. Rev. Nucl. Part. Sci. **52** (2002) 153 [hep-ph/0203272].

[133] B.T. Cleveland, T. Daily, R. Davis, Jr., J.R. Distel, K. Lande, C.K. Lee et al., *Measurement of the solar electron neutrino flux with the Homestake chlorine detector*, Astrophys. J. **496** (1998) 505.

[134] GALLEX collaboration, *GALLEX solar neutrino observations: Results for GALLEX IV*, Phys. Lett. B **447** (1999) 127.

[135] SAGE collaboration, *Measurement of the solar neutrino capture rate with gallium metal*, Phys. Rev. C **60** (1999) 055801 [astro-ph/9907113].

[136] Super-Kamiokande collaboration, *Measurements of the solar neutrino flux from Super-Kamiokande's first 300 days*, Phys. Rev. Lett. **81** (1998) 1158 [hep-ex/9805021].

[137] Super-Kamiokande collaboration, *Measurement of a small atmospheric muon-neutrino / electron-neutrino ratio*, Phys. Lett. B **433** (1998) 9 [hep-ex/9803006].

[138] J.F. Beacom, *The Diffuse Supernova Neutrino Background*, Ann. Rev. Nucl. Part. Sci. **60** (2010) 439 [1004.3311].

[139] G.G. Raffelt, *Stars as laboratories for fundamental physics: The astrophysics of neutrinos, axions, and other weakly interacting particles* (5, 1996).

[140] M. Koshiba, K. Hirata, T. Kajita, M. Koshiba, M. Nakahata, Y. Ohyama et al., *Supernova neutrino signal and kamiokande-ii*, Nuclear Physics B - Proceedings Supplements **3** (1988) 441.

[141] K.S. Hirata et al., *Observation in the Kamiokande-II Detector of the Neutrino Burst from Supernova SN 1987a*, Phys. Rev. D **38** (1988) 448.

[142] Kamiokande-II collaboration, *Observation of a Neutrino Burst from the Supernova SN 1987a*, Phys. Rev. Lett. **58** (1987) 1490.

[143] IMB collaboration, *Angular Distribution of Events From Sn1987a*, Phys. Rev. D **37** (1988) 3361.

[144] R.M. Bionta et al., *Observation of a Neutrino Burst in Coincidence with Supernova SN 1987a in the Large Magellanic Cloud*, Phys. Rev. Lett. **58** (1987) 1494.

[145] S. Ando and K. Sato, *Relic neutrino background from cosmological supernovae*, New J. Phys. **6** (2004) 170 [astro-ph/0410061].

[146] S. Horiuchi, J.F. Beacom and E. Dwek, *The Diffuse Supernova Neutrino Background is detectable in Super-Kamiokande*, Phys. Rev. D **79** (2009) 083013 [0812.3157].

[147] A.M. Hopkins and J.F. Beacom, *On the normalisation of the cosmic star formation history*, *Astrophys. J.* **651** (2006) 142 [astro-ph/0601463].

[148] J. Bahcall, "Solar neutrinos - software and data for solar neutrino research." http://www.sns.ias.edu/~jnb/.

[149] G. Battistoni, A. Ferrari, T. Montaruli and P.R. Sala, *The atmospheric neutrino flux below 100-MeV: The FLUKA results*, *Astropart. Phys.* **23** (2005) 526.

[150] S. Betts et al., *Development of a Relic Neutrino Detection Experiment at PTOLEMY: Princeton Tritium Observatory for Light, Early-Universe, Massive-Neutrino Yield*, in *Community Summer Study 2013: Snowmass on the Mississippi*, 7, 2013 [1307.4738].

[151] PTOLEMY collaboration, *PTOLEMY: A Proposal for Thermal Relic Detection of Massive Neutrinos and Directional Detection of MeV Dark Matter*, 1808.01892.

[152] M. Messina, "The ptolemy experiment, a path from a dream to a challenging project." http://dpnc.unige.ch/seminaire/talks/messina.pdf, 2019.

[153] PTOLEMY collaboration, *Heisenberg's uncertainty principle in the PTOLEMY project: A theory update*, *Phys. Rev. D* **106** (2022) 053002 [2203.11228].

[154] Y. Cheipesh, V. Cheianov and A. Boyarsky, *Navigating the pitfalls of relic neutrino detection*, *Phys. Rev. D* **104** (2021) 116004 [2101.10069].

[155] PTOLEMY collaboration, *Neutrino physics with the PTOLEMY project: active neutrino properties and the light sterile case*, *JCAP* **07** (2019) 047 [1902.05508].

[156] S.S. Masood, S. Nasri and J. Schechter, *Fine structure of beta decay endpoint spectrum*, *Int. J. Mod. Phys. A* **21** (2006) 517 [hep-ph/0505183].

[157] KATRIN collaboration, *KATRIN: A Next generation tritium beta decay experiment with sub-eV sensitivity for the electron neutrino mass. Letter of intent*, hep-ex/0109033.

[158] M. Pospelov, *Neutrino Physics with Dark Matter Experiments and the Signature of New Baryonic Neutral Currents*, *Phys. Rev. D* **84** (2011) 085008 [1103.3261].

[159] M. Pospelov and J. Pradler, *Elastic scattering signals of solar neutrinos with enhanced baryonic currents*, *Phys. Rev. D* **85** (2012) 113016 [1203.0545].

[160] B. Batell, P. deNiverville, D. McKeen, M. Pospelov and A. Ritz, *Leptophobic Dark Matter at Neutrino Factories*, *Phys. Rev. D* **90** (2014) 115014 [1405.7049].

[161] S. Tulin, *New weakly-coupled forces hidden in low-energy QCD*, *Phys. Rev. D* **89** (2014) 114008 [1404.4370].

[162] G. Cowan, *Statistical data analysis* (1998).

[163] G. Cowan, K. Cranmer, E. Gross and O. Vitells, *Asymptotic formulae for likelihood-based tests of new physics*, *Eur. Phys. J. C* **71** (2011) 1554 [1007.1727].

[164] G. Cowan, "Statistics and Discoveries at the LHC." https://indico.cern.ch/event/77830/, 2010.